論文 / 著書情報
Article / Book Information

題目(和文)	DCアーク法によるナノ材料合成における電極現象の研究
Title(English)	Investigation of Electrode Phenomena for Nanomaterial Production by DC Arc Discharge Method
著者(和文)	梁風
Author(English)	FENG LIANG
出典(和文)	学位:博士(工学), 学位授与機関:東京工業大学, 報告番号:甲第9531号, 授与年月日:2014年3月26日, 学位の種別:課程博士, 審査員:渡邉　隆行,馬場　俊秀,山口　猛央,石谷　暖郎,沖野　晃俊
Citation(English)	Degree:Doctor (Engineering), Conferring organization: Tokyo Institute of Technology, Report number:甲第9531号, Conferred date:2014/3/26, Degree Type:Course doctor, Examiner:,,,,
学位種別(和文)	博士論文
Type(English)	Doctoral Thesis

Investigation of Electrode Phenomena for Nanomaterial Production by DC Arc Discharge Method

Tokyo Institute of Technology

Feng Liang

2014

Contents

Acknowledgements

1. Introduction

1.1 Definition of the Plasma State

Plasma is the fourth fundamental state of matter, composed of a mixture of electrons, ions, and neutral species in local electrical neutrality. More than 99% of the observable mass in the universe is dominated by plasma state, which is the fundamental state of material, such as solid, liquid, gas, and plasma.

Plasmas can be distinguished into two main groups: non-thermal plasmas and thermal plasmas. The non-thermal plasmas, also called non-equilibrium plasmas or cold plasmas, refer to the plasmas where the electron temperature was much higher than the plasma ions and the neutrals components which remain at or near room temperature. On the other hand, the thermal plasmas are classically defined by the state in or close to local thermodynamic equilibrium (LTE) where the electron temperature approaches to the temperatures of the plasma ions and the neutrals components (Okazaki and Watanabe 1999).

1.2 Thermal Plasma

1.2.1 Definition of Thermal Plasma

Among these plasmas, thermal plasmas are those in which the temperature of heavy species is approximately equal to the temperature of electron typically in the range 10 000-25 000 K. Thermal plasmas are classically defined by the state in or close to LTE. When high power is injected into a relatively high-pressure (such as 10^5 pa) gas, the high collision frequencies in plasmas make them achieve LTE. Thermal plasmas have been applied in lots of fields due to the following advantages (Okazaki et al. 1999):

(i) High energy density allows them being used for the melting and modification of hard, high temperature materials.

(ii) High enthalpy to enhance the reaction kinetics.

(iii) High chemical reactivity due to the high concentration of the chemical reactive species, such as ions, radicals, and elections.

(iv) Rapid quench rates to obtain non-equilibrium compositions or metastable materials.

(v) Free selectivity of the atmosphere such as inert, oxidation, reduction atmospheres in accordance with required reaction conditions.

1.2.2 The Generation of Thermal Plasma

The most widely used methods for generating thermal plasmas include direct current (DC) arc, alternating current (AC) arc, radio frequency (RF) inductively coupled discharge, microwave discharge and so on (Boulos et al. 1994). These four routes will be introduced in the following section.

(a) DC Arc

The arcs are generated using an electric discharge, capable of independent existence in gases. DC arc is generated by means of a direct current discharge. Electric arcs are initiated by three basically different ways such as electrode contact, pre-ionization of the discharge gap and high-voltage breakdown. Breakdown of the originally non-conducting gas establishes a conducting path between the electrodes. The choice of the method for striking an arc mainly depends on the arc arrangement and the electrode configuration. According to the potential distribution, electric arc can be divided into three regions: the cathodes region, the arc column, and the anode region. Due to the simple generation system and relatively low cost of DC arc, non-transferred arcs and transferred arcs are the most widely used plasma devices for materials processing.

If the arc is operated at current levels $I > 50$ A and pressures $p > 10$ kPa, it can be defined as high intensity arc (Boulos et al. 1994). Compared with low-intensity arcs, high-intensity arcs are characterized by strong macroscopic flows induced by the arc itself (Pfender. 1978). As shown in Fig. 1.1, any variation of the current-carrying cross section of the arc leads to a pumping action by the interaction of the arc current with its own magnetic field. Flow velocities at the order of 100 m s^{-1} are produced in the following case, sufficiently high current over than 100 A, and axial current density variations. The cathode jet phenomenon is a typical example.

(b) AC Arc

The conventional single-phase and three-phase AC power supplies have a characteristic of intermittent discharge which limits the application of arc systems (Fulcheri et al. 2000). To obtain a more effective arc reactor, multi-phase AC has been proposed (Matsuura et al. 2007). Multi-phase AC arc as a new generator of thermal plasma is introduced in this part, which is controlled by multiple electrode configurations The attractive characteristic of a multi-phase AC power supply is larger number of discharging paths among the electrodes. Therefore, discharges among the electrodes always exist to realize smooth arc re-ignition. Consequently, the multi-phase AC arc have been attracted to be applied to waste treatment, synthesis of nano-sized materials, and in-flight glass melting processes (Watanabe et al. 2010). Compared with DC arc, the multiphase arc seems to be more expedient for applying in large scale plasma process.

Multiphase AC arc was applied as an innovative in-flight technology in recent years due to its high energy efficiency, large plasma volume, low velocity, easy scale up, and low cost (Yao et al. 2008). For example, in a 6-phase AC arc, the maximum plasma velocity is up to 20 m s^{-1} and the plasma temperature is over 6000 K when the input power is 22 kW and the sheath gas flow rate is 36 L min^{-1} (Yao et al. 2009). The lower plasma velocity leads to comparatively longer residence time of particles during plasma in-flight treatment.

(c) RF Thermal Plasma

Radio-frequency (RF) inductively coupled thermal plasma is generated by a high-power inductive discharge at or close to atmospheric pressure (Shigeta 2012). The excitation frequency is typically between 200 kHz and 100 MHz. RF thermal plasma offers a large volume of contamination-free plasma with low velocity because it is produced in a large torch without internal electrodes. As a result, RF thermal plasmas have been used as promising tools for spray processes (Boulos 1992), waste treatment (Heberlein and Murphy 2008), and nano-material fabrication (Shigeta and Murphy 2011). However, in contrast to DC arc plasma, the lower productivity of RF plasma process increases the running cost.

(d) Microwave Discharge

Microwave discharges are considered to be viable plasma sources, although electric arcs and inductively coupled RF discharges play a dominant role as thermal plasma sources. The development of more flexible microwave devices is to make use of electromagnetic surface waves or traveling wave discharges (TWD) for sustaining plasmas. In general, a microwave plasma reactor is mainly composed of a microwave power supply, a circulator, an applicator, and a plasma load. The plasma can be generated for frequency ranging from 1 MHz to 10 GHz, pressure from 10^{-3} Pa to several hundred kPa. The plasmas produced by TWD may approach a state of LTE at the high pressure level ($p>10$ kPa).

1.3 Electrode Phenomenon

1.3.1 Electrode Temperature Measurement

The electrode surface temperature affects the distribution of the current density over the electrode surface and as a result has an important role in determining the arc mode of operation. Accurate measurements of electrode temperatures are essential for analysis of interactions between the plasma and the electrode. In addition, electrode temperature is important to understand the erosion phenomena of electrode material and the interactions between the arc and the electrodes. Moreover, the anode surface temperature plays an important role in the evaporation of raw material for nanoparticle syntheses. Therefore, some experimental works have been reported to evaluate the electrode surface temperature (Zhou et al. 1996; Reinelt et al. 2011; Liang et al. 2013).

Cathode temperature distributions with high spatial resolution have been measured by using an optical multichannel analyzer (OMA)/spectrometer system to investigate the erosion mechanism of cathode. Both of single-color pyrometry and two-color pyrometry have been employed to measure the cathode temperature distributions. These methods have their own advantages and disadvantages. The emissivity of cathode surface is required for single-color pyrometry, but it reduces the noise in the intensity signal due to the exponential relationship between the temperature and the intensity. In contrast, two-color pyrometry minimizes the effect of the cathode surface emissivity; however, it amplifies the noise in the intensity signal because intensity ratio is used to estimate the temperature (Zhou et al. 1996).

The surface temperature of various oxide-tungsten cathodes was measured by using a two-wavelength pyrometry. Temperature profiles are also presented for thoriated tungsten cathodes with different cathode cone angles, arc currents and compositions of the gas provided to the arc (Haidar et al. 1995). Two-color pyrometry was conducted to obtain the surface temperature of weld pools, in which the weld pool was photographed by a high-speed camera during arc welding. Two wavelengths (950 and 980 nm) of light in the infrared range were selected from the thermal radiation light emitted from the weld pool at the instant when the arc was extinguished, using an imaging spectroscope (Yamazaki et al. 2010). In addition, the temperature of electrode was measured by two-color pyrometry combined with a high-speed camera to investigate the erosion mechanism of electrode in multi-phase AC arc (Tanaka et al. 2012).

1.3.2 Arc-Anode Attachment

It is now well known that there are three typical arc-anode attachment modes, diffuse attachment, multiple attachments, and constricted attachment at the anode boundary (Dinulescu and Pfender 1980; Sanders et al. 1982; Heberlein et al. 2010). The conceptual diagram of three arc-anode attachment modes is shown in Fig. 1.2. As the cathode jet impinges on the anode surface, a stagnation layer forms in front of the anode resulting in the well-known bell shape of the arc. With increasing current, the strength of the cathode jet increases. In this situation, the anode arc root is rather diffuse. Since the cathode jet is responsible for this particular anode arc root, this mode of anode arc attachment is denoted as cathode jet dominated (CJD) or diffuse mode. An entirely different mode of anode arc attachment is observed with the same current and with the same arc geometry, provided that the flow towards the anode is substantially reduced or entirely eliminated. In this case the anode arc root appears more or less constricted, giving rise to the same type of magnetohydrodynamic (MHD) pumping as observed at the cathode. The entrained gas in the anode region is heated by the arc and accelerated towards the cathode. The flow from the cathode cannot be entirely eliminated; i.e., the flow from the cathode will impinge with the flow from the anode forming a stagnation layer. This so called anode jet dominated (AJD) mode or constricted mode is formed. Multiple attachment mode is considered as the transition between diffuse mode and constricted mode.

Controlling the anode attachment is important in lots of applications because the attachment mode determines anode lifetime and plasma generator performance. Therefore, several studies have been performed over the past 30 years to determine the conditions for which either of the attachment modes will be obtained (Yang and Herberlein 2007). Heberlein *et al* investigated the formation mechanism and the characteristics of arc-anode attachment modes by using water-cooled cupper anode (Yang et al. 2006; Yang and Herberlein, 2007; Heberlein et al. 2010).

Three typical arc-anode attachment models also were observed when using hydrogen arc to prepare nanomaterial. Metal as raw material was put on the water-cooled cupper anode to prepare metal nanoparticle. The formation mechanism of different arc-anode attachment modes was investigated (Watanabe et al. 2013). The anode attachment modes are the results of the competition between the cathode jet and the anode jet. When the cathode jet is strong, the anode attachment mode is the diffuse mode. The arc transitions to the multiple-attachment mode with reducing the cathode jet by controlling the shield gas flow rate. Further decreasing the cathode jet increases the current density, which leads to the strong anode jet flow and to the entrainment of cold gas along the anode towards the arc attachment. The increase of the radial heat loss due to the anode jet makes a single constricted attachment take over the most of the current and stabilizes it.

1.4 The Application of Thermal Plasmas

1.4.1 Waste Treatment

The application of thermal plasma for treatment of wastes has had a fascination for several years, since anything can be vaporized and any chemical bonds can be destroyed in thermal plasma region (Heberlein and Murphy 2008).

Perfluorocompounds (PFCs) were decomposed on a large scale with nitrogen thermal plasma generated from the hollow electrodes plasma torch (Choi et al. 2012). In addition, the water plasma generated by DC arc discharge was employed to decompose hydrofluoroethylene (HFC) (Watanabe et al. 2008), fluorinated compounds (Narengerile et al. 2010), phenol (Narengerile et al. 2011), acetone (Narengerile et al. 2012), decanol emulsion (Choi et al. 2012). The decomposition mechanism of organic compounds in water plasmas was proposed and the roles of intermediate species such as CH, CH_3, and OH have been investigated (Watanabe et al. 2011).

1.4.2 Metallurgy

Thermal plasma technology has the following advantages compared with traditional metallurgical technologies (Taylor and Pirzada 1995).

(i) Almost all of refractory metals can be melted and refined in clean environments by using plasma reactors, since the high enthalpy of thermal plasma.

(ii) The atmosphere in plasma reactors can be changed easily according to the process requirements and refractory lining.

(iii) Post treatment of the raw material is not required, leading to savings in energy and capital on the raw material preparation.

(iv) The steep temperature gradients can prepare the products with valuable metastable phases and special properties.

Moreover, one of the promising directions of accelerating the application of plasma metallurgy is the development of mini plants compared with conventional techniques. The first thermal plasma reactor used in steel melting is Linde reactor (Mccullough. 1962). Argon was employed as plasma gas, water cooled cupper was used as anode, which was connected to the molten pool. Magnetic coil was used for stirring the molten pool. Rapid wear of bottom electrode and high erosion rate of the refractory lining limit its application.

Many efforts have been made to develop the application of thermal plasma in metallurgy. For example, metallurgical grade silicon was purified using hydrogenated argon RF plasma. The purification was carried out by two steps, firstly, the evaporation of silicon particle results in the elimination of the superficial impurities when the silicon was injected into the plasma jet. In addition, the remaining impurities were concentrated in the last crystallized part based on the fusion zone principle (Benmansour et al. 2004).

1.4.3 Welding and Cutting

Arc welding is a type of process which uses a welding power supply to create an electric arc between an electrode and the base material to melt the metals at the welding point. Direct current, alternating current, consumable or non-consumable electrodes can be used. Arc welding is an indispensable process in manufacturing industry. For example, it is used in the construction of ships, bridges, buildings and pipelines, aerospace, automotive, and electronic industries and also in steel mills, since the stable and intense heat source is provided with a relatively low cost (Tanaka et al. 2007).

According to the welding handbook “the plasma arc cutting process severs metal by using a constricted arc to melt a localized area of a work-piece, removing the molten material with a high-velocity jet of ionized gas issuing from the constricting nozzle” (Nemchinsky and Severance 2006). It has wide applications in industrial field. Different metals can be cut by this process, and the shape is controlled by the computer numerically controlled (CNC) machines.

1.4.4 Plasma Spraying

Plasma spraying techniques are coating processes in which melted (or heated) materials are sprayed onto a surface of substrate. Materials are protected against wear, erosion, corrosion, and thermal loads by plasma spraying (Fauchais 2004). Plasma spray is the most versatile of the thermal spray processes. Coating materials available for thermal spraying include metals, alloys, ceramics, plastics and composites. Besides DC torches, RF plasma torches may also be used for this spray process. Plasma spraying has been applied in a wide range of industries, including high added value products, high-tech industries (aeronautic and nuclear industries), and automotive industry.

Although plasma spraying has been known for more than 40 years, our knowledge of understanding fundamentals of the plasma spraying is still incomplete, particular with regard to the behavior of the plasma jet, the interaction of the plasma with the injected powder particles, and the coating formation.

1.4.5 Material Synthesis

Since the thermal plasma provides large evaporation rate, steep temperature gradients, and high chemical reactivity, it is increasingly being recognized as a powerful tool for the synthesis and processing of a wide range of high added value materials. Metal nanoparticles, alloy and intermetallic compounds nanoparticles, oxide nanoparticles, nitride nanoparticles, and carbide nanoparticles were synthesized by thermal plasma successfully. These material synthesized by thermal plasmas will be reviewed in next section.

1.5 Synthesis of Nanoparticle by Thermal Plasmas

1.5.1 DC Arc Discharge

(a) Metal Nanoparticles

Metal nanoparticles of Mg, Ni, Co, Cu, and Fe were prepared by using 50%-H_2 arc for the application of hydrogen storage materials (Shao et al. 2004; Shao et al. 2008). These nanoparticles had a granular structure and the particle size ranges from several nanometers to tens of nanometers. In the case of Ni, Co, Cu, and Fe, the average particle sizes were about 30-50 nm. In contrast, the average particle size was about 300 nm for Mg. The difference of particle sizes between Mg and the other metals was explained by the difference of the vaporization rates. The vaporization rate of Mg was much higher than that of other metals resulting in the higher metal-vapor concentration in the growth region.

Especially, nickel nanoparticles have attracted much attention because of their excellent chemical, physical, and electronic properties. Fine nickel powders have great potential technological applications such as chemical catalysts, microwave absorbing materials, medical diagnosis, magnetic recording media, and internal electrode in multi-layer ceramic capacitors (MLCCs) (Lan et al. 2011; Zhang et al. 2006; Hernandez et al. 2002; Cordente et al. 2001; Park et al. 2006). Ni nanoparticles were prepared at the rate of 1.3 g/min by anodic arc plasma (Wei et al. 2006). The effect of arc current and gas pressure were investigated, the yield rate and particle size increase with the increase of the arc current or gas pressure.

(b) Alloy and Intermetallic Compounds Nanoparticles

Spherical shape Sn-Ag nanoparticles with several tens nanometers were successfully prepared by DC arc plasma with hydrogen addition. The vaporization of Sn from Sn-Ag mixture was enhanced by hydrogen in arc plasma, due to the formation of intermediate products such as hydride and/or activity modification (Tanaka and Watanabe 2008; Tanaka and Watanabe 2013). As shown in Fig. 1.3, the formation mechanism of nanoparticle in DC arc discharge method can be explained as follows, the metal vapor grows into nanoparticle by condensation and collision after nucleation.

Fe-Ni alloy with mean particle size less than 35 mm were prepared with productive rate of ~0.1 g min^{-1} by the arc discharge method (Li et al. 1997a). The Fe-Ni mixture was selected as the raw materials. The saturation magnetization of the prepared nanoparticles decrease significantly compared with the bulk Fe-Ni alloys. In addition, Fe-Cr alloy over wide composition range with an average diameter less than 35 nm were also synthesized by the hydrogen plasma- metal reaction (HPMR) method (Li et al. 1997b).

The preparation of the intermetallic nanoparticles has also attracted much attention, since the intermetallic compounds have excellent properties such as high melting temperature, lightweight, good corrosion resistance, and excellent mechanical properties. These intermetallics have great potential for applying in the field of automobile engines, aircraft, and electricity generation and energy conversion equipment. Si-based intermetallic compounds nanoparticles were successfully synthesized from Si-M (Mo, Ti, V) mixture by the arc discharge method (Watanabe et al. 2001). $MoSi_2$ nanoparticles were prepared from 85wt%-Mo raw material by 50%-H_2 arc. In addition, $TiSi_2$ nanoparticles were successfully prepared from the raw material composed of 60wt%-Ti by 50%-H_2 arc, and single phase VSi_2 nanoparticles were successfully synthesized from the raw material composed of 60wt%-V at the same arc condition.

(c) Oxide Nanoparticles

Fe_3O_4 nanoparticle as magnetic material was prepared from the raw material of Fe ingot by the DC arc discharge method at air atmosphere (Chazelas et al. 2006). In order to control the particle size distributions, the anode heat transfer was regulated by rotating the anode material, leading to the anode surface with controlled temperature and well-controlled vaporization rates of the anode material.

Oxidation of Fe ultrafine particles were prepared by DC arc discharge method (Li et al. 1998). A piece of bulk Fe was melted by the arc at a mixing 50% H_2 and 50% Ar gas of 0.1 MPa. In order to prevent Fe ultrafine particles from burning up, particles were passivated with an Ar/air mixture before they were taken out from the arc melting chamber. It was found that α-Fe_2O_3 and γ-Fe_2O_3 are formed at different temperatures, which leads to significant changes in the particle features and magnetic properties.

(d) Nitride Nanoparticles

AlN ultrafine powders were synthesized by non-transferred DC plasma arc at atmospheric pressure (Oh et al. 1998). Aluminum vapor did not react with nitrogen properly in the cold-wall reactor, but the extent of conversion was improved by using NH_3 gas. Amorphous AlN was formed by rapid quenching from a water-cooled reactor wall. In the hot-wall reactor, the powder deposited on the graphite wall was well crystallized, but the powder deposited on the collection vessel did not react properly in nitrogen atmosphere.

Composites Fe-TiN nanoparticles were successfully prepared from the metal ingots of Fe and Ti by N_2 arc plasma using two electrodes in a conventional arc chamber (Sakka et al. 2002). The morphology of Fe was spherical and that of the composite Fe-TiN nanoparticles was dumbbell-like. The hydrogen absorption-desorption characteristics were investigated. Hydrogen desorption at above 450 K was observed for the composite Fe-TiN nanoparticles.

1.5.2 RF Thermal Plasma

Spherical nickel nanoparticles are prepared by RF plasma via hydrogen reduction of nickel hydroxide/carbonate (Bai et al. 2009). The metallic nickel powders could be obtained. Well-dispread spheres particle with an average diameter of about 60-100 nm, and high tap density were obtained. The use of nickel hydroxide/carbonate could keep the product with high purity and environmental safety.

Spherical submicron-sized powder of copper are synthesized through the condensation from a vapor phase with a significantly high degree of super saturation in RF thermal plasmas (Kobayashi et al. 2008). Powder feed rate, reactor pressure, and gas flow rate of hydrogen were selected to control the size of synthesized spherical particles. The particle size was deiced by the concentration of the metal vapor.

Metals doped TiO_2 with high photocatalytic performance was synthesized via Ar/O_2 RF thermal plasma. At high temperature of RF plasma, Nb^{5+} doping played an important role not only in restraining nanoparticle growth but also in avoiding binding between crystallites (Zhang et al. 2011). In addition, titanium boride functional nanoparticles with the average crystalline diameter ranging from 10 to 30 nm were synthesized by RF induction thermal plasma. The experimental and numerical results showed good agreement that the crystalline diameter of the product increases with the powder feed rate and titanium content in the feeding powders. The growth mechanism was suggested in the term of condensational growth (Cheng et al. 2012).

1.6 Synthesis of Carbon Nanomaterial by Thermal Plasmas

Carbon has many kinds of allotropes such as graphite, diamond, amorphous carbon, fullerene, carbon onion, nanotube, graphene and so on due to its hybridization state and atomic arrangement. Because of their excellent chemical, physical, and electronic properties, they have enormous applications. Thermal plasmas are considered as an attractive route to synthesize carbon nanomaterial with the following advantages. It can be operated at atmospheric pressure;

high volume of carbon nanomaterial can be fabricated; arc discharge method is a low cost and eco-friendly technique; moreover, the carbon nanomaterial with low defects can be obtained. The syntheses of carbon nanomaterial and the formation mechanism were reviewed in this section.

1.6.1 Arc Discharge

(a) Fullerene

Fullerene was scraped from the chamber wall in helium arc discharge at 100 Torr (Krätschmer et al. 1990). Discharge parameters including pressure, arc current, and electrode gap distance were optimized with respect both to the anode erosion rate and the weight percentage of fullerenes in the soot. C_2 was considered as the main precursor for the formation of C_{60}. The results indicate that the best conditions for favorable fullerene formation strongly correlate with both the existence of a steeper temperature gradient and an off-axis maximum of the C_2 density (Saïdane et al. 2004).

According to the experimental data available, the formation of fullerene is schematically summarized in Fig.1. 4. Carbon atoms are formed when the graphite is evaporated due to the heat flux from the arc. These atoms subsequently cluster to a mixture of chains, monocyclic rings, polycyclic rings and fullerenes. In an annealing process these clusters rearrange, especially efficiently via monocyclic rings, to fullerenes. During this annealing, stable fullerenes are formed by loss of small fragments such as C_2 or C_3, and by ring rearrangements (e.g. Stone-Wales rearrangement). However, the availability of fullerenes by several methods implies the existence of several different formation mechanisms; these mechanisms may also operate simultaneously (Hirsch and Brettreich 2004).

(b) Multi-Wall Carbon Nanotube (MWNT)

Multi-wall carbon nanotube (MWNT) was obtained in the inner of cathode deposit at low pressure argon arc (Iijima 1991). A number of factors have been done to investigate the yield of high quality nanotube. The purity and the yield depend sensitively on the gas pressure in the reaction vessel. A significantly increase in the number of tubes is evident as the pressure is increased. No obvious change can be observed when the pressure is above 500 Torr (Ebbesen and Ajayan 1992). High-purity MWNT (purity >95%) was synthesized by an arc discharging controlled by a magnetic field. The concentration of carbon monomer was increased by applying the magnetic field, since the magnetic force can confine the plasma and suppress the fluctuation of the arc (Anazawa et al. 2002). In addition, the vapor density of carbon is considered as the main factor which determines the self-assembly of carbon nanotube by studying the microstructure of cathode deposits in detail (Ajayan et al. 1997).

Most early theories of nanotube formation in the arc assumed that nucleation and growth occurred as a result of direct condensation from the vapor, or plasma, phase. It was also thought that the electric field of the arc played an essential role in inducing the 1-dimensional growth which leads to the formation of tubes.

In this model the tips of parallel nanotubes in zone 1 (column top) act as field emitters of electrons into the plasma (Colbert et al. 1994). This electron injection produces a high degree of carbon ionization leading to concentration of carbon ion current flow above the columns, which provides the main feedstock for the growth of column. The helium buffer gas is drawn in by the carbon ion flux to the top of the columns, is swept to the side, and then returns back to the plasma over zone 2, which is the intermediate area between adjacent columns. Fig. 1.5 illustrated the refinement of this model. In the absence of a large amount of vertically oriented nanotubes, the emission of electrons from zone 1 is likely to be mainly thermionic in nature and occurs from a variety of constituents of the columns. The dominating abundance of horizontally nanotubes packed over the column top surface, indicating that the effect of electric field at the open end of a nanotube is not a governing factor for its growth.

Those nanotubes that were originally located near the very hot top of a hemisphere could then undergo evaporation, yielding neutral carbon particles. An estimate has shown that the majority of carbon precipitated on columns must evaporate back as neutrals. Evaporation enriches the central part of a column in multiwall polyhedral particles (MPPs) and graphitic particles to the extent eventually observed by the scanning electron microscope (Smalley1993). Another reason for the enrichment of the central part of a column with graphitic particles is that they probably carry large positive charges while moving toward the cathode (Abrahamson1974) and are strongly attracted by the negatively charged volume over the column top. Helium transports re-evaporated neutral carbon molecules to zone 2, where they serve as a principal feedstock for the growth of new nanotubes

(c) Single-Wall Carbon Nanotube (SWNT)

The scientists at IBM and NEC companies discovered single-wall carbon nanotubes (SWNT) independently in early 1993 by the arc discharge method when metals as the catalyst were employed (Iijima et al. 1993; Bethune et al. 1993). In contrast to MWNT, the SWNTs are produced when the transition metal catalysts are used. The process of SWNT growth in arc discharge utilizes a composite anode, usually in hydrogen or argon atmosphere. The anode is made as a composition of graphite and a metal, such as Ni, Fe, Co, Pd, Ag, Pt, etc. or the mixtures of Co, Fe, Ni with other elements like Co-Ni, Fe-Ni, Fe-No, Co-Cu, Ni-Cu, Ni-Ti, etc. The metal catalyst plays a significant role in the process yield. To ensure high efficiency, the process also needs to be held on a constant gap distance between the electrodes which ensures stable current density and anode consumption rate. In this process, unwanted products such as MWNTs or fullerenes are usually produced too (Prasek et al. 2011).

The SWNT was found in a “collaret” around the cathode deposit, the web-like structure suspended between cathode and walls, and cloth-like soot suspended in the chamber walls (Keidar et al. 2009). High purity SWNT was directly synthesized macroscopically by the modified arc discharge method. The cathode was graphite rod with a sharp end toward the anode, the arc was operated at a current of 80 A in a helium atmosphere when Y-Ni alloy and FeS as the catalyst were employed (Li et al. 2004). N-doped SWNT was synthesized when melamine was introduced into the graphite anode together with catalysts. It opens new routes for the synthesis of doped SWNTs in high temperature experiment (Glerup et al. 2004). The effects including momentum, charge and energy transfer between SWNT and plasma are considered to explain the formation mechanism of SWNT by atmospheric-pressure anodic carbon arc (Keidar et al. 2009; Keidar 2006a; Keidar et al. 2006b).

The growth mechanism of SWNT from a core particle is illustrated in Fig. 1.6 (Saito 1995). When metal catalysts and carbon are evaporated by arc discharge simultaneously, carbon and metal atoms condense and form alloy (or binary mixed) particles. When the particles are cooled, carbon dissolved in the particles segregates onto the surface, since the solubility of carbon decreases with decreasing temperature. Some singular surface structures or compositions in an atomic scale may contribute to the formation of SWNT. After the formation of the nuclei of SWNT, carbon may be supplied from the core particle to the roots of SWNT, and then the tubes grow longer, maintaining capped tips with a hollow. Additional carbon atoms (and C_2) from the gas phase attaching to the tips of the tubes may also contribute to the growth of tubes.

(d) Polyhedral Graphit Particle (PGP)

Polyhedral graphite particle (PGP) is polyhedral shape nanoparticle consisting of concentric graphitic shells. It was obtained in the cathode deposit in a 100 mbar helium atmosphere (Ugarte 1992 a). MWNT and PGP were prepared by the helium arc at various pressures in a range of 10-500 Torr, suggesting the mechanism that carbon ions and C_n cluster are the precursors for the growth of PGP and MWNT from a similar initial seed (Saito et al 1993). In addition, PGP and MWNT were prepared selectively by controlling the relative intensity of carbon ion to carbon radical using a transferred arc under atmospheric pressure (Liang et al. 2012).

As show in Fig. 1.7, the formation mechanism of PGP can be explained as follows (Saito et al 1993). Firstly, carbon vapor and C^+ ions deposited on a surface of cathode coagulate with each other into small clusters. The clusters grow up to particles with the size observed experimentally here through an accretion of carbon atoms and co-alescence between clusters. The structure of the particles have high structural fluidity (liquid-like) at this growth stage due to high temperature of the electrode around 3500 K and ion bombardment. Concerning the effect of bombardment of energetic particles, the high structural fluidity of carbon soot particles has actually been observed under intense electron beam irradiation (Ugarte. 1992 b). Since the voltage drop around 10 V near the negative electrode occurs in a thin layer within 10^{-3} to 10^{-4} cm from the electrode surface, bombardment of He^+ and C^+ ions with average kinetic energy of 10 eV on the particles enhances the fluidity of the structure.

Carbon vapor deposition and ion bombardment onto the particles will continue until the particles are shadowed by the growth of tubes and other particles surrounding them, and then graphitization (formation of graphitic sheets) starts. Since the cooling proceeds from the surface to the center of the particle, the graphitization initiates at the external surface of the particle and progresses toward its center. The internal layers grow, keeping their planes parallel to the external layer. The flat planes of the particle consist of nets of six-membered rings, while five-membered rings could be located at the corners of the polyhedra. The closed structure containing pentagonal rings, which minimizes dangling bonds and lowers the total en-gated particles would be energy of a particle.

Because the density of highly graphitized carbon (2.2 g cm^{-3}) is higher than that of amorphous carbon (1.3-1.5 g cm^{-3}), a pore will be left in the center of a particle. The proposed graphitization process from the surface into the core is compatible with the presence of multi-cored particles. If the nucleation occurs firstly and then the outer shells forms subsequently in the process of graphitization, it will not be employed to explain the formation of the multi-core particles.

(e) Graphene Flakes

Graphene flakes were produced in the inner wall of the chamber under hydrogen atmosphere (Subrahmanyam et al. 2009). Large scale production of graphene nanosheets was achieved by arc evaporation of a graphite rod in air under different pressures (Wang et al. 2010), indicating high pressure facilitates the formation of graphene nanosheets. Large scale of few-layered graphene was prepared by using a buffer gas containing carbon dioxide. The optimized condition for the production of graphene flakes was high buffer gas pressure (Wu et al. 2010). Moreover, Y-Ni as the catalyst was employed to prepare graphene flakes using a non-uniform magnetic field (Levchenko et al. 2010). Nucleation and growth of the graphene flakes on the small newly-nucleated catalyst particles starts when the temperature falls below 1500 K. The arc discharge method is eminently suited to obtain B and N-doped graphene in the presence of B_2H_6 and NH_3, exhibiting p and n-type semiconducting electronic properties (Panchakarla et al. 2009; Li et al. 2010).

The formation mechanism of graphene flake is still unclear by arc discharge method, although lots of efforts have been done. It appears that H_2 plays a key role in the formation of graphene by preventing the rolling of sheets into nanotubes and graphitic polyhedral particles (Subrahmanyam et al. 2009).

(f) Other Carbon Nanomaterials

Single-wall carbon nanohorn (SWNH) particles were generated by simple pulsed arc discharge between pure carbon rods at the atmospheric pressure of air. Purity of SWNHs was reached higher than 90%, and the heating in dry air at 500 ºC was useful for removal of amorphous carbon. The mean size of SWNH particles was around 50 nm (Yamaguchi et al. 2004). High-yield syntheses of peculiar carbon 'necklace'-like morphologies have been obtained based on a 3-phase alternative current (AC) plasma technology (Okuno et al. 2004).

1.6.2 RF Thermal Plasma

Microcrystals and microcrystalline films of diamond were prepared on molybdenum substrates by the RF thermal plasma under 1 atm pressure (Matsumoto et al. 1987). Carbon nano-flakes were obtained by decomposition of methane using RF thermal plasma. The product has a crystalline graphitic structure, with a stacking of between 6 and 16 planes and a nano-flake morphology with particles dimensions of approximately 100 nm long, 50 nm wide and 5 nm thick (Pristavita et al. 2011). A carbon soot product which contains approximately 40wt% of SWCNTs can be continuously synthesized at the high production rate of 100 g h^{-1} by induction thermal plasma (Kim et al. 2009).

MWNT were synthesized through raw-material evaporation and condensation in RF thermal plasmas to investigate condensation process of the vapor mixture of carbon and metals.

Addition of 10wt%-Ni was the most effective for the CNT synthesis, while Co, Fe, Mo, LaB_6 had poor activity. These metal combinations presented synergy effect for the CNT formation. The combinations of Ni-Co, Ni-Fe, and Ni-LaB_6 provided more effective activity in the MWNT synthesis. Furthermore, the MWNT growth mechanism from the vapor mixture of carbon and metals was discussed. Heterogeneous condensation model and carbon–metal molten model were selected as the CNT growth model (Watanabe et al. 2006).

1.7 Objective of This Work

As mentioned above, lots of nanoparticles have been prepared by arc discharge method. However, there are only limited studies about electrode phenomena such as arc-anode attachment and electrode temperature, although these phenomena play an important role in controlling the nanoparticle syntheses.

Arc-anode attachment is one of important phenomena in arc discharge method, the influence of this phenomenon on the nanoparticle syntheses is unclear. In particular, the electrode temperature cannot be observed by traditional temperature measurement method due to the strong radiation from the arc. Therefore, the relationship of attachment mode and temperature behavior is also obscure when using DC arc discharge method to prepare nanomaterial.

In the past several years, researchers provided lots of mechanisms to explain the growth of carbon nanomaterial by arc discharge method. However, the formation mechanism of carbon nanomaterial remains rather poorly understood, since they neglected the effect of plasma characteristics. The lack of detailed understanding of these mechanisms has been a serious impediment to apply the arc discharge method for the preparation of carbon nanomaterial. In order to solve these problems, the following work was conducted based on the investigation of electrode phenomena.

The objective of the present study is to investigate two important electrode phenomena, the electrode temperature and the arc-anode attachment by DC arc discharge method for nanoparticle preparation. Nickel and graphite as raw material were selected, due to the enormous potential applications of nickel nanoparticle and carbon nanomaterial. In order to prepare carbon nanomaterial in large scale selectively, the formation mechanism of carbon material was investigated based on these electrode phenomena.

1.8 Contents of This Dissertation

Fig. 1.8 shows the flowchart of this dissertation. The contents of each chapter in this dissertation are as follows:

In chapter 2, the relationship between arc-anode attachment mode and temperature of anode surface was investigated when using DC arc discharge method to prepare nickel nanoparticle. Diffuse, multiple, and constricted modes were observed in helium and argon arcs by changing hydrogen concentration and shield gas flow rate. Furthermore, the effect of attachment mode on the characteristics of nickel nanoparticle was investigated by comparing the difference of helium arc and argon arc. In addition, anode surface temperature in helium arc was measured by two-color pyrometry combined with a high-speed camera which employed suitable band-pass filters. Therefore, the relationship between dynamic behavior of arc-anode attachment and anode temperature was investigated by two synchronized high-speed cameras.

In chapter 3, the relationship between arc-anode attachment mode and temperature of carbon electrode was investigated by DC arc discharge method. Diffuse and multiple arc-anode attachment modes were observed in helium and argon arcs. During the arc discharge, the surface temperature of the electrode was successfully measured. The difference between argon and helium was compared based on investigating the arc-anode attachment mode and temperature behavior. The results about these two important electrode phenomena provide a new way to explain the formation mechanism of carbon nanomaterial.

In chapter 4, nano-graphite particles, multi-wall carbon nanotube (MWNT), and pyrolytic graphite were prepared at different positions of the anode deposit by arc discharge method. In addition, the necklace-like carbon, and spherical carbon particle were obtained on the anode surface. The deposition temperature of these carbon nanomaterials were measured by two-color pyrometry. According to the temperature results, the formation mechanism of these carbon nanomaterials was investigated by quenching effect.

In chapter 5, cathode deposit mainly composed of PGPs, MWNTs, graphene flakes, and turbostratic graphite was selectively synthesized by arc discharge method. The relative ratio of carbon ions to carbon radicals near the cathode tip was examined as an important parameter to control the growth of these carbon nanomaterials. Based on the different energies of the precursors, the mechanisms of carbon nanomaterial formation in the cathode deposit are suggested.

In chapter 6, all of the results of this dissertation are summarized, and the direction for future research of the nanoparticle synthesis by DC arc method is suggested.

References

Abrahamson J. “Graphite sublimation temperatures, carbon arcs and crystallite erosion.” *Carbon* **12**(2), 111-118 (1974).

Ajayan P. M., Ph. Redlich and M. Rühle. “Balance of graphite deposition and multishell carbon nanotube growth in the carbon arc discharge.” *Journal of Materials Research* **12**(1), 244-252 (1997).

Bai L., J. Fan, P. Hu, F. Yuan, J. Li and Q. Tang. “RF plasma synthesis of nickel nanopowders via hydrogen reduction of nickel hydroxide/carbonate.” *Journal of Alloys and Compounds* **481**, 563-567 (2009).

Benmansour M., M. Nikravech, D. Morvan, J. Amouroux and J. Chapelle. “Diagnostic by emission spectroscopy of an argon-hydrogen RF inductive thermal plasma for purification of metallurgical grade silicon.” *Journal of Physics D: Applied Physics* **37**, 2966-2974 (2004).

Bethune D. S., C. H. Kiang, M. S. Devries, G. Gorman, R. Savoy, J. Vazquez and R. Beyers. "Cobalt-catalyzed growth of carbon nanotubes with single-atomic-layer walls". *Nature* **363**(6430), 605-607 (1993).

Boulos, M. I. “RF Induction plasma spraying: state-of-the-art review.” *Journal of thermal spray technology* **1**, 33-40 (1992).

Boulos, M. I., P. Fauchais and E. Pfender. “*Thermal Plasmas: Fundamentals and Applications.*” New York, Plenum Press. (1994)

Chazelas, C., J. F. Coudert, J. Jarrige and P. Fauchais. "Synthesis of ultra fine particles by plasma transferred arc: Influence of anode material on particle properties." *Journal of the European Ceramic Society* **26**(16), 3499-3507 (2006).

Cheng Y., M. Shigeta, S. Choi and T. Watanabe. “Formation mechanism of titanium boride nanoparticles by RF induction thermal Plasma.” *Chemical Engineering Journal* **183**, 483-491 (2012).

Cordente N., M. Respaud, F. Senocq, M. J. Casanove, C. Amiens and B. Chaudret. “Synthesis and Magnetic Properties of Nickel Nanorods” *Nano Letters* **1**(10), 565-568 (2001).

Dinulescu H. A. and E. Pfender. “Analysis of the anode boundary layer of high intensity arcs.” *Journal of Applied Physics* **51**(6), 3149-3157 (1980).

Colbert D. T., J. Zhang, S. M. McClure, P. Nikolaev, Z. Chen, J. H. Hafner, D. W. Owens, P. G. Kotula, C. B. Carter, J. H. Weaver, A. G. Rinzler and R. E. Smalley. “Growth and Sintering of Fullerene Nanotubes.” *science* **266**, 1218-1222 (1994).

Ebbesen T. W. and P. M. Ajayan. “Large-scale synthesis of carbon nanotubes” *Nature* **358**, 220-222 (1992).

Fauchais, P. “Understanding Plasma Spraying.” *Journal of Physics D: Applied Physics* **37**, R86-R108 (2004).

Fulcheri L., Y. Schwob, F. Fabry, G. Flamant, L.F.P. Chibante and D. Laplaze. “Fullerene production in a 3-phase AC plasma process.” *Carbon* **38**, 797-803 (2000).

Glerup M., J. Steinmetz, D. Samaille, O. Stephan, S. Enouz, A. Loiseau, S. Roth and P. Bernier. “Synthesis of n-doped SWNT using the arc-discharge procedure.” *Chemical Physics Letters* **387**, 193-197 (2004).

Haidar J. and A. J. D. Farmer. “Surface temperature measurements for tungsten-based cathodes of high-current free-burning arcs”. *Journal of Physics D: Applied Physics* **28**, 2089-2094. (1995).

Heberlein, J. and A. B. Murphy. “Thermal plasma waste treatment.” *Journal of Physics D:*

Applied Physics **41**, 053001 (2008).

Heberlein J. V., J. Mental and E. Pfender. “The anode region of electric arcs: a survey.” *Journal of Physics D: Applied Physics* **43**, 023001 (2010).

Hernandez R., S. Polizu, S. Turenne and L. Yahia, “Characteristics of porous nickel titanium alloys for medical applications.” *Bio-Medical Materials and Engineering* **12**, 37-45 (2002).

Hirsch A. and M. Brettreich. “Fullerenes.” WILEY-VCH (2004).

Iijima, S. "Helical microtubules of graphitic carbon." *Nature* **354**(6348), 56-58 (1991).

Iijima, S. and I. Toshinari. "Single-shell carbon nanotubes of 1-nm diameter." *Nature* **363** (6430), 603-605 (1993).

Kazunori A., K.Shimotani, C. Manabe, H. Watanabe and M. Shimizu. “High-purity carbon nanotubes synthesis method by an arc discharging in magnetic field.” *Applied Physics Letters* **81**(4), 739-741 (2002).

Keidar M., A. M. Waas, Y. Raitses and E. I. Waldorff. “Modeling of the Anodic Arc Discharge and Conditions for Single-Wall Carbon Nanotube Growth.” *Journal of Nanoscience and Nanotechnology* **6**, 1309-1314 (2006).

Keidar M. “Factors affecting synthesis of single wall carbon nanotubes in arc discharge.” *Journal of Physics D: Applied Physics* **40**, 2388-2393 (2007).

Keidar M. and I. I. Beilis. “Modeling of atmospheric-pressure anodic carbon arc producing carbon nanotubes.” *Journal of applied physics* **106**, 103304 (2009).

Kim K. S., A. Moradian, J. Mostaghimi, Y. Alinejad, A. Shahverdi, B. Simard and G. Soucy. “Synthesis of Single-Walled Carbon Nanotubes by Induction Thermal Plasma.” *Nano Research* **2**, 800-817 (2009).

Kobayashi N., Y. Kawakami, K. Kamada, J. G. Li, R. Ye, T. Watanabe and T. Ishigaki. “Spherical submicron-size copper powders coagulated from a vapor phase in RF induction thermal plasma.” *Thin Solid Films* **516**, 4402 (2008).

Krätschmer W., L. Lamb, K. Fostiropoulos and D.R. Huffman. “Solid C_{60}: a new form of carbon.” *Nature* **347**, 354-358 (1990).

Lan R. and S. Tao “Preparation of nano-sized nickel as anode catalyst for direct urea and urine fuel cells.” *Journal of Power Sources* **196**, 5021-5026 (2011).

Levchenko I., O. Volotskova, A. Shashurin, Y. Raitses, K. Ostrikov and M. Keidar. “The large-scale production of graphene flakes using magnetically-enhanced arc discharge between carbon electrodes.” *Carbon* **48**(15), 4556-4577 (2010).

Li H., L. Guan, Z. Shi and Z. Gu. “Direct Synthesis of High Purity Single-Walled Carbon Nanotube Fibers by Arc Discharge” *Journal of physical chemistry. B* **108**(15), 4573-4575 (2004).

Li N., Z. Wang, K. Zhao, Z. Shi, Z. Gu and S. Xu. “Large scale synthesis of N-doped multi-layered graphene sheets by simple arc-discharge method.” *Carbon* **48**, 255-259 (2010).

Li, X. G., A. Chiba and S. Takahashi. "Preparation and magnetic properties of ultrafine particles of Fe-Ni alloys." *Journal of Magnetism and Magnetic Materials* **170**(3), 339-345 (1997a).

Li, X. G., A. Chiba, S. Takahashi and K. Ohsaki. "Preparation, oxidation and magnetic properties of Fe-Cr ultrafine powders by hydrogen plasma-metal reaction." *Journal of Magnetism and Magnetic Materials* **173**(1-2), 101-108 (1997b).

Li, X. G., A. Chiba, S. Takahashi and M. Sato. "Oxidation characteristics and magnetic properties of iron ultrafine particles." Journal of Applied Physics 83(7), 3871-3875 (1998a).

Liang F., T. Shimizu, M. Tanaka, S. Choi and T. Watanabe. “Selective preparation of polyhedral graphite particles and multi-wall carbon nanotubes by a transferred arc under atmospheric pressure.” *Diamond and Related Materials* **30**, 70-76 (2012).

Liang F., M. Tanaka, S. Choi and T. Watanabe. “Electrode Temperature Measurement for Carbon Nanomaterial Production by Arc Discharge Method” ISPC21 proceeding.

Tanaka M. and W. Takayuki. “Mechanism of Enhanced Vaporization from Molten Metal Surface by Argon–Hydrogen Arc Plasma” *Japanese Journal of Applied Physics* **52**, 076201 (2013).

Matsumoto S., M. Hino and T. Kobayashi. “Synthesis of diamond films in a rf induction thermal plasma.” *Applied Physics Letters* **51**, 737-739 (1987).

Matsuura T., K. Taniguchi and T. Watanabe. “A new type of arc plasma reactor with 12-phase alternating current discharge for synthesis of carbon nanotubes.” *Thin Solid Films* **515**, 4240-4246 (2007).

Mccullough R. “Plasma arc furnace, a new concept in melting metals.” *Journal of metals* **14**(12), 907-911 (1962).

Narengerile, H. Saito and T. Watanabe. “Decomposition Mechanism of Fluorinated Compounds in Water Plasmas Generated Under Atmospheric Pressure.” *Plasma Chemistry and Plasma Processing* **30**, 813-829 (2010).

Narengerile, M.H. Yuan and T. Watanabe. “Decomposition mechanism of phenol in water plasmas by DC discharge at atmospheric pressure.” *Chemical Engineering Journal* **168**, 985-993 (2011).

Narengerile, and T. Watanabe. “Acetone decomposition by water plasmas at atmospheric pressure.” *Chemical Engineering Science* **69**, 296-303 (2012).

Nemchinsky V. A. and W. S. Severance. “What we know and what we do not know about plasma arc cutting.” *Journal of Physics D: Applied Physics* **39**, R423-R438 (2006).

O’Brien R. L. “Welding Processes.” American Welding Society Press 2, (1991).

Oh S. M. and D. W. Park. “Preparation of AlN fine powder by thermal plasma processing” *Thin Solid Films* **316**, 189-194 (1998).

Okazaki, K. and T. Watanabe. “Annual review of heat transfer,” New York, Wallingford, U.K. **10**, 30-38 (1999).

Okuno H., E. Grivei, F. Fabry, T. M. Gruenberger, J. Gonzalez-Aguilar, A. Palnichenko, L. Fulcheri, N. Probst and J. C. Charlier. “Synthesis of carbon nanotubes and nano-necklaces by thermal plasma process.” *Carbon* **42**, 2543-2549 (2004).

Panchakarla L. S., K. S. Subrahmanyam, S. K. Saha, Achutharao Govindaraj, H. R. Krishnamurthy, U. V. Waghmare and C. N. R. Rao. “Synthesis, Structure, and Properties of Boron- and Nitrogen-Doped Graphene.” *Advanced Materials* **21**, 4726-4730 (2009).

Park J. W., E.H. Chae, S. H. Kima, J. H. Lee, J. W. Kim, S. M. Yoon and J.Y. Choi. “Preparation of fine Ni powders from nickel hydrazine complex.” *Materials Chemistry and Physics* **97**, 371-378 (2006).

Pfender E., “Electric arcs and arc gas heaters,” chapter 5 in Gaseous Electronics, vol.1, M.N. Hirsh and H.J. Oskam, Eds. (New York: Academic press, 1978): 291-398.

Prasek J., J. Drbohlavova, J. Chomoucka, J. Hubalek, O. Jasek, V. Sdam and R. Kizek. “Methods for carbon nanotubes synthesis—review.” J*ournal of Materials Chemistry* **21**, 15872 (2011).

Pristavita R., J. L. Meunier and D. Berk. “Carbon Nano-Flakes Produced by an Inductively Coupled Thermal Plasma System for Catalyst Applications.” *Plasma Chemistry and Plasma Processing* **31**, 393-403 (2011).

Reinelt J., M. Westermeier, C. Ruhrmann, A. Bergner, P. Awakowicz and J. Mentel. “Investigating the dependence of the temperature of high-intensity discharge (HID) lamp electrodes on the operating frequency by pyrometric measurements.” *Journal of Physics D: Applied Physics* **44**, 095204 (2011).

Saïdane K., M. Razafinimanana, H. Lange, A. Huczko, M. Baltas, A. Gleizes and J.L. Meunier. “Fullerene synthesis in the graphite electrode arc process: local plasma characteristics and correlation with yield.” *Journal of Physics D: Applied Physics* **37**, 232-239 (2004).

Sakka, Y., H. Okuyama, T. Uchikoshi and S. Ohno. "Synthesis and characterization of Fe and composite Fe-TiN nanoparticles by dc arc-plasma." *Journal of Alloys and Compounds* **346**(1-2), 285-291 (2002).

Sanders N., K. Etemadi, K. C. Hsu and E. Pfender. “Studies of the anode region of a high-intensity argon arc.” *Journal of Applied Physics* **53**(6), 4136-4145 (1982).

Saito Y., T. Yoshikawa and M. Inagaki. “Growth and structure of graphitic tubules and polyhedral particles in arc-discharge.” *Chemical Physics Letter* **204**, 277-282 (1993).

Saoto Y. “Nanoparticles and filled nanocapsules.” *Carbon* **33**(7), 979-988 (1995).

Shao, H. Y., Y. T. Wang, H. R. Xu and X. G. Li. "Hydrogen storage properties of magnesium ultrafine particles prepared by hydrogen plasma-metal reaction." Materials Science and Engineering: B-Solid State Materials for Advanced Technology 110(2), 221-226 (2004).

Shao, H. Y., T. Liu, Y. T. Wang, H. R. Xu and X. G. Li. "Preparation of Mg-based hydrogen storage materials from metal nanoparticles." *Journal of Alloys and Compounds* **465**(1-2), 527-533 (2008).

Shigeta, M. and A. B. Murphy. “Thermal plasmas for nanofabrication.” *Journal of Physics D: Applied Physics* **44** (174025), 1-16 (2011).

Shigeta, M. “Time-dependent 3D simulation of an argon RF inductively coupled thermal plasma.” *Plasma Sources Science and Technology* **21** (055029), 1-14 (2012).

Smalley R. E. “From dopyballs to nanowires.” *Materials Science and Engineering: B* **19**, 1 (1993).

Sooseok C., S. H. Hong, H. S. Lee and T. Watanabe. “A comparative study of air and nitrogen thermal plasmas for PFCs decomposition.” *Chemical Engineering Journal* **185-186**, 193-200 (2012).

Sooseok C. and T. Watanabe. “Decomposition of 1-Decanol Emulsion by Water Thermal Plasma Jet”. *IEEE Transactions on Plasma Science* **40**(11), 2831-2836 (2012).

Subrahmanyam K. S., L. S. Panchakarla, A. Govindaraj and C. N. R. Rao. “Simple method of preparing graphene flakes by an arc-discharge method.” *Journal of Physical Chemistry C* **113**(11), 4257-4259 (2009).

Tanaka M. and J. J. Lowke. “Predictions of weld pool profiles using plasma physics.” *Journal of Physics D: Applied Physics* **40** R1-R23 (2007).

Tanaka M. and T. Watanabe. “Vaporization mechanism from Sn-Ag mixture by Ar-H_2 Arc for nanoparticle preparation.” *Thin Solid Films* **51**(19), 6645-6649 (2008).

Tanaka M., T. Ikeba, Y. Liu, T. Matsuura and T. Watanabe. “Electrode temperature measurements of multi-phase AC arc by high-speed video camera”. *Journal of Physics: Conference Series* **406**(012008), 1-8 (2012).

Tanaka, M. and T. Watanabe. “Mechanism of Enhanced Vaporization from Molten Metal Surface by Argon-Hydrogen Arc Plasma.” *Japanese journal of applied physics* **52** 076201, 1-6 (2013).

Taylor P. and S. Pirzada. “Plasma Technology in Extractive and Process Metallurgy.” *Mineral Processing and Extractive Metallurgy Review* **12**, 257-269 (1995).

Ugarte D. “Morphology and structure of graphitic soot particles generated in arc-discharge C_{60} production.” *Chemical Physics Letter* **198**, 596-602 (1992 a) (1992 b)

Ugarte D. “Curling and closure of graphitic networks under electron-beam irradiation.” *Nature* **359**, 707-709 (1992).

Wang Z., N. Li, Z. Shi and Z. Gu. “Low-cost and large-scale synthesis of graphene nanosheets by arc discharge in air.” *Nanotechnology* **21**(17), 175602 (2010).

Watanabe, T., H. Itoh and Y. Ishii. "Preparation of ultrafine particles of silicon base intermetallic compound by arc plasma method." *Thin Solid Films* **390**(1-2), 44-50 (2001).

Watanabe T., T Notoya, T. Ishigaki, H. Kuwano, H. Tanaka, Y. Moriyoshi. “Growth mechanism for carbon nanotubes in a plasma evaporation process.” *Thin Solid Films* **506– 507** 263 -267(2006).

Watanabe T. and T. Tsuru. “Water plasma generation under atmospheric pressure for HFC destruction.” *Thin Solid Films* **516**, 4391-4396 (2008).

Watanabe T., K. Yatsuda, Y. Yao, T. Yano and T. Matsuura. “Innovative in-flight glass-melting technology using thermal plasmas.” *Pure and Applied Chemistry* **82**, 1337-1351 (2010).

Watanabe T., Narengerile and H. Nishioka. “Role of CH, CH_3, and OH Radicals in Organic Compound Decomposition by Water Plasmas.” *Plasma Chemistry and Plasma Processing* **32**, 123-140 (2012).

Watanabe, T., M. Tanaka, T. Shimizu and F. Liang. “Metal Nanoparticle Production by Anode Jet of Argon-Hydrogen DC Arc.” *Advanced Materials Research* **628**, 11-14 (2013).

Wei Z., T. Xia, L. Bai, J. Wang, Z. Wu and P. Yan. “Efficient preparation for Ni nanopowders by anodic arc plasma”. *Materials Letters* **60**, 766-770 (2006).

Wu Y., B. Wang, Y. Ma, Y. Huang, N. Li, F. Zhang and Y. Chen. “Efficient and Large-Scale Synthesis of Few-Layered GrapheneUsing an Arc-Discharge Method and Conductivity Studies of the Resulting Films.” *Nano Research* **3**(9), 661-669 (2010).

Yamaguchi T., S. Bandow and S. Iijima. “Synthesis of carbon nanohorn particles by simple pulsed arc discharge ignited between pre-heated carbon rods.” *Chemical Physics Letters* **389**, 181-185 (2004).

Yamazaki K., E. Yamamoto, K. Suzuki, F. Koshiishi, S. Tashiro, M. Tanaka and K. Nakata. “Measurement of surface temperature of weld pools by infrared two color pyrometry.” *Science and Technology of Welding & Joining* **15**, 40-47 (2010).

Yang G., J. V. Heberlein and E. Pfender. “Experimental investigations of the anode boundary layer in high intensity arcs with cross flow.” *Journal of Physics D: Applied Physics* **39**, 2764 (2006).

Yang G. and J. Herberlein. “Anode attachment modes and their formation in a high intensity argon arc.” *Plasma Sources Science and Technology* **16**, 529-542 (2007).

Yao, Y., K. Yatsuda, T. Watanabe, F. Funabiki and T. Yano. “Investigation on in-flight melting behavior of granulated alkali-free glass raw material under different conditions with

12-phase AC arc." *Chemical Engineering Journal* **144**, 317-323 (2008).

Yao, Y., K. Yatsuda, T. Watanabe, T. Matsuura and T. Yano. "Characteristics of multi-phase alternating current arc for glass in-flight melting," *Plasma Chemistry and Plasma Processing* **29**(5), 333-346 (2009).

Zhang C. N., J. G. Li, Y. H. Leng, T. Uchikoshi, T. Watanabe and T. Ishigaki. "(Eu^{3+}-Nb^{5+})-codoped TiO_2 nanopowders synthesized via Ar/O_2 radio frequency thermal plasma oxidation processing: Phase composition and photoluminescence properties through energy transfer." *Thin Solid Films* **518**, 3531-3534 (2010).

Zhang C. N., M. Ikeda, T. Uchikoshi, J. G. Li and T. Ishigaki. "High-concentration niobium (V) doping into TiO_2 nanoparticles synthesized by thermal plasma processing." *Journal of material research* **26**(5), 658-671 (2011).

Zhang X. F., X. L. Dong, H. Huang, Y. Y. Liu, W. N. Wang, X. G. Zhu, B. Lv and J. P. Lei. "Microwave absorption properties of the carbon-coated nickel nanocapsules" *Applied Physics letter* **89**, 053115 (2006).

Zhou X., B. J. Ding and J. Herberlein. "Temperature measurement and metallurgical study of cathodes in DC arcs." *IEEE Transactions on Components and Packaging Technologies* **19**, 320-328 (1996).

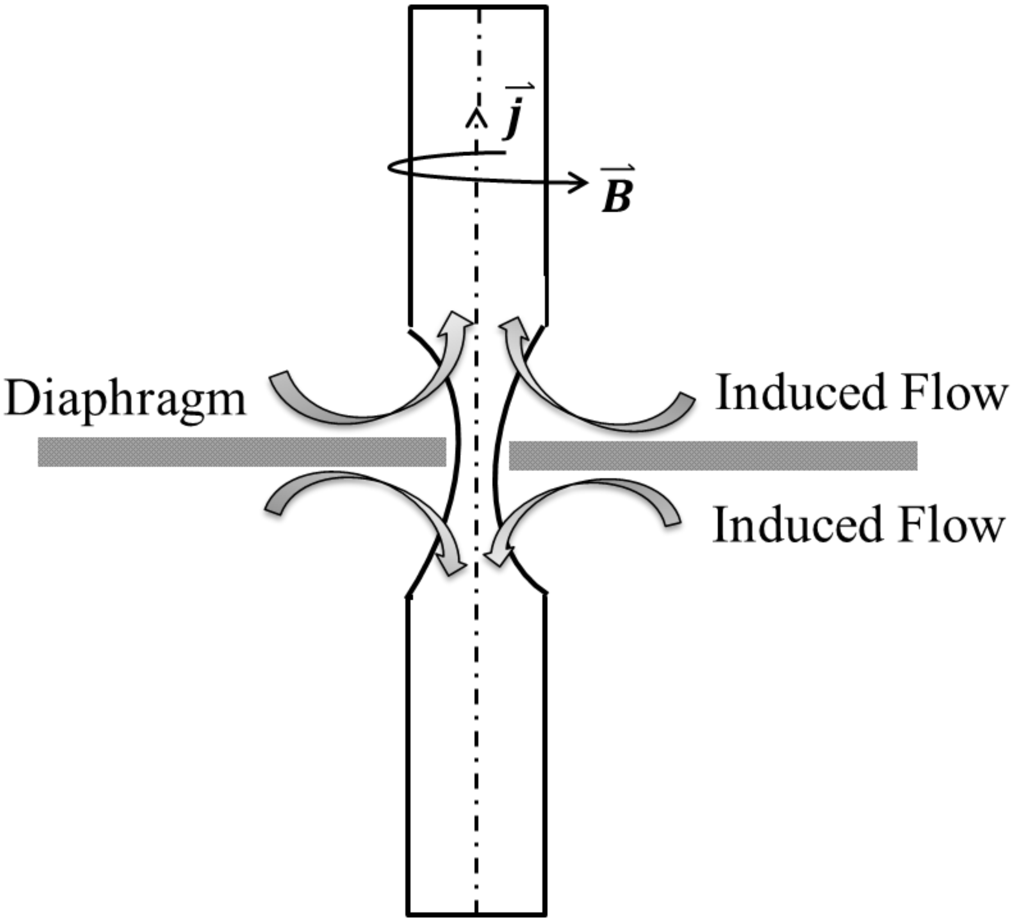

Fig. 1.1 Schematic of the pumping action induced by arc constriction (Pfender 1978).

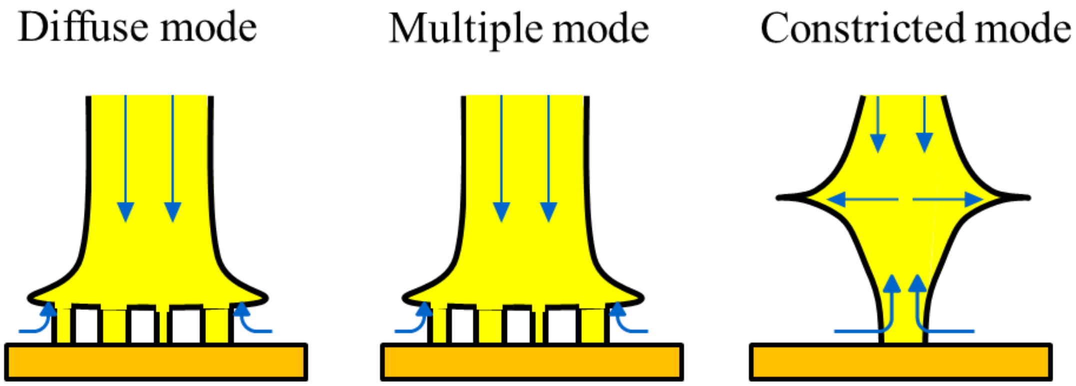

Fig. 1.2 Conceptual diagram of three arc-anode attachment modes.

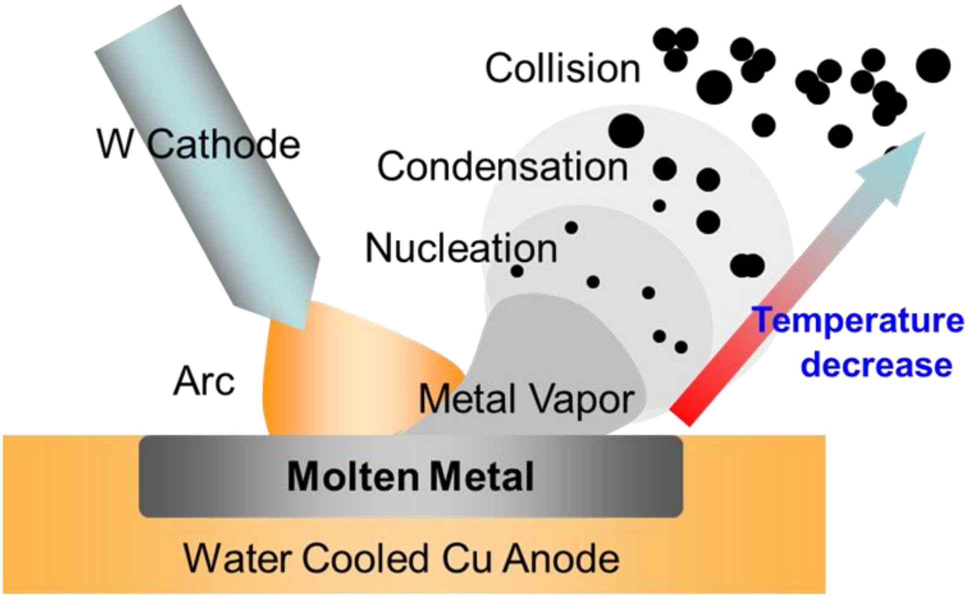

Fig. 1.3 Conceptual diagram of nanoparticle formation process by DC arc discharge method (Tanaka and Watanabe 2008).

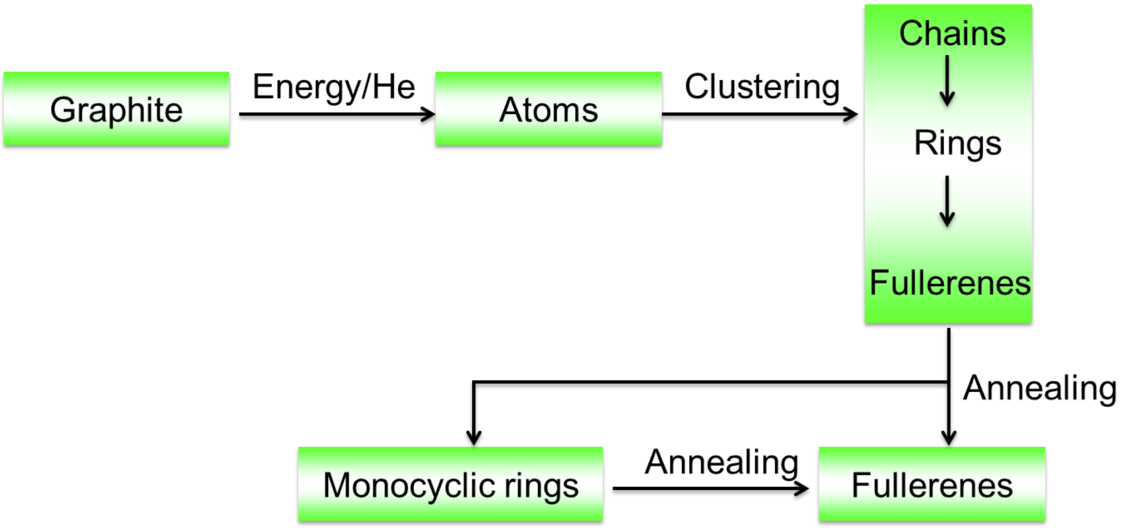

Fig. 1.4 Schematic of the formation of fullerene (Hirsch and Brettreich, 2004).

.

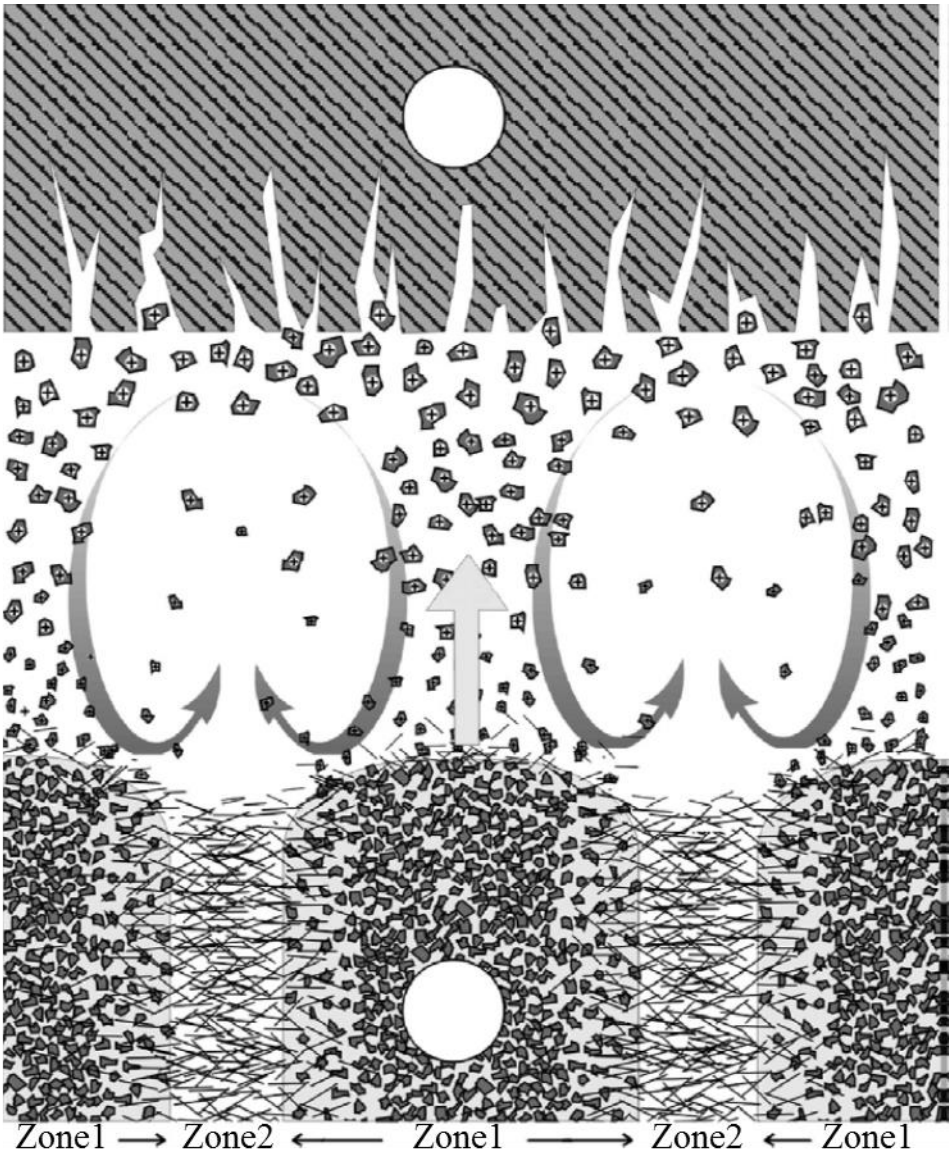

Fig. 1.5 Schematic of carbon nanotube growth model in a DC arc (Colbert et al. 1994).

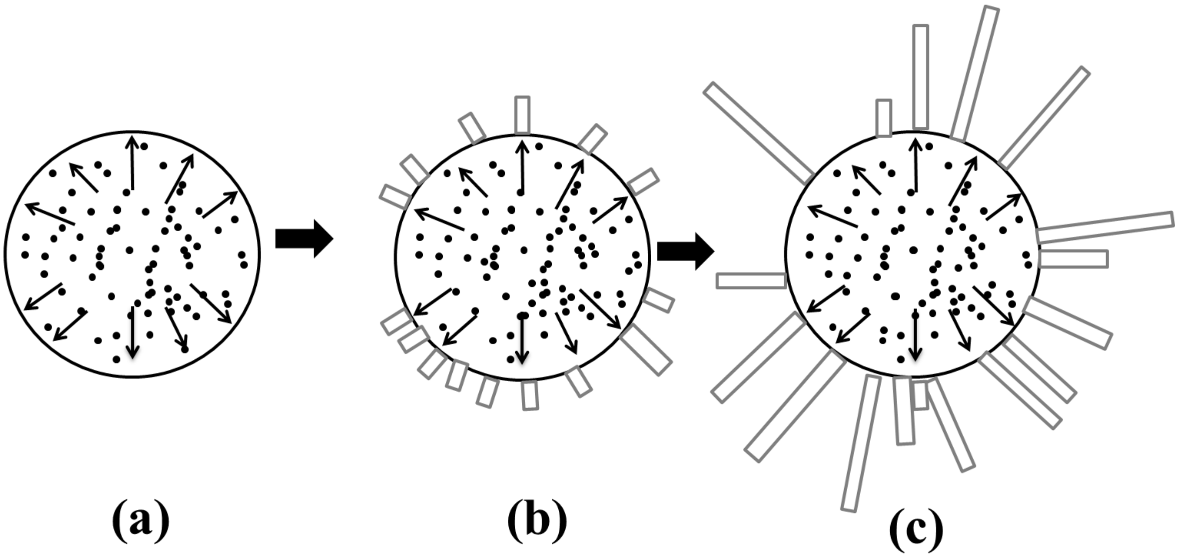

Fig. 1.6 The mechanism of growing SWNT from a metal/carbon alloy particle: (a) segregation of carbon toward the surface, (b) nucleation of signal wall tubes on the particle surface and, (c) growth of the signal wall tubes (Saito 1995).

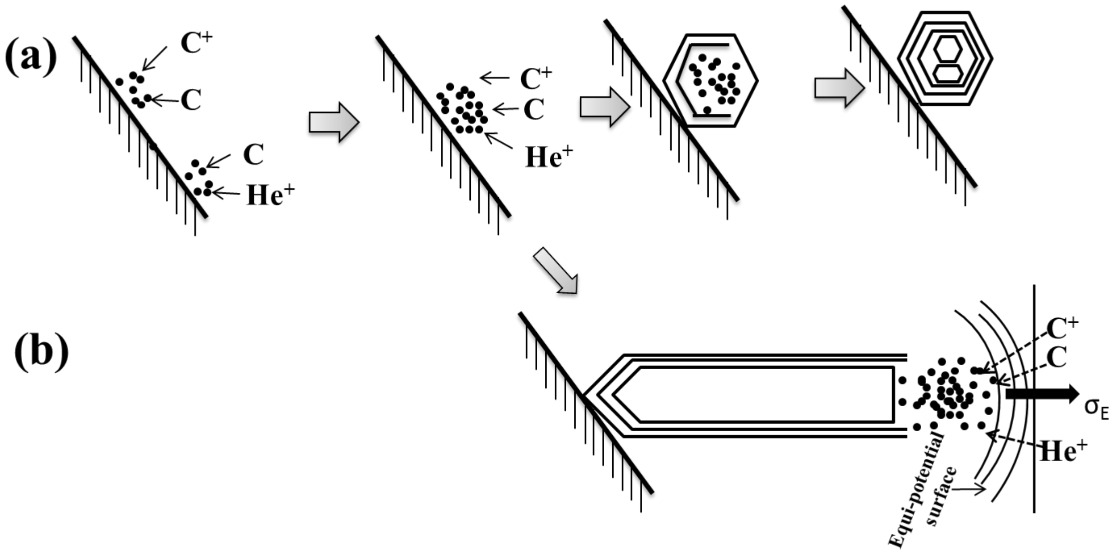

Fig. 1.7 Schematic illustration of growth process for (a) polyhedral graphite particle and (b) a carbon nanotube. σ_E represents the tension due to an electric field at the tip of a tube (Saito et al 1993).

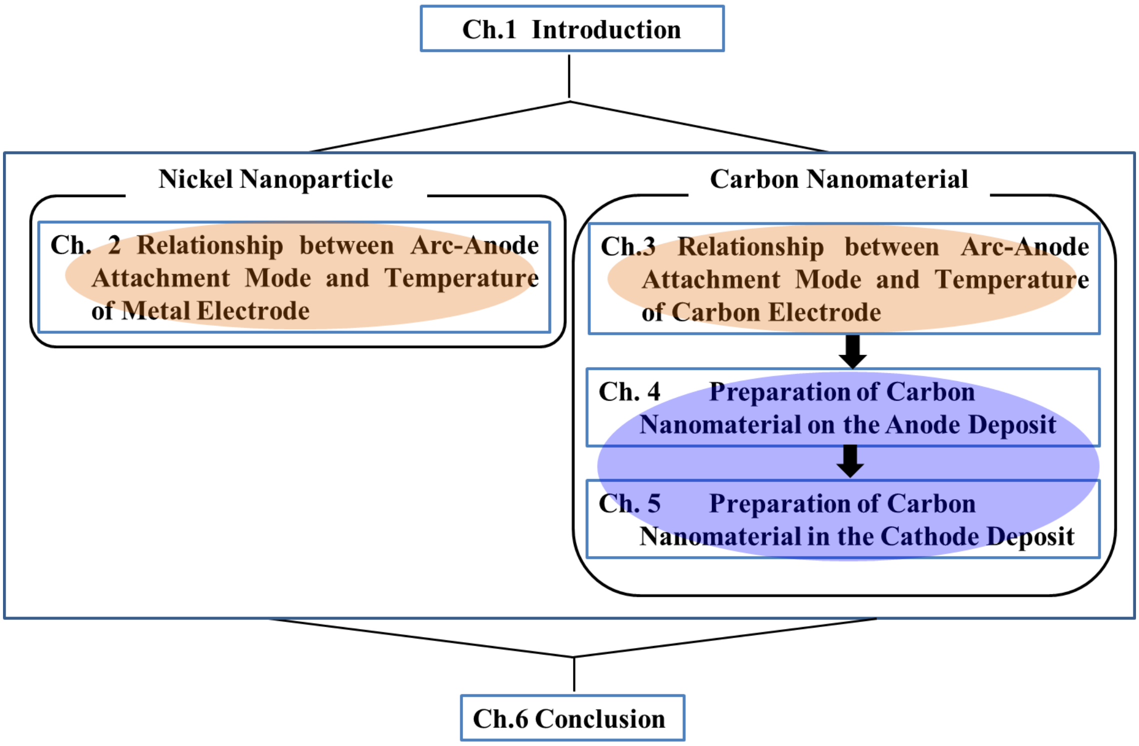

Fig. 1.8 The flow chart of this study.

2. Relationship between Arc-Anode Attachment Mode and Temperature of Metal Electrode

2.1 Introduction

Since the thermal plasma provides rapid evaporation rate, steep temperature gradients, and high chemical reactivity, it is an attractive route for nanomaterial synthesis. DC arc plasma has been applied in syntheses of carbon nanomaterial (Iijima 1991; Liang et al. 2012), high purity metal nanopowders (Shao et al. 2004; Wei et al. 2006), alloy (Tanaka and Watanabe 2008; Tanaka and Watanabe 2013), oxide (Li et al. 1998; Chazelas et al. 2006), and intermetallic compound (Liu et al. 2003). Especially, nickel nanoparticles have attracted much attention because of their excellent chemical, physical, and electronic properties. Fine nickel powders can be used as chemical catalysts, microwave absorbing materials, medical diagnosis, magnetic recording media, and internal electrode in multi-layer ceramic capacitors (MLCCs) (Lan et al. 2011; Zhang et al. 2006; Hernandez et al. 2002; Cordente et al. 2001; Park et al. 2006).

In the arc discharge method, the anode provides the raw material for preparing nanoparticle, and the anode ablation rate determines the productivity of nanoparticle production. Therefore, further analysis of the anode region and anode phenomena is required to improve the productivity and control the size of nanoparticle. For the anode boundary, there are three typical arc-anode attachment modes of diffuse attachment, multiple attachments, and constricted attachment (Dinulescu and Pfender 1980, Sanders et al. 1982, Heberlein et al. 2010). These anode attachment modes are the results of the competition between the cathode jet and the anode jet. However, the arc-anode attachment modes in helium/argon-hydrogen arcs for nanoparticle production have not been studied enough. This lack of understandings is due to the strong interaction of electrical, magnetic, thermal, and fluid-dynamic effects.

In addition, the anode surface temperature is an important parameter which influences the evaporation rate of anode material and the growth rate of nanoparticle. Due to the strong radiation from the arc, however, the electrode temperature cannot be observed by traditional temperature measurement method. As a result, the relationship between arc-anode attachment mode and anode temperature is still unclear.

In this chapter, diffuse, multiple, and constricted modes were observed in helium and argon arcs when using DC arc discharge method to prepare nickel nanoparticle. The effects of hydrogen concentration and shield gas flow rate on the formation of different arc-anode attachment modes were investigated in argon and helium arcs. Furthermore, the effect of attachment mode on the characteristics of nickel nanoparticles was investigated. The difference between helium and argon for nickel nanoparticle production was compared by investigating the arc-anode attachment modes.

Anode surface temperature in helium arc was measured by two-color pyrometry combined with a high-speed camera which employed suitable band-pass filters. The anode temperature variation on the millisecond time scale was obtained during arc discharge. Therefore, the relationship between dynamic behavior of arc-anode attachment and anode temperature was investigated by two synchronized high-speed cameras.

2.2. Experimental

2.2.1 Experimental Setup

Fig. 2.1 indicates the schematic illustration of an experimental apparatus for preparing nickel nanoparticles and two synchronized high-speed cameras for anode temperature measurement and arc behavior observation, respectively. The setup consists of a power supply (DAIHEN, COMPA P500), an arc discharge chamber, a particle collector, and a gas circulator. The plasma gas of He and/or H_2 was introduced to the system after evacuating the arc discharge chamber. A cylindrical nickel ingot as an anode was placed on the water-cooled copper. Metal fume was formed from the raw material surface after ignition the arc. The nanoparticles grow after nucleation, co-condensation, and collision (Tanaka and Watanabe 2008). Synthesized nanoparticles were collected at the filter by a gas circulation pump. He and H_2 gases without the entrained particles were reintroduced into the chamber by the gas circulation pump to form shield gas. Shield gas that was injected into the arc discharge chamber around the cathode was controlled by a gas flow meter.

2.2.2 Experimental Conditions

The experimental conditions are shown in Table 2.1. Nickel (99.9%, Nilaco., Ltd) ingot of 50 g as an anode was placed on the water-cooled copper. A cathode rod made of 2wt% thoria added tungsten with the diameter of 6 mm was placed at an oblique angle from the anode. The arc was generated for 10 min in He and the mixture of He-H_2 environment at atmospheric pressure. The arc current and electrode gap distance were fixed at 100 A and at 6 mm, respectively. Hydrogen concentration was controlled at 0, 10, 20, 30, and 50vol%. In order to examine the effect of shield gas flow rate on the process it was controlled at 0, 10, and 20 L/min at the fixed hydrogen concentration of 20vol%.

In order to investigate the effect of gas species on the arc-anode attachment mode and characteristics of nanoparticles, argon was selected for comparison. The experimental conditions are shown in Table 2.2. Hydrogen concentration was controlled at 0, 30, and 50vol% in the case of argon arc. The shield gas flow rates were 0, 10, and 20 L/min when the hydrogen concentration was fixed at 30vol%.

2.2.3 Temperature Measurements

Two-color pyrometry was selected to measure the temperature of electrode based on the ratio of radiation intensities at two different wavelengths. The following equation explains the ratio of radiation intensities by substituting the wavelength and radiation emissivity into Plank's radiation law:

$$\frac{I_1}{I_2} = \frac{\varepsilon_2}{\varepsilon_1}(\frac{\lambda_2}{\lambda_1})^5 \frac{1 - exp(C_b/\lambda_2 T)}{1 - exp(C_b/\lambda_1 T)} \qquad (1)$$

where, λ_1 and λ_2 are selected wavelengths (nm) through band-pass filters; I_1 and I_2 correspond to radiation intensities (W·m^{-3}·sr^{-1}) at the wavelength of λ_1 and λ_2, respectively; ε_1, ε_2 are emissivities; C_b equals to 0.014388 mK; T is temperature (K). According to the Wien's approximation of Planck's law, the spectrum of thermal radiation from a blackbody is used to determine the electrode temperature at the selected wavelengths. A real body has surface emissivity ε less than 1, it means the real body emits less thermal radiation than the blackbody. Since the emissivity is unknown for many applications, the gray body assumption of $\varepsilon(\lambda_1) = \varepsilon(\lambda_2)$ is used based on the hypothesis that the surface emissivity is independent of wavelength (Tanaka et al. 2012). As a result, equation (2) is derived from equation (1) with the gray body assumption:

$$\frac{I_1}{I_2} = (\frac{\lambda_2}{\lambda_1})^5 \frac{exp(C_b/\lambda_2 T)}{exp(C_b/\lambda_1 T)} \qquad (2)$$

According to equation (2), T can be expressed as follows:

$$T = \frac{C_b(\lambda_1 - \lambda_2)}{\lambda_1 \lambda_2} \frac{1}{ln(I_1 \lambda_1^5 / I_2 \lambda_2^5)} \qquad (3)$$

Fig. 2.2 shows the schematic illustration of two-color pyrometry for the temperature measurement of anode surface during arc discharge. The radiation emitted from the anode surface was divided by a splitting mirror, and then it passed through two band-pass filters. Spectroscopic measurements (iHR550, Horiba Jobin Yvon) were conducted to determine appropriate wavelengths. Band-pass filters were selected with no line emission in the bandwidth of them. As shown in Fig. 2.3, two band-pass filters of 785±1.5 and 880±2.5 nm were employed for temperature measurements in order to eliminate the influence of line emission from the arc.

As demonstrated in Figs. 2.4 (a) and (b), images of the electrode at wavelengths of 880±2.5 and 785±1.5 nm were simultaneously recorded by the high-speed camera (FASTCAM-SA WTI, Photron). Measurement conditions of the high-speed camera were 2,000 fps (frame per second) and 25 μs for the frame rate and the shutter speed, respectively. Considering the bandwidth of band-pass filters and the sensitivity of high-speed camera, the two-color pyrometry system was calibrated by employing a tungsten lamp as a standard light source, which is provided by Japan Calibration Service System. The procedure of calibration is as follows:

(i) The irradiance of standard tungsten lamp was measured by this two-color system with two band-pass filters. The irradiance measured by band-pass filter of 785 nm can be defined as I_{785MW}, and the irradiance measured by band-pass filter of 880 nm can be defined as I_{880MW}.

(ii) The irradiance values of standard tungsten lamp at 785 and 880 nm are provided by Japan Calibration Service System, they are defined as I_{785SW} and I_{880SW}, respectively.

(iii) Relative intensity of measured standard tungsten lamp to real standard tungsten lamp at different wavelengths can be expressed as follows:

$$K_{785RW}= I_{785MW}/I_{785SW};\ K_{880RW}= I_{880MW}/I_{880SW}$$

(iv) Coefficient of two band pass filters at 785 nm and 880 nm (η) can be obtained as follows:

$$\eta=K_{785RW}/K_{880RW}$$

(v) The real relative ratio of thermal radiation can be calculated by using measured relative ratio thermal radiation of electrode from two band-pass filters (I_{785ME}/I_{880ME}) to divide the above coefficient (η) as follows:

$$K_r = (I_{785ME}/I_{880ME})/\eta$$

Therefore, the influences from the lens, mirror, and other parts of this two-color pyrometry system can be eliminated by above calibration. As demonstrated in Fig. 2.4 (c), a temperature distribution map was obtained by the equation (3) with the measured intensity ratio of selected radiations. Since the sensitivity of high-speed camera was poor at the low temperature region, only high temperature region where the temperature is over than 1,600 K was shown in the temperature distribution map.

2.2.4 High-Speed Camera Measurements

The dynamic arc behavior was observed by using the same optical system with the temperature measurements. As shown in Fig. 2.5, the emissions from atomic hydrogen and nickel were observed by the band-pass filters with the central wavelength of 500 and 656 nm, respectively. Typical frame rate and the exposure time of the measurements were 10,000 fps and 100 μs, respectively.

2.2.5 Oscilloscope Measurements

The arc voltage and current were recorded by an oscilloscope (Scope Corder DL 850, Yokogawa) at 1 MHz, which was synchronized with two high-speed cameras. These two high-speed cameras were employed to measure anode surface temperature and observe arc behavior, respectively.

2.2.6 Sample Characterization

The phase identification of the prepared nickel nanoparticles were carried out by X-ray diffractometry (XRD, MXP3TA, Mac Science) operated with Cu Kα source (k=0.1541 nm). The diffraction data was collected using a continuous scan mode with the speed of 2º (2θ)/min in the range of 30-80º with a step size of 0.04º. The accelerating voltage and applied current were 40 kV and 20 mA, respectively. The morphologies of as prepared nickel nanoparticles were examined by field emission scanning electron microscopy (FE-SEM: S-5200, Hitachi) and transmission electron microscopy (TEM: JEM-2010F, JEOL). For the size distribution, we considered about 200 nanoparticles of the product from the FE-SEM or TEM images, and the diameter of each particle was measured.

2.3 Results and Discussion

Two synchronized high-speed cameras were employed to observe arc behavior and measure anode temperature simultaneously. The effects of H_2 concentration and shield gas flow rate on the characteristics of nickel nanoparticles in helium and argon arcs were discussed in the following sections. However, as a result of the continuous emission of argon arc, anode temperature could not be measured successfully in argon arc by above two-color pyrometry system.

2.3.1 Effect of Hydrogen Concentration

(a) Arc-Anode Attachment Mode under Helium

Fig. 2.6 shows the snapshots of high-speed camera of helium arc with different H_2 concentrations. Figs. 2.6 (a), (b), and (c) correspond to H_2 concentration of 10, 20, and 30vol%, respectively. Two typical arc-anode attachment modes are observed at different H_2 concentrations. Several small anode spots can be seen at the anode boundary simultaneously, which is the characteristic of multiple attachment mode (Heberlein et al. 2010). Consequently, multiple arc-anode attachment mode is formed when the hydrogen concentrations are 10 and 20vol%. The area of anode jet in 20vol% of hydrogen is larger than that of 10vol% hydrogen arc. Multiple attachments are considered to result from electron overheating instabilities (Baksht et al. 1997).

As demonstrated in Fig. 2.6 (c), an entirely different arc-anode attachment mode appears with the same current and with the same electrode gap distance, provided that the H_2 concentration is substantially increased. In this case the anode arc root appears more or less constricted, giving rise to the same type of magnetohydrodynamics (MHD) pumping as observed at the cathode (Boulos et al.1994). It can be explained by two effects as follows:

(i) Metal evaporation leads to higher electrical conductivity, resulting in the constriction of arc at anode region (Watanabe et al. 2013);

(ii) The entrained gas in the anode region is heated by the arc and accelerated towards the cathode, enhancing the anode jet (Sanders et al. 1982).

As a result, the constricted mode is formed at the hydrogen concentration of 30vol%.

Fig. 2.7 shows the snapshots of high-speed camera in helium arc when H_2 concentration is 10vol% and shield gas flow rate is 0 L/min. The cathode jet and anode jet are the upper one and the lower one in this figure, respectively. The emissions of HI and NiI are observed by using the band-pass filters of 656 and 500 nm, respectively. As demonstrated in these snapshots, the anode jet and cathode jet are observed successfully by using these suitable band-pass filters. The multiple attachments can be seen at anode jet region. The variations of anode jet area and cathode jet area with time will be discussed below from these snapshots quantitatively.

Fig. 2.8 demonstrates the snapshots of high-speed camera observed by the band-pass filters of 656 and 500 nm when H_2 concentration is 20vol% and shield gas flow rate is 0 L/min. In contrast to the anode jet at hydrogen concentration of 10vol%, the area of anode jet is larger when the hydrogen concentration is increased to 20vol%. Higher hydrogen concentration leads to larger evaporation rate of anode owing to the thermal pinch effect when hydrogen is added in helium arc (Murphy et al. 2009).

The reprehensive snapshots of high-speed camera for helium arc with 30vol%-hydrogen are shown in Fig. 2.9. Compared with low hydrogen concentration case, the largest area of anode jet appears in 30vol%-hydrogen arc. The shape of cathode jet shows significant variation with time because of the instability of the arc. The area of anode jet is equal to that of cathode jet sometimes. The constriction of anode jet can be clearly noticed, because higher hydrogen concentration leads to the transition of attachment mode from multiple mode into constricted mode by enhancing the evaporation rate of anode.

Fig. 2.10 shows the waveforms of anode/cathode jet area variation (upper) and synchronized arc current and voltage waveforms (lower) for helium arc with different hydrogen concentrations. Figs. 2.10 (a)-(a1), (b)-(b1), and (c)-(c1) correspond to the hydrogen concentration of 10, 20, and 30vol%, respectively. As shown in these figures, the largest cathode jet area and the smallest anode jet area can be observed simultaneously, since cathode jet and anode jet compete against each other. The average areas of anode jet are 4840, 6404, and 8313 pixels, corresponding to the hydrogen concentration of 10, 20, and 30vol%, respectively. In the cases of 10 and 20vol% hydrogen arc, the main frequency of cathode jet area and anode jet area variation is 100 Hz, which comes from the DC power supply. Moreover, the shape of cathode jet area variation is similar to the waveform of arc current. However, as shown in Fig. 2.10 (b), the anode jet area variation with small fluctuation can be observed, which is caused by the variation of anode spot on the anode surface in multiple attachments. In contrast to relatively strong cathode jet, the effect of anode jet area variation is too weak to influence the waveform of cathode jet variation, though the cathode jet and the anode jet balance each other. As a result, cathode jet area variation still follows the waveform of arc current. The area of anode jet is larger than that of cathode jet at some cases in the constricted attachment mode. Since the anode jet fluctuates with the time significantly and the cathode jet should be balanced by the anode jet, the cathode jet area variation could not follow the waveform of arc current very well.

(b) Anode Temperature under Helium

In order to analyze an evident correlation among the arc behavior, the anode surface temperature, and the arc current waveform, the operating current waveform synchronized with snapshots of arc behavior and calculated temperature distribution map are shown in Fig. 2.11. The nickel anode jet area variation is strongly affected by the ripple of the arc current. The area of hydrogen cathode jet becomes larger at the peak of the arc current, while the hydrogen cathode jet becomes smaller at the valley of the arc current. On the contrary, the area of nickel anode jet becomes smaller at the peak of the arc current, while the area of nickel anode jet becomes larger at the valley of the arc current. This is because higher arc current leads to the enhancement of cathode jet, while the anode jet becomes weaker due to the strong cathode jet. However, according to the synchronized temperature distribution map, no significant difference can be noticed between the peak and the valley of arc current.

Fig. 2.12 shows the current and voltage waveforms synchronized with temperature distribution maps and snapshots of arc behavior when the hydrogen concentration is 20vol%. Similar to 10vol%-hydrogen arc, the hydrogen cathode jet has large area at the peak of arc current, while the area reduces at the valley of arc current. Contrastingly, the variation tendency of nickel anode jet area is opposite to that of hydrogen cathode jet area. As shown in the synchronized temperature distribution map, the highest temperature of anode surface increases with increasing hydrogen concentration by comparing with Fig. 2.11. It can be explained by the thermal pinch effect, the constriction of arc at higher hydrogen concentration leads to higher anode temperature.

In addition, the current and voltage waveforms of helium arc with 30vol% hydrogen synchronized with temperature distribution maps and the snapshots of arc behavior are shown in Fig. 2.13. The relatively large nickel anode jet can be observed at the peak of arc current. In particular, the significant movement of anode spot can be seen in the constricted mode. However, the arc current does not affect the area of anode jet owing to the instability of the arc. In addition, this figure does not indicate the clear relationship between arc current and temperature of anode surface.

The time averaged temperature distribution maps at different hydrogen concentrations are indicated in Fig. 2.14. The total time is 20 ms for the time averaged temperature calculation. The size of high temperature region (over than 2400 K) increases with increasing hydrogen concentration. In contrast to multiple attachment mode, anode surface has the highest temperature in constricted attachment mode, which leads to the largest evaporation rate of nickel anode. Therefore, anode jet with the largest area presents in constricted mode. As discussed in previous section, the variation of anode temperature is caused by the constriction of anode spot due to the thermal pinch effect.

The time variation of the highest temperature region is shown in Fig. 2.15, the calculated region corresponds to the area of 4×4 pixels in the temperature distribution map. The highest temperatures are 2145, 2350, and 3000 K corresponding to the hydrogen concentration of 10, 20, and 30vol%, respectively. The highest temperature region fluctuates with a high frequency can be noticed in Figs. 2.15 (a) and (b), which depends on the high frequency of anode spot variation in multiple attachment mode. The synchronized waveforms of the anode and cathode jet area variations are shown in Fig. 2.15 for comparison. As shown in Figs. 2.15 (b) and (b1), the shape of the highest temperature region variation is similar to that of anode jet area variation in multiple attachment mode. High temperature contributes to large evaporation rate of nickel anode, thus large area of anode jet. However, a little difference between the waveform of anode jet area variation and the highest temperature variation are shown in Figs. 2.15 (a) and (a1). It can be explained by the fact that the large cathode jet at the hydrogen concentration of 10 L/min is too strong to identify the variation of anode jet. It is supposed that the good consistency exists between the variation of the highest temperature region and anode jet area variation in constricted mode. However, as shown in Fig. 2.15 (c), the shape of the highest temperature region variation is different from the shape of anode jet area variation. The reason can be explained by the technical limitation of temperature measurement. Because the observation window for temperature measurement is easy to be covered by evaporated nanoparticles, the frame rate of 1000 fps was chosen to maintain the relatively strong emission intensity of the anode surface for temperature measurement. Since the time interval for each snapshot is large in temperature measurement, the measured temperature variation could not present the actual temperature variation well.

The effects of hydrogen concentration on the variation of the highest temperature and standard deviation of temperature are shown in Fig. 2.16. As shown in Fig. 2.16 (a), the highest temperature increases with increasing hydrogen concentration because of the thermal pinch effect. Fig. 2.16 (b) shows the standard deviation of temperature variation in helium arc, indicating that temperature reveals larger standard deviation in constricted mode than multiple mode.

(c) Characteristics of Nickel Nanoparticle under Helium The XRD patterns of the prepared nickel nanoparticles in helium arc at different hydrogen concentrations are demonstrated in Fig

2.17. The XRD patterns clearly show the single phase of nickel without any observable impurities. Three typical diffraction peaks of the patterns can be indexed into (110), (200), and (220) planes of nickel, respectively. According to the Scherer's formula, the average grain size can be calculated based on the (111) diffraction peaks for different samples. Since the full width of half maximum (FWHM) of the diffraction peak (111) reduces with increasing hydrogen concentration, the average grain size increases with increasing hydrogen concentration can be concluded.

Fig. 2.18 indicates the FE-SEM images of nickel nanoparticles at different hydrogen concentrations from 10 to 30vol%. Nickel nanoparticles with the spherical shape are obtained in both multiple and constricted attachment modes. It is clearly revealed in Fig. 2.18 (b) that the nickel nanoparticles have the size distribution in the range of 10 to 90 nm when hydrogen concentration is 20vol%. As shown in Fig. 2.18 (c), the nanoparticles with larger diameter can be obtained at hydrogen concentration of 30vol%.

The particle size distribution is shown in Fig. 2.19. The mean diameters of nanoparticles are 28, 35, and 50 nm, corresponding to the hydrogen concentration of 10, 20, and 30vol%, respectively. The average particle size increases with increasing hydrogen concentration. According to the formation mechanism of nanoparticle by DC arc discharge method (Tanaka and Watanabe 2008), higher vapor concentration enhances the nanoparticles growth by condensation. Therefore, higher hydrogen concentration contributes to large particle size, because the large evaporation rate of anode caused by the constriction of arc. The standard deviations of nanoparticle sizes are 7, 10, and 12 nm, corresponding to hydrogen concentration of 10, 20, and 30vol%, respectively. The uniformity of nanoparticles becomes poor when the arc anode attachment transits to constricted mode.

The particle size distribution is large by DC arc method due to the intrinsic characteristics of this method. Both of temporal and spatial factors affect the size of nanoparticle. There are two kinds of time fluctuation in DC arc, one fluctuation has the frequency of 100 Hz, which is attributed to the DC power supply. According to numerical simulation result (Shigeta and Watanabe. 2010), the time constant for nanoparticle growth in thermal plasma is about 10 ms. Therefore, DC arc with the fluctuation of 100 Hz has strong effect on the particle size owing to different thermal histories of nanoparticles. In addition, the other fluctuation is induced by the arc-anode attachment mode. According to FFT spectrum of voltage waveform and the high-speed camera image in multiple attachment mode, the frequency of arc spot is around 10 kHz, temperature fluctuation has the same frequency with it. Time constant of temperature fluctuation is 0.1 ms, which is smaller than the time constant of nanoparticle growth. As a result, the fluctuation with the frequency of 10 kHz does not have strong effect on the particle size.

The spatial vapor pressure distribution and spatial velocity distribution have strong effect on the size of nanoparticle. According to the formation mechanism of nanoparticles by DC arc discharge method (Tanaka and Watanabe 2008), the vapor starts to nucleate at suitable vapor pressure, and then it will grow into nanoparticles by condensation and collision. Therefore, the nanoparticle size is mainly determined by the vapor pressure distribution and the residence time. The non-uniform vapor distributions in DC arc leads to the particles have different thermal histories, thus different particle sizes (Murphy. 2013; Watanabe and Shigeta. 2010). For example, if the vapor nucleates at the position with high vapor pressure, the nucleation temperature is high. According to the equations of nucleation rate and critical diameter (Shigeta and Watanabe. 2007), higher nucleation temperature leads to lower nucleation rate, larger critical diameter (Shigeta and Watanabe. 2007), and smaller number of nuclei. Since the consummation of vapor for nucleation is low at high vapor pressure position, the significant condensation leads to nuclei growth into nanoparticles with large size because of large amount of remained vapors. In contrast, the nucleation starts at the position with low vapor pressure, resulting in a large number of nuclei grow into nanoparticles with relatively small size. Consequently, the spatial distribution of vapor pressure affects the size of nanoparticle significantly. In addition, the residence time can be evaluated by the velocity of plasma flow based on the assumption that the velocities of particle and plasma flow are same. The lower velocity leads to longer residence time, thus large nanoparticle size. Therefore, the non-uniform velocity distribution in DC arc also leads to nanoparticles with different sizes.

(d) Arc-Anode Attachment Mode under Argon

Fig. 2.20 shows the snapshots of high-speed camera of argon arc with different H_2 concentrations. Figs. 2.20 (a), (b), and (c) correspond to H_2 concentration of 0, 30, and 50vol%, respectively. Three typical arc-anode attachment modes were observed in argon arc at different H_2 concentrations. As shown in Fig. 2.20 (a), the cathode jet impinges on the anode surface, a stagnation layer forms in front of the anode, resulting in the well-known bell shape of the arc. In this situation, the anode arc root is rather diffuse. This arc-anode attachment mode is denoted as diffuse attachment mode (Sanders et al. 1982). According to the explanation about arc-anode attachment of helium arc in previous section, Figs. 2.20 (b)-(c) correspond to multiple attachment mode and constricted attachment mode, respectively. Multiple attachment mode has been considered as a transition mode between the diffuse mode and the constricted mode. The transition of attachment mode is mainly related to the variation of anode evaporation rate caused by different hydrogen concentrations. The formation mechanism of attachment mode will be explained in next section.

Fig. 2.21 indicates the snapshots of high-speed camera of argon arc when hydrogen concentration is 30vol% and shield gas flow rate is 0 L/min. The cathode jet and anode jet are the upper one and the lower one in this figure, respectively. As demonstrated in these snapshots, the anode jet and the cathode jet are observed successfully by using these band-pass filters of 656 and 500 nm, respectively. As shown in these snapshots, the multiple attachments are formed at anode jet region when hydrogen concentration is 30vol%. These images are used to evaluate the variation of anode jet area and cathode jet area quantitatively. Current and voltage waveforms synchronized with snapshots are shown in Fig. 2.22. Similar results to the helium arc are also reached. In multiple attachment mode, the area of hydrogen cathode jet becomes larger at the peak of arc current than that of the valley of arc current. On the contrary, the hydrogen cathode jet is larger at the valley of arc current than that of the peak of arc current.

Fig. 2.23 shows the snapshots of high-speed camera for argon arc with 50vol% hydrogen. Constricted mode can be clearly seen at the anode boundary. The area of nickel anode jet increases with increasing hydrogen concentration, while the hydrogen cathode jet area reduces with increasing the hydrogen concentration because of the strong intensity of cathode jet. The current and voltage waveforms of argon arc with 50vol% hydrogen synchronized with the snapshots of arc behavior are shown in Fig. 2.24. The relatively large nickel anode jet can be noticed at the peak of arc current. In addition, significant movement of anode spot can be seen in the constricted mode, which is also confirmed by the large fluctuation of voltage waveform. However, there is no clear relationship between arc current and the area of anode jet due to the instability of arc.

Fig. 2.25 shows time variation of anode/cathode jet area (upper) and synchronized arc current and voltage waveforms (lower) for argon arc with different hydrogen concentrations. Figs 2.25 (a)-(a1) and (b)-(b1) correspond to the hydrogen concentration of 30 and 50vol%, respectively. Similar results to helium arc are also observed; as shown in the waveform, the peak of cathode jet area variation and the valley of anode jet area variation appear simultaneously. The average areas of cathode jet are 2850 and 4000 pixels, corresponding to the hydrogen concentration of 30 and 50vol%, respectively. As shown in this figure, the waveform of cathode jet variation follows the shape of arc current in diffuse attachment mode at 30vol% of hydrogen. Contrastingly, there is no clear relationship between arc current and the area of anode jet in constricted mode. Both of cathode jet area and anode jet area variation show large fluctuation in constricted mode, it is attributed to the instability of arc. The effect of hydrogen concentration on the formation of different attachment modes is similar to that of helium arc, high hydrogen concentration contributes to the formation of constricted mode. However, in order to form the same attachment mode, higher hydrogen concentration is required for argon arc when other experimental conditions are same. The effect of evaporation rate on the formation of different arc-anode attachment modes will be discussed in the formation mechanism section.

(e) Characteristics of Nickel Nanoparticle under Argon

The XRD patterns of the prepared nickel nanoparticles in argon arc with different hydrogen concentrations are shown in Fig 2.26. As discussed in previous section, the XRD patterns clearly show the single phase of nickel without any observable impurities. Three typical diffraction peaks of the patterns can be fully indexed into (110), (200), and (220) planes of nickel, respectively.

Fig. 2.27 indicates the TEM images of nickel nanoparticles obtained at different hydrogen concentrations from 0 to 50vol%. As shown in Fig. 2.27 (a), the shape of nanoparticles is dominated by spherical besides some irregular shapes when the hydrogen concentration is 0vol%. It is clearly seen in Figs. 2.27 (b) and (c), all of nanoparticles have spherical shape. Compared with nanoparticles obtained in diffuse and multiple modes, the particle size becomes larger in constricted mode. The particle size distribution is shown in Fig. 2.28. The mean diameters of nanoparticle are 20, 33, and 63 nm, corresponding to the hydrogen concentration of 0, 30, and 50vol%, respectively. As a result of the enhanced evaporation rate of nickel anode, the average particle diameter increases with increasing hydrogen concentration. Higher vapor concentration would enhance the nanoparticles growth by condensation, as a result particle size becomes larger. The standard deviations of nanoparticle sizes are 13, 18, and 36 nm, corresponding to hydrogen concentration of 0, 30, and 50vol%, respectively. It is deducted that the uniformity of nanoparticles becomes poor when the arc anode attachment transits to constricted mode by varying the hydrogen concentration.

(f) Comparison of Helium with Argon

Fig. 2.29 shows the comparison of the evaporation rate of nickel anode in helium and argon arcs at different hydrogen concentrations. The evaporation rate of anode material increases with increasing hydrogen concentration in both of argon and helium arcs. The evaporation rate of nickel is higher in helium arc than that of argon arc when the hydrogen concentration is same; this is a consequence of the high thermal conductivity of helium and the constriction of helium arc. The evaporation of anode material plays an important role in forming different attachment modes. In order to form the same constricted attachment, higher hydrogen concentration is necessary for argon arc. In addition, the attachment mode transitions to constricted mode from diffuse mode by increasing the evaporation rate for helium and argon arcs.

Fig. 2.30 shows the effect of hydrogen concentration on the average particle diameter in helium and argon arcs. Different evaporation rates lead to nickel nanoparticles with different sizes. For example, the average diameter of nickel nanoparticles is 50 nm in helium arc, which is larger than that of 33 nm in argon arc when hydrogen concentration is fixed at 30vol%. Different anode evaporation rates in helium and argon arcs contribute to this variation. Larger vapor concentration leads to large particle size by condensation. However, the mean size is 50 nm in helium arc with 30vol% hydrogen, which is smaller than the mean particle size of 63 nm in argon arc with 50vol%, although the evaporation rate in helium arc is larger than that of argon arc. The relatively large particle size in argon arc may be related to the short residence time for nanoparticle grown in helium arc due to the constriction of arc.

2.3.2 Effect of Shield Gas Flow Rate

(a) Arc-Anode Attachment Mode under Helium

The effects of shield gas flow rate on anode attachment mode and temperature variation are investigated in helium arc when the hydrogen concentration is 20vol%. Fig. 2.31 shows the representative snapshots of high-speed camera in helium arc when hydrogen concentration is 20vol% and shield gas flow rate is 10 L/min. As shown in Fig. 2.31, the width of arc column at shield gas flow rate of 10 L/min becomes smaller than that without shield gas as shown in Fig. 2.8. In addition, anode attachment mode is changed into the constricted mode when shield gas flow rate is 10 L/min, though there is a small component of multiple attachments sometimes. This is considered to result from injecting cool gas into arc region, leading to the constriction of the arc column induced by thermal pinch effect. The constriction of arc results in larger heat flux and larger evaporation rate of anode material. In addition, the entrained gas in the anode region is heated by the arc and accelerated towards the cathode. These two reasons contribute to form constricted mode when shield gas flow rate is 10 L/min at hydrogen concentration of 20vol% helium arc.

Fig. 2.32 shows the representative snapshots of high-speed camera in helium arc when H_2 concentration is 20vol% and shield gas flow rate is 20 L/min. The nickel anode jet is dominated by the multiple attachment mode. The area of anode jet at shield gas flow rate of 20 L/min becomes smaller in contrast to shield gas flow rate of 10 L/min. According to the snapshot, the shape of nickel anode jet has greatly variation with time, and the position of anode spot moves with time remarkably. This is a consequence of unstable arc at shield gas flow rate of 20 L/min. The effect of shield gas flow rate on the arc behavior will be discussed in next paragraph.

Fig. 2.33 indicates the time variation of anode/cathode jet area of helium arc with 20vol%-hydrogen by changing shield gas flow rate. The synchronized arc current and voltage waveforms locate under the waveforms of anode/cathode jet area variation for comparison. The opposite variation tendency between cathode jet and anode jet still exists. The average anode jet areas are 6404, 8163, and 6565 pixels, corresponding to the shield gas flow rate of 0, 10, and 20 L/min, respectively. In the multiple attachments, hydrogen cathode jet variation exhibits similar shape to arc current waveform. In addition, the waveform of cathode jet variation is also similar to the waveform of arc current in constricted mode. This result is different from that of hydrogen concentration of 30vol% in helium arc, although the constricted mode is formed. It can be explained by the fact that the anode spot is fixed by shield gas in constricted mode. In addition, the intensity of anode jet is not strong enough to affect the variation of cathode jet at shield gas flow rate of 10 L/min. Consequently, the cathode jet variation follows the waveform of arc current. As shown in Fig. 2.33 (c), the shape of hydrogen cathode jet could not follow the arc current waveform owing to the instability of arc at larger shield gas flow rate of 20 L/min. Larger shield gas flow rate results in cathode jet with strong intensity, therefore, relatively small area of anode jet can be observed at shield gas flow rate of 20 L/min.

Fig. 2.34 demonstrates the effect of shield gas flow rate on the area of anode jet. Shield gas has two main effects; increasing the intensity of cathode jet and enhancing the evaporation rate of anode material by thermal pinch effect. As shown in Fig. 2.34, anode jet area increases with increasing shield gas flow rate before it reaches to 10 L/min, which is mainly caused by the thermal pinch effect when large amounts of cool plasma gas is injected into the arc. However, the anode jet area reduces when shield gas flow rate is over than 10 L/min, since larger shield gas flow rate leads to increase the intensity cathode jet. Moreover, arc becomes unstable at large shield gas flow rate induced by a large amount of cool gas. As a result of the strong cathode jet and the fast movement of anode spot on the anode surface, the average area of anode jet decreases at shield gas flow rate of 20 L/min.

(b) Anode Temperature under Helium

Fig. 2.35 shows the current and voltage waveforms of helium arc synchronized with temperature distribution maps and the snapshots of arc behavior when the shield gas flow rate is 10 L/min. The largest area of hydrogen cathode jet appears at the peak of arc current, while the smallest hydrogen cathode jet can be seen at the valley of arc current. As demonstrated in the temperature distribution map, the highest temperature appears at the valley of arc current. It is predicted that arc spot with relatively small size at the valley of arc current leads to large heat flux. The temperature behavior is different from the constricted mode obtained in helium arc at the hydrogen of 30vol%. As shown in Fig. 2.33, because the waveform of cathode jet variation follows that of the arc current, and the tendency of cathode jet variation is opposite to that of anode jet, the largest anode jet area can be observed at the valley of the arc current.

Fig. 2.36 indicates the current and voltage waveforms of helium arc synchronized with temperature distribution maps and the snapshots of arc behavior when the shield gas flow rate is 20 L/min. The instability of arc leads to high frequency of arc voltage fluctuation. The hydrogen cathode jet has irregular shape at different valleys of arc current, and the anode spot moves to far away region with long arc column sometimes. All of these irregular arc behaviors come from the instability of the arc.

Fig. 2.37 indicates time averaged temperature of the anode surface in helium arc at different shield gas flow rates. The highest temperature appears at the appropriate shield gas flow rate of 10 L/min. The appropriate shield gas flow rate leads to high temperature of the anode surface owing to the thermal pinch effect, while larger shield gas flow rate results in the movement of anode spot on anode, as a result of the low temperature of anode surface.

The time variation of the highest temperature at different shield gas flow rates is given in Fig. 2.38. The highest temperatures are 2350, 3185, and 3180 K, corresponding to shield gas flow rate of 0, 10, and 20 L/min, respectively. It can be deduced that constricted mode leads to the highest temperature. The shape of the highest temperature variation with time is similar to that of anode jet area variation in the case of multiple and constricted attachment modes, which confirms the prediction in Fig. 2.15 well. High temperature leads to large evaporation rate of nickel and large area of anode jet.

Figs. 2.39 (a) and (b) demonstrate the highest temperature variation and standard deviation of temperature in helium arc when changing the shield gas flow rate, respectively. The highest temperature is obtained at shield gas flow rate of 10 L/min, since constricted mode leads to the largest heat flux. And then the highest temperature reduces with increasing the shield gas flow rate. The variation tendency of temperature is caused by two effects of shield gas flow rate on the arc behavior. Suitable shield gas flow rate leads to the constriction of the arc due to the thermal pinch effect. As a result, temperature increases with increasing the shield gas flow rate. However, arc becomes unstable when shield gas flow rate reaches to some value, anode temperature decreases when a large amount of shield gas is injected. As shown in Fig. 2.39 (b), the standard deviation of temperature has the same variation tendency with the highest temperature. Constricted mode contributes to the largest standard deviation of anode temperature.

(c) Characteristics of Nickel Nanoparticle under Helium

The FE-SEM images of nickel nanoparticles at different shield gas flow rates are shown in Fig. 2.40. Figs. 2.40 (a)-(c) correspond to the shield gas flow rate of 0, 10, and 20 L/min, respectively, when hydrogen concentration is fixed at 20vol%. All of the nanoparticles have spherical shape regardless of the shield gas flow rate. The largest particle size can be obtained at shield gas flow rate of 10 L/min. However, the uniformity of nanoparticles is poor at the shield gas flow rate of 20 L/min. It is mainly caused by low evaporation of nickel nanoparticle and a significant movement of arc spot on anode surface at large shield gas flow rate, leading to different residence time for nanoparticles growth.

Fig. 2.41 shows the particle size distribution at different shield gas flow rates. A narrow size distribution can be obtained when shield gas flow rate is 10 L/min, which can be explained by the fact that suitable shied gas flow rate can fix the arc spot on the anode surface, resulting in the particles with a narrow size distribution. The average particle sizes are 35, 40, and 29 nm, corresponding to shield gas flow rate of 0, 10 and 20 L/min, respectively. As discussed in previous section, the variation of average particle size is caused by the evaporation rate of anode at different shield gas flow rates. Higher vapor concentration leads to the growth of nanoparticles by condensation. The standard deviations of nanoparticle sizes are 10, 8, and 11 nm, corresponding to shield gas flow rate of 0, 10, and 20 L/min, respectively. The uniformity of nanoparticle becomes better at the suitable shield gas flow rate in helium arc. In summary, constricted mode contributes to high productivity of nickel nanoparticle with relatively large average particle size. In order to obtain the nickel nanoparticles with large productivity and a narrow size distribution, 20vol%-hydrogen arc with suitable shield gas flow rate is the best condition.

(d) Arc-Anode Attachment Mode under Argon

Fig. 2.42 shows the snapshots of high-speed camera for argon arc when hydrogen concentration is 30vol% and shield gas flow rate is 10 L/min. The formation of multiple attachments is confirmed at anode boundary. Current and voltage waveforms synchronized with snapshots are shown in Fig. 2.43. Similar results to shield gas flow rate of 0 L/min are also observed. In multiple attachment mode, the area of hydrogen cathode jet becomes larger at the peak of the arc current, while the nickel anode jet becomes smaller at the peak of the arc current. Similar reasons to helium arc can be employed to explain this result.

Fig. 2.44 shows the snapshots of high-speed camera for argon arc when hydrogen concentration is 30vol% and shield gas flow rate is 20 L/min. Multiple attachments still can be seen clearly at anode boundary. Compared with the anode jet area at shield gas flow rates of 0 and 10 L/min, the nickel anode jet area increases when the shield gas flow rate is 20 L/min owing to the thermal pinch effect. Fig. 2.45 indicates voltage and current waveforms of argon arc synchronized with snapshots of arc behavior when H_2 concentration is 30vol% and shield gas flow rate is 20 L/min. The anode jet area is smaller at the peak of arc current than that of the valley of arc current. In some cases, the anode jet could not be seen at the peak of arc current due to the strong intensity of cathode jet.

Fig. 2.46 indicates the time variation of anode jet area and cathode jet area in 30vol%-hydrogen arc when changing shield gas flow rate. The opposite variation tendency between cathode jet area and anode jet area still exists. The average anode jet areas are 2840, 3360, and 3450 pixels, corresponding to the shield gas flow rate of 0, 10, and 20 L/min, respectively. The synchronized current and voltage waveforms locate under the waveforms of anode/cathode jet area variation. Hydrogen cathode jet variation exhibits similar shape to the arc current waveform at low shield gas flow rates of 0 and 10 L/min. However, as a result of the instability of arc at larger shield gas flow rate of 20 L/min, the large fluctuation of anode jet leads to large fluctuation of cathode jet. The waveform of cathode jet variation is different from the waveform of arc current because of the instability of the arc.

Fig. 2.47 indicates the effect of shield gas flow rate on the average area of anode jet in argon arc. The average area of anode jet increases with increasing the shield gas flow rate, indicating the thermal pinch effect is dominated at low shield gas flow rate. However, a small increase of the anode jet area when the shield gas flow rate changes from 10 to 20 L/min. It can be explained by the effects of increasing the intensity of cathode jet and inducing the instability of arc by large flow rate of shield gas.

(e) Characteristics of Nickel Nanoparticle under Argon

The TEM images of nickel nanoparticles in argon arc at different shield gas flow rates are shown in Fig. 2.48. Figs. 2.48 (a) and (b) correspond to shield gas flow rate of 0 and 20 L/min, respectively, when the hydrogen concentration is fixed at 30vol%. All of the nanoparticles have spherical shape. According to the TEM image, the particle size distribution is calculated. Fig. 2.49 shows particle size distribution by changing shield gas flow rate. The average particle sizes are 33 and 32 nm, corresponding to the shield gas flow rate of 0 and 20 L/min, respectively. The standard deviations of nanoparticle sizes are 18 and 20 nm, corresponding to shield gas flow rate of 0 and 20 L/min, respectively. The uniformity of nanoparticle is poor at shield gas flow rate of 20 L/min in argon arc. However, the particles have large size distribution when shield gas is increased to 20 L/min, even some particles reach to the size of 160 nm. The movement of arc spot on anode surface at large shield gas flow rate leads to the significant variation of residence time for nanoparticle growth. As a result, nanoparticles have large size distribution.

(f) Comparison of Helium with Argon

Fig. 2.50 indicates the effect of shield gas flow rate on the evaporation rate of nickel anode in helium and argon arcs. Helium arc with 20vol% hydrogen and argon arc with 30vol% hydrogen are selected for comparison, these two conditions correspond to the multiple attachment mode. As shown in Tables. 2.3-2.6, input power does not show significant difference in these two conditions. The evaporation rate of nickel anode in helium arc is 10 times larger than that of argon arc, although the hydrogen concentration is higher in argon arc. The reason is attributed to higher thermal conductivity of helium and the constriction of helium arc. However, the effect of shield gas flow rate on the evaporation rate of anode demonstrates different tendencies. Strong thermal pinch effect leads to the enhancement of anode evaporation at large shield gas flow rate of 20 L/min in argon arc, although the arc becomes unstable. However, the arc becomes dramatically unstable and the evaporation rate reduces at large shield gas flow rate of 20 L/min in helium arc, because the effects of arc stability and the strong cathode jet are dominated in helium arc with 20vol% hydrogen.

Therefore, suitable shield gas flow rate leads to the attachment transition to constricted mode in helium arc. Because shield gas stabilizes the arc spot on the anode surface, nanoparticles with narrow size distribution can be obtained. However, the attachment mode does not change in argon arc when increasing shield gas flow rate. Fig. 2.51 indicates the effect of shield gas flow rate on average particle diameter in helium and argon arcs. Because shield gas flow rate could not affect the evaporation rate of anode material significantly in argon arc, there is no significant variation of average nanoparticle size. In the case of helium arc, large shield gas flow rate of 20 L/min leads to the movement of arc spot on the anode surface, the nanoparticles with small average size and large size distribution are obtained.

Figs. 2.52 (a)-(b) show the effects of input power on the evaporation rate and the average particle diameter, respectively. The values of input power are shown in Tables. 2.3-2.6. As shown in Fig. 2.52, for the effect of hydrogen concentration, the evaporation rate increases with increasing input power for helium and argon arcs. In particular, the evaporation rate in helium arc is higher than that of argon arc, although the input power in argon arc is higher than that of helium arc. It is related to large heat flux in helium arc caused by the constriction of helium arc and high thermal conductivity of helium. In the case of shield gas flow rate effect, the evaporation rate increases with increasing shield gas flow rate for argon arc. That is because the thermal pinch effect is dominated in these conditions. However, the evaporation rate becomes small at shield gas flow rate of 20 L/min in helium arc. It can be explained by the fact that the instability of arc reduces the heat flux. As shown in Fig. 2.52 (b), the variation of average particle diameter indicates the same tendency with evaporation rate. According to the formation mechanism of nanoparticle, larger vaporization rate leads to higher vapor concentrations and higher growth rate of nanoparticles. As a consequent, the particle with large size can be obtained at large evaporation rate. However, the average particle size in argon arc is larger than that of helium arc, although the evaporation rate is large in helium arc. It may be related to the short residence time for nanoparticle grown in the constricted helium arc.

2.3.3 Mechanism of Different Arc-Anode Attachment Modes

Fig. 2.53 shows the conceptual diagram of the formation mechanism of different arc-anode attachment modes when using DC arc discharge to prepare nanoparticle. The formation of different arc-anode attachment modes is the results of the competition of the cathode jet and the anode jet. The evaporation of anode material plays an important role in the transition of arc-anode attachment from diffuse mode to constricted mode. It is well known that the cathode jet is formed by a pumping action due to the interaction of arc current with its own magnetic field in the high density arc. Cathode jet is rather diffuse since the evaporation of anode is low or shield gas flow rate is large, forming diffuse attachment mode. The evaporation of anode material leads to the transition of arc-anode attachment easily. Larger metal evaporation rate results in higher electrical conductivity, reducing the size of anode spot. In addition, as a result of the effect of entrainment gas, the attachment mode is separated into several small spots, forming the multiple attachments. However, the multiple attachment mode is unstable, larger evaporation rate leads to the constriction of arc spot because of higher electrical conductivity. In addition, entrained gas in the anode region is heated by the arc and accelerated towards the cathode (Sanders et al. 1982), generating relatively strong anode jet. Similar to the formation of cathode jet, the anode jet is enhanced by MHD pumping, leading to the formation of constricted attachment. In turn, constricted mode will enhance the anode evaporation simultaneously due to large heat flux. Therefore, anode evaporation plays an important role in forming different arc-anode attachment modes. In addition, the formation of different arc-anode attachment modes is influenced by other experimental conditions, such as shield gas flow rate and electrode gap distance and so on.

Fig. 2.54 demonstrates the effects of shield gas flow rate and hydrogen concentration on the formation of different arc-anode attachment modes. Figs. 2.54 (a) and (b) corresponds to helium arc and argon arc, respectively. Higher hydrogen concentration leads to the transition of attachment mode to constricted mode by enhancing evaporation rate of anode. According to above formation mechanism, large evaporation rate leads to constricted mode. However, the shield gas has two main functions on the formation of different attachment modes. As demonstrated in Fig. 2.54 (a), large shield gas flow rate leads to the transition of attachment from constricted to multiple in argon arc at the hydrogen concentration of 50vol%. In these cases, shield gas plays an important role in enhancing the cathode jet. In contrast, the arc-anode attachment mode is constricted mode at shield gas flow rate of 10 L/min in helium arc when hydrogen concentration is 20vol%. It can be explained by the reason that thermal pinch effect is dominated at suitable shield gas flow rate, while large shields gas flow rate of 20 L/min leads to the transition of arc-anode attachment mode to multiple mode in helium arc. It is attributed to the strong intensity of cathode jet and the instability of the arc. Therefore, the thermal pinch effect and the effect of enhancing cathode jet intensity should be considered when investigating the effect of shield gas flow rate on the formation of different attachment modes.

2.4 Conclusion

Diffuse, multiple, and constricted modes were observed in helium and argon arcs when using DC arc discharge method to prepare nickel nanoparticles. The attachment mode transitions from diffuse mode to constricted mode when increasing hydrogen concentration. Suitable shield gas flow rate leads to the enhancement of anode jet. The average particle size increases when the attachment mode transitions from diffuse mode to constricted mode. Nickel nanoparticles with large productivity and narrow size distribution were obtained in helium arc. The relatively small average nanoparticles size of 40 nm with a narrow size distribution can be obtained by controlling shield gas flow rate in helium arc.

In addition, anode surface temperature in helium arc was measured by two-color pyrometry combined with a high-speed camera which employed the band-pass filters of 880±2.5 and 785±1.5 nm. Anode surface with high temperature was measured in constricted mode due to the constriction of arc spot. The anode jet variation follows the highest temperature variation, while the cathode jet variation is opposite to anode jet variation. In multiple attachment mode, the variation of cathode jet follows the arc current variation. Contrastingly, the cathode jet variation could not follow the arc current variation in constricted mode.

The formation mechanism of attachment mode was considered to result from the evaporation of anode material. Anode evaporation leads to higher electrical conductivity, resulting in the constriction of the arc in anode region. As a result, the attachment mode transitions to constricted mode in the case of large evaporation rate.

References:

Baksht, F. G., G. A. Dyuzhev, N. K. Mitrofanov and S. M. Shkolnik. “Experimental investigation of the anode region of a free-burning atmospheric-pressure inert-gas arc: II. Intermediate current regime-multiple anode constriction. ”*Technical Physics* **42**(1), 35-38 (1997).

Chazelas, C., J. F. Coudert, J. Jarrige and P. Fauchais. “Synthesis of ultra-fine particles by plasma transferred arc: Influence of anode material on particle properties.” *Journal of the European Ceramic Society* **26**(16), 3499-3507 (2006).

Cordente N., M. Respaud, F. Senocq, M. J. Casanove, C. Amiens and B. Chaudret. “Synthesis and Magnetic Properties of Nickel Nanorods.” *Nano Letters* **1**(10), 565-568 (2001).

Dinulescu H. A. and E. Pfender. “Analysis of the anode boundary layer of high intensity arcs.” *Journal of Applied Physics* **51**(6), 3149-3157 (1980).

Heberlein J. V., J. Mental and E. Pfender. “The anode region of electric arcs: a survey.” *Journal of Physics D: Applied Physics* **43**, 023001 (2010).

Hernandez, R., S. Polizu, S. Turenne and L. Yahia. “Characteristics of porous nickeltitanium alloys for medical applications.” *Bio-Medical Materials and Engineering* **12**, 37-45 (2002).

Iijima, S. “Helical microtubules of graphitic carbon.” *Nature* **354**, 56-58 (1991).

Lan, R. and S. Tao “Preparation of nano-sized nickel as anode catalyst for direct urea and urine fuel cells.” *Journal of Power Sources* **196**, 5021-5026 (2011).

Li, X.G., A. Chiba, S. Takahashi and M. Sato. “Oxidation characteristics and magnetic properties of iron ultrafine particles.” *Jornal of Applied Physics* **83**(7), 3871-3875 (1998).

Liang, F., T. Shimizu, M. Tanaka, S. Choi and T. Watanabe. “Selective preparation of polyhedral graphite particles and multi-wall carbon nanotubes by a transferred arc under atmospheric pressure.” *Diamond and Related Materials* **30**, 70-76 (2012).

Liu, T., H. Y. Shao and X. G. Li: “Oxidation behavior of Fe_3Al nanoparticles prepared by hydrogen plasma-metal reaction." *Nanotechnology* **14**, 542-545 (2003).

Murphy, A. B., M. Tanaka, S. Tashiro, T. Sato and J. J. Lowke. "A computational investigation of the effectiveness of different shielding gas mixtures for arc welding." *Journal of Physics D: Applied Physics* **42**, 115205 (2009).

Murphy A. B. "Influence of metal vapour on arc temperatures in gas–metal arc welding: convection versus radiation." *Journal of Physics D: Applied Physics* **46**, 224004 (2013).

Park, J. W., E.H. Chae, S. H. Kima, J. H. Lee, J. W. Kim, S. M. Yoon and J.Y. Choi. "Preparation of fine Ni powders from nickel hydrazine complex." *Materials Chemistry and Physics* **97**, 371-378 (2006).

Sanders, N., K. Etemadi, K. C. Hsu and E. Pfender "Studies of the anode region of a high-intensity argon arc." *Journal of Applied Physics* **53**(6), 4136-4145 (1982).

Shao, H. Y., Y. T. Wang, H. R. Xu and X. G. Li. "Hydrogen storage properties of magnesium ultrafine particles prepared by hydrogen plasma-metal reaction." *Material Science and Engineering B* **110**(2), 221-226 (2004).

Shigeta M and T. Watanabe. "Growth mechanism of silicon-based functional nanoparticles fabricated by inductively coupled thermal plasmas." *Journal of Physics D: Applied Physics* **40,** 2407-2419 (2007).

Shigeta M and T. Watanabe. "Growth model of binary alloy nanopowders for thermal plasma synthesis" *Journal of Applied Physics* **108**, 043306 (2010).

Tanaka, M. and T. Watanabe. "Vaporization mechanism from Sn-Ag mixture by Ar-H_2 Arc for nanoparticle preparation." *Thin Solid Films* **516**(19), 6645-6649 (2008).

Tanaka M., T. Ikeba, Y. Liu, T. Matsuura and T. Watanabe. "Electrode temperature measurements of multi-phase AC arc by high-speed video camera." *Journal of Physics: Conference Series* **406**, 012008 (2012).

Tanaka, M. and T. Watanabe. "Mechanism of Enhanced Vaporization from Molten Metal Surface by Argon-Hydrogen Arc Plasma." *Japanese journal of applied physics* **52**, 076201(2013).

Watanabe, T., M. Tanaka, T. Shimizu and F. Liang. "Metal Nanoparticle Production by Anode Jet of Argon-Hydrogen DC Arc."*Advanced Materials Research* **628**, 11-14 (2013).

Wei, Z. Q., P. Yan, W. Feng, J. Dai, Q. Wang and T. Xia. "Microstructural characterization of Ni nanoparticles prepared by anodic arc plasma." *Materials Characterization* **57**, 176-181 (2006).

Zhang, X. F., X. L. Dong, H. Huang, Y. Y. Liu, W. N. Wang, X. G. Zhu, B. Lv and J. P. Lei. "Microwave absorption properties of the carbon-coated nickel nanocapsules." *Applied Physics letter* **89**, 053115 (2006).

Table 2.1 Experimental conditions for helium arc

Arc current [A]	100
Electrode gap distance [mm]	6
Arc voltage [V]	25-40
Pressure [kPa]	101.3 (Atmospheric pressure)
Plasma gas	Helium and hydrogen
Hydrogen concentration [vol%]	0, 10, 20, 30, 50
Shield gas flow rate [slpm]	0, 10, 20
Discharge time [min]	5-10
Cathode	Tungsten (2wt % thoria)
Anode	Nickel

Table 2.2 Experimental conditions for argon arc

Arc current [A]	100
Electrode gap distance [mm]	6
Arc voltage [V]	25-35
Pressure [kPa]	101.3 (Atmospheric pressure)
Plasma gas	Argon and hydrogen
Hydrogen concentration [vol%]	0, 30, 50
Shield gas flow rate [slpm]	0, 10, 20
Discharge time [min]	5-10
Cathode	Tungsten (2wt % thoria)
Anode	Nickel

Table 2.3 Input powers in helium arc when changing hydrogen concentration

Hydrogen concentration [vol%]	10	20	30
Arc current [A]	100	100	100
Arc voltage [V]	28.3	30.5	32.7
Input power [W]	2830	3050	3270

Table 2.4 Input powers in helium arc when changing shield gas flow rate

Shield gas flow rate [L/min]	0	10	20
Arc current [A]	100	100	100
Arc voltage [V]	30.5	31.5	36.7
Input power [W]	3050	3150	3670

Table 2.5 Input powers in argon arc when changing hydrogen concentration

Hydrogen concentration [vol%]	0	30	50
Arc current [A]]	100	100	100
Arc voltage [V]	23.4	28.2	33.1
Input power [W]	2340	2820	3310

Table 2.6 Input powers in argon arc when changing shield gas flow rate

Shield gas flow rate [L/min]	0	10	20
Arc current [A]	100	100	100
Arc voltage [V]	28.2	28.3	29.4
Input power [W]	2820	2830	2940

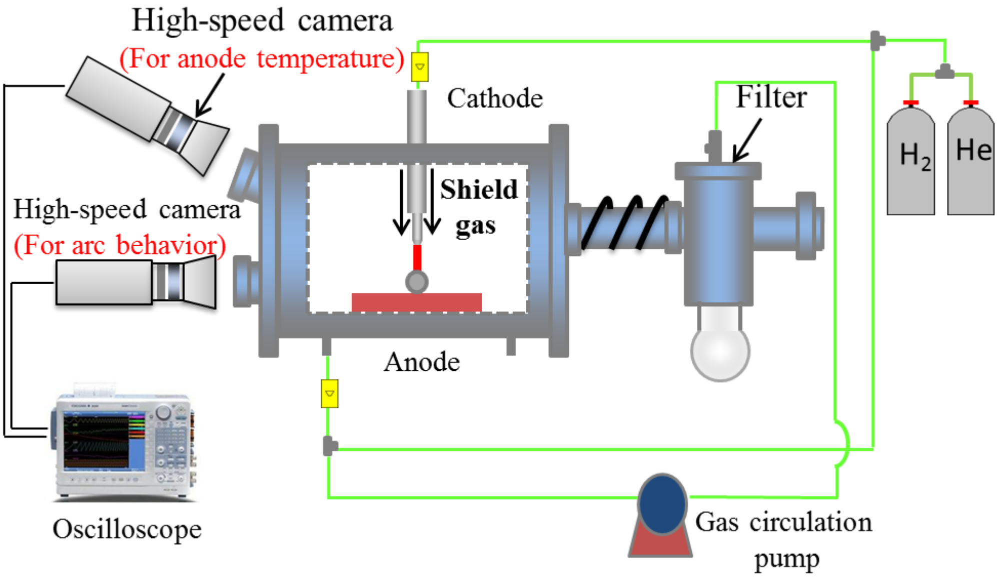

Fig. 2.1 Schematic of the experimental setup for nickel nanoparticles production by DC arc discharge method.

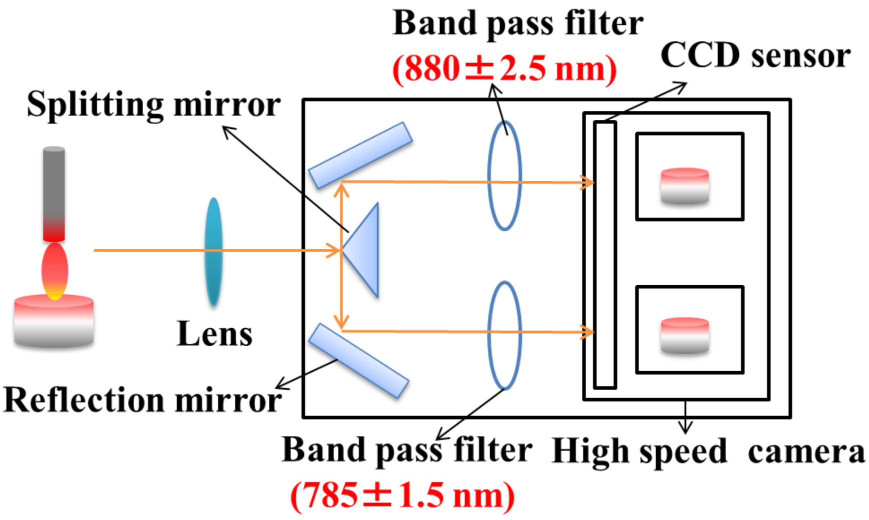

Fig. 2.2 Schematic illustration of temperature measurement system by two-color pyrometry.

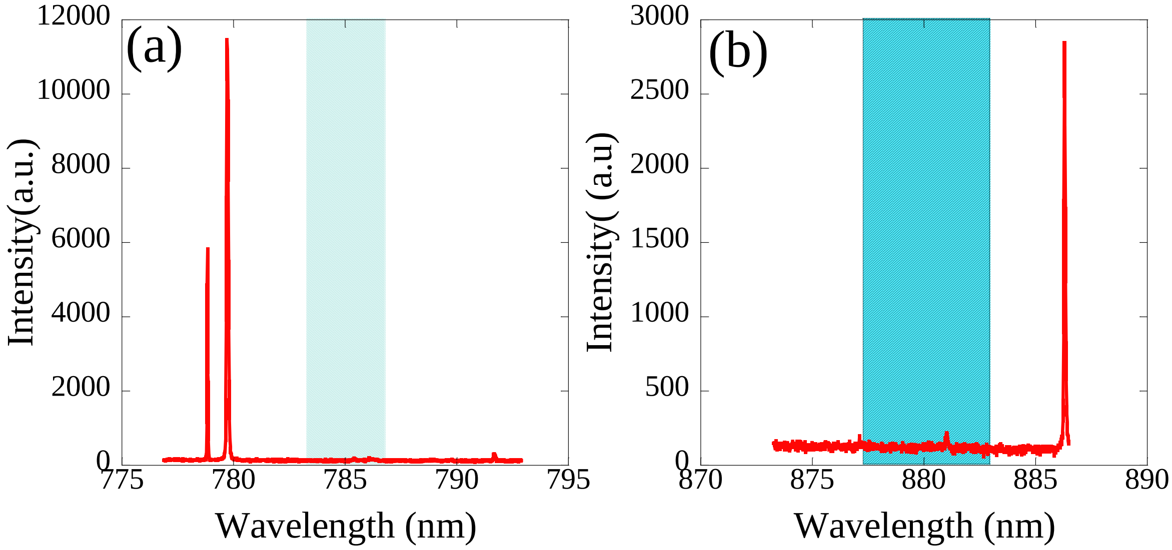

Fig. 2.3 Optical emission spectra of helium arc with 20vol% hydrogen at different wavelengths. The shadow region indicates the wavelength of band-pass filter: (a) 785±1.5 nm, (b) 880±2.5 nm.

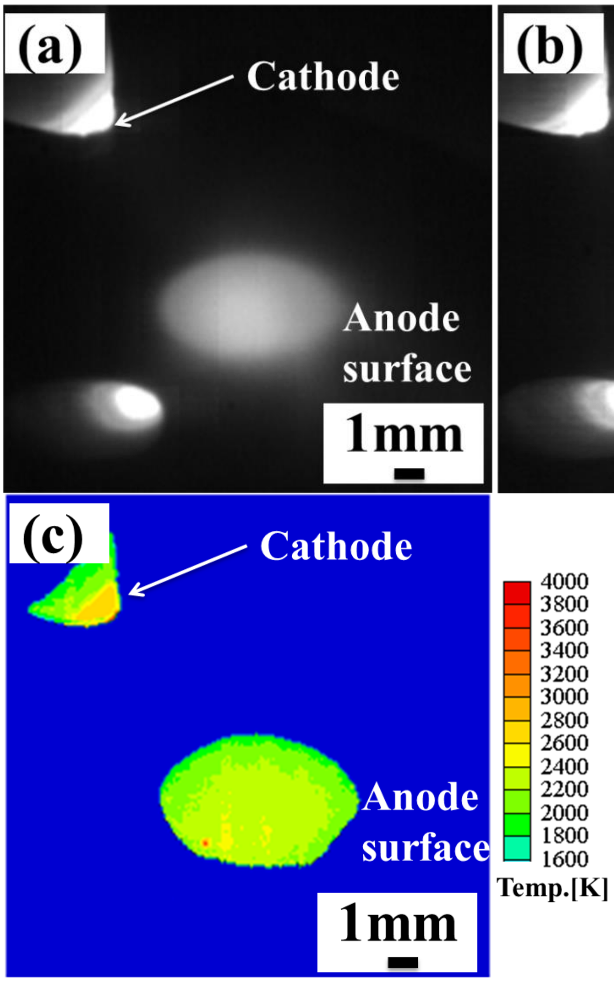

Fig. 2.4 Images of the electrode at wavelength of (a) 880±2.5 nm and (b) 785±1.5 nm recorded by high-speed camera, and (c) a corresponding temperature distribution map calculated by Plank’s law based on radiation intensity from images (a) and (b).

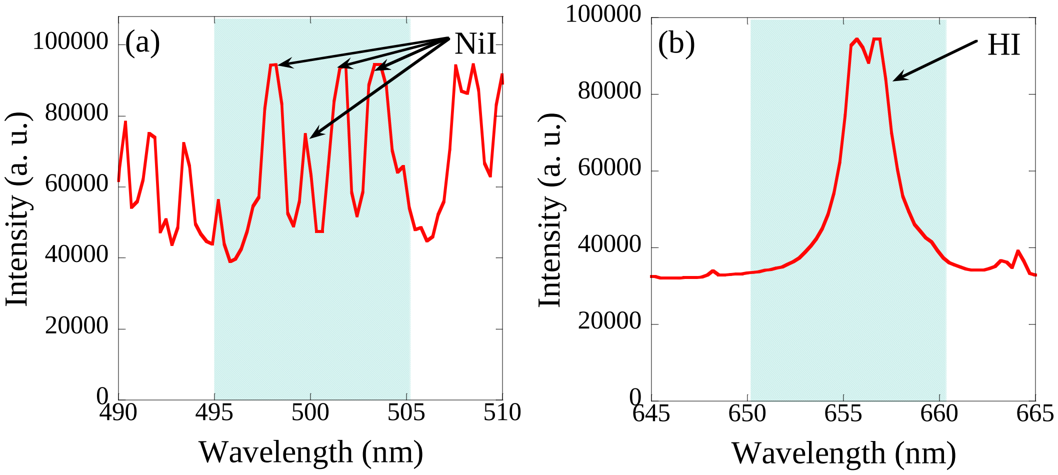

Fig. 2.5 Optical emission spectra of NiI (a) and HI (b) for choosing the suitable band pass filter for cathode jet and anode jet observation.

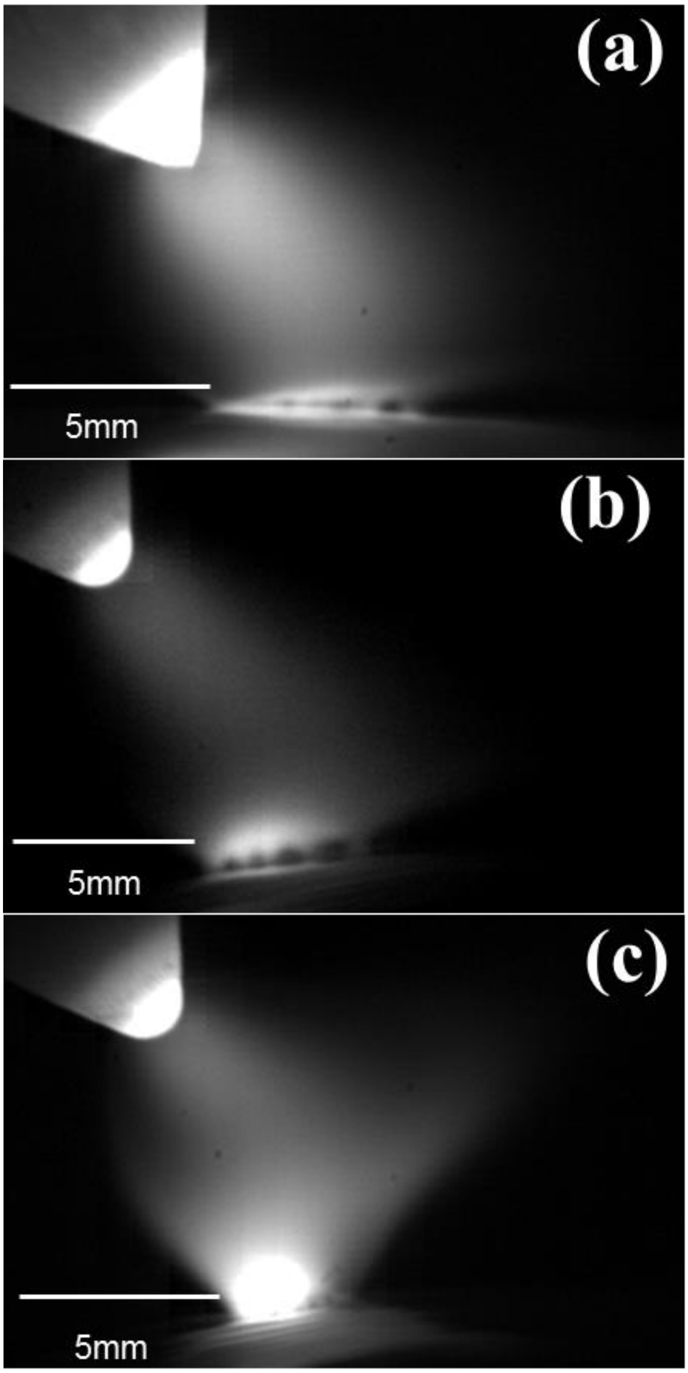

Fig. 2.6 Snapshots of high-speed camera for helium arc with different hydrogen concentrations (a) 10vol%, (b) 20vol%, and (c) 30vol%, respectively.

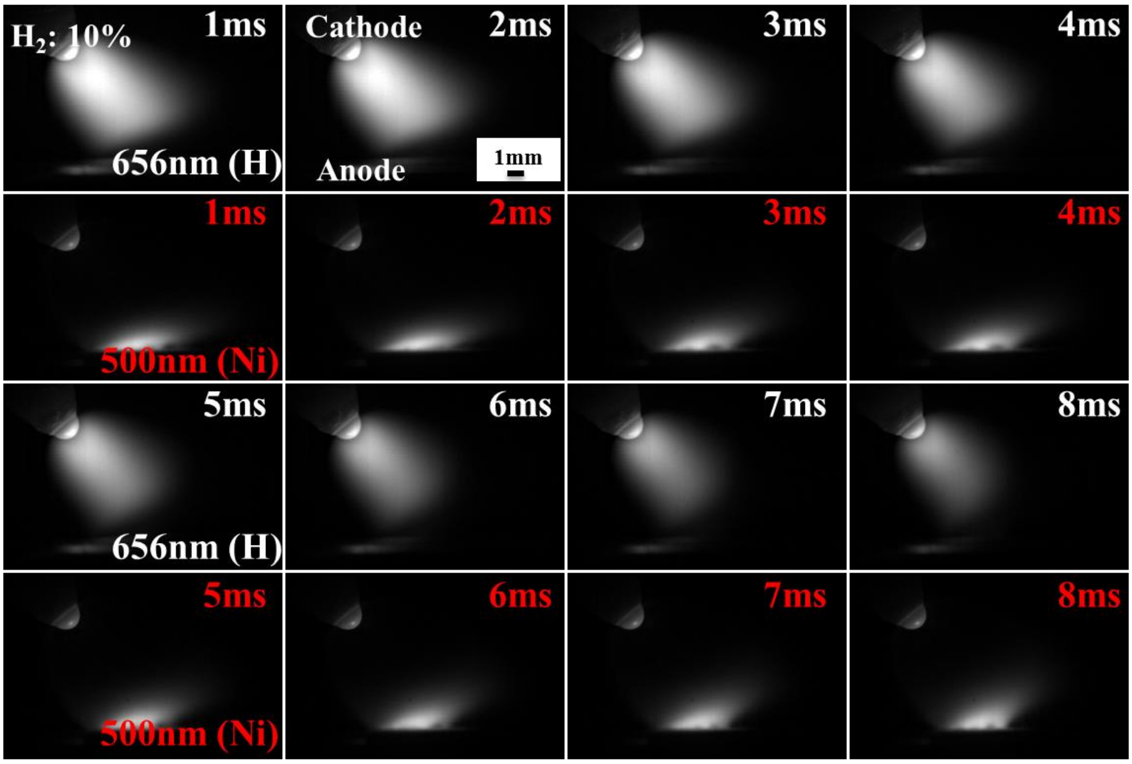

Fig. 2.7 Representative snapshots of high-speed camera in helium arc when hydrogen concentration is 10vol% and shield gas flow rate is 0 L/min. H emission is the upper one, and Ni emission is the lower one.

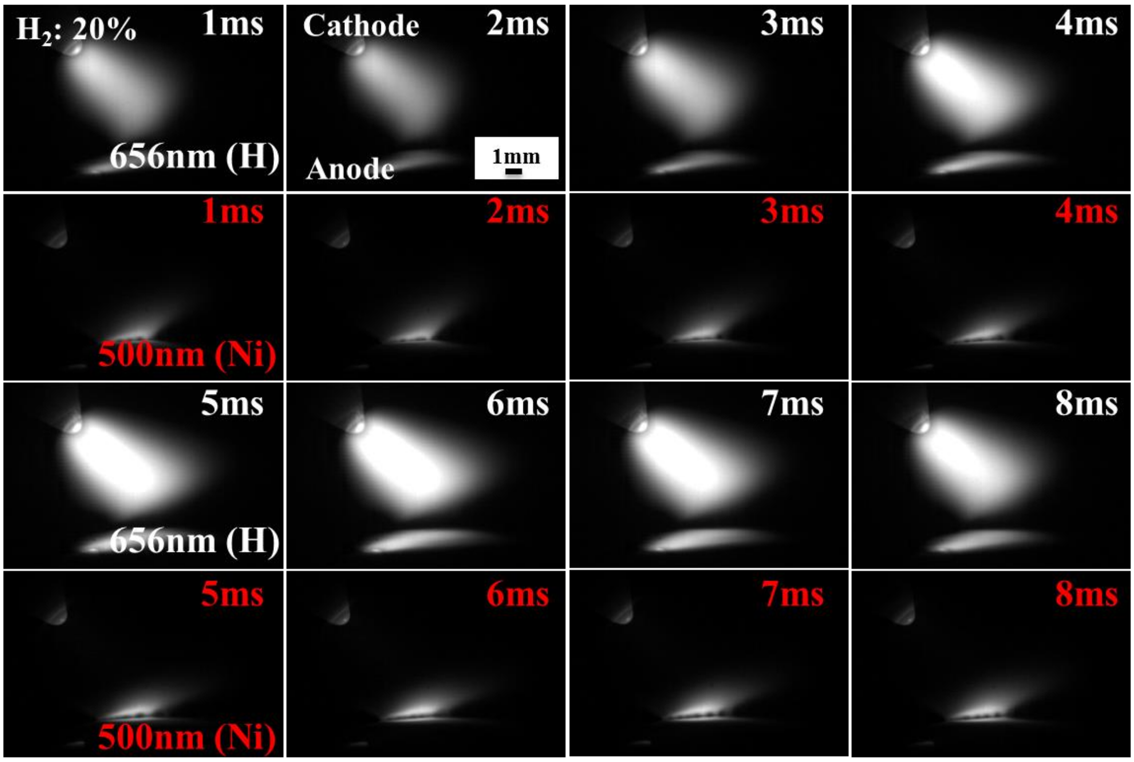

Fig 2.8 Representative snapshots of high-speed camera in helium arc when hydrogen concentration is 20vol% and shield gas flow rate is 0 L/min. H emission is the upper one, and Ni emission is the lower one.

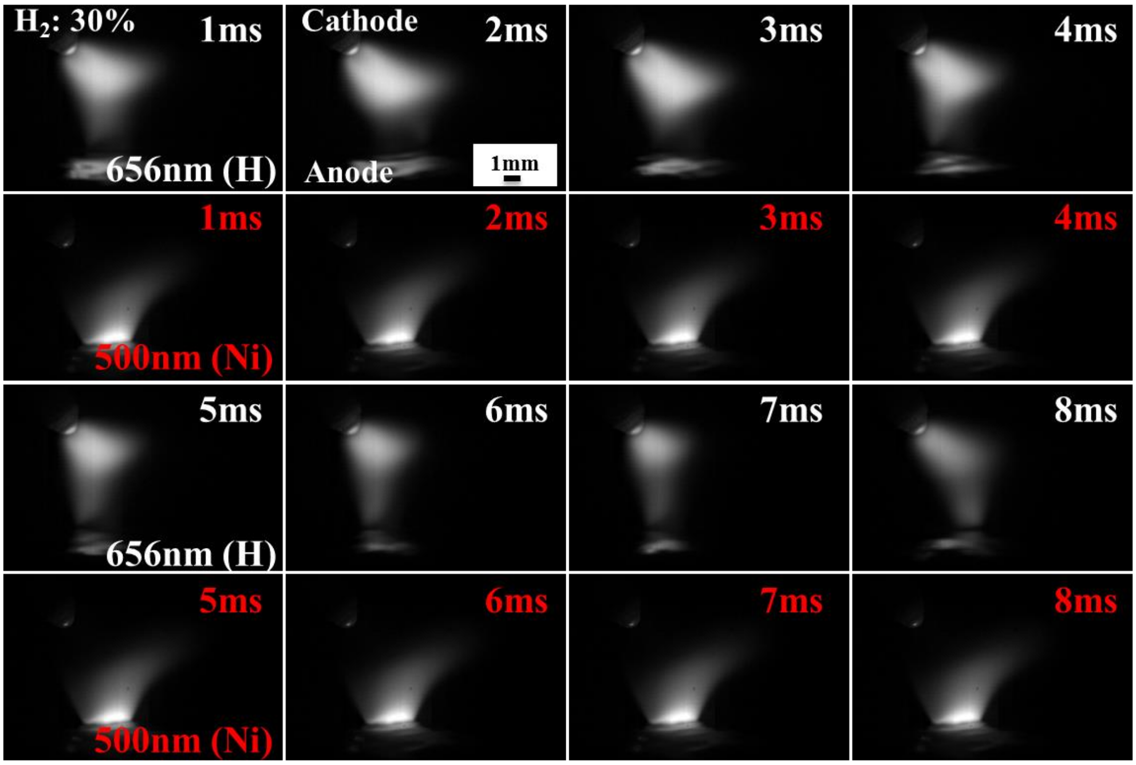

Fig. 2.9 Representative snapshots of high-speed camera in helium arc when hydrogen concentration is 30vol% and shield gas flow rate is 0 L/min. H emission is the upper one, and Ni emission is the lower one.

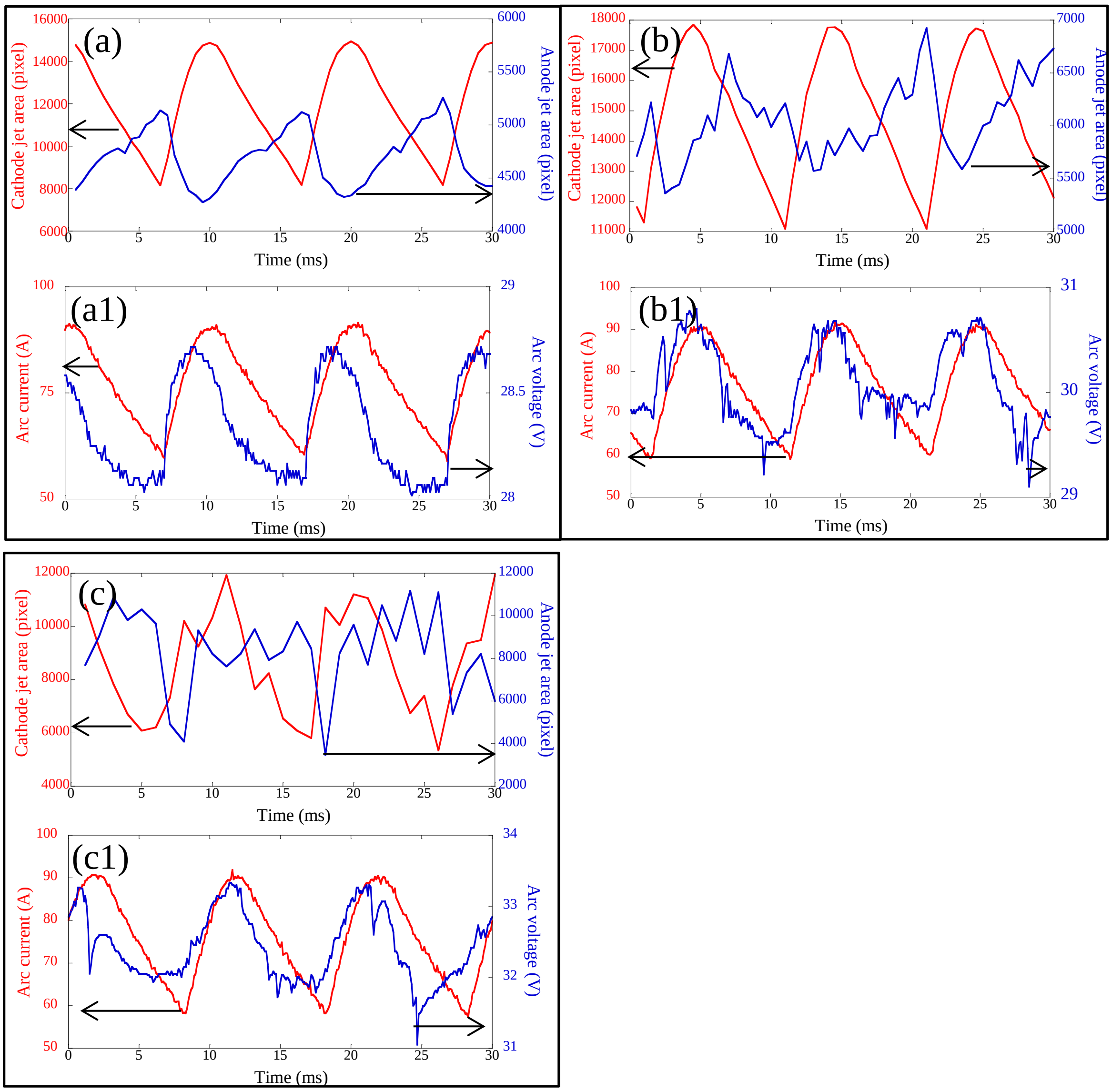

Fig. 2.10 The waveform of anode/cathode jet area variation (upper) and synchronized arc current and voltage waveforms (lower) for helium arc with different hydrogen concentrations. (a)-(a1), (b)-(b1), and (c)-(c1) correspond to the hydrogen concentration of 10vol%, 20vol%, and 30vol%, respectively.

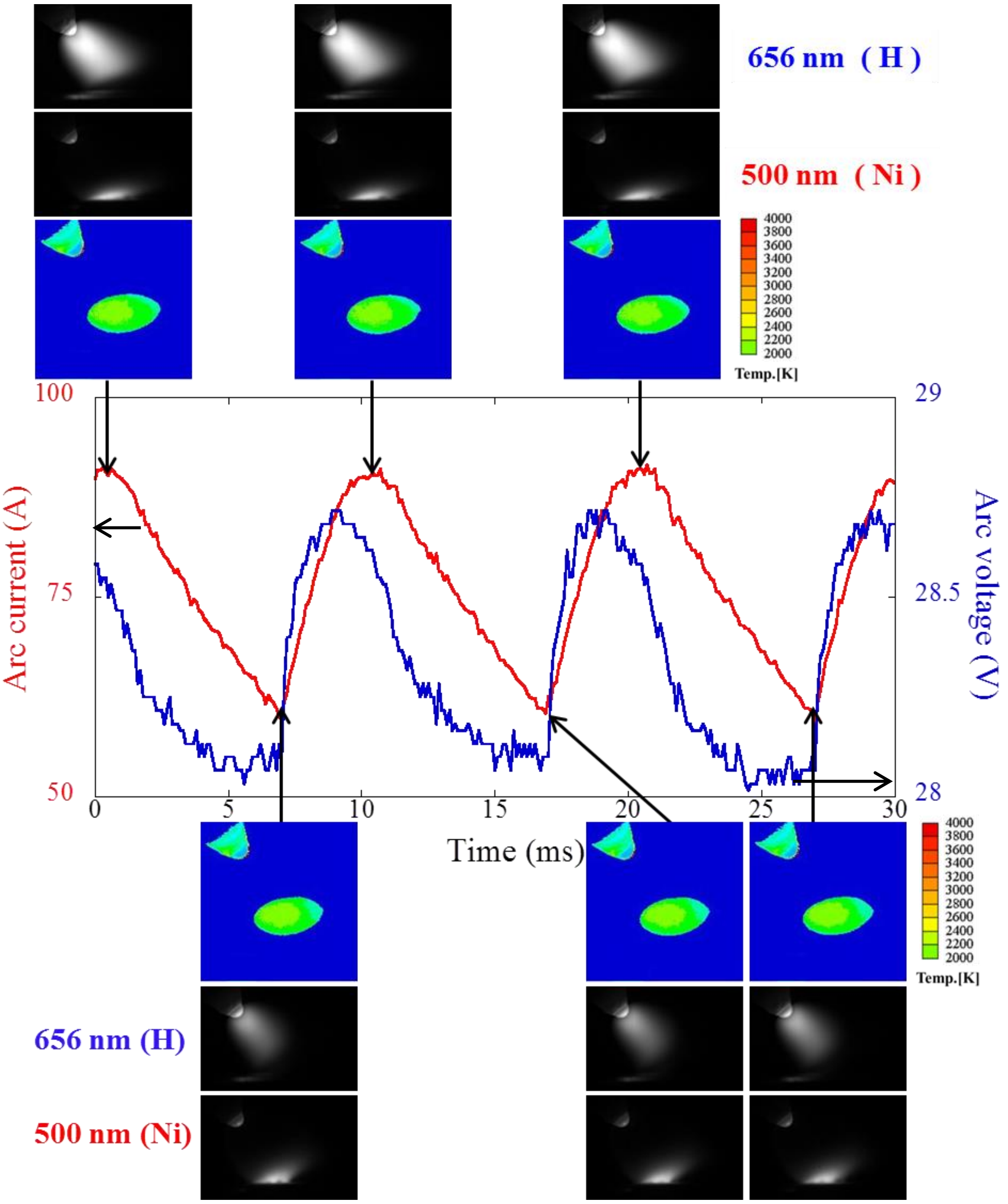

Fig. 2.11 Voltage and current waveform of helium arc synchronized with anode temperature distribution map, the snapshots of H emission and Ni emission when hydrogen concentration is 10vol% and shield gas flow rate is 0 L/min.

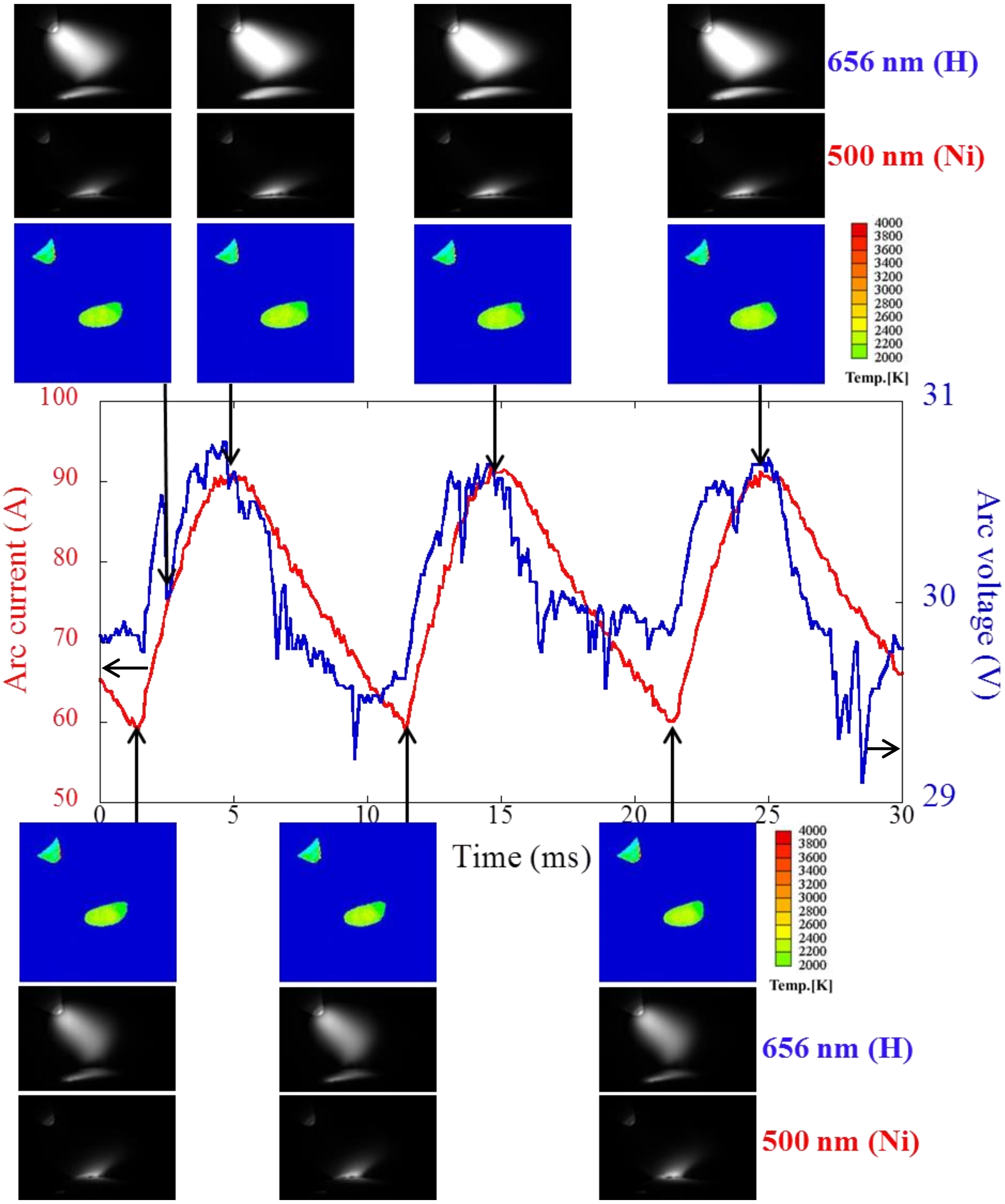

Fig. 2.12 Voltage and current waveform of helium arc synchronized with anode temperature distribution map, the snapshots of H emission and Ni emission when hydrogen concentration is 20vol% and shield gas flow rate is 0 L/min.

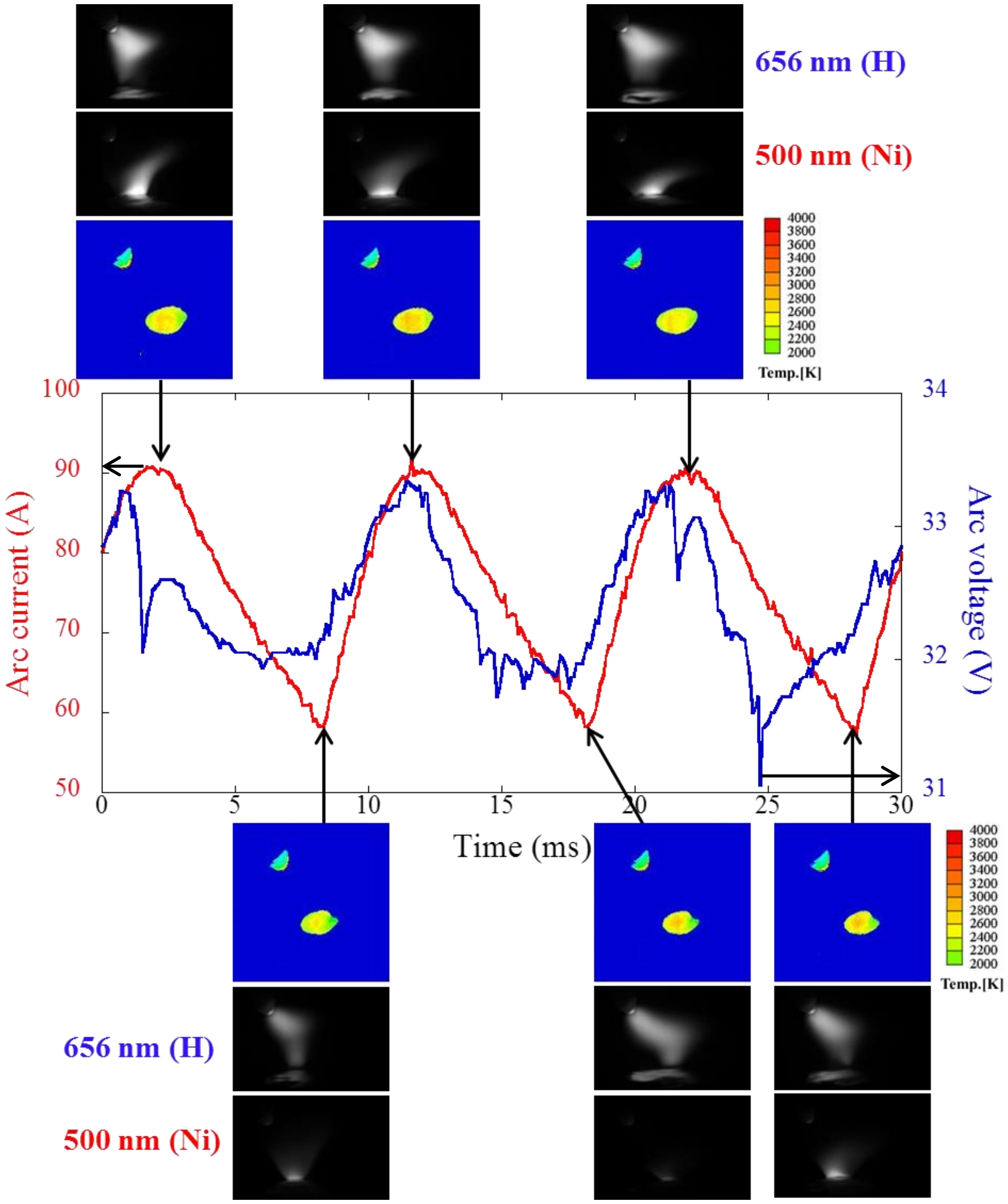

Fig. 2.13 Voltage and current waveform of helium arc synchronized with anode temperature distribution map, the snapshots of H emission and Ni emission when hydrogen concentration is 30vol% and shield gas flow rate is 0 L/min.

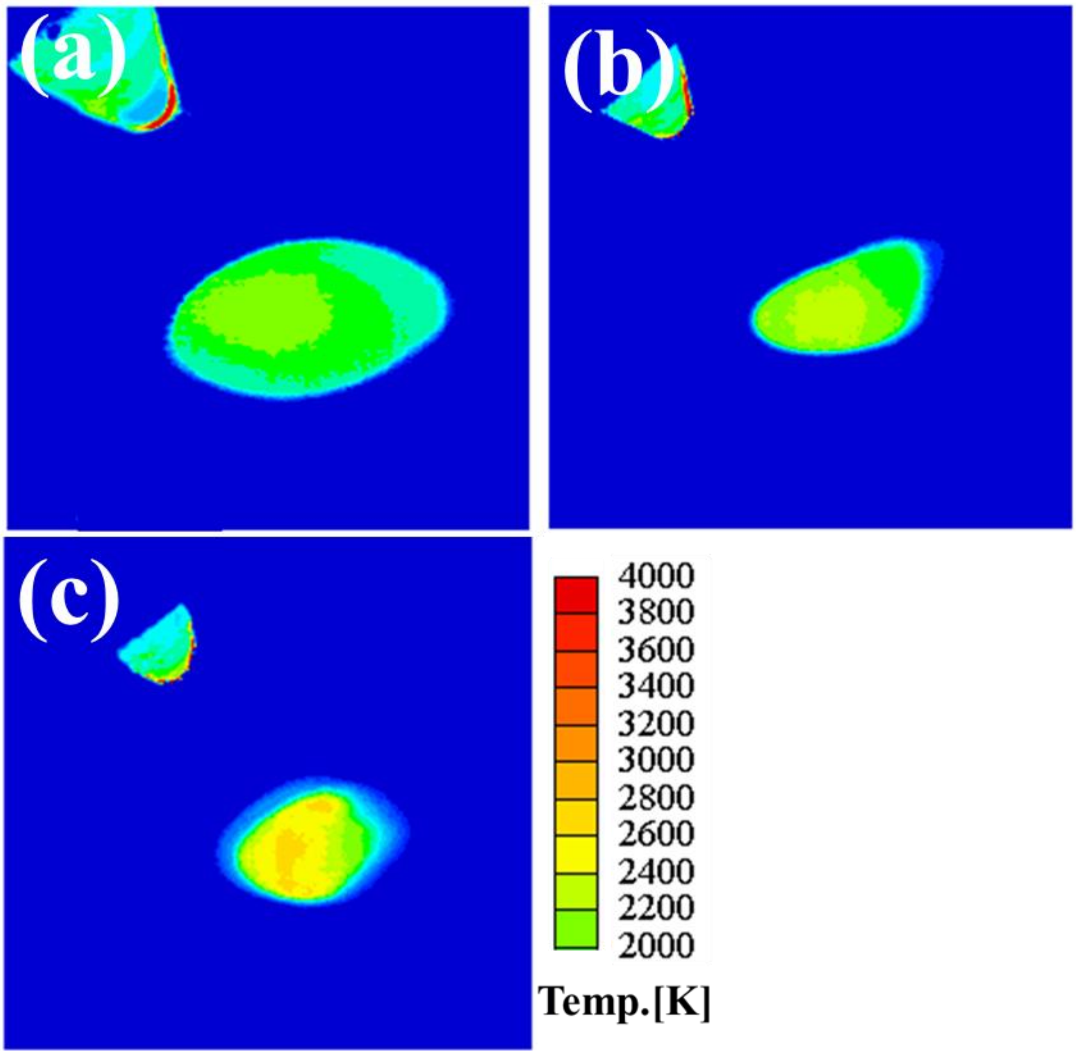

Fig. 2.14 Time average temperature of the anode surface in helium arc for different hydrogen concentrations, (a) 10%, (b) 20%, and (c) 30%, respectively.

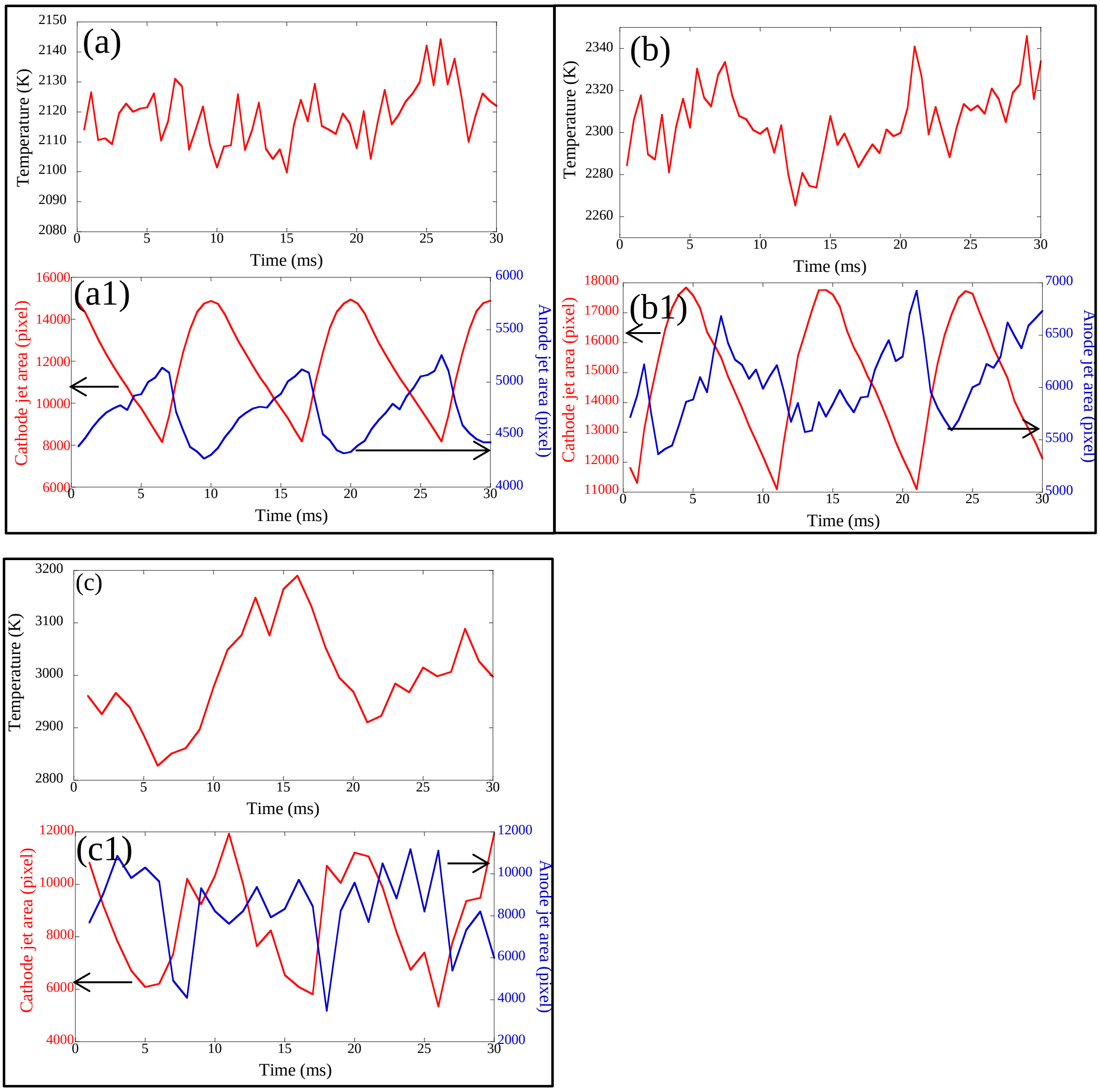

Fig. 2.15 Time variation of the highest temperature (upper) and synchronized time variation of the anode jet area and the cathode jet area (lower) for helium arc with different hydrogen concentrations when shield gas flow rate is 0 L/min. (a)-(a1), (b)-(b1), and (c)-(c1) correspond to the hydrogen concentration of 10vol%, 20vol%, and 30vol%, respectively.

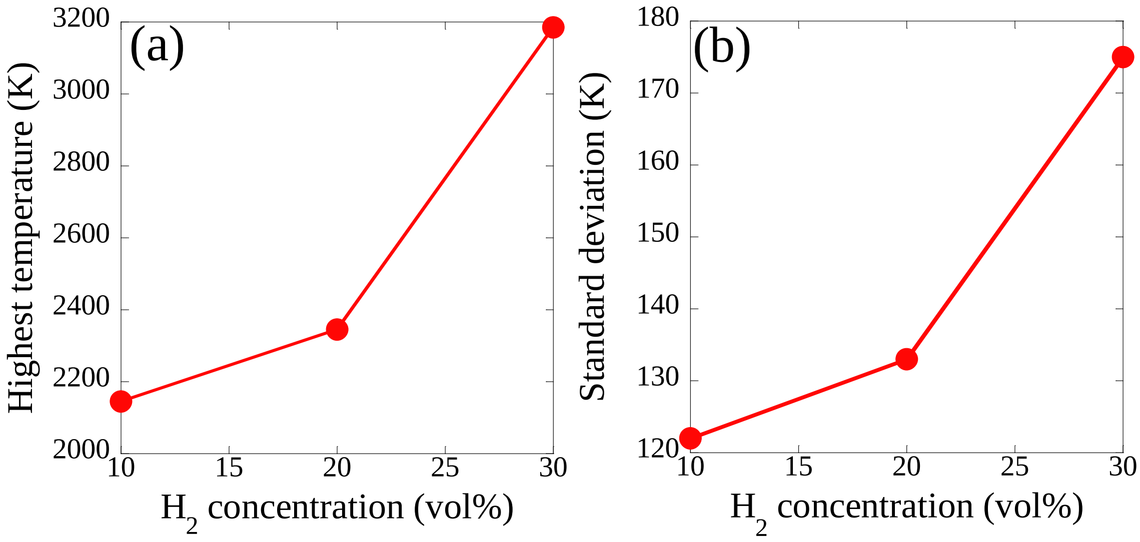

Fig. 2.16 Effects of hydrogen concentration on (a) highest temperature, (b) standard deviation in helium arc.

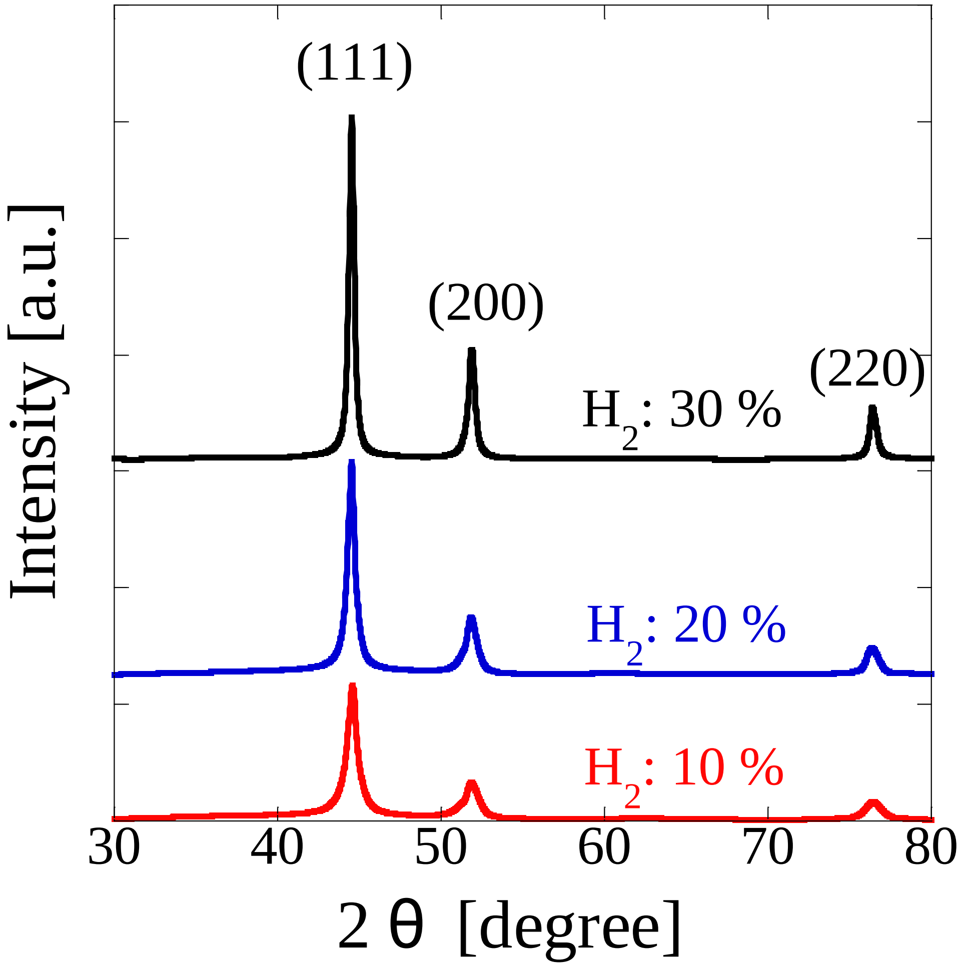

Fig. 2.17 XRD patterns of nickel nanoparticles in helium arc at different hydrogen concentrations.

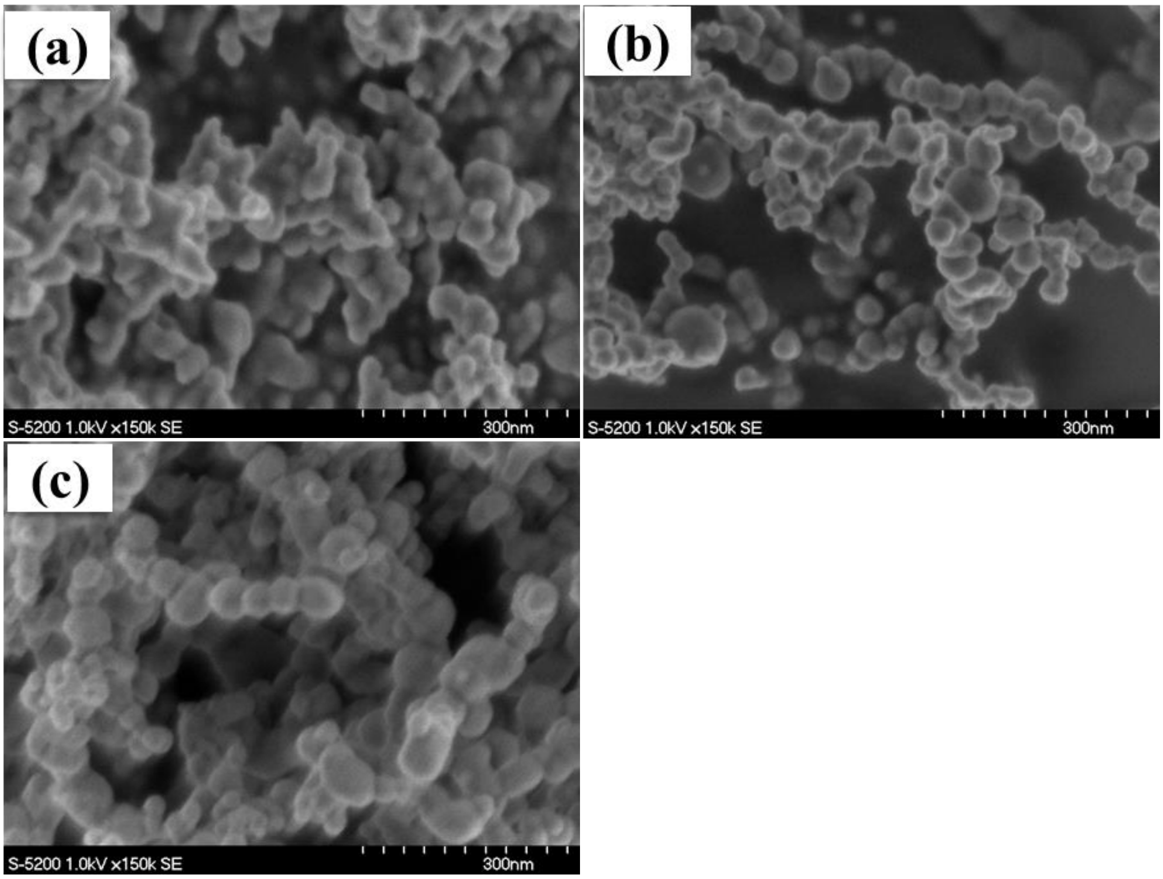

Fig. 2.18 FE-SEM images of nickel nanoparticles in helium arc at different hydrogen concentrations. (a), (b), and (c) correspond to the hydrogen concentration of 10, 20, and 30vol%, respectively.

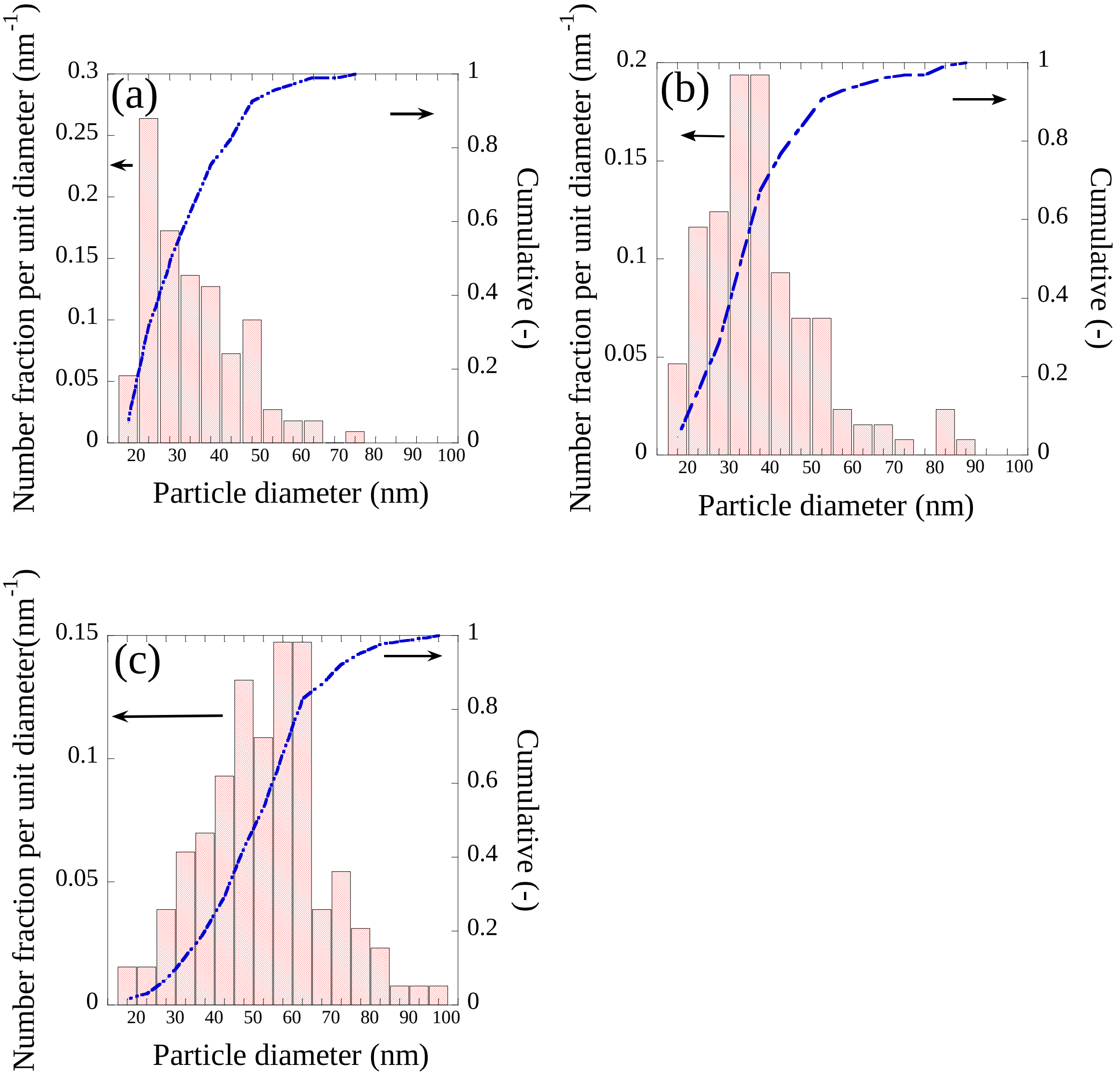

Fig. 2.19 Particle size distributions of nickel nanoparticles in helium arc at different hydrogen concentrations. (a), (b), and (c) correspond to the hydrogen concentration of 10, 20, and 30vol%, respectively.

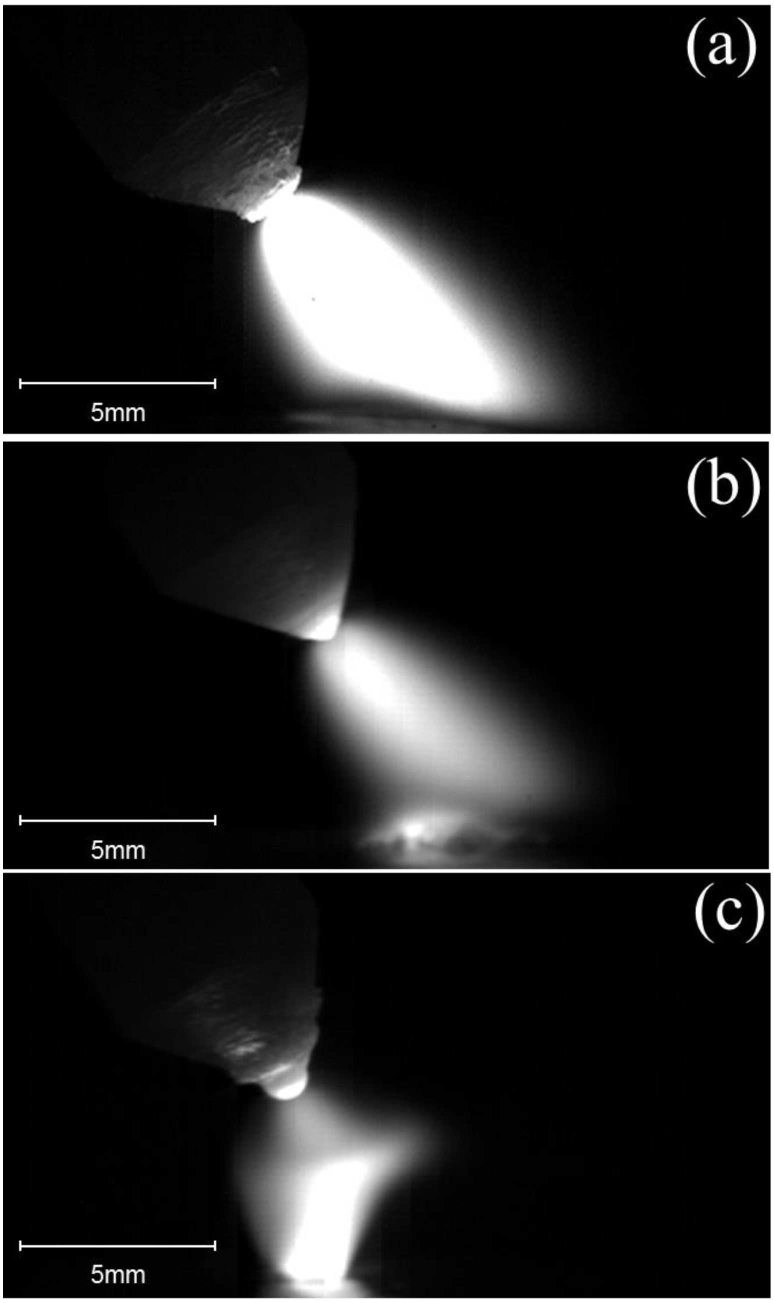

Fig. 2.20 Snapshots of high-speed camera for argon arc with different hydrogen concentrations (a) 0vol%, (b) 30vol%, and (c) 50vol%, respectively.

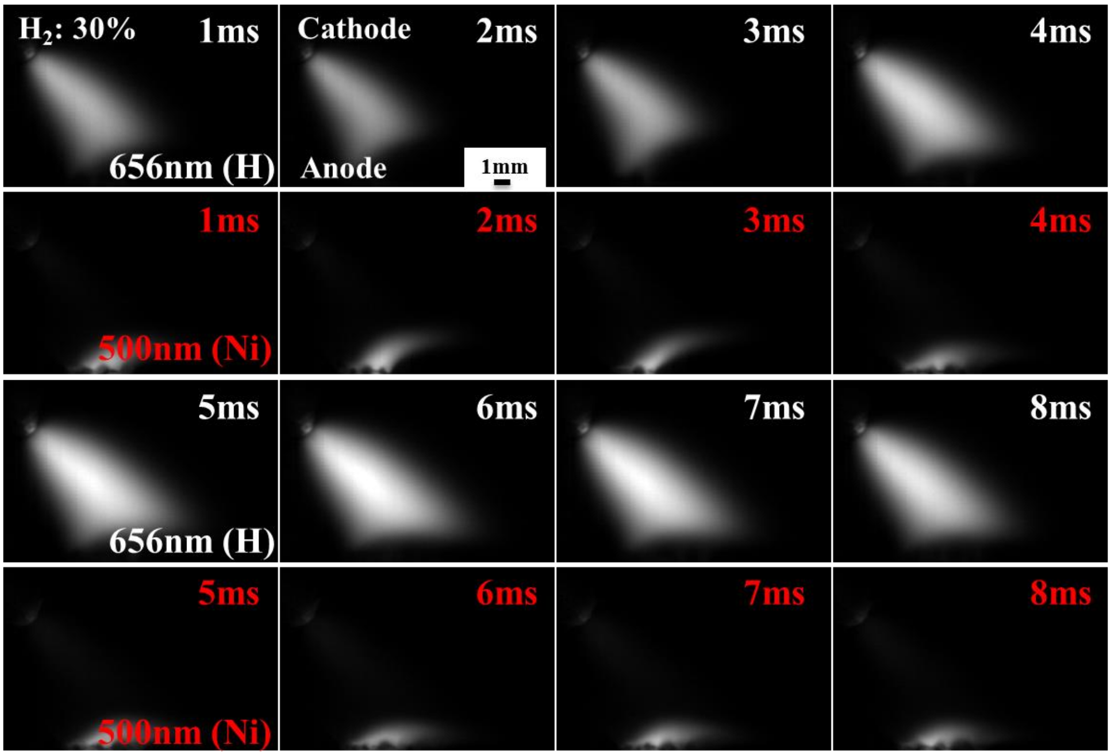

Fig. 2.21 Representative snapshots of high-speed camera in argon arc when hydrogen concentration is 30vol% and shield gas flow rate is 0 L/min. H emission is the upper one, and Ni emission is the lower one.

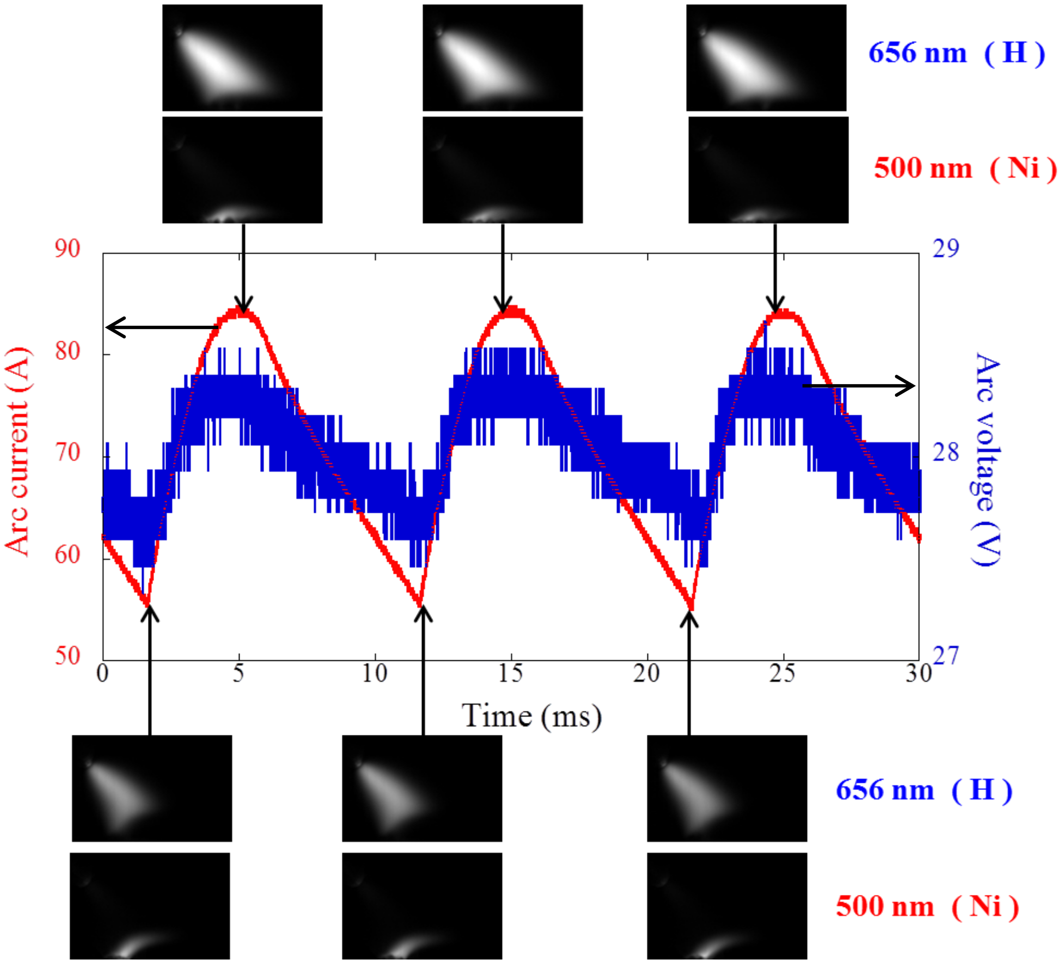

Fig. 2.22 Voltage and current waveform of argon arc synchronized with the snapshots of H emission and Ni emission when H_2 concentration is 30vol% and shield gas flow rate is 0 L/min.

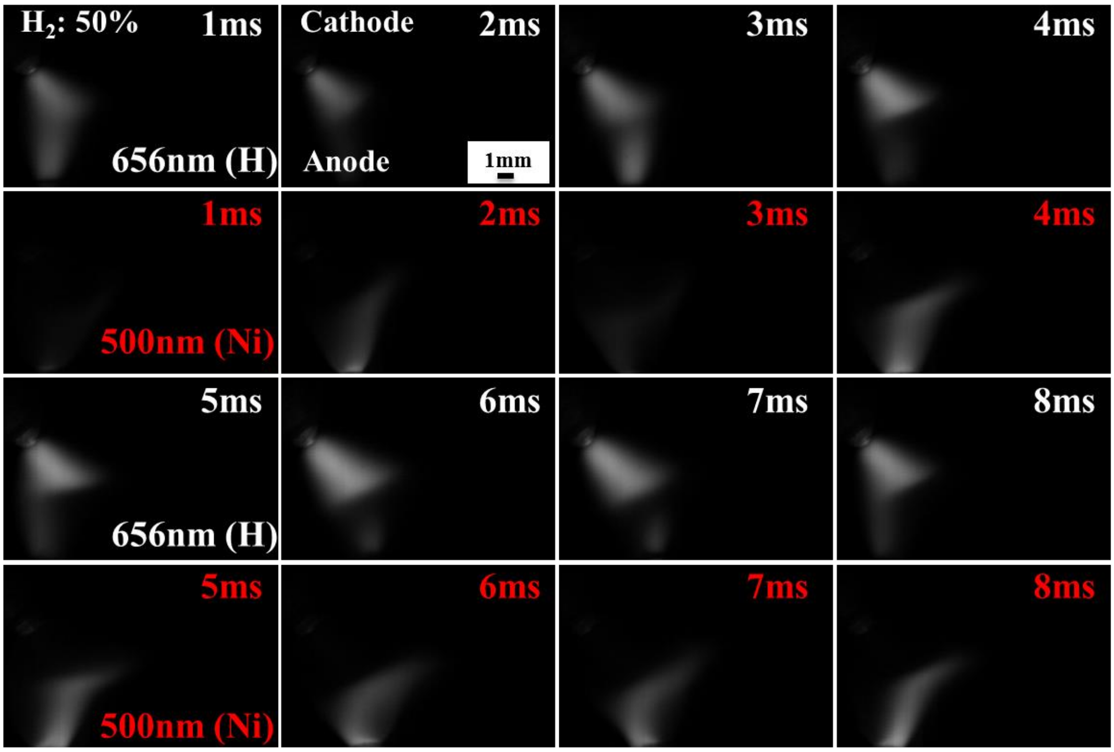

Fig. 2.23 Representative snapshots of high-speed camera in argon arc when hydrogen concentration is 50vol% and shield gas flow rate is 0 L/min. H emission is the upper one, and Ni emission is the lower one.

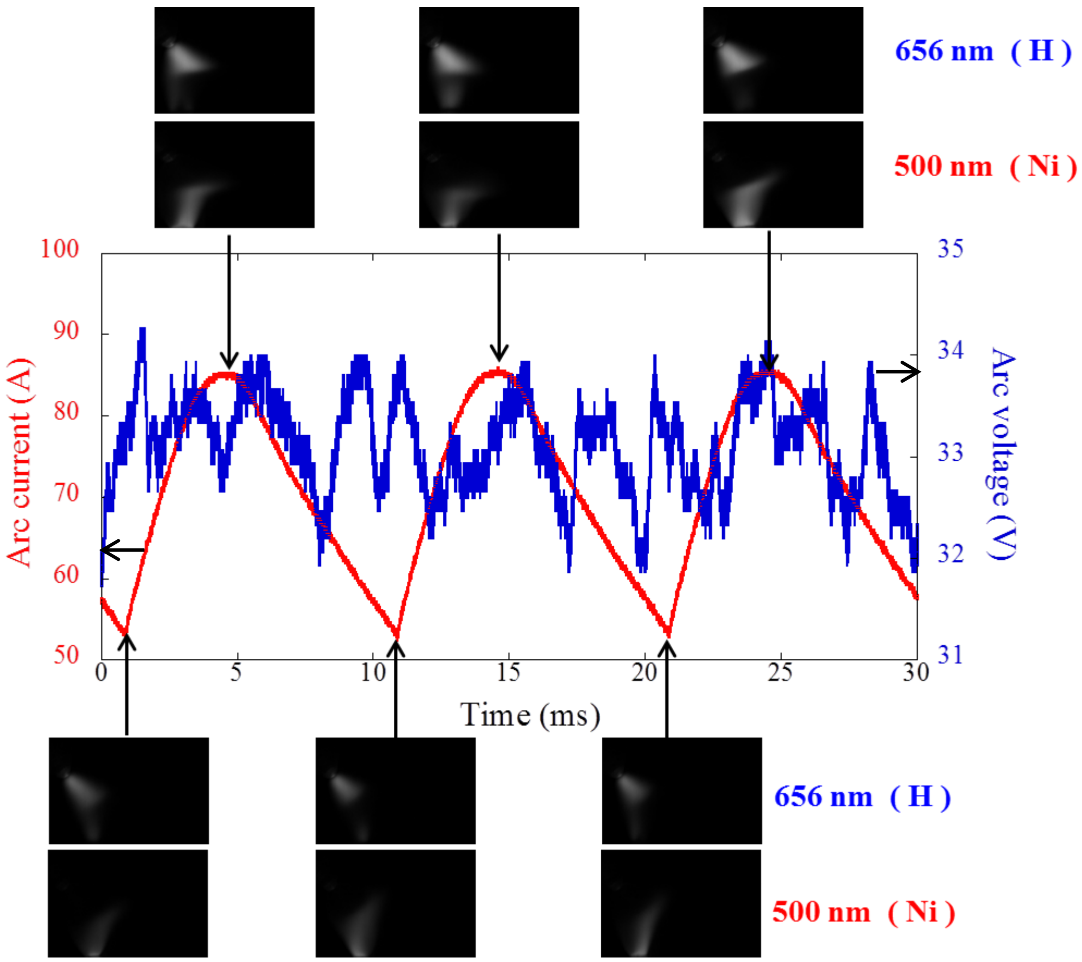

Fig. 2.24 Voltage and current waveform of argon arc synchronized with anode temperature distribution map, the snapshots of H emission and Ni emission when hydrogen concentration is 50vol% and shield gas flow rate is 0 L/min.

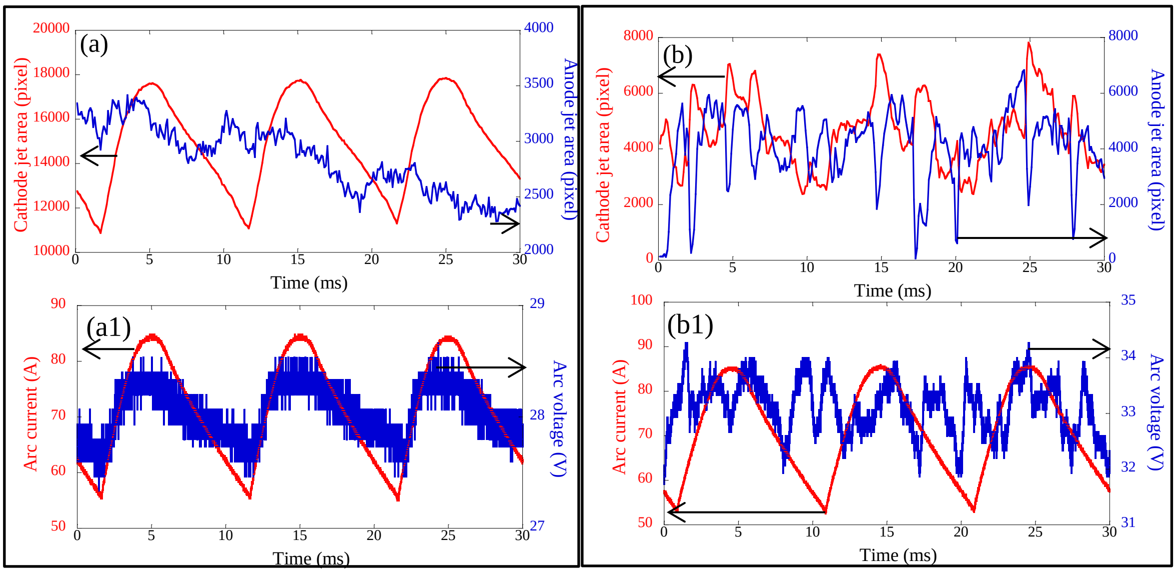

Fig. 2.25 The waveform of anode/cathode jet area variation (upper) and synchronized arc current and voltage waveforms (lower) for argon arc with different hydrogen concentrations. (a)-(a1) and (b)-(b1) correspond to the hydrogen concentration of 30% and 50vol%, respectively.

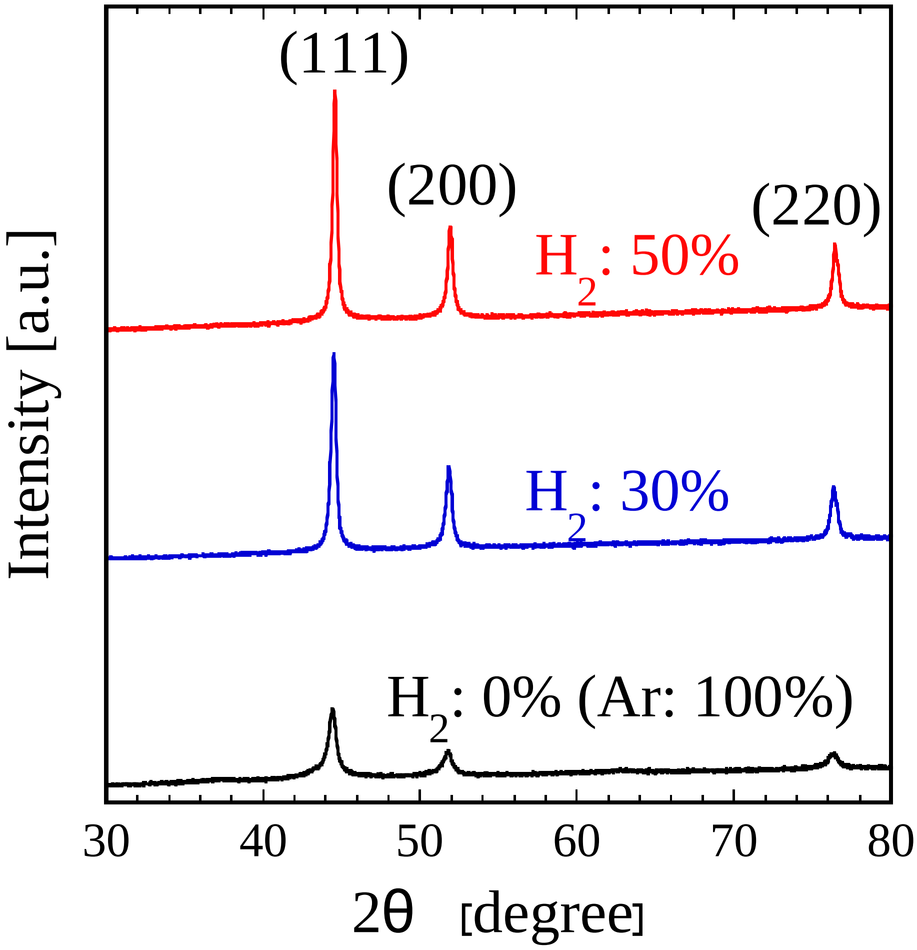

Fig. 2.26 XRD patterns of nickel nanoparticle in argon arc at different hydrogen concentrations.

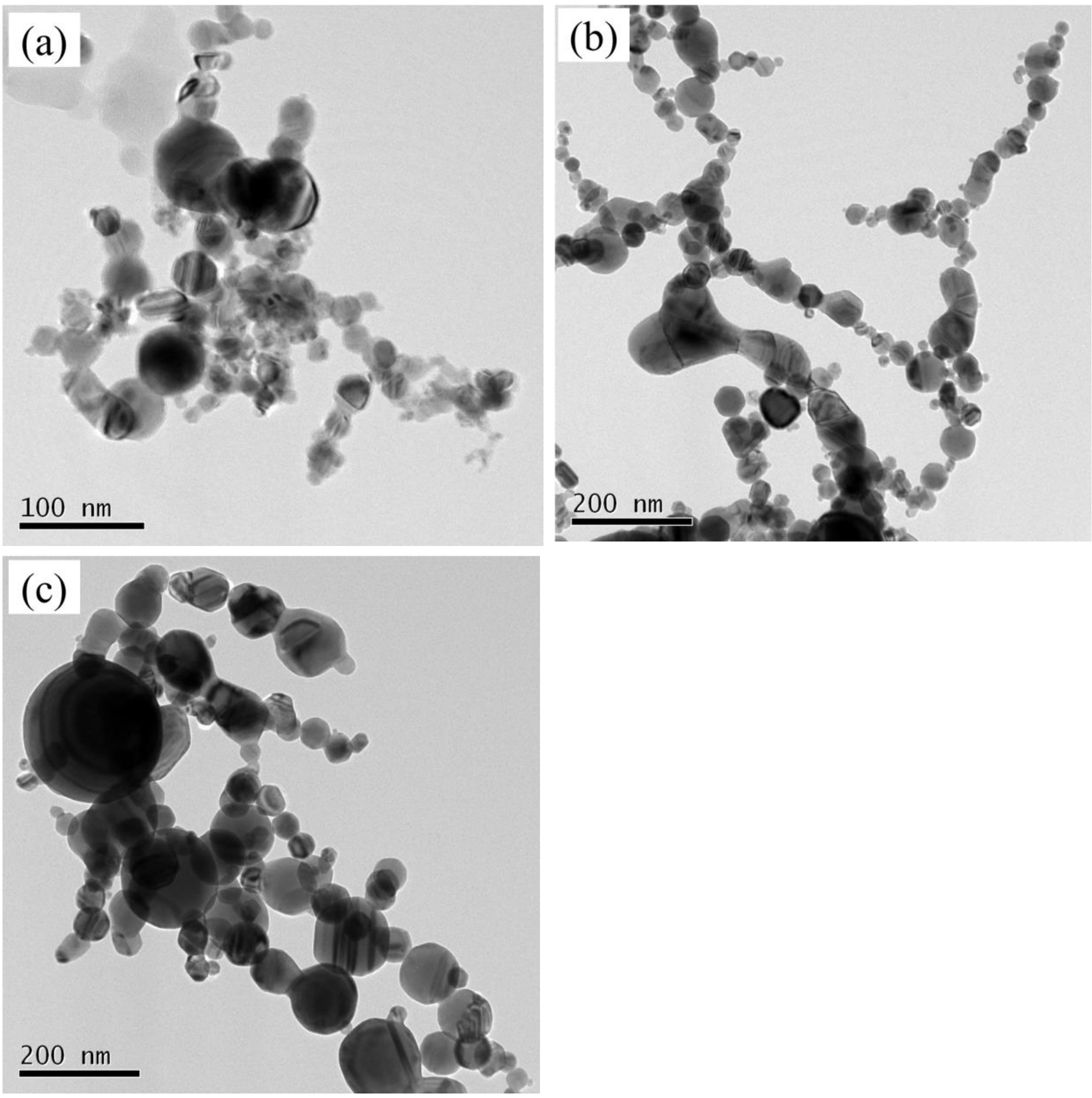

Fig. 2.27 TEM images of nickel nanoparticle in argon arc at different hydrogen concentrations. (a), (b), and (c) correspond to hydrogen concentration of 0, 30, and 50vol%, respectively.

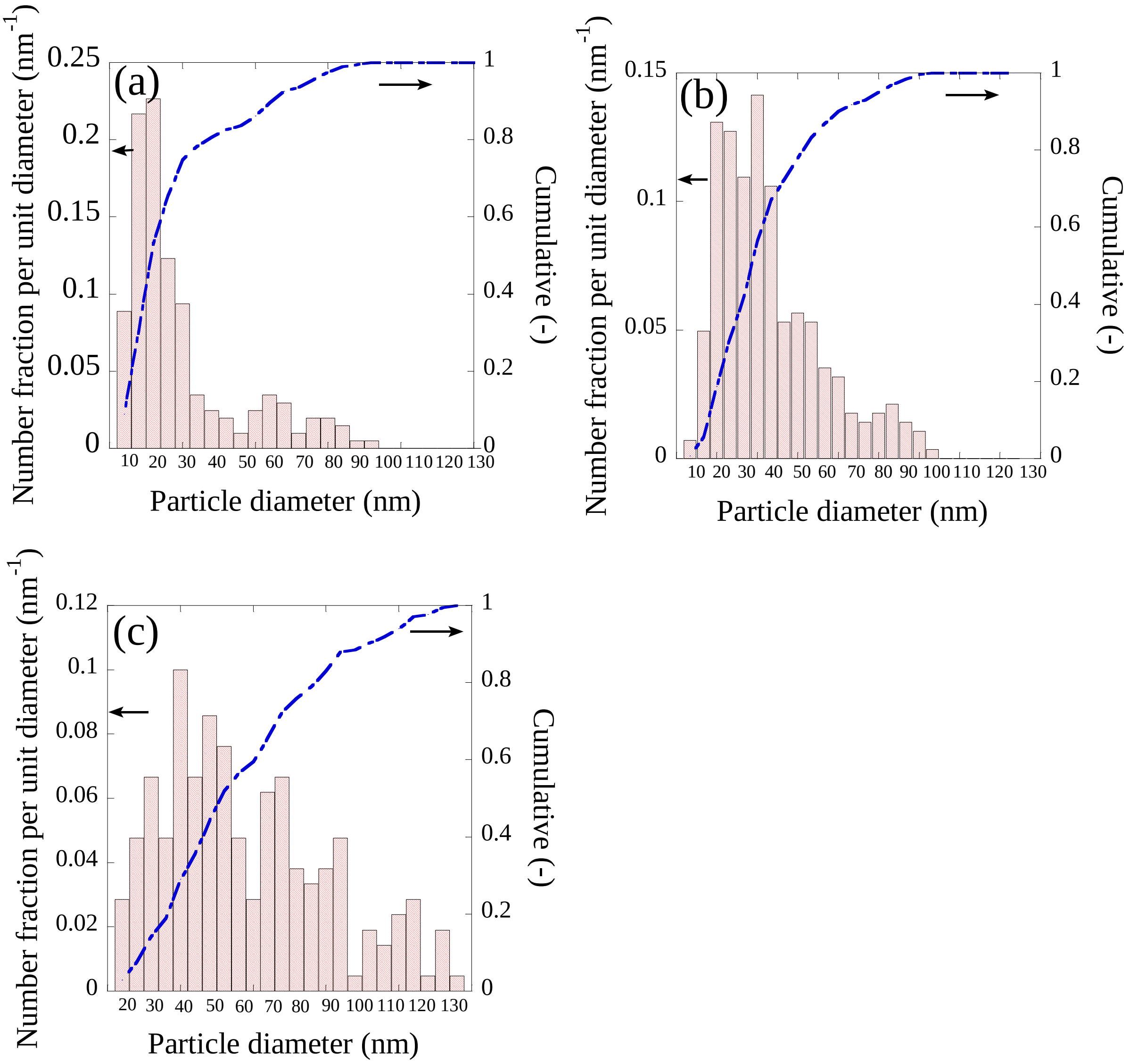

Fig. 2.28 Particle size distributions of nanoparticles in argon arc at different hydrogen concentrations. (a), (b), and (c) correspond to hydrogen concentration of 0, 30, and 50vol%, respectively.

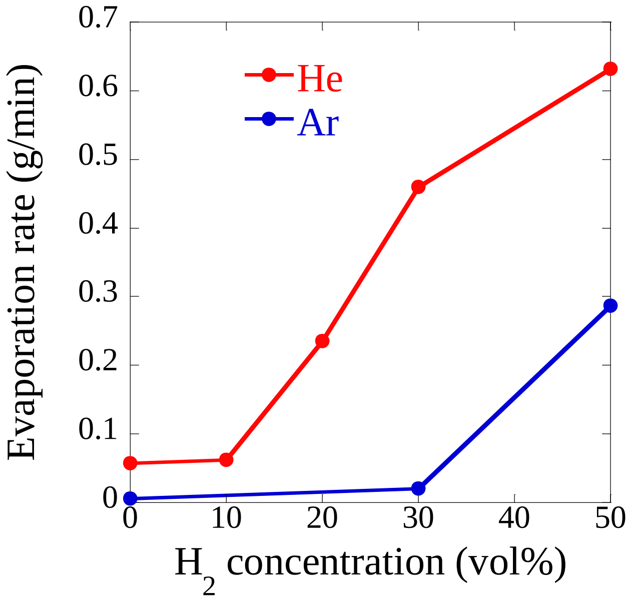

Fig. 2.29 Comparison of the evaporation rate of nickel anode between helium arc and argon arc at different hydrogen concentrations.

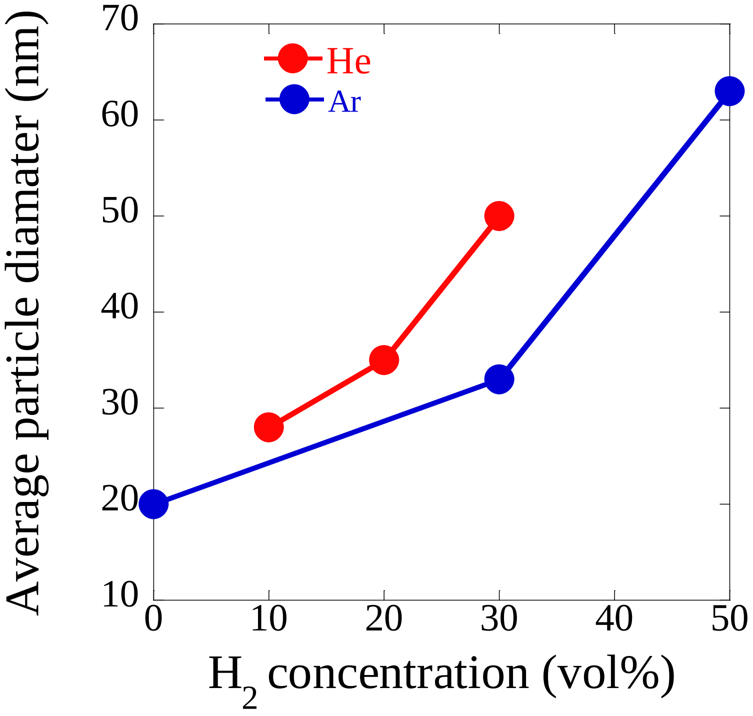

Fig. 2.30 Effect of hydrogen concentration on average particle diameter in helium and argon arc.

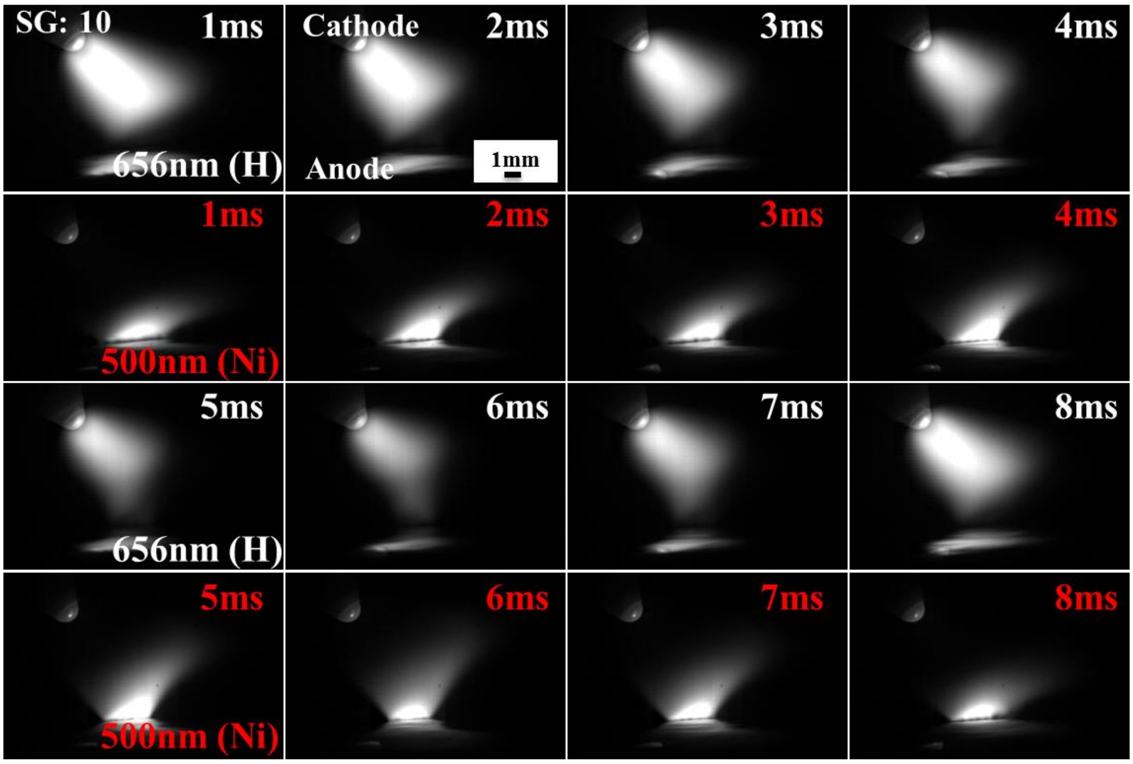

Fig. 2.31 Representative snapshots of high-speed camera in helium arc when hydrogen concentration is 20vol% and shield gas flow rate is 10 L/min. H emission is the upper one, and Ni emission is the lower one.

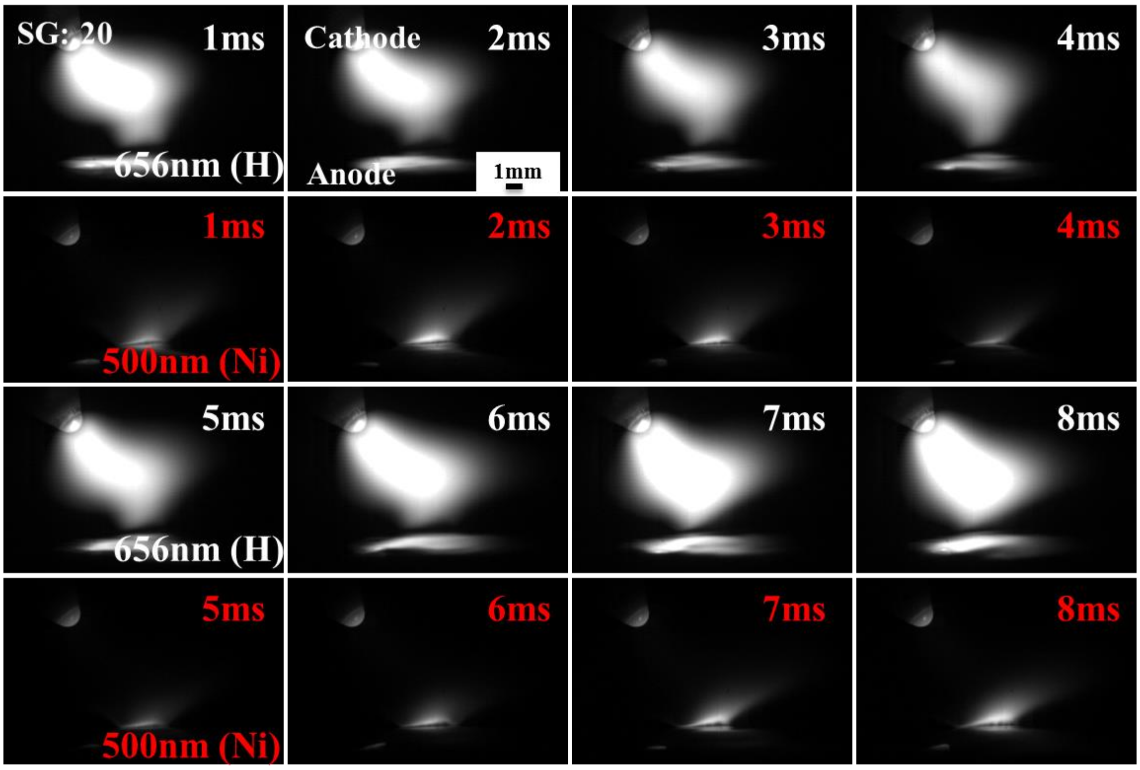

Fig. 2.32 Representative snapshots of high-speed camera in helium arc when hydrogen concentration is 20vol% and shield gas flow rate is 20 L/min. H emission is the upper one, and Ni emission is the lower one.

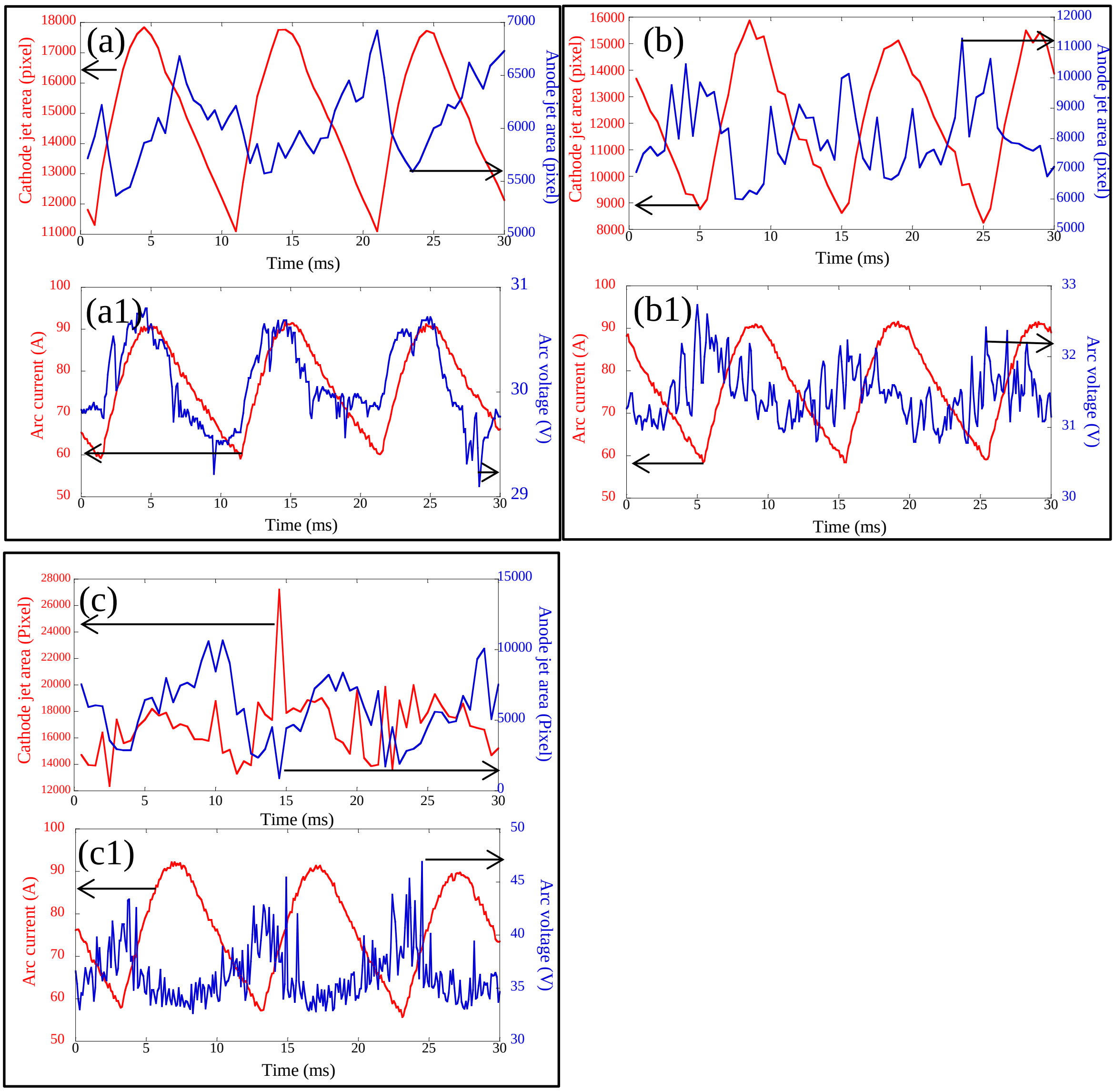

Fig. 2.33 The waveform of anode/cathode jet area variation (upper) and synchronized arc current and voltage waveforms (lower) for helium arc with different shield gas flow rates. (a)-(a1), (b)-(b1), and (c)-(c1) correspond to shield gas flow rates of 0, 10, and 20 L/min, respectively.

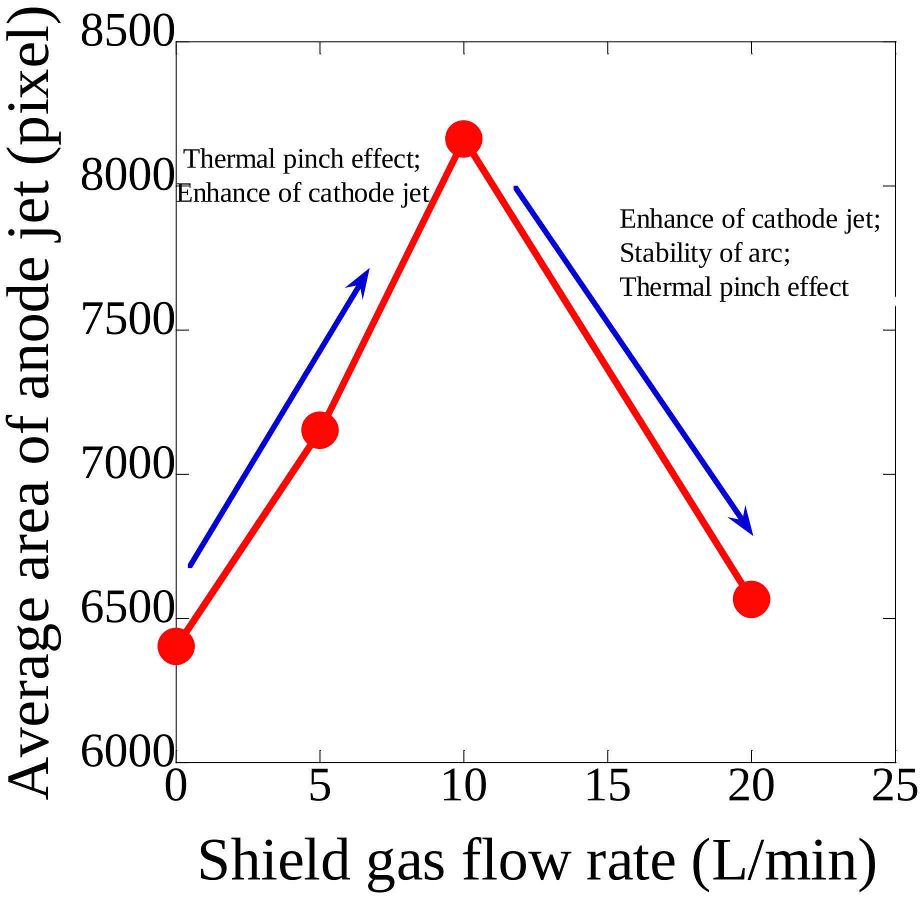

Fig. 2.34 Effect of shield gas flow rate on the averaged area of anode jet in helium arc.

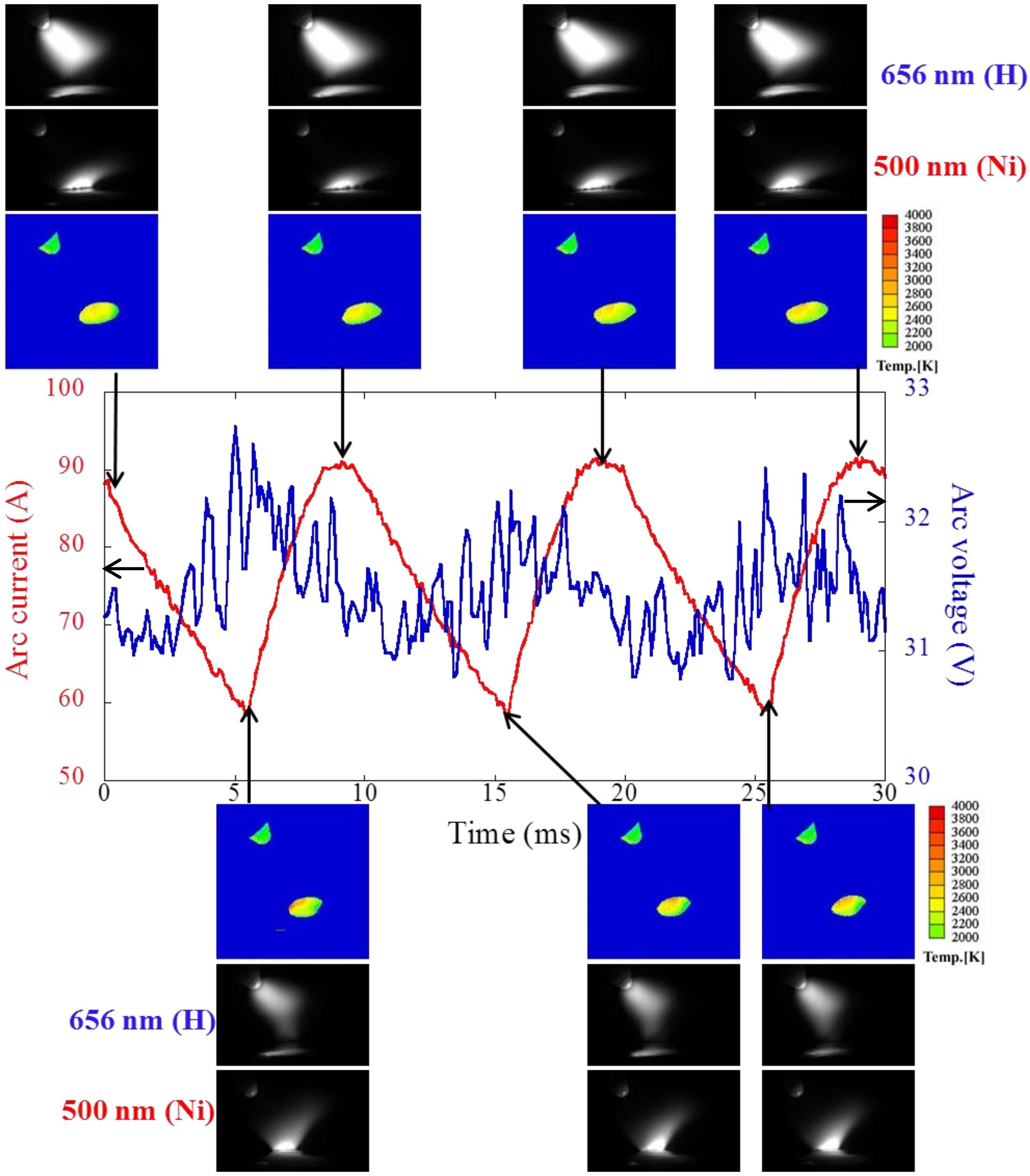

Fig. 2.35 Voltage and current waveform of helium arc synchronized with anode temperature distribution map, the snapshots of H emission and Ni emission when hydrogen concentration is 20vol% and the shield gas flow rate is 10 L/min.

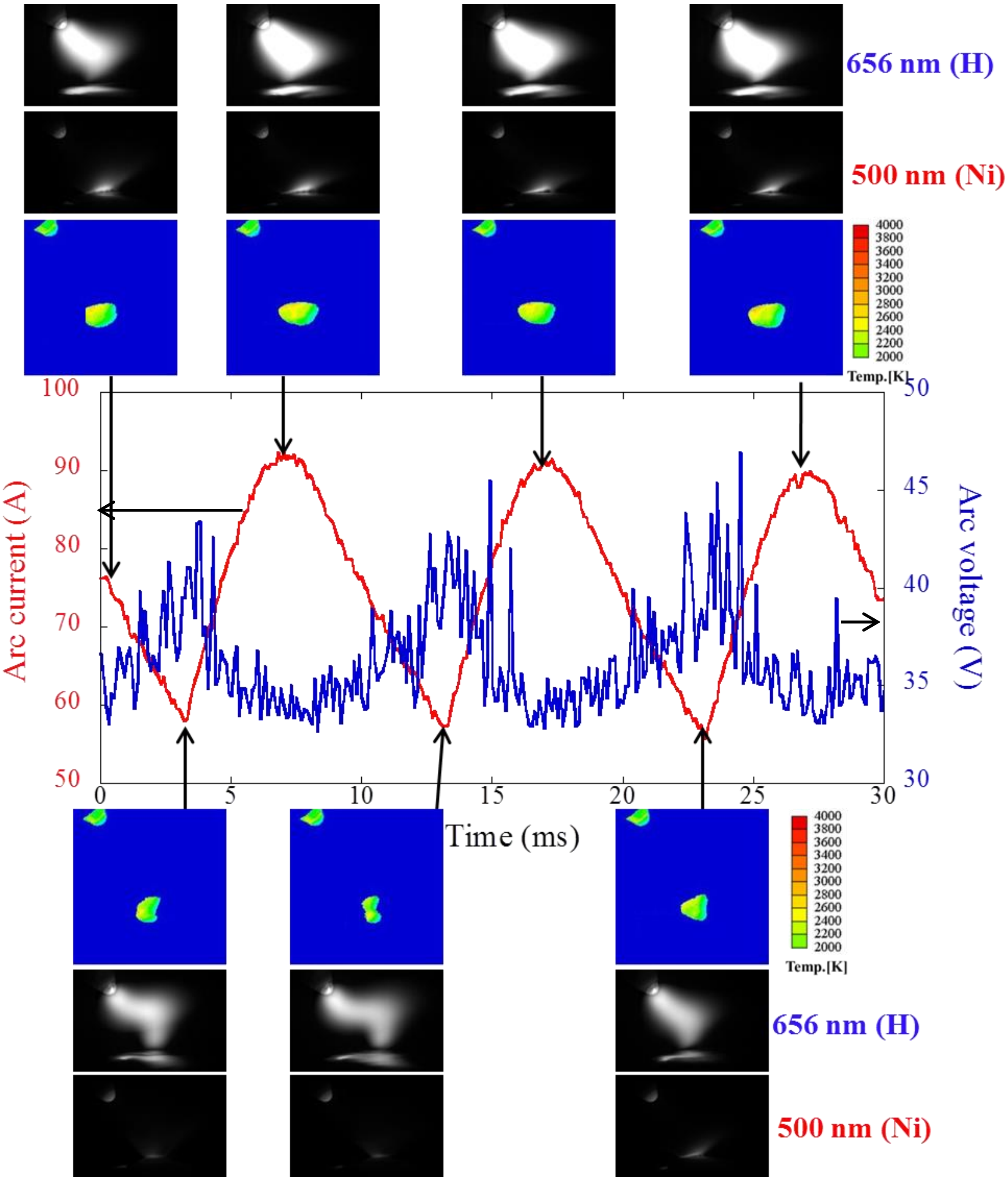

Fig. 2.36 Voltage and current waveform of helium arc synchronized with anode temperature distribution map, the snapshots of H emission and Ni emission when hydrogen concentration is 20vol% and shield gas flow rate is 20 L/min.

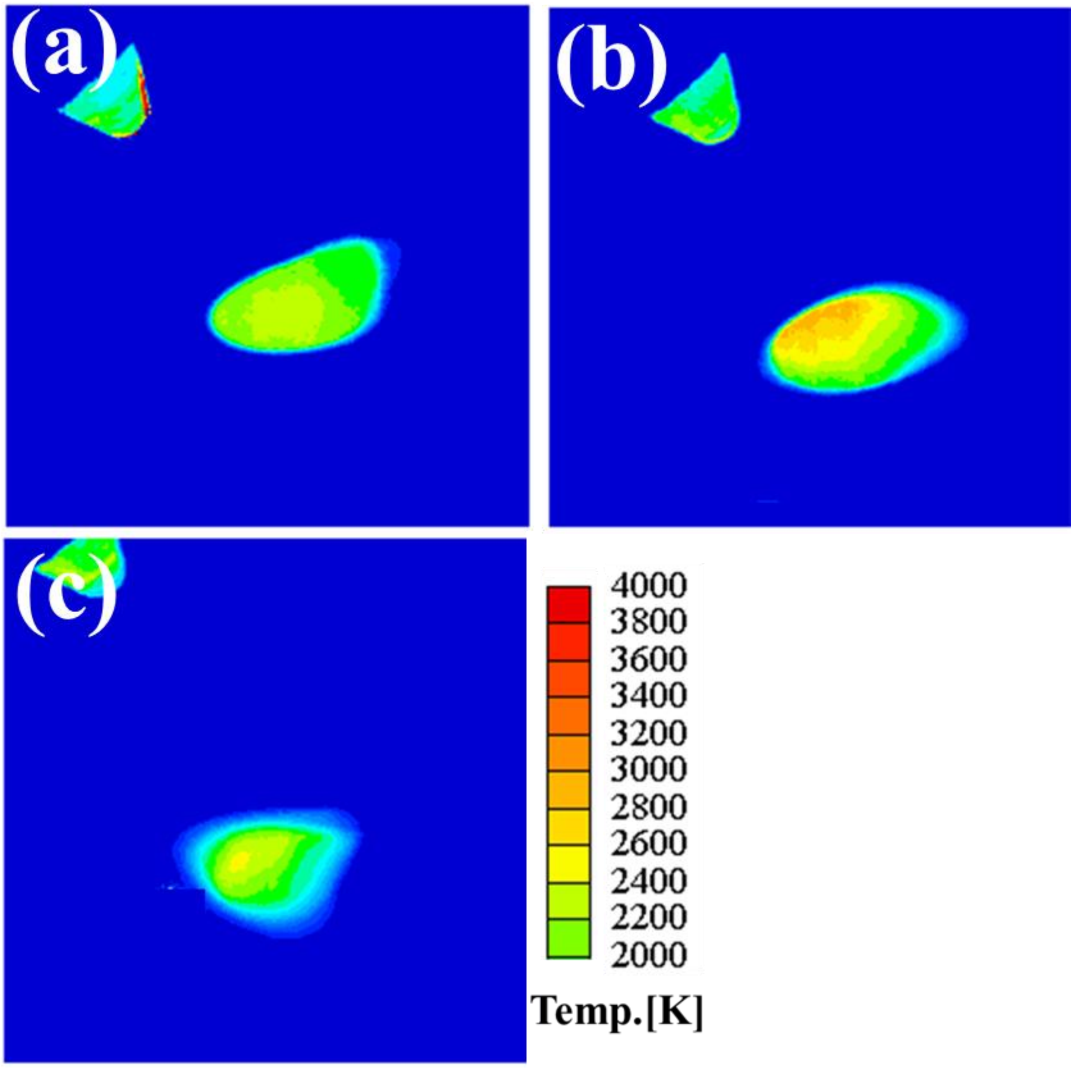

Fig. 2.37 Time average temperature of the anode surface in helium arc for different shield gas flow rates when hydrogen concentration is fixed at 20vol%, (a) 0 L/min, (b) 10 L/min, and (c) 20 L/min, respectively.

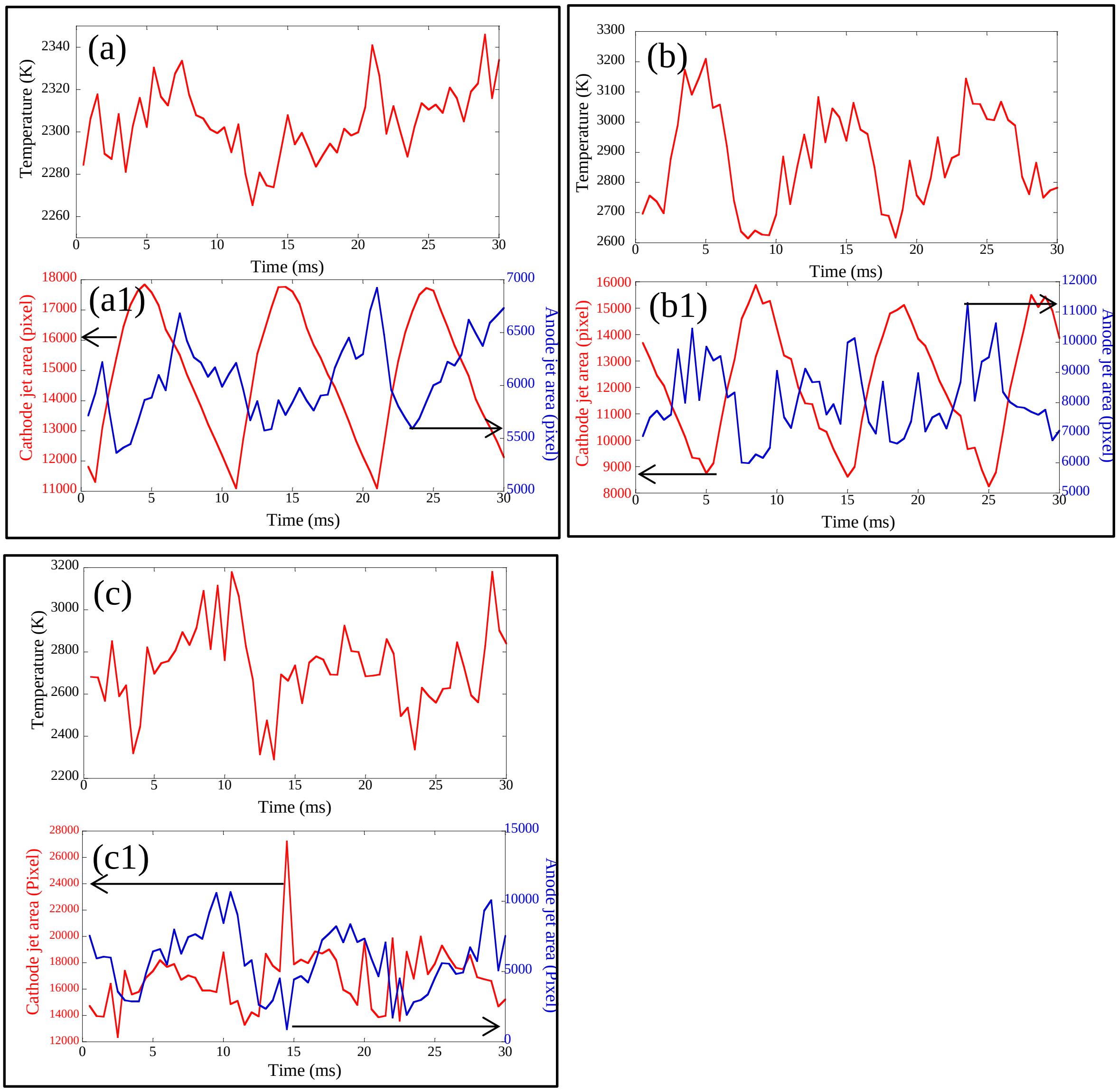

Fig. 2.38 The waveform of highest temperature variation (upper) and synchronized time variation of the anode jet area and the cathode jet area (lower) for helium arc with different shield gas flow rates. (a)-(a1), (b)-(b1), and (c)-(c1) correspond to shield gas flow rates of 0, 10, and 20 L/min, respectively.

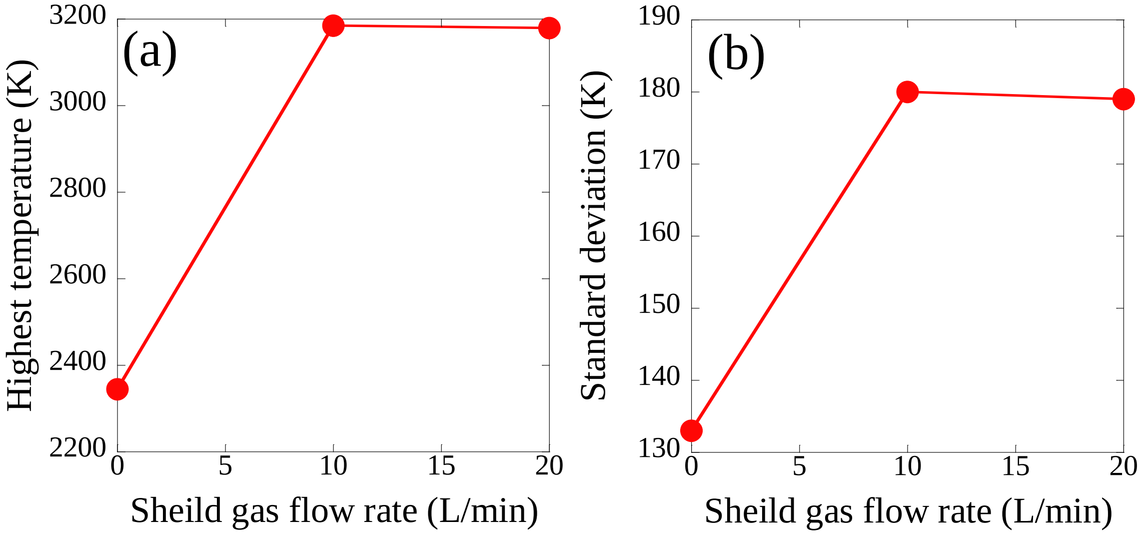

Fig. 2.39 Effects of shield gas flow rate on (a) highest temperature, (b) standard deviation in helium arc.

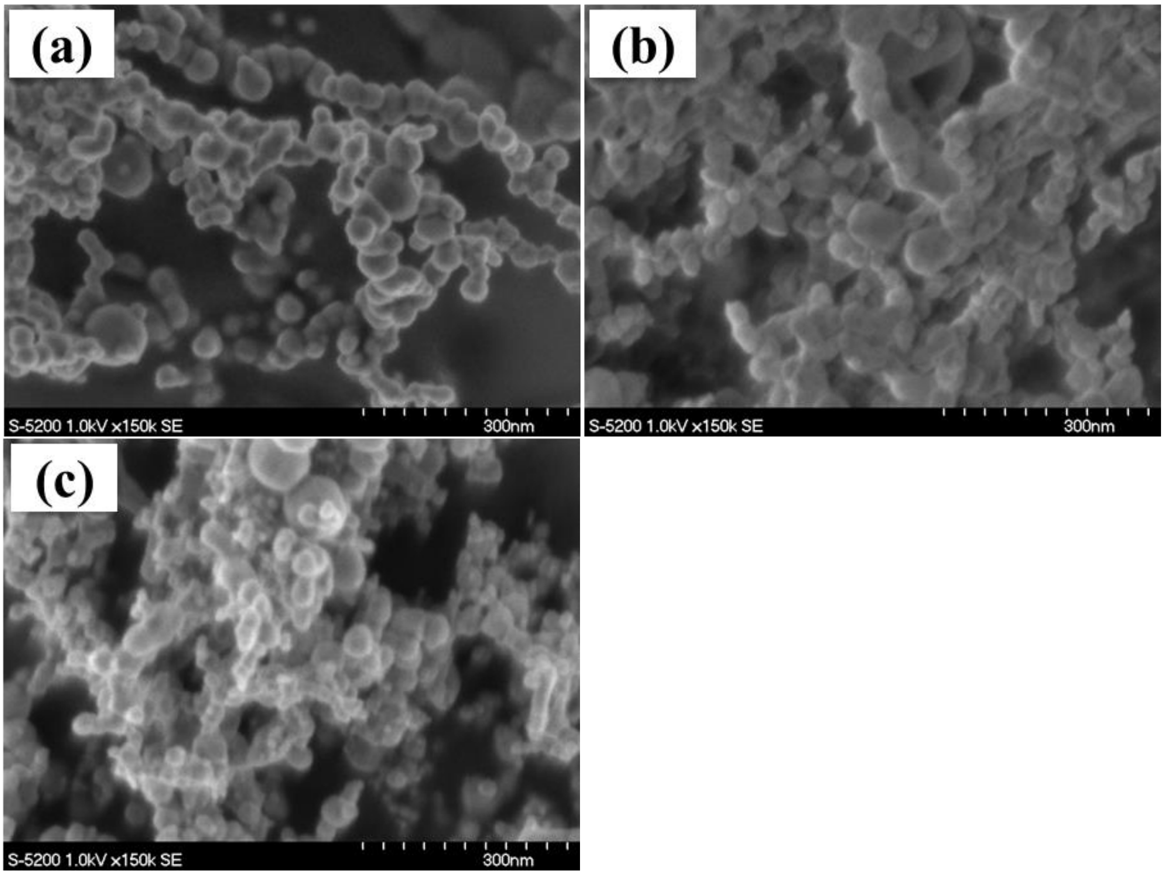

Fig. 2.40 FE-SEM images of nickel nanoparticles in helium arc at different shield gas flow rates when hydrogen concentration is 20vol%. (a), (b), and (c) correspond to shield gas flow rate of 0, 10, and 20 L/min, respectively.

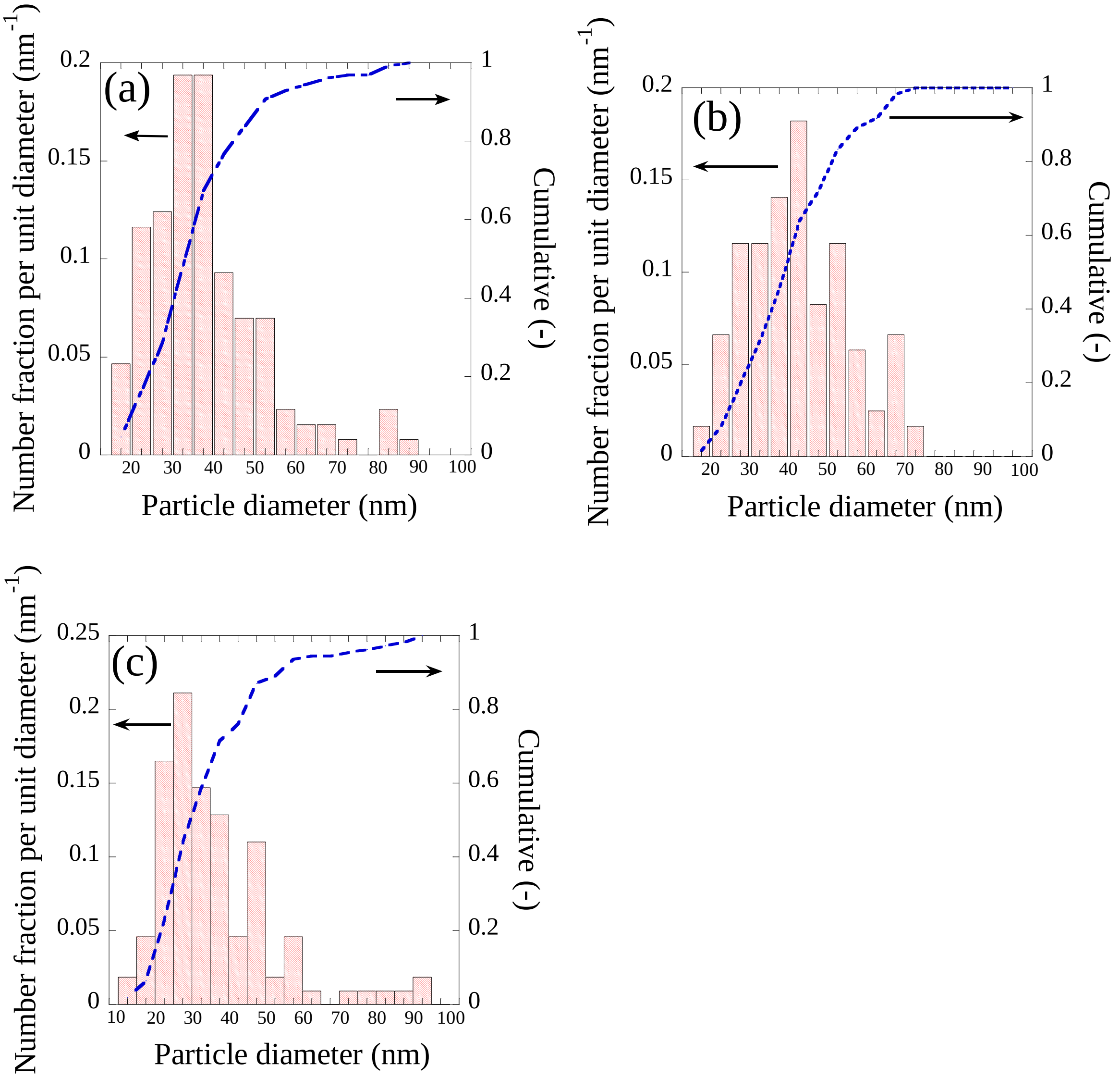

Fig. 2.41 Particle size distributions of the nanoparticles in helium arc at different shield gas flow rates when hydrogen concentration is 20vol%. (a), (b), and (c) correspond to shield gas flow rate of 0, 10, and 20 L/min, respectively.

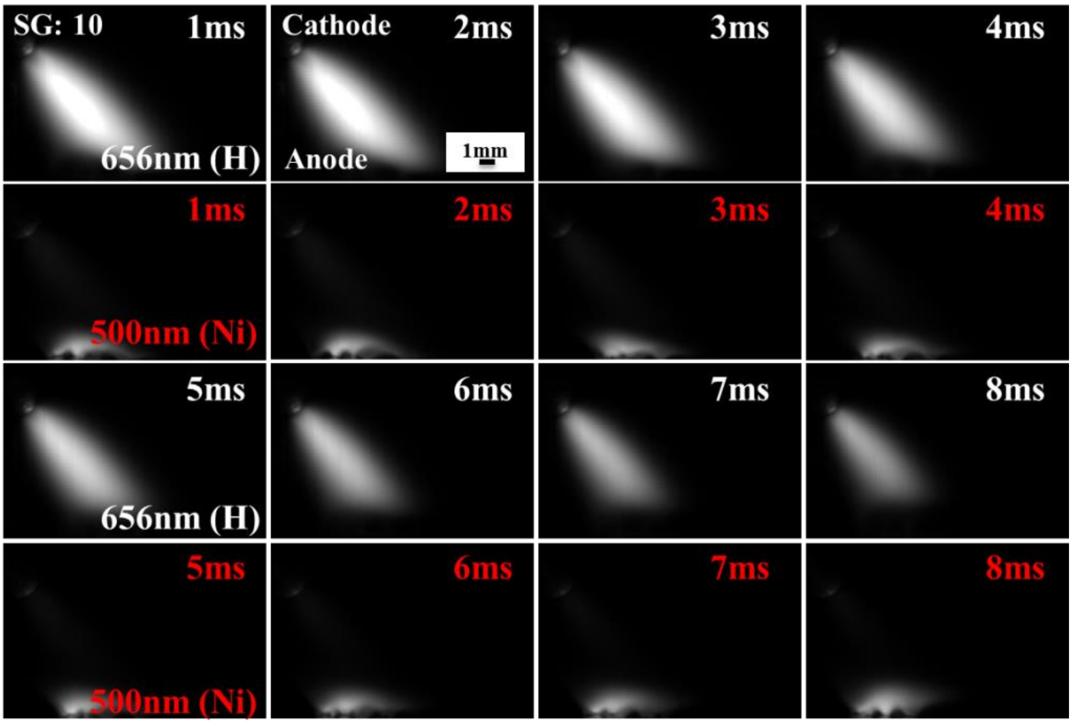

Fig. 2.42 Representative snapshots of high-speed camera in argon arc when hydrogen concentration is 30vol% and shield gas flow rate is 10 L/min. H emission is the upper one, and Ni emission is the lower one.

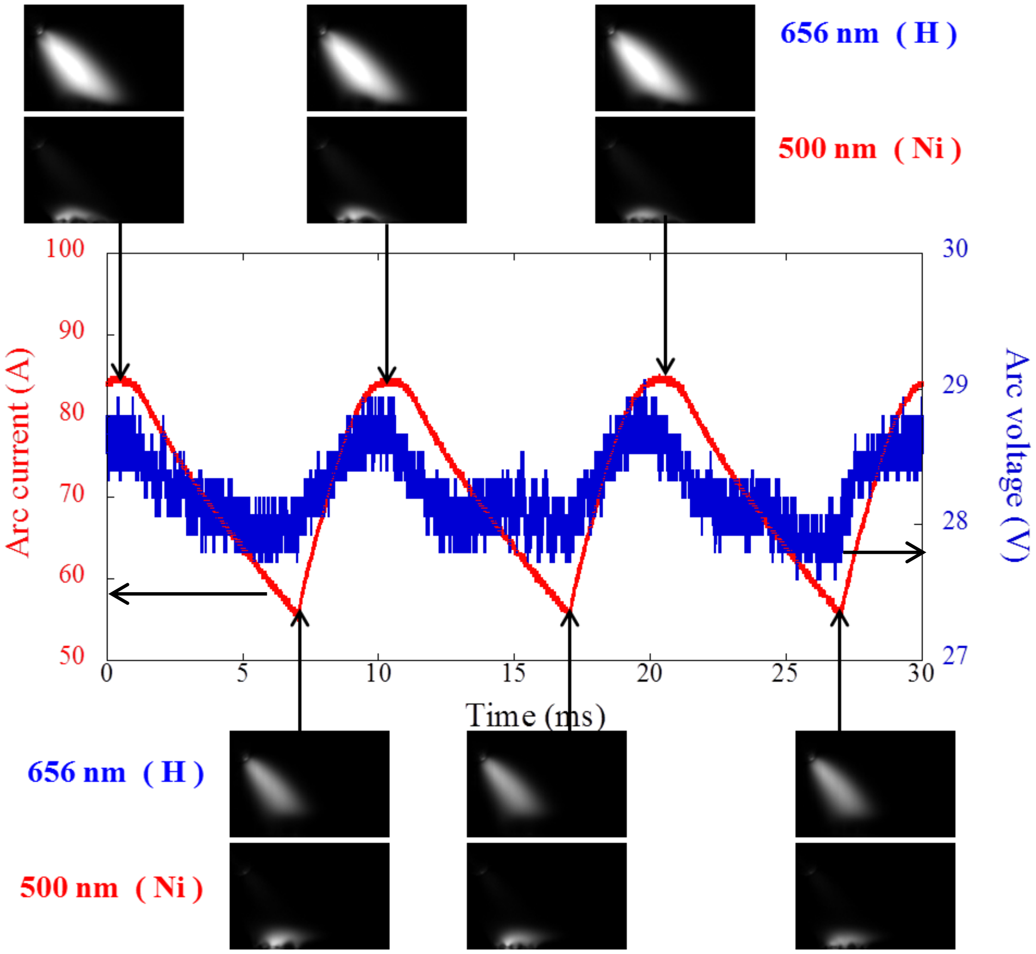

Fig. 2.43 Voltage and current waveform of argon arc synchronized with snapshots of H emission and Ni emission when hydrogen concentration is 30vol% and shield gas flow rate is 10 L/min.

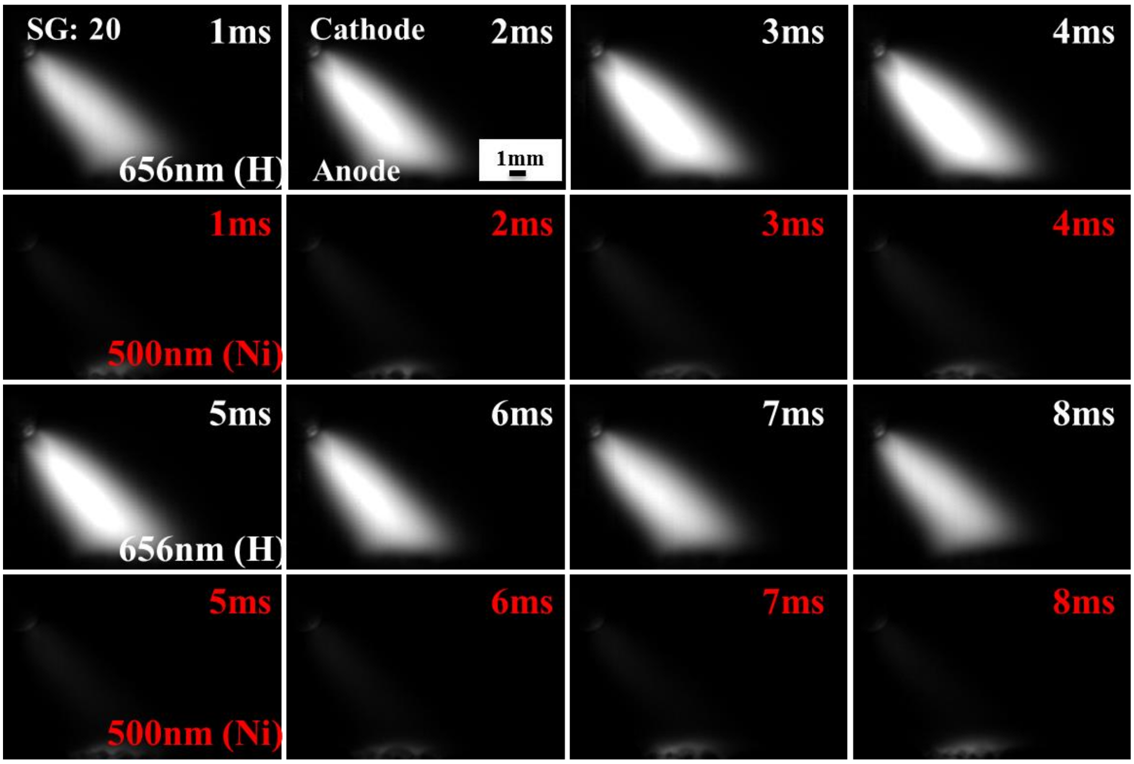

Fig. 2.44 Representative snapshots of high-speed camera in argon arc when hydrogen concentration is 30% and shield gas flow rate is 20 L/min. H emission is the upper one, and Ni emission is the lower one.

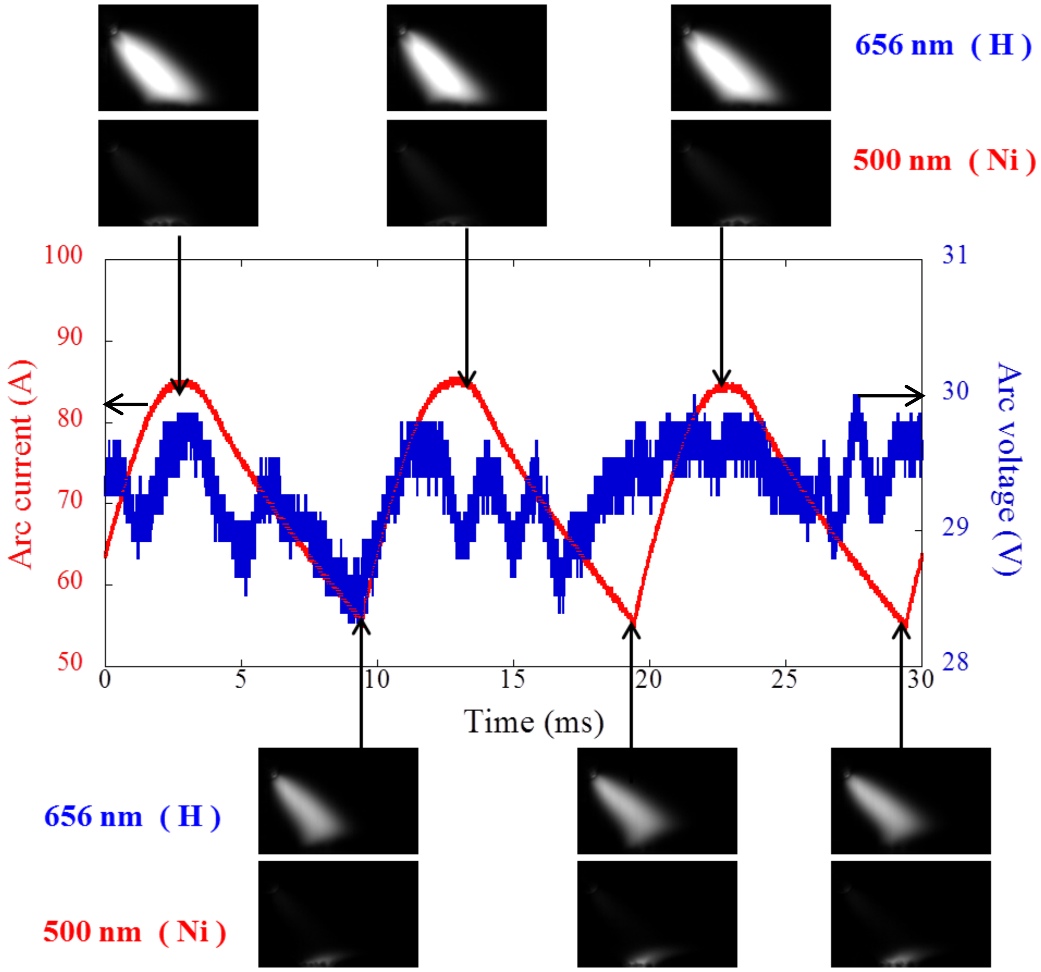

Fig. 2.45 Voltage and current waveform of argon arc synchronized with snapshots of H emission and Ni emission when hydrogen concentration is 30vol% and shield gas flow rate is 20 L/min.

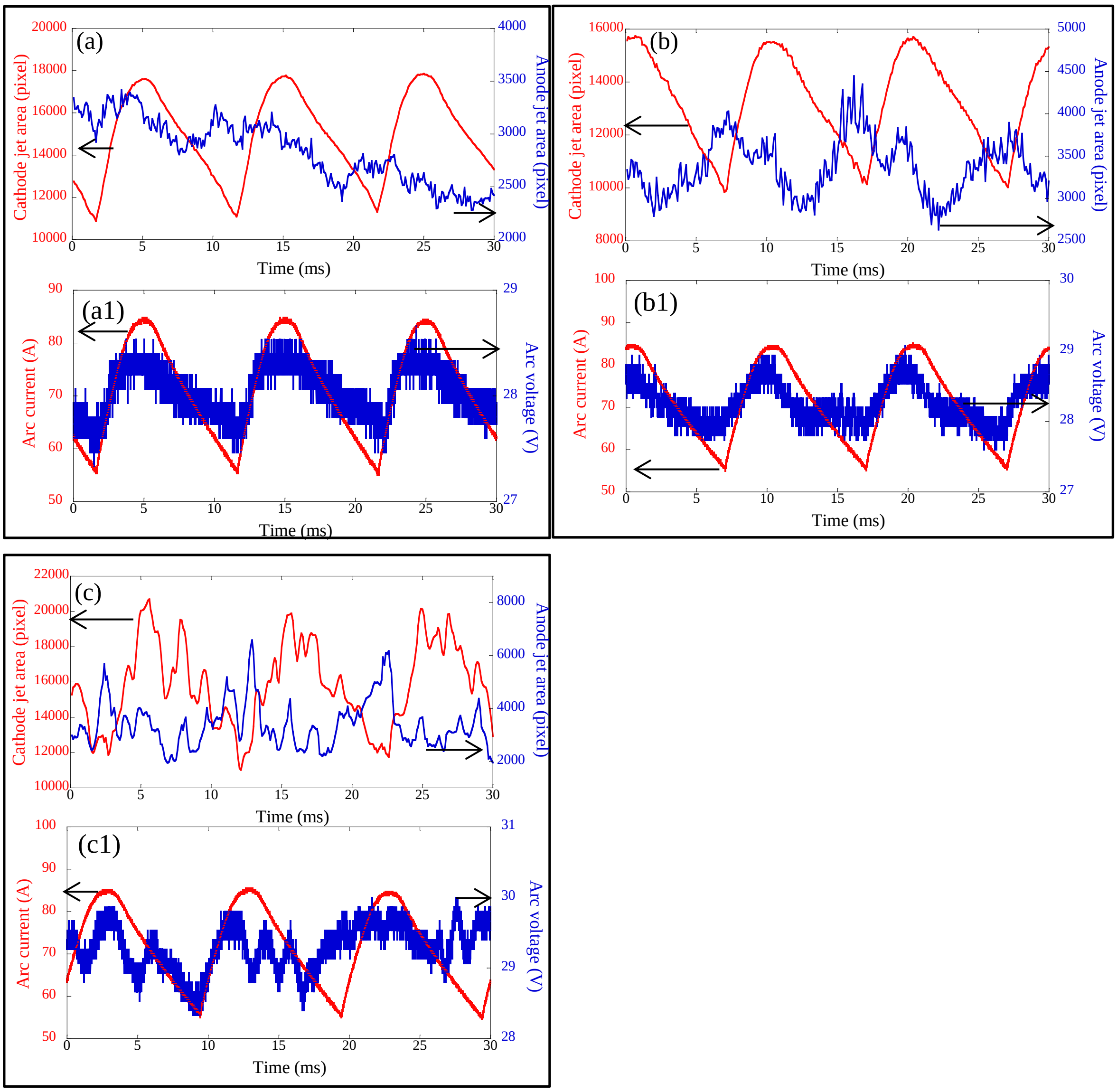

Fig. 2.46 The waveforms of anode and cathode jet area variation (upper) and synchronized arc current and voltage waveforms (lower) for argon arc with different shield gas flow rates. (a)-(a1), (b)-(b1), and (c)-(c1) correspond to shield gas flow rates of 0, 10, and 20 L/min, respectively.

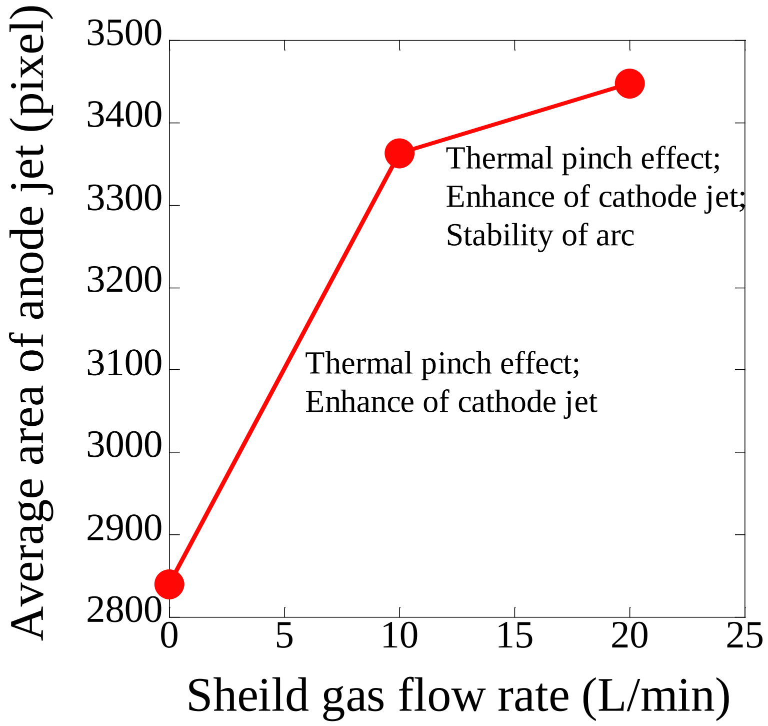

Fig. 2.47 Effect of shield gas flow rate on the averaged anode jet area in argon arc.

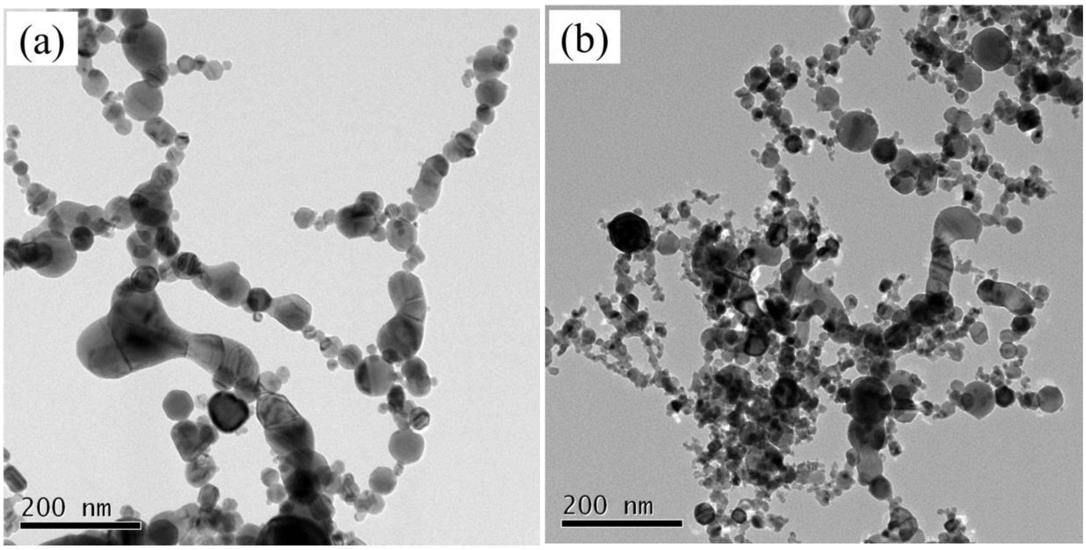

Fig. 2.48 FE-SEM images of nickel nanoparticles in argon arc at different shield gas flow rates when hydrogen concentration is 30vol%. (a) and (b) correspond to shield gas flow rate of 0 and 20 L/min, respectively.

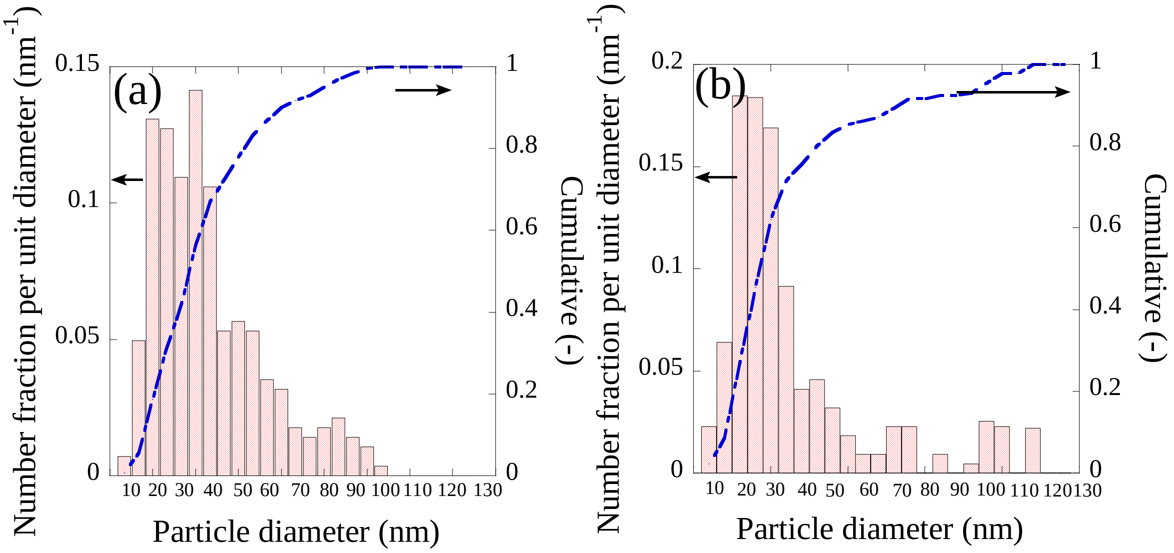

Fig. 2.49 Particle size distributions of the nanoparticles in argon arc at different shield gas flow rates when hydrogen concentration is 30%. (a) and (b) correspond to shield gas flow rate of 0 and 20 L/min, respectively.

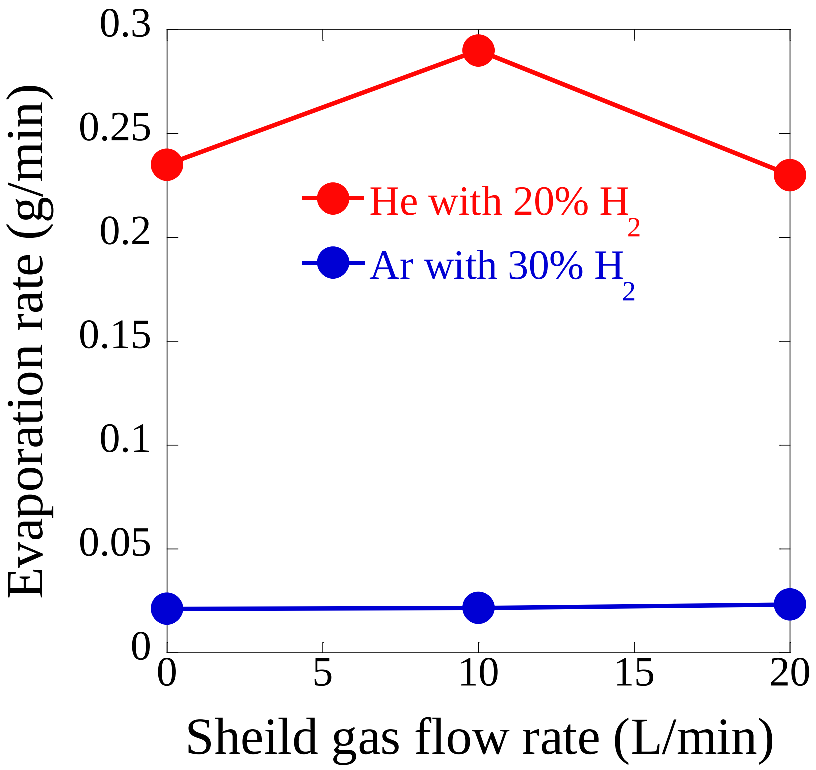

Fig. 2.50 Comparison of the effect of shield gas flow rate on evaporation rate of nickel anode between helium arc and argon arc.

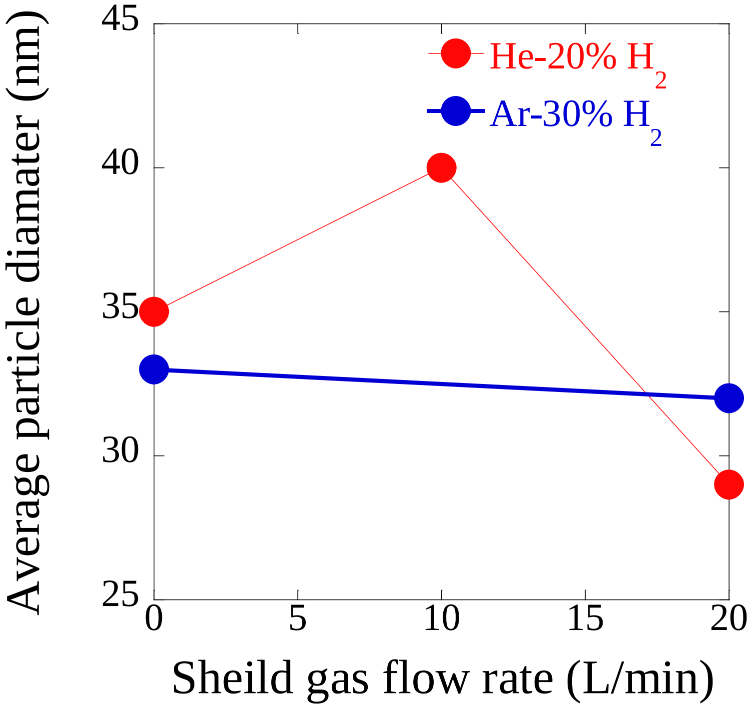

Fig. 2.51 Effect of shield gas flow rate on average particle diameter in helium and argon arcs.

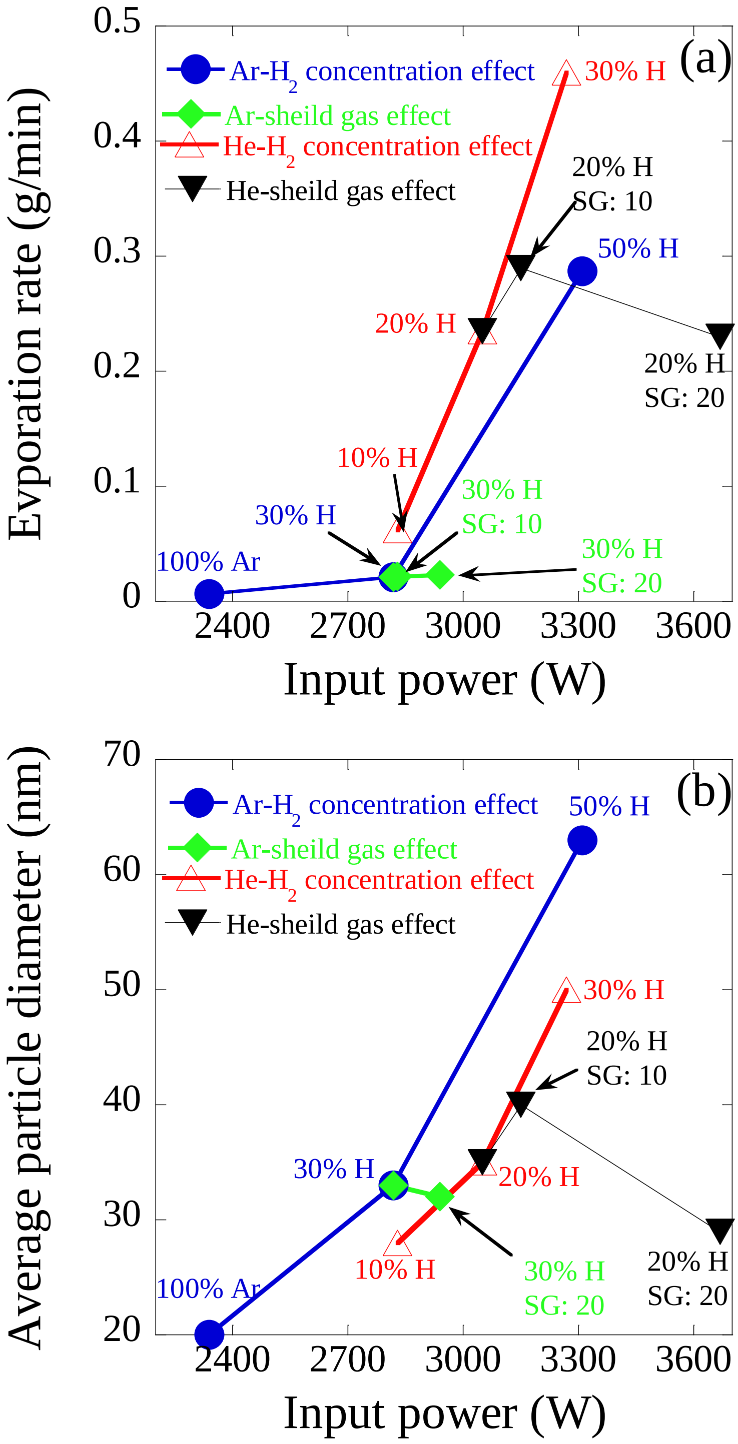

Fig. 2.52 The dependence of anode evporation rate (a) and average particle diameter (b) on input power in helium and argon arcs.

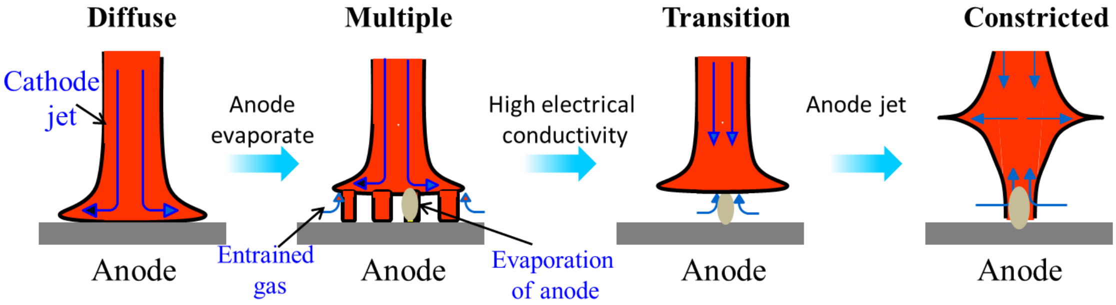

Fig. 2.53 Conceptual diagram of the formation mechanism of different arc-anode attachment modes.

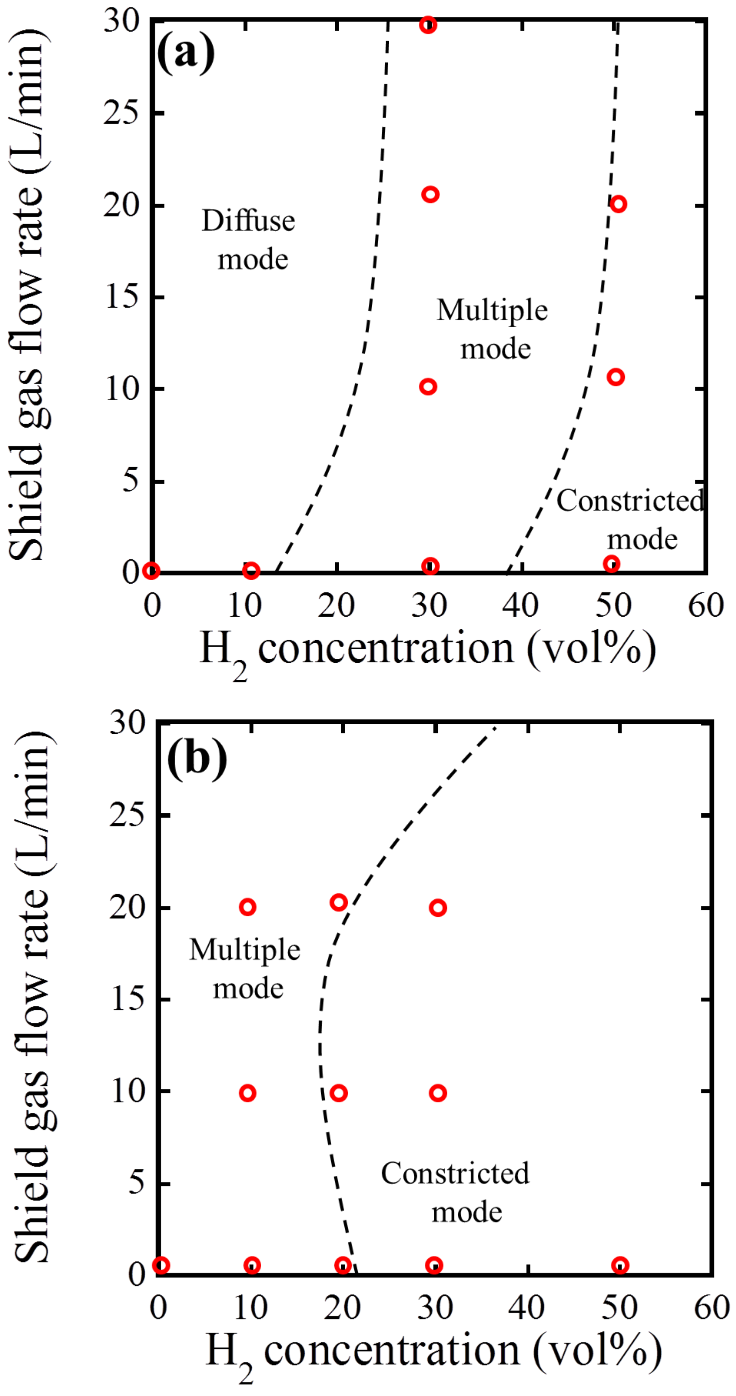

Fig. 2.54 Effects of hydrogen concentration and shield gas flow rate on the formation of different attachment modes. (a): argon arc, (b): helium arc.

3. Relationship between Arc-Anode Attachment Mode and Temperature of Carbon Electrode

3.1 Introduction

The arc discharge is an attractive method to prepare carbon nanomaterials with several advantages (Keidar et al. 2011). Firstly, it is an environmentally benign technique without generating any toxic by-products and hazardous gases. In addition, the high temperature of arc plasma provides the products with fewer defects. Finally, high productivity in the arc discharge method reduces the manufacturing cost.

The arc discharge method has also been employed to prepare lots of carbon nanomaterials successfully. Fullerene was scraped from the chamber wall in helium arc discharge at low pressure (Krätschmer et al. 1990); multi-wall carbon nanotube (MWNT) was collected from the cathode deposit at low pressure argon arc (Iijima 1991); single-wall carbon nanotube was found in a “collaret” around the cathode deposit, the web-like structure suspended between cathode and chamber wall, and cloth-like soot suspended in the chamber wall by using the catalyst in helium arc (Keidar et al. 2008); and graphene flakes was produced in the inner wall of the chamber under hydrogen atmosphere (Subrahmanyam et al. 2009).

In spite of considerable efforts on the arc discharge method, however, the formation mechanism of carbon nanomaterial has not been understood yet. Understanding the characteristics of thermal plasma is necessary to explain the formation mechanism of carbon nanomaterial. The anode provides the sublimated carbon species for the production of carbon nanomaterial, and the anode ablation rate determines the productivity. Therefore, in-depth research into the anode region and anode phenomena is helpful to improve the production of carbon nanomaterial by the arc discharge method. There are three typical arc-anode attachment modes at the anode boundary, diffuse attachment, multiple attachments, and constricted attachment (Dinulescu and Pfender 1980; Sanders et al. 1982; Heberlein et al. 2010). The anode attachment modes are the results of the competition between the cathode jet and the anode jet. When the cathode jet is strong, the anode attachment mode is the diffuse mode. The arc transitions to the multiple-attachment mode with reducing the cathode jet. Further decreasing the cathode jet increases the current density, which leads to the strong anode jet flow and the entrainment of cold gas along the anode towards the cathode. The increase of radial heat loss due to the anode jet makes a single constricted attachment take over the most of the current and stabilizes it. Heberlein *et al* investigated the formation mechanism and the characteristics of arc-anode attachment modes with a water cooling metal anode (Yang et al. 2006; Yang et al. 2007; Heberlein et al. 2010). However, the arc-anode attachment modes in the carbon electrode and the effect of attachment mode on electrode temperature fluctuation have not been reported.

The temperature of carbon electrode is an important parameter which affects the formation of carbon nanomaterial and its characteristics. Consequently, an accurate temperature measurement is required to understand the growth mechanism of carbon nanomaterial in dynamic interaction between electrode and arc plasma. The measurement of electrode temperature, however, is difficult by conventional methods owing to the strong radiation and dynamic behavior of the arc.

In this chapter, the two-color pyrometry combined with a high-speed camera which employed appropriate two band-pass filters was applied to measure the surface temperature of carbon electrode during the arc discharge. The objective of this work is to investigate the effect of arc-anode attachment mode on the electrode temperature behavior. In order to achieve the purpose, the effects of arc current and electrode gap distance on arc behavior and anode temperature were investigated in helium and argon arcs. In addition, arc-anode attachment mode and anode temperature behavior between helium and argon arcs were compared.

3.2. Experimental

3.2.1. Experimental Setup

Fig. 3.1 indicates the schematic illustration of an arc discharge system for preparing carbon nanomaterials, and a high-speed camera system for temperature measurement, which is similar to the setup for nickel nanoparticle production. A graphite anode rod (99.99%, Toyo Tanso Co., Ltd.) with an inclined top plane was put on a water-cooling copper plate. A graphite rod (99.99%, Toyo Tanso Co., Ltd.) was placed at an oblique angle from the anode. More information about this experimental setup was mentioned in chapter 2 in detail.

3.2.2. Experimental Conditions

The experimental conditions are shown in Table 3.1. The diameters of cathode and anode are 6 and 30 mm, respectively. The arc was generated for 5 min in helium or argon environment at atmospheric pressure. The arc current was controlled at 100, 150, and 200 A when the electrode gap distance was fixed at 3 mm. In addition, the electrode gap distance was controlled at 1, 3, and 5 mm and the arc current was fixed at 200 A.

3.2.3. Temperature measurement

Fig. 3.2 shows the schematic illustration of two-color pyrometry for temperature measurement of electrode surface during the arc discharge. This optical system has been introduced in chapter. 2, band-pass filters were selected with no line emission in the bandwidth of them. Optical emission spectroscopy (OES) measurements (iHR550, Horiba Jobin Yvon) were conducted to determine appropriate wavelengths. As shown in Fig. 3.3, two band-pass filters of 763±3 and 880±5 nm were employed for the temperature measurement in helium arc in order to eliminate the influence of line emission from the arc. In addition, according to OES results in Fig. 3.4, two band-pass filters of 785±1.5 and 880±2.5 nm as suitable band-pass filter were selected for carbon anode temperature measurement in argon arc.

As shown in Figs. 3.5 (a) and (b), images of the electrode in different wavelengths at 880±5 and 763±3 nm were simultaneously recorded by the high-speed camera (FASTCAM-SA WTI, Photron). As mentioned in chapter 2, plank’s law was used to evaluate 2-dimensional temperature distribution of the electrode surface in two-color pyrometry. The frame rate was fixed at 10,000 fps (frame per second) and the shutter speed was fixed at 20 μs. Since the sensitivity of the high-speed camera was poor at a low temperature region, only high temperature region where the temperature is over than 2,000 K was shown in the temperature distribution map.

3.2.4 High-Speed Camera Measurements

In order to observe the dynamic arc behavior, the same high-speed camera with temperature measurement was used at the frame rate of 10,000 fps and the exposure time of 20 μs.

3.2.5. Oscilloscope Measurement

Arc voltage and current were recorded by an oscilloscope (Scope Corder DL 850, Yokogawa) at 10 MHz.

3.3. Results and Discussion

In order to investigate the relationship between arc-anode attachment mode and temperature behavior in helium and argon arcs, the effects of electrode gap distance and arc current were discussed in this section.

3.3.1 Effect of Arc Current

(a) Arc-Anode Attachment Mode under Helium

Fig. 3.6 shows the snapshots of high-speed camera at different arc currents of 100, 150 and 200 A. A band-pass filter with the wavelength of 763±3 nm is used. Several small bright regions appear on the anode surface randomly without periodicity at the lowest arc current of 100 A. These bright regions represent the anode spot because of the high temperature of these regions. It means that the multiple arc-anode attachment mode was formed (Heberlein et al. 2010). In addition, multiple arc-anode attachment mode is also observed at 150 A. In contrast, a bright region with a relatively large size appears on the anode surface when the arc current reaches to 200 A. In particular, the bright region rotates on the anode surface periodically. A single arc spot is explained by the formation of diffuse attachment mode (Sanders et al. 1982； Heberlein et al. 2010). However, one bright region is separated into several small regions at 4 and 5 ms in Fig. 3.6 like as the multiple attachment mode. Therefore, the arc-anode attachment mode is the mixture of diffuse attachment and multiple attachment modes, dominated by diffuse attachment mode in the case of 200 A. As shown in Fig. 3.6, the rotation frequency of bright area is about 125 Hz when the arc current is 200 A. The Lorenz force induced by the arc itself contributes to the periodical arc behavior (Collares and Pfender 1997). The reason for the rotation of arc spot will be explained in next section.

In order to examine the characteristics of dynamic arc behavior, the change of arc voltage according to time was traced. Fig. 3.7 shows the waveforms of the arc voltage and the corresponding Fast Fourier Transform (FFT) spectra at different arc currents. These voltage waveforms exhibit similar shapes derived from the current ripple of the power supply. As a result, the main frequency is 100 Hz which comes from the power supply. According to the FFT spectrum of the voltage waveform in a wide range, the arc voltage fluctuated with high frequency about 10 kHz in multiple attachments. Contrastingly, the relatively small amplitude is noticed in the FFT spectrum of voltage waveform with the highest arc current of 200 A because of the diffuse attachment mode. In addition to the common peak at 100 Hz and its harmonics, the peak around 125 Hz is found at the arc current of 200 A. This characteristic frequency corresponds to arc rotation which was measured by the high-speed camera in Fig. 3.6.

As demonstrated in Fig. 3.8, the frequency of arc spot on the anode surface was confirmed when the frame rate of high-speed camera was fixed at 100,000 fps and the shutter speed was fixed at 0.37 μs. The arrow indicates one typical spot on the anode surface. The existence time of one spot on the anode surface is about 0.08 ms which was calculated by the snapshot of high-speed camera. The corresponding frequency is approximately 12.5 kHz, which confirms the frequency around 10 kHz in multiple attachment evaluated by the FFT of voltage waveform.

(b) Anode Temperature under Helium

Fig. 3.9 shows the snapshots of electrode temperature distribution according to time at different arc currents. The high temperature regions on anode surface and the bright areas in the snapshots of high-speed camera in Fig. 3.6 are corresponding very well. At the arc current of 200 A, it was evaluated that the rotation frequency of high temperature region is about 125 Hz which is the same as arc spot rotation as shown in high-speed camera.

Time average temperature distribution maps of anode surface are shown in Fig. 3.10. These images demonstrate the average temperature distribution in 20 ms. Figs. 3.10 (a), (b), and (c) correspond to the arc current of 100, 150, and 200 A, respectively. In contrast to the arc current of 100 and 150 A, the size of high temperature region (over than 2000 K) at arc current of 200 A is larger, which is caused by large input power in the case of arc current of 200 A.

Fig. 3.11 indicates the radial temperature distribution from the central to the edge of anode surface in helium arc when changing arc current. The radial temperature distribution was calculated from the time average temperature distribution map in Fig. 3.10. The temperature at the central of anode surface does not show big difference between 150 and 200 A, although the input power is increased. It can be explained by the fact that the rotation of arc spot in diffuse attachment at 200 A leads to low heat flux to the anode. Compared with the relatively high heat flux at 150 A, there is no significant difference of temperature value in the central of anode surface between 200 A and 150 A owing to the different arc-anode attachment modes. Different temperature behavior between 100 and 150 A is caused by input power at the same attachment mode. In addition, the temperature reduces along the radial direction gradually at arc current of 200 A. However, the temperature does not decrease along the radial direction gradually at 150 and 100 A. Since anode spots with the highest temperature distribute on the anode surface randomly in multiple attachments, no significant temperature difference can be observed along the radial direction in multiple attachments.

Fig. 3.12 shows the time variation of the anode temperature in central region for helium arc during 30 ms. Figs. 3.12 (a), (b), and (c) correspond to the arc current of 100, 150, and 200 A, respectively. The waveform of temperature fluctuation could not follow the waveform of arc current in multiple attachments because arc spot moves with high frequency. As a result of the rotation of arc spot in diffuse attachment, there is no clear relationship between arc current and temperature variation. In particular, the temperature has higher fluctuation frequency when the arc currents are 100 and 150 A. The high frequency of anode temperature fluctuation is attributed to the formation of multiple arc-anode attachments. Contrastingly, four peaks about temperature fluctuation are clearly found during 30 ms at the arc current of 200 A. The temperature fluctuation at 200 A is strongly influenced by the arc rotation, which can be seen only in the diffuse attachment mode.

The FFT spectra of above temperature fluctuation are shown in Fig. 3.13 when changing the arc current from 100 to 200 A. As shown in Figs. 3.13 (a)-(b), no significant peak can be observed in the range of 0 to 500 Hz in multiple attachment modes when the arc currents are 100 and 150 A. However, Fig. 3.13 (c) indicates that a dominant peak around 125 Hz appears in the diffuse attachment mode when the arc current reaches to 200 A, which is same as the frequency of arc rotation evaluated by both the voltage analysis and the high-speed image analysis. It can be deducted that the rotation of arc spot induces this characteristic frequency of 125 Hz in diffuse attachment at 200 A.

(c) Arc-Anode Attachment Mode under Argon

Fig. 3.14 shows the snapshots of high-speed camera in argon arc at different arc currents of 100, 150, and 200 A when the electrode gap distance is fixed at 3 mm. A bright region with a relatively large size appears on the anode surface when the arc currents are 100 and 150 A, indicating that the formation of diffuse arc-anode attachment mode (Sanders et al. 1982; Heberlein et al. 2010). The diffuse attachment mode mixed with a small component of multiple attachments is formed at the arc current of 200 A. However, no significant rotation can be observed from the snapshots of high-speed camera in diffuse attachment mode for argon arc.

The waveforms of the arc voltage and the corresponding FFT spectra in argon arc at different arc currents are shown in Fig. 3.15. Similar results to helium arc are obtained; the main frequency is 100 Hz which derives from the current ripple of the power supply. Since all of the attachment modes are dominated by diffuse mode, the FFT spectra of voltage waveform in a wide range do not show obvious amplitude by changing the arc current. In particular, no significant amplitude can be seen at the arc current of 200 A, although there is small component of multiple attachments. This is mainly caused by the fact that the component of multiple attachments is too small to affect the fluctuation of voltage waveform.

(d) Anode Temperature under Argon

Fig. 3.16 shows the dependence of electrode temperature distribution on time for argon arc at different arc currents. As shown in Fig. 3.16, the high temperature regions on anode surface are in accordance with the bright areas in the snapshots of high-speed camera. Each temperature distribution map doses not change with time at the fixed arc current, indicating argon arc is relatively stable. In addition, Fig. 3.17 indicates time average temperature distribution of anode surface in argon arc when changing the arc current. These average temperature distribution images are calculated in 20 ms. The size of high temperature region (over than 2000 K) increases with increasing the arc current due to the high input power, since all of these conditions correspond to the diffuse attachment mode.

Radial temperature distribution of carbon anode in argon arc is shown in Fig. 3.18. The temperature distribution was calculated based on the time average temperature distribution map in Fig. 3.17. As a result of these conditions correspond to diffuse attachment, the temperature decreases from the central to the edge of anode surface gradually. The size of high temperature distribution region (over than 2000 K) is large at the arc current of 200 A, which comes from the largest input power. Compared with helium arc, temperature is lower and the size of high temperature region is smaller in argon arc when the experimental conditions are same.

Fig. 3.19 shows the time variation of the anode temperature in the central region for argon arc during 30 ms when changing the arc current. Compared with the temperature fluctuation in helium arc, no significant fluctuation can be noticed at different arc currents. The corresponding

FFT spectra of temperature fluctuation are shown in Fig. 3.20. Figs. 3.20 (a), (b), and (c) correspond to the arc current of 100, 150, and 200 A, respectively. A small peak at 100 Hz can be observed in the range of 0 to 500 Hz in diffuse attachment mode, which depends on the power supply.

(e) Comparison of Helium with Argon

As shown in previous section, there are obvious differences of arc-anode attachment modes and temperature behavior in helium and argon arcs when changing arc current. Fig. 3.21 shows the radial temperature distribution from the central to the edge of anode surface under different gases. The typical results obtained at the arc current of 150 A and the electrode gap distance of 3 mm are chosen for comparison. As shown in this figure, the temperature at the central of anode surface in helium arc is higher than that of argon arc. In addition, the radius of high temperature region (over than 2000 K) is about 1.1 mm in argon arc, which is smaller than that of 1.8 mm in helium arc. The main reason is related to the high thermal conductivity of helium and the constriction of helium arc.

The highest temperature and standard deviation of temperature are compared between helium arc and argon arc when changing arc current. The highest temperature region with the corresponding size of 4×4 pixels was calculated from the time average temperature distribution map in Fig.3.21. As shown in Fig. 3.22 (a), the highest temperature increases with increasing arc current for helium and argon arcs due to the increase of input power. The highest temperature in helium arc is higher than that of argon arc at the same experimental conditions. It can be explained by higher thermal conductivity of helium and the constriction of helium arc. Fig. 3.22 (b) shows the standard deviation of temperature in helium and argon arcs. Because diffuse attachment with significant rotation of arc spot is formed at 200 A in helium arc, temperature also shows the largest standard deviation. There is no significant difference for the standard deviation of temperature between 100 and 150 A in helium arc, because the multiple attachments are formed in these conditions. Because all of conditions correspond to diffuse attachment in argon arc and the arc is relatively stable, no significant variation of standard deviation of temperature can be observed by increasing the arc current in argon arc.

Fig. 3.23 indicates the evaporation rate of carbon anode in argon and helium arcs when changing the arc current. It shows the same tendency with highest temperature variation as shown in Fig. 3.22 (a). The evaporation rate increases with increasing arc current on account of the high input power. In contrast to argon arc, the evaporation rate of carbon anode increases dramatically in helium arc at the same arc current. All of these results can be explained by the large heat flux to anode caused by the constriction of helium arc and higher thermal conductivity of helium.

The transition of arc-anode attachment from multiple to diffuse can be obtained with increasing arc current in helium arc. On the other hand, only diffuse attachment can be seen in argon arc when increasing the arc current except a small component of multiple attachments at high arc current of 200 A. Therefore, the arc-anode attachment mode is different between argon arc and helium arc at the same experimental condition. This is strongly related to properties of gas species and the formation mechanism of different arc-anode attachments. As discussed in previous section, the differences of thermal conductivity and electrical conductivity between helium and argon lead to different arc behaviors. Moreover, compared with helium arc, arc spot without significant rotation is observed in diffuse attachment mode of argon arc. The mode for explaining the rotation of arc spot will be introduced in next section in detail.

3.3.2 Effect of Electrode Gap Distance

(a) Arc-Anode Attachment Mode under Helium

Fig. 3.24 shows the snapshots of high-speed camera for helium arc at different electrode gap distances of 1, 3 and 5 mm when the arc current is fixed at 200 A. A band-pass filter which has the wavelength of 763±3 nm is used for arc behavior observation. A bright region with a relatively large size appears on the anode surface when the electrode gap distances are 1 and 3 mm. In addition, the bright region rotates on the anode surface periodically. As discussed in previous section, it indicates the formation of diffuse attachment at the electrode gap distances of 1 and 3 mm. The arc-anode attachment mode is the mixture of diffuse attachment and multiple attachment modes and is dominated by diffuse attachment mode when the electrode gap distance is 3 mm. Contrastingly, several small bright regions appear on the anode surface randomly without periodicity at the largest electrode gap distance of 5 mm, indicating that the multiple arc-anode attachment modes are formed (Heberlein et al. 2010). As shown in Fig. 3.24, the rotation frequencies of bright area are about 190 and 125 Hz corresponding to the electrode gap distances of 1 and 3 mm, respectively.

Fig. 3.25 shows the waveforms of the arc voltage and the corresponding FFT spectra at different electrode gap distances. Similar to the results of the voltage waveform at different arc currents, the main frequency is 100 Hz which derives from the current ripple of the power supply. FFT spectra of the voltage waveform in a wide range indicate the arc voltage fluctuated with high frequency about 10 kHz in multiple attachment mode. In contrast, the relatively small amplitude of the peak is observed in the FFT spectrum of voltage waveform at the electrode gap distance of 3 mm, it is related to the mixture of diffuse and multiple attachment modes. Two peaks at 190 and 125 Hz are found in the FFT spectra of voltage waveform when the electrode gap distances are 1 and 3 mm, respectively. These characteristic frequencies correspond to the arc spot rotation as measured by the high-speed camera in Fig. 3.24.

(b) Anode Temperature under Helium

Fig. 3.26 demonstrates the snapshots of electrode temperature distribution according to time in helium arc at different electrode gap distances. The high temperature regions on anode surface correspond to the bright areas in the snapshots of high-speed camera. It was evaluated that the rotation frequencies of high temperature region are about 190 and 125 Hz corresponding to electrode gap distance of 1 and 3 mm, respectively, which are the same frequency as the arc spot rotation. Fig. 3.27 indicates time average temperature distribution map in helium arc at different electrode gap distances when the arc current is fixed at 200 A. Figs. 3.27 (a), (b), and (c) correspond to the electrode gap distance of 1, 3, and 5 mm, respectively. The size of high temperature region (over than 2000 K) and the value of the highest temperature increase with increasing the electrode gap distance. All of these results are related to the increase of input power by changing arc current.

Fig. 3.28 shows the radial temperature distribution from the central to the edge of anode surface in helium arc when changing electrode gap distance. As discussed in previous section, radial temperature distribution is related to the attachment mode. Diffuse attachment leads to radial temperature decreases dramatically, while the multiple attachments do not result in the radial temperature decrease significantly due to the random distribution of anode spots. Because multiple attachment modes are formed at the electrode gap distance of 5 mm, temperature does not reduce gradually along the radial direction. In contrast, as a result of the formation of diffuse attachment mode, the temperature reduces from the central to the edge gradually at the electrode gap distances of 1 and 3 mm,

Fig. 3.29 indicates the temperature variation of anode surface with the time in helium arc at different electrode gap distances when the arc current is fixed at 200 A. Figs. 3.29 (a), (b), and (c) correspond to the electrode gap distance of 1, 3, and 5 mm, respectively. Almost six peaks about temperature fluctuation are clearly found during 30 ms at the electrode gap distance of 1 mm, indicating the high frequency of temperature fluctuation at electrode gap distance of 1mm, which is larger than that of 125 Hz at the electrode gap distance of 3 mm. Contrastingly, the temperature has higher fluctuation frequency when the electrode gap distance is 5 mm owing to multiple arc-anode attachment mode.

Fig. 3.30 indicates the corresponding FFT spectra of anode temperature at different electrode gap distances. Figs. 3.30 (a), (b), and (c) corresponding to the electrode gap distance of 1, 3, and 5 mm, respectively. In the range of 0 to 500 Hz, the dominant peaks around 190 and 125 Hz can be observed in the diffuse attachment mode when the electrode gap distances are 1 and 3 mm, respectively. These fluctuation frequencies of anode temperature come from the rotation of arc spot evaluated by both the voltage analysis and the high-speed image analysis. However, as shown in Fig. 3.30 (c), no significant peak appears in multiple attachment modes when the electrode gap distance is 5 mm.

(c) Arc-Anode Attachment Mode under Argon

Fig. 3.31 shows the snapshots of high-speed camera for argon arc at different electrode gap distances of 1, 3, and 5 mm and the fixed arc current of 200 A. A bright region with a relatively large size and several small bright regions appear on the anode surface when the electrode gap distances are 1 and 3 mm. Several arc spots with small size are explained by the formation of multiple attachment mode (Heberlein et al. 2010). A single arc spot with large size is explained by the formation of diffuse attachment mode (Sanders et al. 1982; Heberlein et al. 2010). As a result, the mixture of diffuse and multiple attachment modes are obtained at electrode gap distances of 1 and 3 mm. In addition, the arc spot rotates on the anode surface periodically at the electrode gap distance of 1 mm, the rotation frequency is about 110 Hz. In contrast, no significant rotation can be noticed at the electrode gap distance of 3 mm. However, only one bright region like as the diffuse attachment mode can be observed when the electrode gap distance is 5 mm. The formation of diffuse attachment at the largest electrode gap distance is the result of the largest amount of evaporation of cathode material (Table. 3.2). The evaporation of cathode material leads to enhance the intensity of cathode jet. In contrast to helium, the rotation phenomenon is not so significant in argon arc.

Fig. 3.32 shows the waveforms of the arc voltage in argon arc and the corresponding FFT spectra at different electrode gap distances. Similar to results in helium arc are observed, the main frequency of these voltage waveforms is 100 Hz derived from the power supply. As shown in the FFT spectrum of the voltage waveform in a wide range, the arc voltage fluctuates with high frequency about 10 kHz at electrode gap distance of 1 mm due to the large component of multiple attachments, which is similar to the frequency of multiple attachments in helium arc. On the other hand, no significant amplitude can be observed in the FFT spectrum of voltage waveform at the large electrode gap distances of 3 and 5 mm because of the diffuse attachment mode. The peak at 110 Hz is found in addition to the common peak at 100 Hz and its harmonics when the electrode gap distance is 1 mm. As confirmed by high-speed camera, this characteristic frequency corresponds to arc rotation.

(d) Anode Temperature under Argon

The snapshots of electrode temperature distribution according to time in argon arc at different electrode gap distances are shown in Fig. 3.33. The high temperature regions on the anode surface and the bright area in the snapshots of high-speed camera in Fig. 3.31 are corresponding very well. It is evaluated that the rotation frequency of high temperature region is about 110 Hz corresponding to the electrode gap distance of 1 mm, which is the same frequency with arc spot rotation.

Time average temperature distribution map at different electrode gap distances are shown in Fig. 3.34. The size of high temperature region (over than 2000 K) does not vary with the electrode gap distance. However, the value of highest temperature at electrode gap distance of 5 mm is lower than that of electrode gap distances of 3 and 1 mm. It can be explained by the fact that diffuse attachment leads to low heat flux.

Fig. 3.35 shows the temperature distribution of carbon anode along the radial direction in argon arc when changing electrode gap distance. The temperature decreases along the radial direction gradually on account of the formation of diffuse attachment. As shown in Fig. 3.35, the temperature value at the electrode gap distance of 5 mm is lower than that of 3 and 1 mm at the fixed position. It is caused by different heat flux by changing arc-anode attachment mode. As shown in the snapshot of high-speed camera in Fig. 3.31, the anode spot has relatively large diameter at large electrode gap distance. As a result, the heat flux reduces with increasing electrode gap distance, although the input power increases a little by increasing the electrode gap distance (Table. 3.5). The effect of anode spot diameter is larger than the effect of the input power when increasing the electrode gap distance. As a consequence, the temperature reduces with increasing the electrode gap distance in argon arc when the attachment mode is diffuse mode.

Fig. 3.36 shows temperature variation of anode surface with the time in argon arc at different electrode gap distances when the arc current is fixed at 200 A. Figs. 3.36 (a), (b), and (c) correspond to the electrode gap distance of 1, 3, and 5 mm, respectively. These figures shows the temperature variation in the central region during 30 ms. Three peaks about temperature fluctuation are clearly found during 30 ms at the electrode gap distance of 1 mm. In contrast, no significant fluctuation can be observed at the electrode gap distances of 3 and 5 mm, since argon arc is relatively stable in diffuse arc-anode attachment of. Fig. 3.37 indicates the corresponding FFT spectra of anode temperature at different electrode gap distances. Figs. 3.37 (a), (b), and (c) correspond to the electrode gap distance of 1, 3, and 5 mm, respectively. The dominant peak located around 110 Hz can be noticed at the electrode gap distance of 1 mm. This fluctuation frequency drives from the rotation of arc spot. However, no significant peak appears when the electrode gap distances are 3 and 5 mm, indicating argon arc is stable when diffuse attachment is formed.

(e) Comparison of Helium with Argon

Fig. 3.38 shows the radial temperature distribution from the central to the edge of anode surface under different gases. Temperature radial distribution in helium and argon arcs as a typical example are selected for comparison when the arc current is 200 A and the electrode gap distance is 3 mm. The temperature in helium arc is larger than that of argon arc at the fixed position. This difference comes from the higher thermal conductivity of helium and the constriction of helium arc.

The comparison of the highest temperature and standard deviation of temperature variation between helium and argon arcs are shown in Fig. 3.39. Fig. 3.39 (a) indicates the highest temperature variation in helium and argon arcs. The selected region corresponds to 4×4 pixels in time average temperature distribution map. The highest temperature increases with increasing electrode gap distance for helium arc, which can be explained by the increase of input power and the transition of attachment mode from diffuse to multiple. However, the highest temperature reduces with increasing the electrode gap distance in argon arc; it is related to large size of arc spot in the case of large electrode gap distance As a result, the heat flux is lower in diffuse attachment in argon arc. Fig. 3.39 (b) shows the standard deviation of temperature in helium and argon arcs. The largest standard deviation at the electrode gap distance of 3 mm is obtained in helium arc, which is caused by the rotation of arc spot in diffuse attachment. The standard deviation of temperature reduces with increasing electrode gap distance in argon arc. The rotation of arc spot at electrode gap distance of 1 mm leads to large standard deviation. In addition, the stable arc at the electrode gap distances of 3 and 5 mm lead to the small standard deviation.

Fig. 3.40 indicates the evaporation rate of carbon anode in helium arc and argon arc at different electrode gap distances when arc current is fixed at 200 A. The highest temperature and the evaporation rate show the same variation tendency in helium and argon arcs. In contrast to argon arc, carbon evaporation rate in helium arc is higher at the same experimental condition, which can be explained by the constriction of helium arc and higher thermal conductivity of helium. In the case of argon, anode evaporation rate decreases with increasing the electrode gap distance at the fixed arc current of 200 A. As discussed in previous section, the heat flux is mainly determined by the size of anode spot when the input power is similar (Table. 3.5). The heat flux reduces with increasing electrode gap distance due to the formation of diffuse attachment mode. Therefore, the smaller heat flux can be obtained at large electrode gap distance in argon arc. Consequently, the evaporation rate reduces with increasing the electrode gap distance in argon arc.

Fig 3.41 (a) shows the relationship between input power and the highest temperature in helium arc and argon arc. The input powers are shown in Tables. 3.3-3.6. The highest temperature in helium arc is higher than that of argon arc, although the input power in argon arc is higher than that of helium arc. It can be explained by the constriction of helium arc and the high thermal conductivity of helium. As discussed in previous section, the highest temperature increases with increasing arc current in helium arc and argon arc. In addition, the highest temperature increases with increasing the electrode gap distance in helium arc. However, the highest temperature reduces with increasing the electrode gap distance in argon arc because of the formation of diffuse attachment. Fig 3.41 (b) indicates the variation of evaporation rate of carbon anode with input power in helium arc and argon arc. The same tendency with highest temperature variation can be obtained. The variation of evaporation rate can be explained by the reason which is similar to the highest temperature variation.

According to the high-speed camera observation, the transition of arc-anode attachment from diffuse mode to multiple modes occurs with increasing electrode gap distance in helium arc. In contrast, the arc-anode attachment transitions to diffuse with increasing the electrode gap distance in argon arc. The opposite tendency is caused by the different properties of argon and helium. The different of thermal conductivity and electrical conductivity in helium and argon lead to different arc behaviors. In addition, different heat fluxes between helium and argon arcs lead to the variation of evaporation rate.

The representative model for explaining the rotation of arc spot is indicated in Fig. 3.42. The unbalanced Lorenz force induced by the curvature of arc column is employed to explain the rotation of arc spot. When the arc is generated between cathode and anode, the arc current passed through the arc column, generating the self-induced magnetic field. As a result of the arc current and the self-induced magnetic field, the Lorenz force is generated. Since the arc column is axisymmetric, the directions of Lorenz force are toward to the central of the arc column, Lorenz forces are balanced. Anode is evaporated by the heat flux from arc column when the arc is generated, forming an evaporation hole on the anode surface. Therefore, the length of arc column increases with increasing the depth of the evaporation hole. And then the anode spot will move to a new position of the anode surface because of the Steenbeck’s minimum principle (Finkelnburg and Maecker 1956). The arc column becomes curved due to the movement of anode spot on the anode surface, which generates unbalanced Lorenz force, because the current density at two sides of the curved arc column is different. When the arc becomes more curved, the unbalanced Lorenz force becomes larger. The cathode spot moves due to the formation of cathode deposit, which generates the curvature of arc column near the cathode. These two unbalanced Lorenz force leads to the rotation of arc spot (Tanaka and Matsumura 2001).

At steady state the Lorentz force and the aerodynamic drag should balance (Szentet et al 1990; Wilson et al 2008). F_d represents the aerodynamic drag force and is represented by the following equation:

$$F_d = 0.5 C_d \rho u^2 d \qquad (1)$$

where, C_d is the coefficient of drag, ρ is the density of the gas through which the discharge moves, u is the discharge's tangential velocity, and d is the diameter of the anode spot. Typical values of C_d are on the order of 1 for a large range of Reynolds numbers (Gangoli et al. 2005). The density of helium is approximately 0.1347 kg m^{-3}; and as shown in the snapshot in Figure 3.24, the typical diameter of arc column is on the order of 1.2 mm. The velocity u can be calculated from the rotational frequency of discharge rotation and the diameter of the circle traced by the anode spot using the following equation:

$$u = \pi f D \qquad (2)$$

where, f is the discharge rotational frequency and D is the diameter of the circle traced. A typical frequency of rotation is 190 Hz, and from visualization, the typical corresponding diameter is 8 mm. From these estimated values and using equation (2), $u \approx 4.8$ ms^{-1}. Using this value in equation (1), a typical value of force is on the order of $\sim 10^{-6}$ N. Therefore, the driving force is also on the order of 10^{-6} N.

3.3.3 Formation Mechanism of Different Arc-Anode Attachment Modes

The arc-anode attachment mode is the competition of the cathode jet and the anode jet (Sanders et al. 1982). Strong cathode jet results in the formation of diffuse attachment mode, while strong anode jet leads to the constricted attachment mode. The transition between diffuse attachment and constricted attachment is the multiple attachments. The schematic illustration for the formation of different anode attachment modes is shown in Fig. 3.43. The formation mechanism of different arc-anode attachment in carbon electrode is similar to that of metal electrode in chapter 2. As discussed in chapter 2, the evaporation of anode material plays an important role in the formation of different arc-anode attachment modes. In this section, the arc current and electrode gap distance as two main factors are discussed to explain the formation of different attachment modes in helium arc.

Firstly, the effect of arc current on the formation of different attachment modes is explained at the same electrode gap distance. The cathode jet intensity increases with increasing arc current, on the other hand, the intensity of anode jet increases with increasing the arc current due to the large anode evaporation rate. The relative intensity of cathode jet to anode jet should be compared to explain the formation of different attachment modes. When the electrode gap distance is fixed at 3 mm, the cathode jet is significantly week at low arc currents of 100 and 150 A. The evaporation of anode will generate a relatively strong anode jet. Therefore, the multiple attachments are generated at arc currents of 100 and 150 A. However, the cathode jet is dominated when the arc current is over than 150 A, because the effect of anode jet (evaporation of anode) is weak when the arc current increases from 150 to 200 A. In this case, the increase of input power could not affect the anode jet (evaporation of anode) significantly because of the high sublimation temperature of graphite. Consequently, the attachment transitions from multiple to diffuse when increasing the arc current at the fixed electrode gap distance of 3 mm. The same reason can be used to explain the formation of arc-anode attachment in argon arc. Since graphite has high sublimation temperature, the evaporation rate of anode in carbon anode is lower than that of nickel anode. As a result, constricted mode is difficult to form in the case of carbon electrode.

In addition, the formation of different arc-abode attachment modes is explained by changing electrode gap distance at the same arc current. Large electrode gap distance leads to large input power, which enhances the intensity of anode jet by increasing the evaporation rate of anode material. Meanwhile, the intensity of cathode jet becomes weak with increasing electrode gap distance. These two reasons lead to the transition of attachment mode from diffuse mode to multiple mode by increasing electrode gap distance, since the arc-anode attachment mode is the competition of cathode jet and anode jet. Multiple attachments are formed at electrode gap distance of 5 mm, because the cathode jet is weak and the anode jet is strong. And then cathode jet become stronger and anode jet become weaker at the electrode gap distance of 1 mm, forming diffuse attachment.

3.4. Conclusion

Multiple and diffuse arc-anode attachment modes were observed in helium and argon arcs. Arc-anode attachment mode transformed from diffuse mode into multiple mode in helium arc when increasing the electrode gap distance. Contrastingly, the attachment mode changed from multiple mode into the diffuse mode in argon arc by increasing electrode gap distance. In addition, low arc current led to the formation of multiple mode in helium arc. Contrastingly, all of attachments were diffuses modes in argon arc when changing arc current at the fixed electrode gap distance.

The arc spot has the frequency around 10 kHz in multiple attachment mode for helium and argon arcs. However, the arc spot moved with a constant frequency in the diffuse attachment mode of helium arc. In contrast, no significant rotation of arc spot was seen in diffuse attachment of argon arc due to the relatively stable arc.

The temperature of carbon electrode was successfully measured by using two-color pyrometry. The highest temperature in helium arc is higher than that of argon arc, although the input power in argon arc is higher than that of helium arc. The main reasons are the constriction of helium arc and large thermal conductivity of helium. In particular, the temperature behavior is decided by arc-anode attachment mode. The heat flux is low in diffuse attachment when the input power is same. Arc-anode attachment mode and temperature behavior in carbon electrode provide a new way to investigate the formation mechanism of carbon material by DC arc discharge method.

References

Boulos, M. I., P. Fauchais and E. Pfender (1994). Thermal Plasmas: Fundamentals and Applications. New York, Plenum Press.

Collares M. P. and E. Pfender. “Effect of current connection to the anode nozzle on plasma torch efficiency.” *IEEE Transactions on Plasma Science* **25**(5), 864-871 (1997).

Dinulescu H. A. and E. Pfender. “Analysis of the anode boundary layer of high intensity arcs.” *Journal of Applied Physics* **51**(6), 3149-3157 (1980).

Finkelnburg W. and H. Maecker 1956 Electric arcs and thermal plasmas *Encyclopedia of Physics* vol XXII (Berlin:Springer)

Gangoli S., A. Gutsol and A. Fridman. “Rotating non-equilibrium gliding arc plasma disc for enhancement in ignition and combustion of hydrocarbon fuels” *17th International. Symposium on Plasma Chemistry (Toronto)*Abstracts and Full-Paper CD, 1042-1043 (2005).

Heberlein J. V., J. Mental and E. Pfender. “The anode region of electric arcs: a survey.” *Journal of Physics D: Applied Physics* **43,** 023001 (2010).

Iijima S. “Helical microtubules of graphitic carbon.” *Nature* **354**, 56-58 (1991).

Keidar M., I Levchenko, T. Arbel, M. Alexander, A. M. Waas and K. Ostrikov. “Increasing the length of single-wall carbon nanotubes in a magnetically enhanced arc discharge.” *Applied Physics Letters* **92**, 043129 (2008).

Keidar M., A. Shashurin, J. Li, O. Volotskova, M. Kundrapu and T. Zhuan. “Arc plasma synthesis of carbon nanostructures: where is the frontier?” *Journal of Physics D: Applied Physics* **44,** 174006 (2011).

Krätschmer W., L. Lamb, K. Fostiropoulos and D.R. Huffman. “Solid C_{60}: a new form of carbon.” *Nature* **347**, 354-358 (1990).

Murphy A. B., M. Tanaka, S. Tashiro, T. Sato and J. J. Lowke. “A computational investigation of the effectiveness of different shielding gas mixtures for arc welding.” *Journal of Physics D: Applied Physics* **42,** 115205 (2009).

Sanders N., K. Etemadi, K. C. Hsu and E. Pfender. “Studies of the anode region of a high-intensity argon arc. ”*Journal of Applied Physics* **53**(6), 4136-4145 (1982).

Subrahmanyam K. S., L. S. Panchakarla, A. Govindaraj and C. N. R. Rao. “Simple method of preparing graphene flakes by an arc-discharge method.” *Journal of Physical Chemistry C* **113**(11), 4257-4259 (2009).

Szentet R. N., R. J Munzt and M. G. Droue. “The influence of the cathode surface on the movement of magnetically driven electric arcs.” *Journal of Physics D: Applied Physics* **23,** 1193-1200 (1990).

Tanaka, S and T. Matsumura. “Characteristic dynamic behavior of dc arc near graphite bar electrodes with short gap.” *Journal of Applied Physics* **89**, 4247-4254 (2001).

Wilson A., D. Staack, T. Farouk, A. Gutsol, A. Fridman and B. Farouk “Self-rotating dc atmospheric-pressure discharge over a water-surface electrode: regimes of operation” *Plasma Sources Science and Technology* **17**, 045001 (2008).

Yang G., J. V. Heberlein and E. Pfender. “Experimental investigations of the anode boundary layer in high intensity arcs with cross flow.” *Journal of Physics D: Applied Physics* **39**, 2764 (2006).

Yang G. and J. V. Heberlein. “Anode attachment modes and their formation in a high intensity argon arc.” *Plasma Sources Science and Technology* **16**, 529-542 (2007).

Table 3.1 Experimental conditions

Arc current [A]	100-200
Electrode gap distance [mm]	1, 3, 5
Arc voltage [V]	30-40
Pressure [kPa]	101.3 (Atmospheric pressure)
Plasma gas	Helium and Argon
Diameter of cathode [mm]	6
Diameter of anode [mm]	30
Discharge time [min]	5-10
Cathode	Graphite
Anode	Graphite

Table 3.2 Evaporation rates of cathode and anode when changing electrode gap distance at 200 A in argon arc

Electrode gap distance [mm]	Cathode evaporation rate [mg/min]	Anode evaporation rate [mg/min]
1	12.8	2.3
3	8.2	3.1
5	3.9	4.4

Table 3.3 Input powers in helium arc when changing arc current

Arc current [A]	100	150	200
Electrode gap distance [mm]	3	3	3
Arc voltage [V]	22.8	22.7	22.1
Input power [W]	2280	3405	4420

Table 3.4 Input powers in helium arc when changing electrode gap distance

Electrode gap distance [mm]	1	3	5
Arc current [A]	200	200	200
Arc voltage [V]	19.6	22.1	25.8
Input power [W]	3920	4420	5160

Table 3.5 Input powers in argon arc when changing arc current

Arc current [A]	100	150	200
Electrode gap distance [mm]	3	3	3
Arc voltage [V]	15.2	16.5	16.9
Input power [W]	1520	2475	3380

Table 3.6 Input powers in argon arc when changing electrode gap distance

Electrode gap distance [mm]	1	3	5
Arc current [A]	200	200	200
Arc voltage [V]	16.0	16.9	18.7
Input power [W]	3200	3380	3740

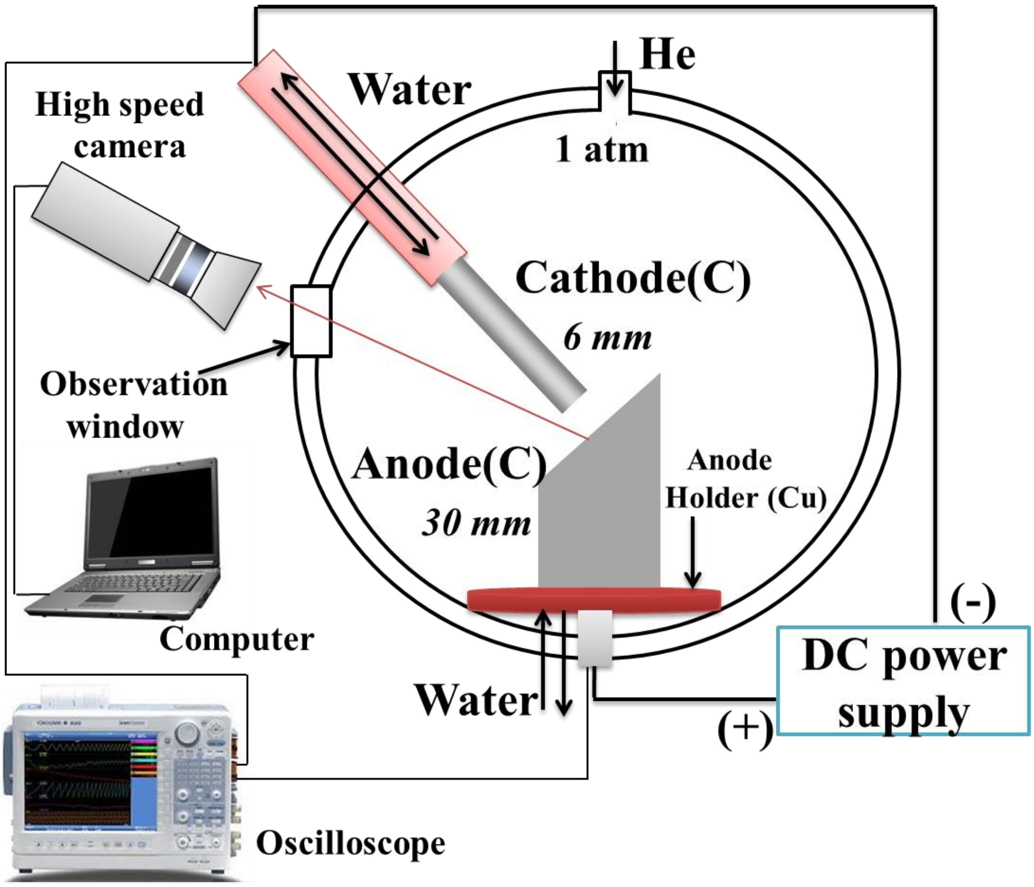

Fig. 3.1 Schematic diagram of an arc discharge system for the preparation of carbon nanomaterials by DC arc discharge method.

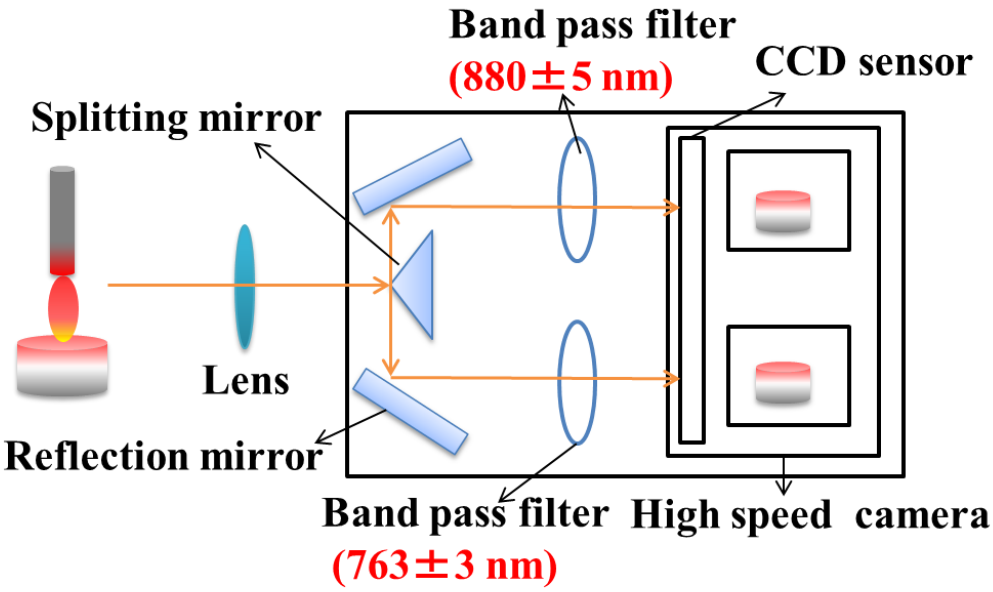

Fig. 3.2 Schematic illustration of temperature measurement system by two-color pyrometry.

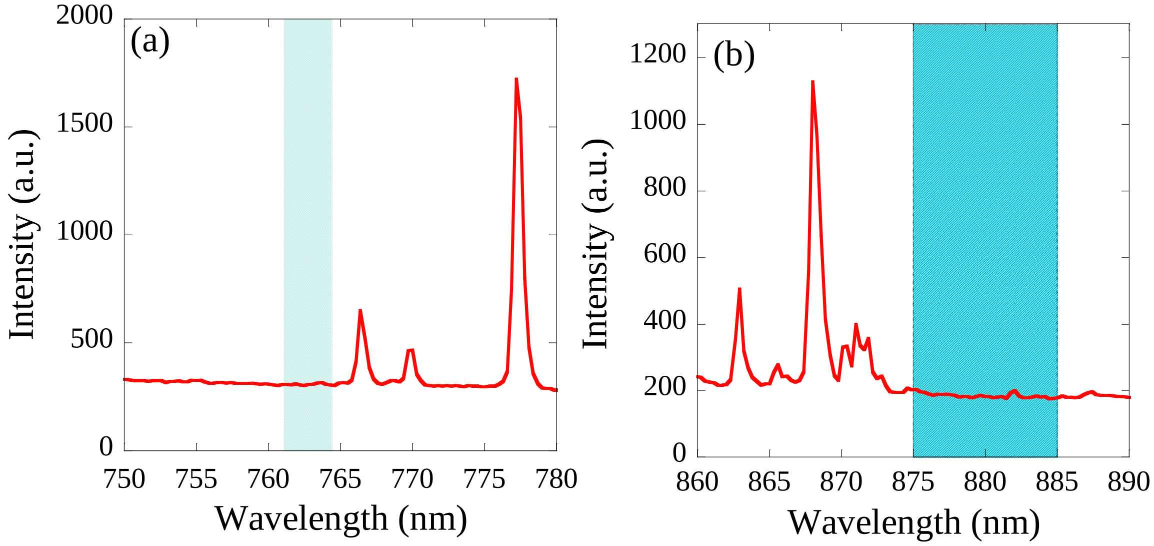

Fig. 3.3 Optical emission spectra of helium arc at different wavelengths. The shadow region indicates the wavelength of band-pass filter: (a) 763±3 nm, (b) 880±5 nm.

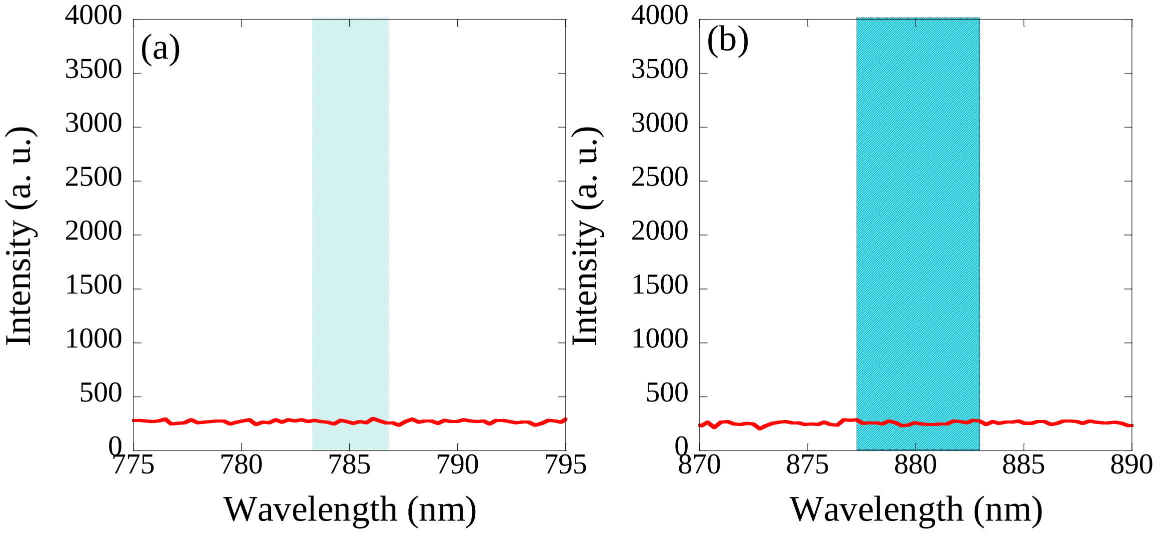

Fig. 3.4 Optical emission spectra of argon arc at different wavelengths. The shadow region indicates the wavelength of band-pass filter: (a) 785±1.5 nm, (b) 880±2.5 nm.

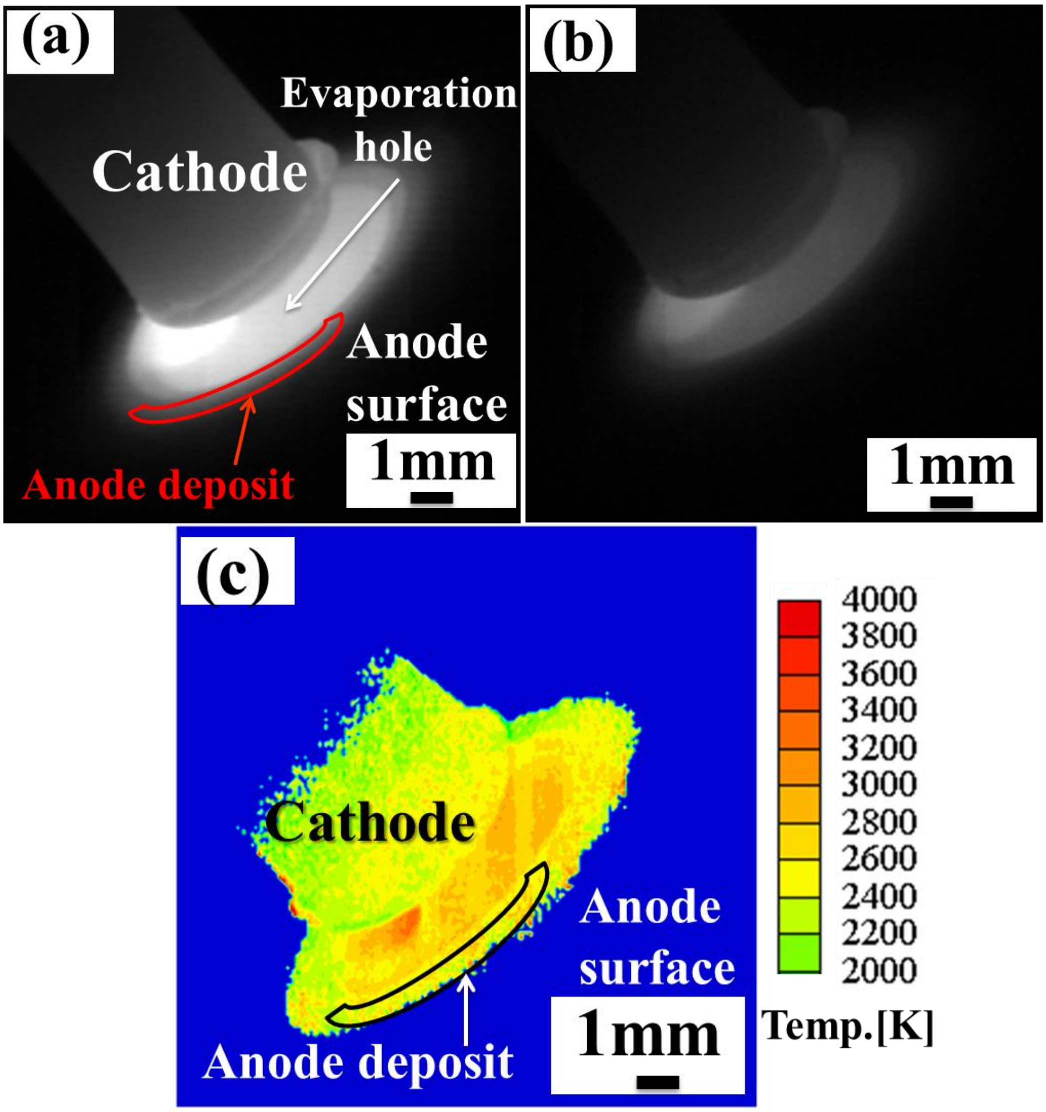

Fig. 3.5 Images of the electrode at the wavelength of (a) 880±5 nm and (b) 763±3 nm recorded by the high-speed camera, and (c) a corresponding temperature distribution map calculated by Plank’s law based on radiation intensity from images (a) and (b).

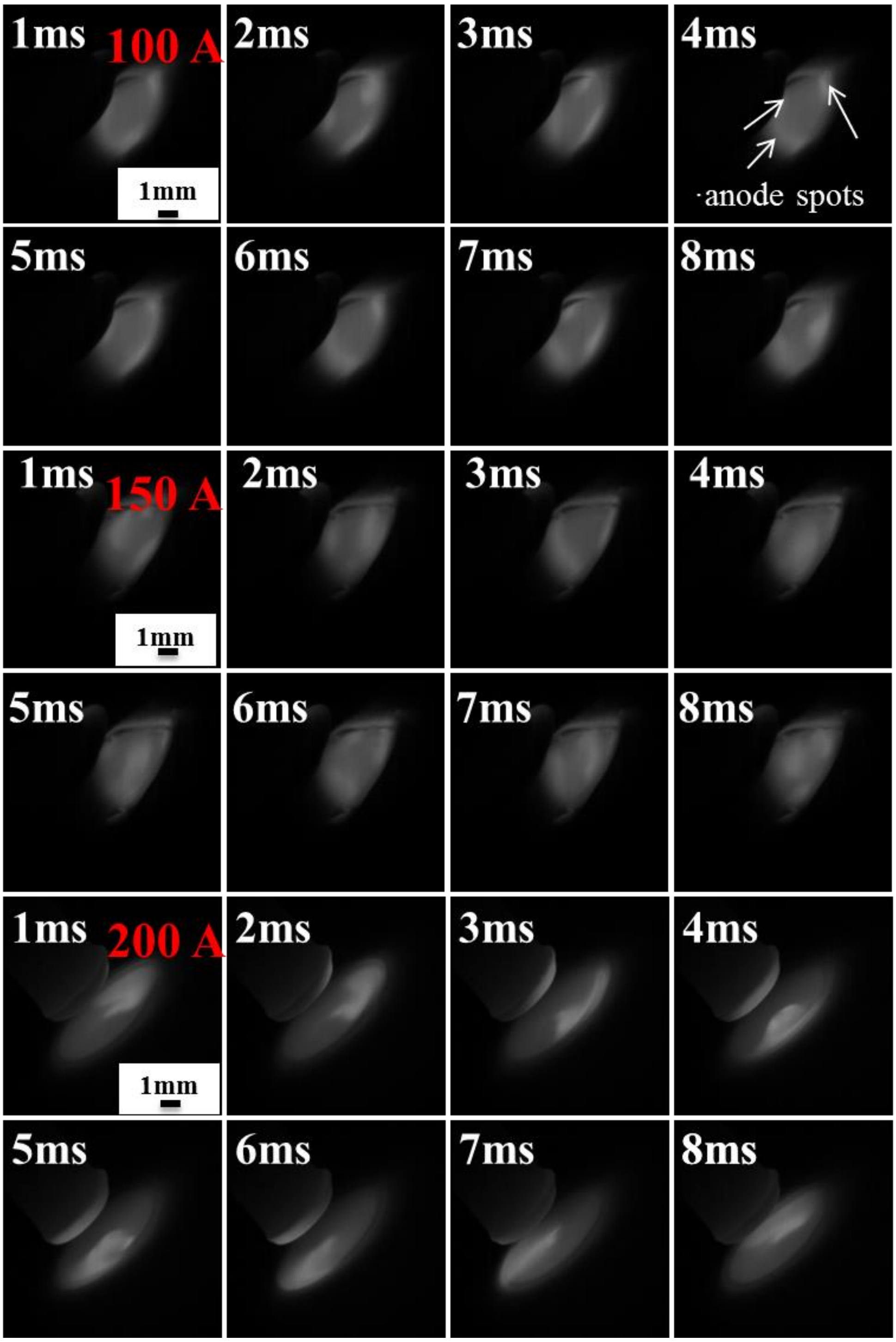

Fig. 3.6 Representative snapshots of high-speed camera for helium arc at different arc currents when the electrode gap distance is fixed at 3 mm.

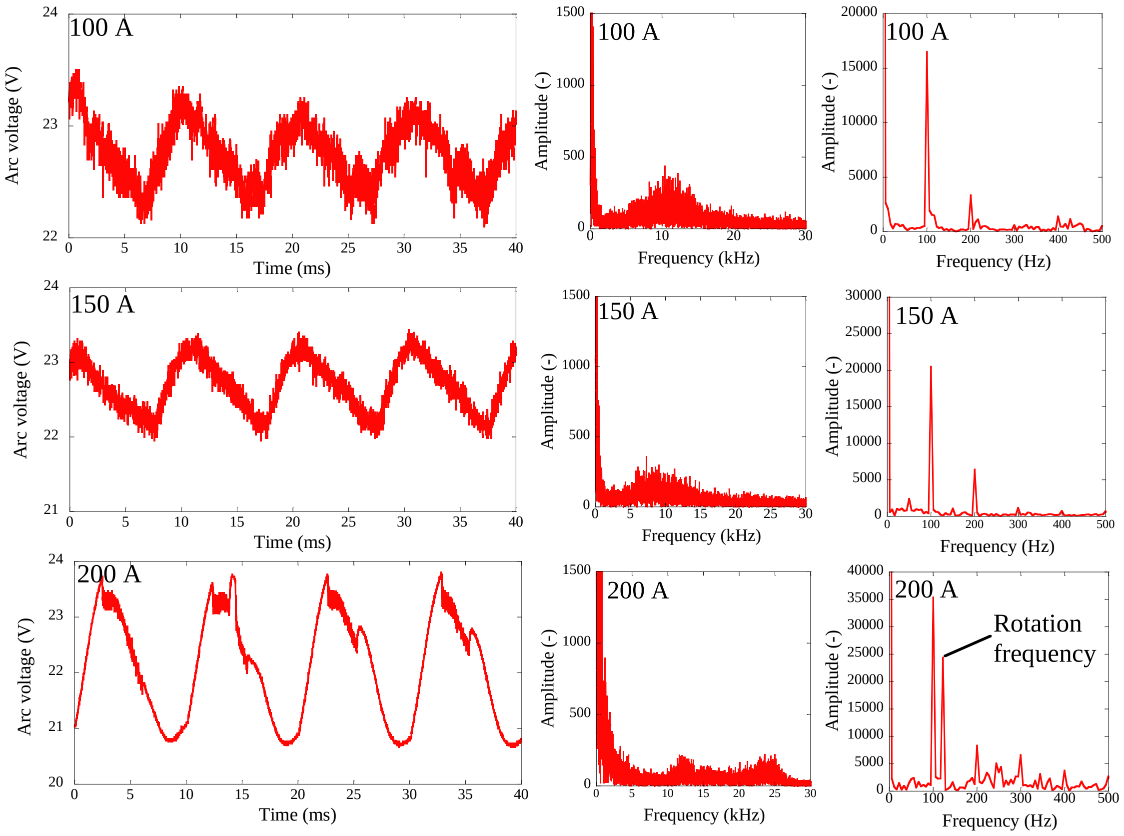

Fig. 3.7 Voltage waveform of helium plasma at different arc currents: 100, 150, and 200 A when the electrode gap distance is fixed at 3 mm. The corresponding FFT spectra of voltage waveform at different frequency ranges.

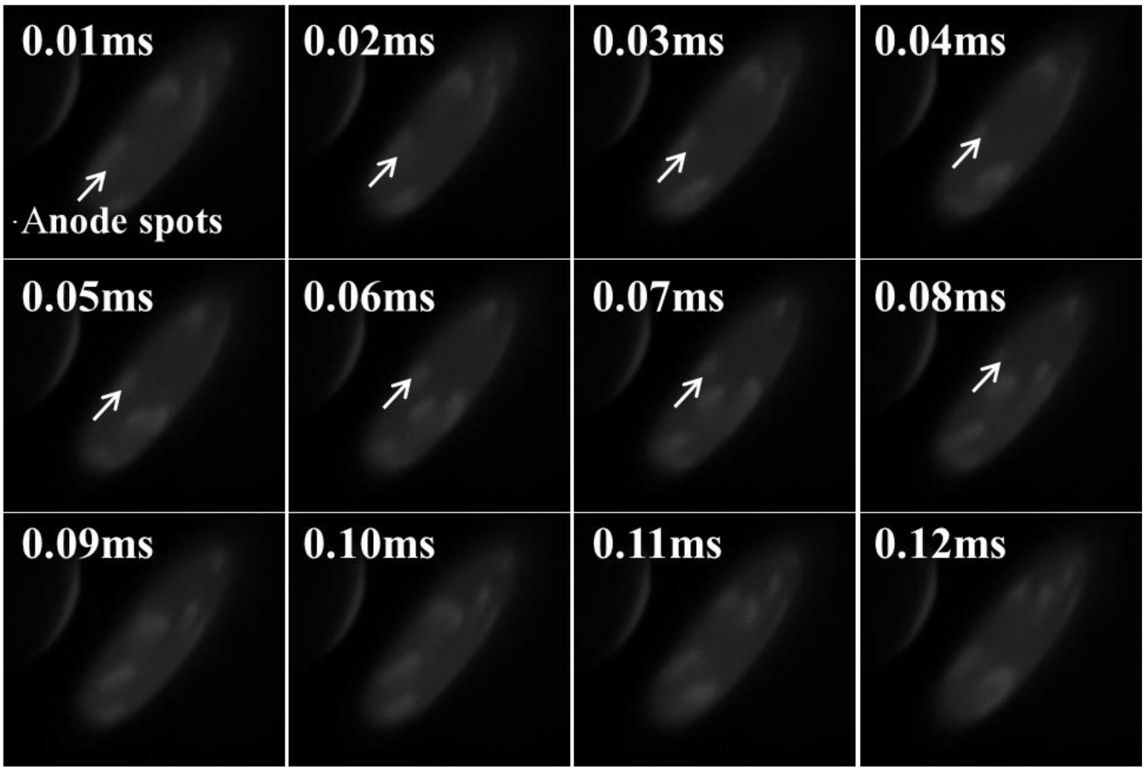

Fig. 3.8 Representative snapshots of high-speed camera for helium arc at short exposure time of 0.37 μm.

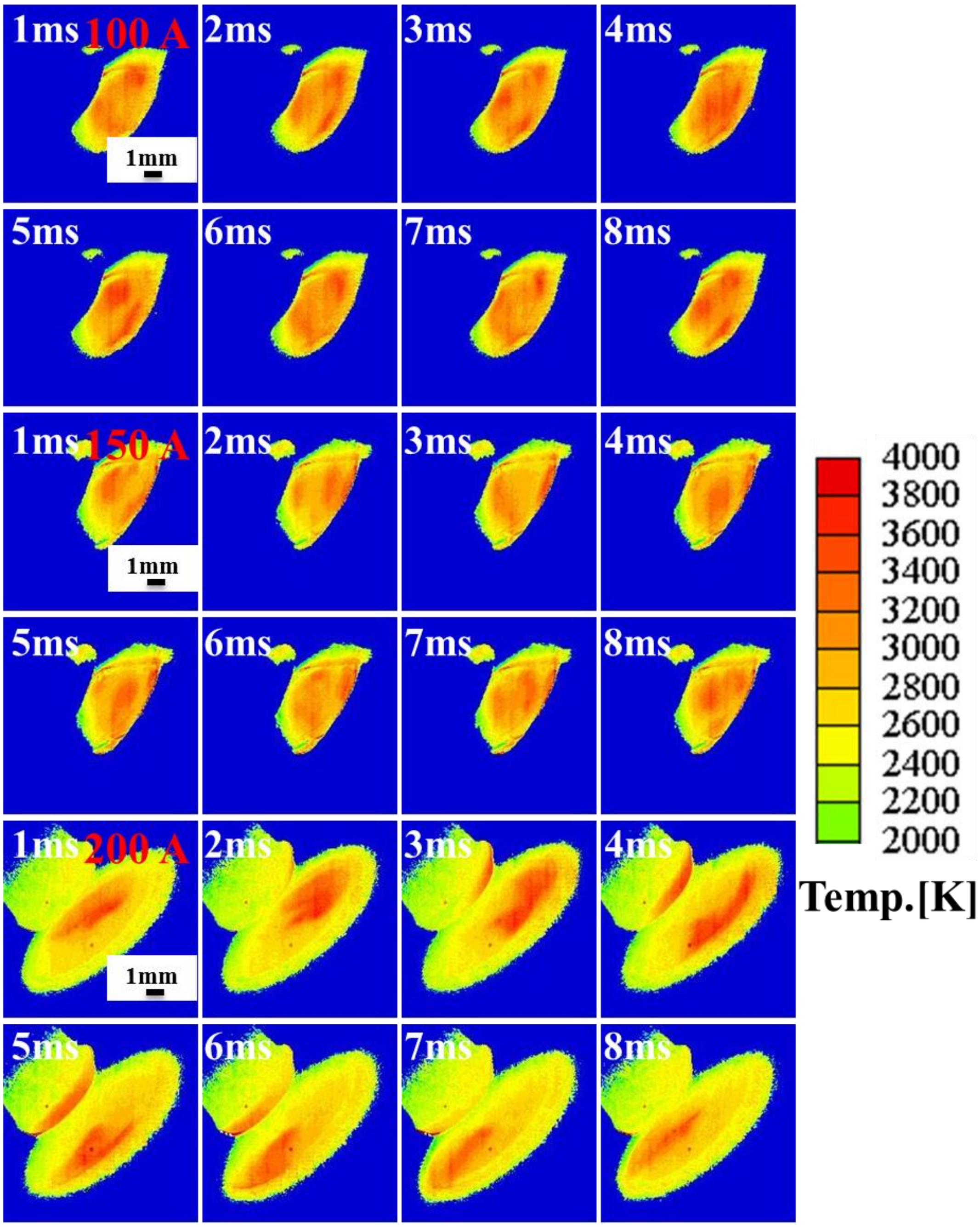

Fig. 3.9 Snapshots of temperature distribution map according to time in helium arc at different arc currents when the electrode gap distance is fixed at 3 mm.

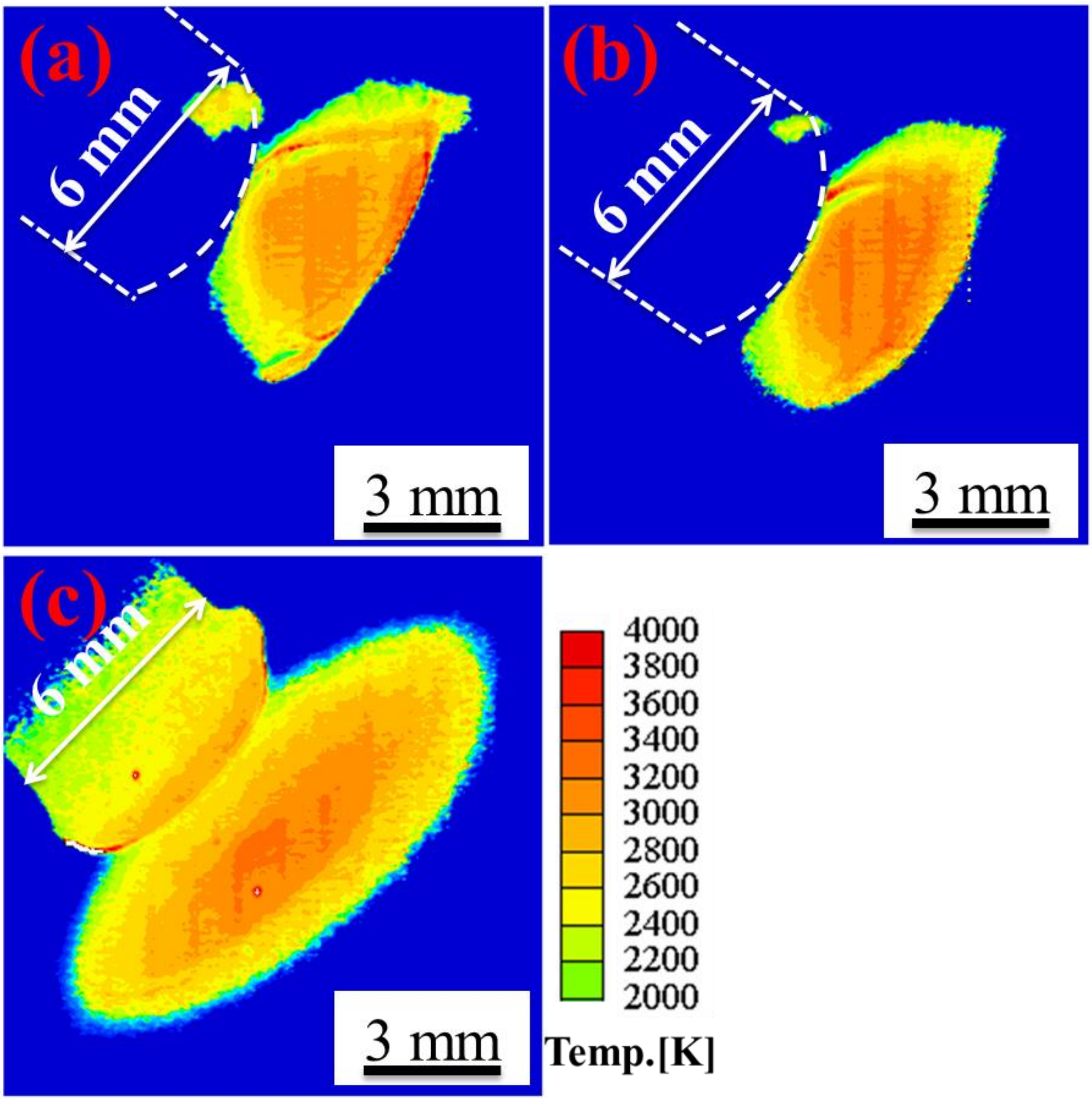

Fig. 3.10 Time average temperature distribution map in helium arc at different arc currents when the electrode gap distance is fixed at 3 mm. (a), (b), and (c) corresponding to the arc current of 100, 150, and 200 A, respectively.

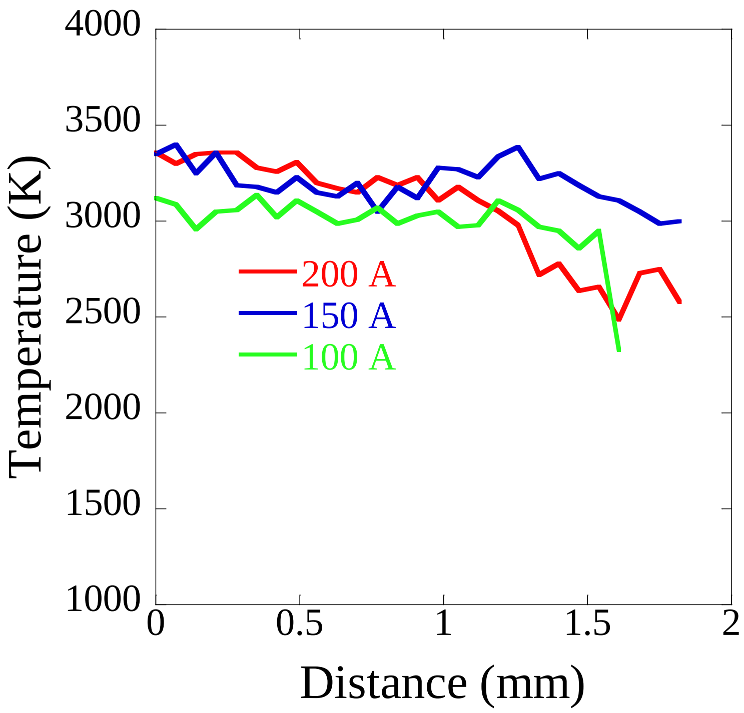

Fig. 3.11 Radical temperature distribution from the central to the edge of anode surface in helium arc when changing the arc current.

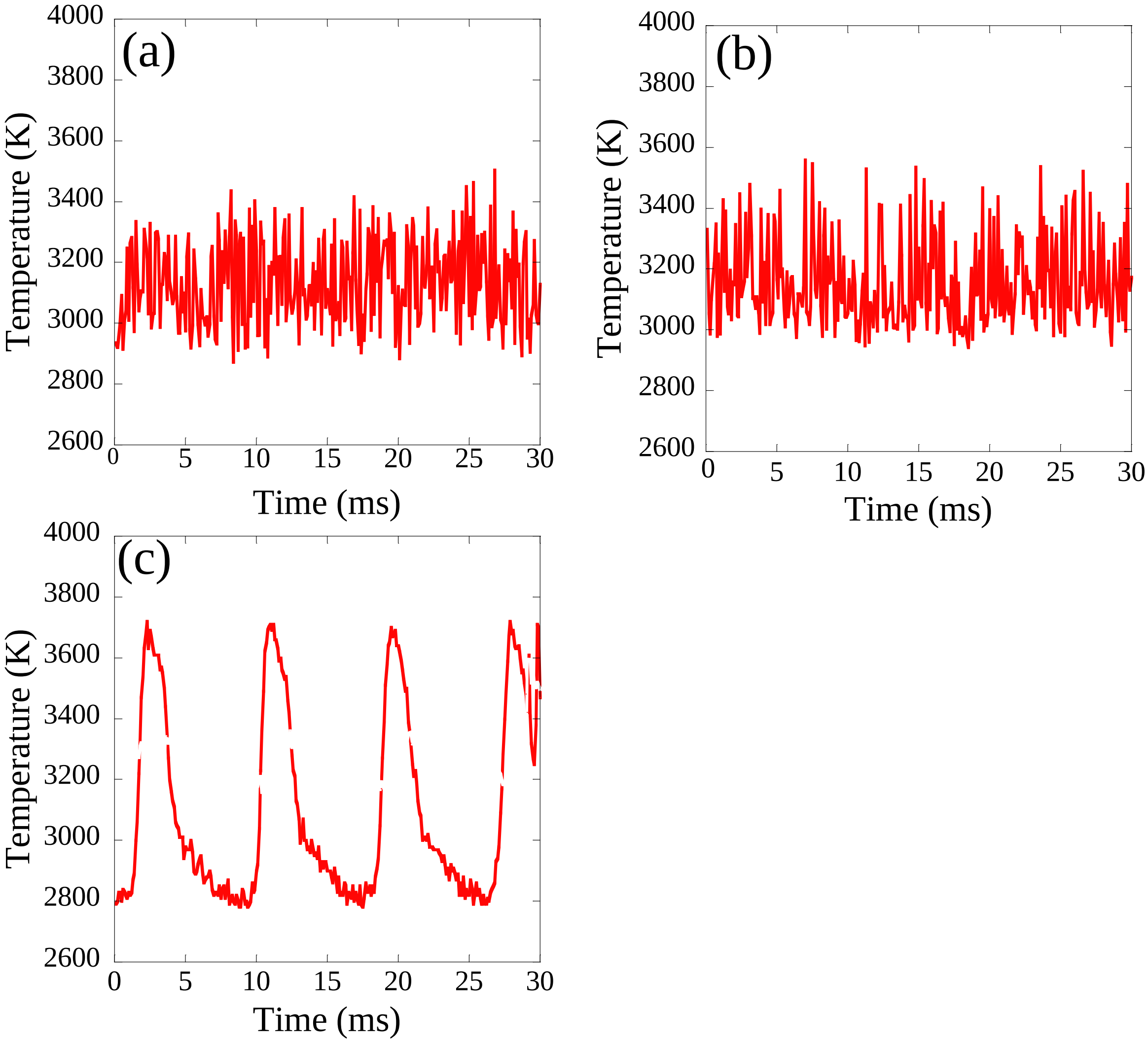

Fig. 3.12 Temperature variation of anode surface with the time in helium arc at different arc currents when the electrode gap distance is fixed at 3 mm. (a), (b), and (c) corresponding to the arc current of 100, 150, and 200 A, respectively.

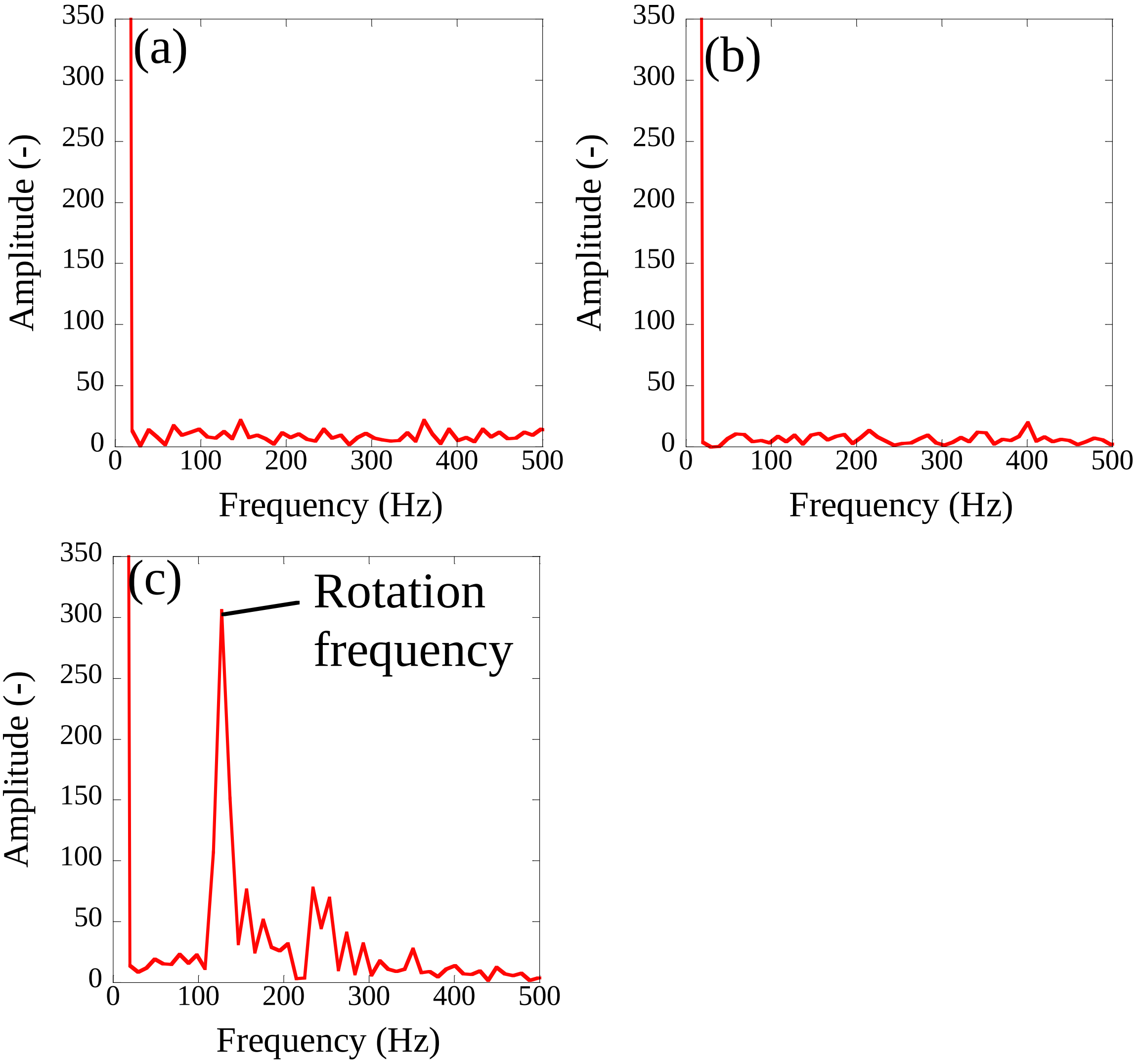

Fig. 3.13 The FFT spectra of anode temperature in helium arc at different arc currents when the electrode gap distance is fixed at 3 mm. (a), (b), and (c) corresponding to the arc current of 100, 150, and 200 A, respectively.

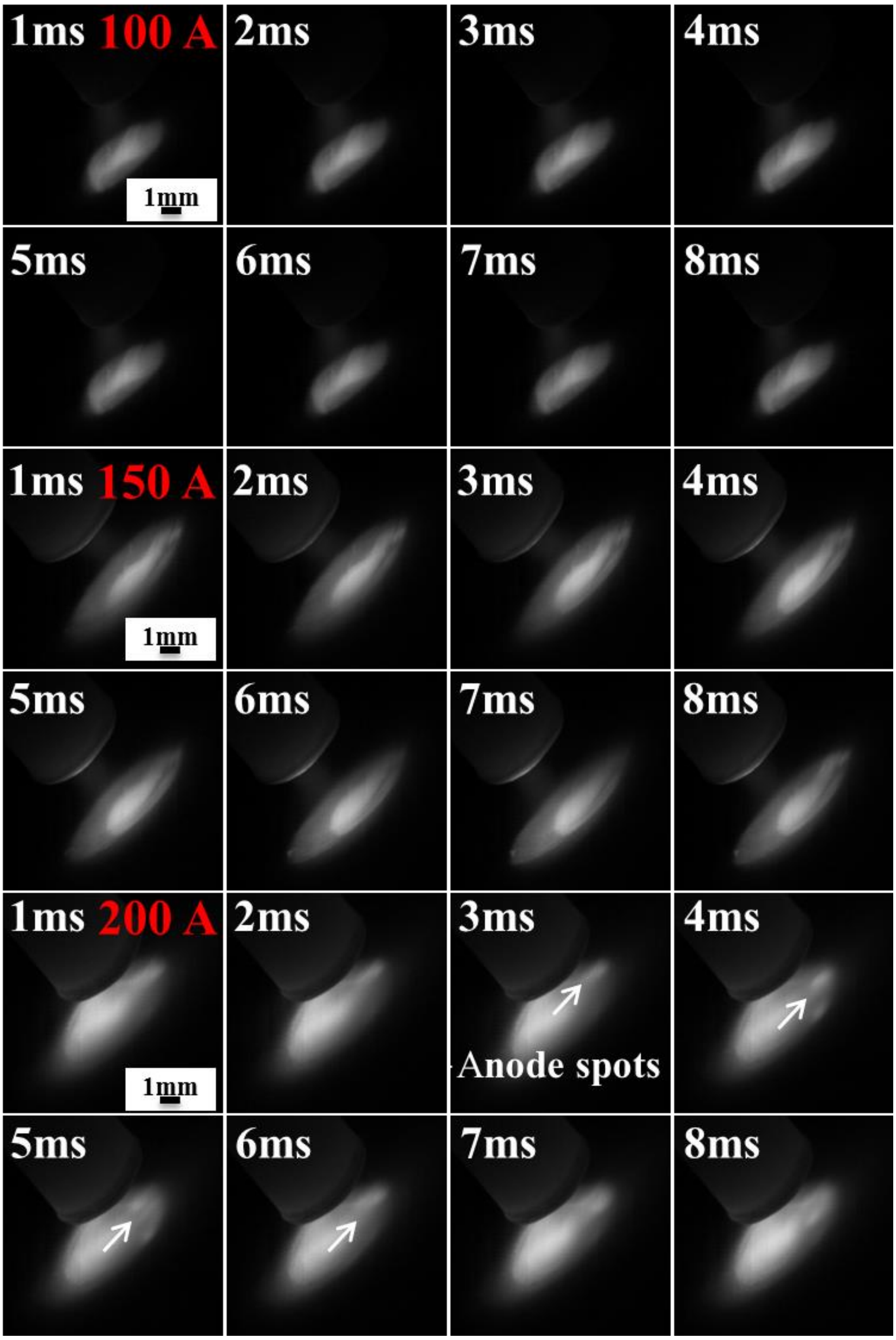

Fig. 3.14 Representative snapshots of high-speed camera for argon arc at different arc currents when electrode gap distance is fixed at 3 mm.

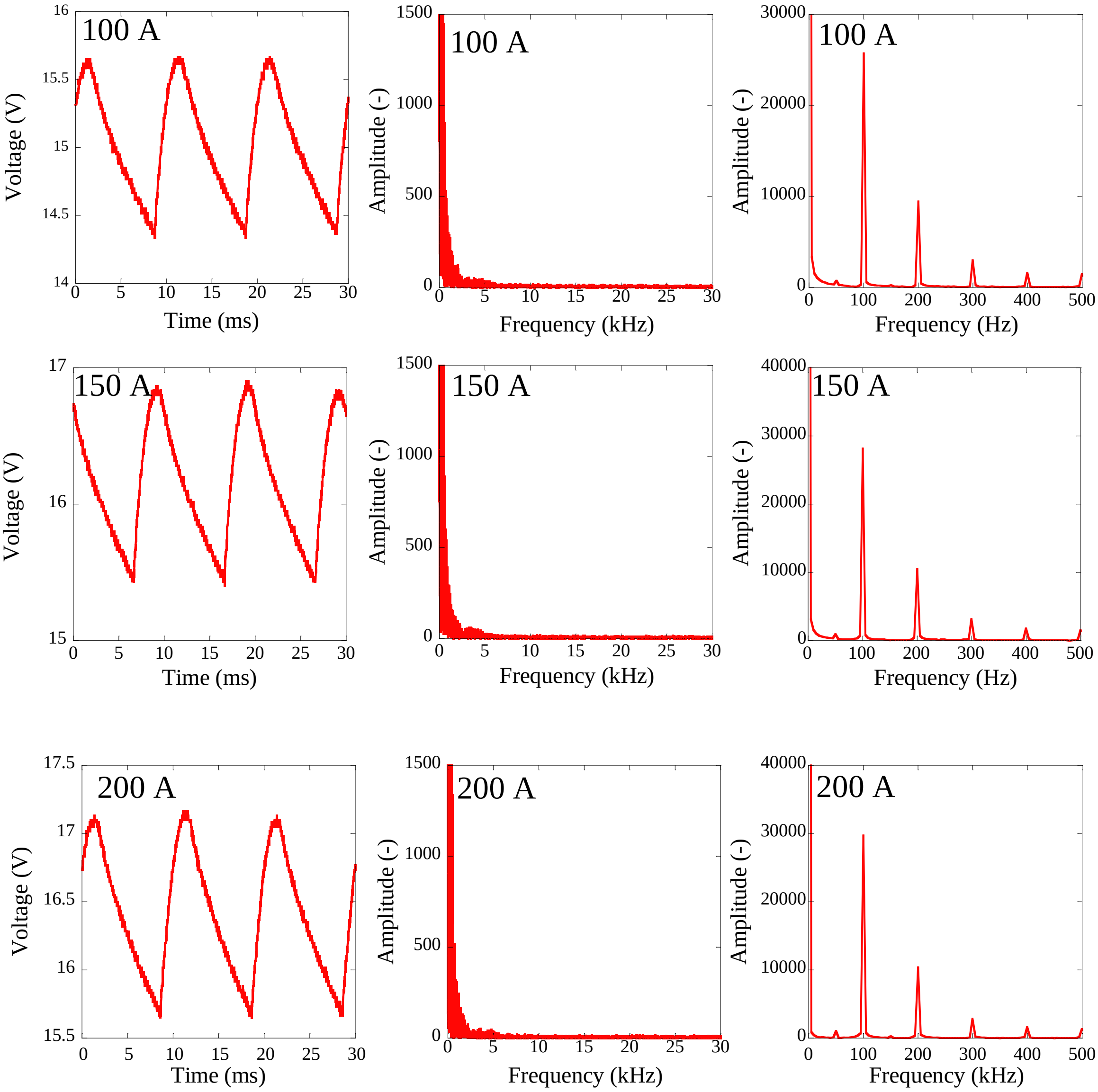

Fig. 3.15 Voltage waveform of argon arc at different arc currents: 100, 150, and 200 A when the electrode gap distance is fixed at 3 mm. The corresponding FFT spectra of voltage waveform at different frequency ranges.

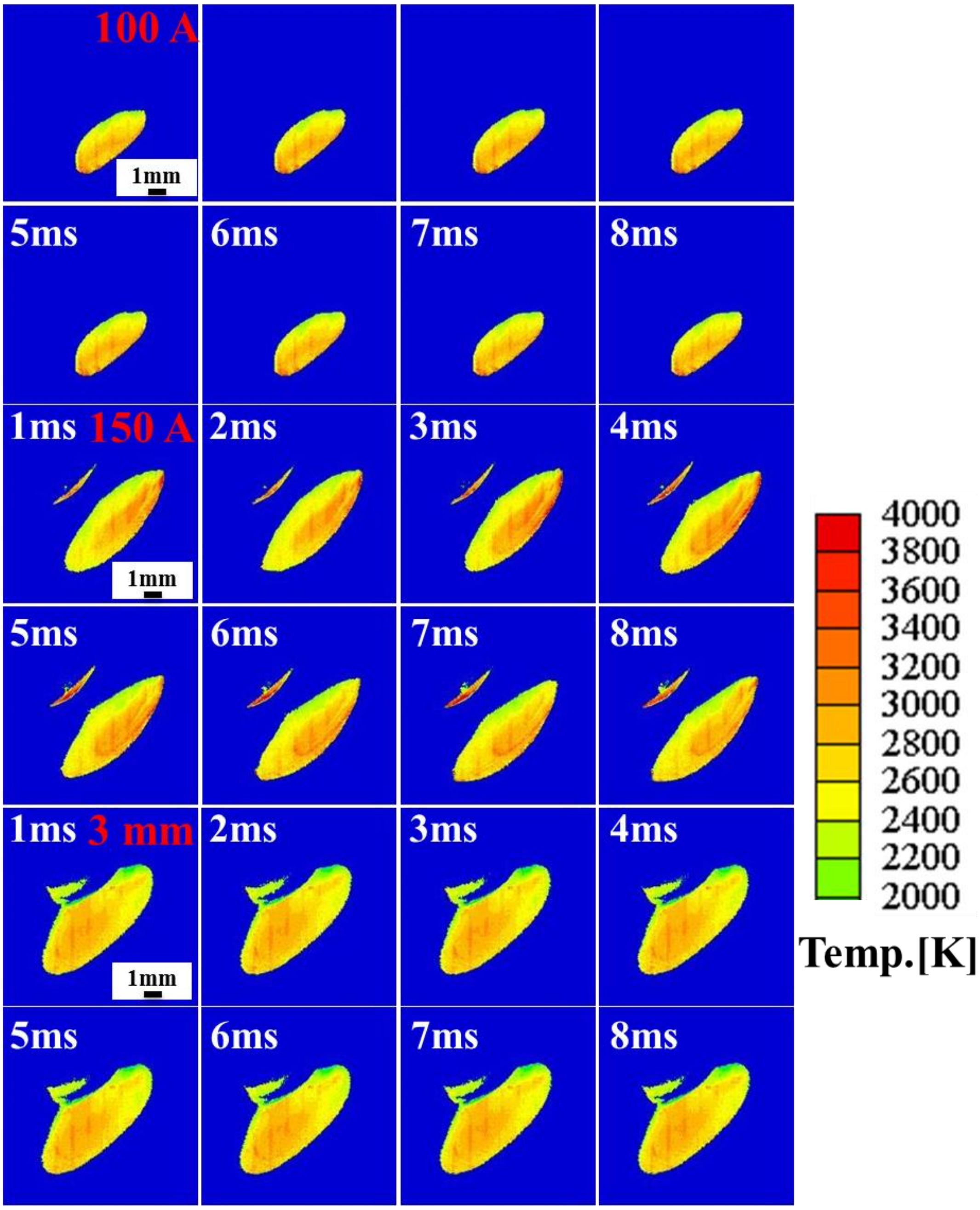

Fig. 3.16 Snapshots of temperature distribution map according to time in argon arc at different arc currents when the electrode gap distance is fixed at 3 mm.

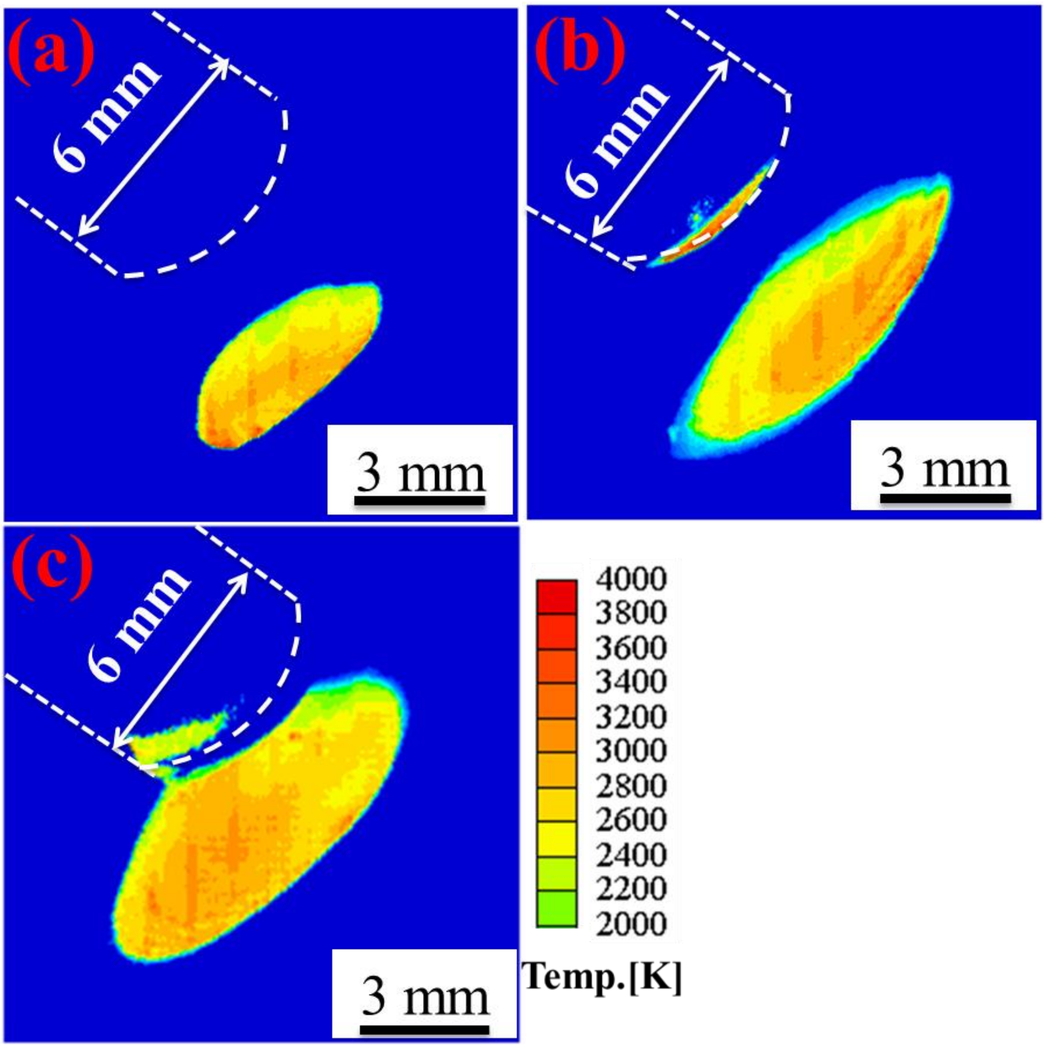

Fig. 3.17 Time average temperature distribution map in argon arc at different arc currents when the electrode gap distance is fixed at 3 mm. (a), (b), and (c) corresponding to the arc current of 100, 150, and 200 A, respectively.

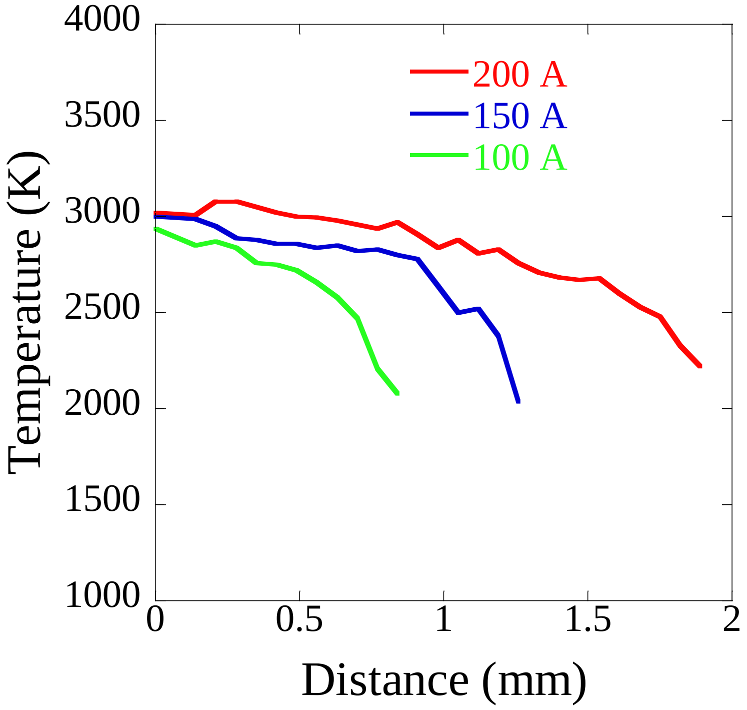

Fig. 3.18 Radical temperature distribution from the central to the edge of anode surface in argon arc when changing arc current.

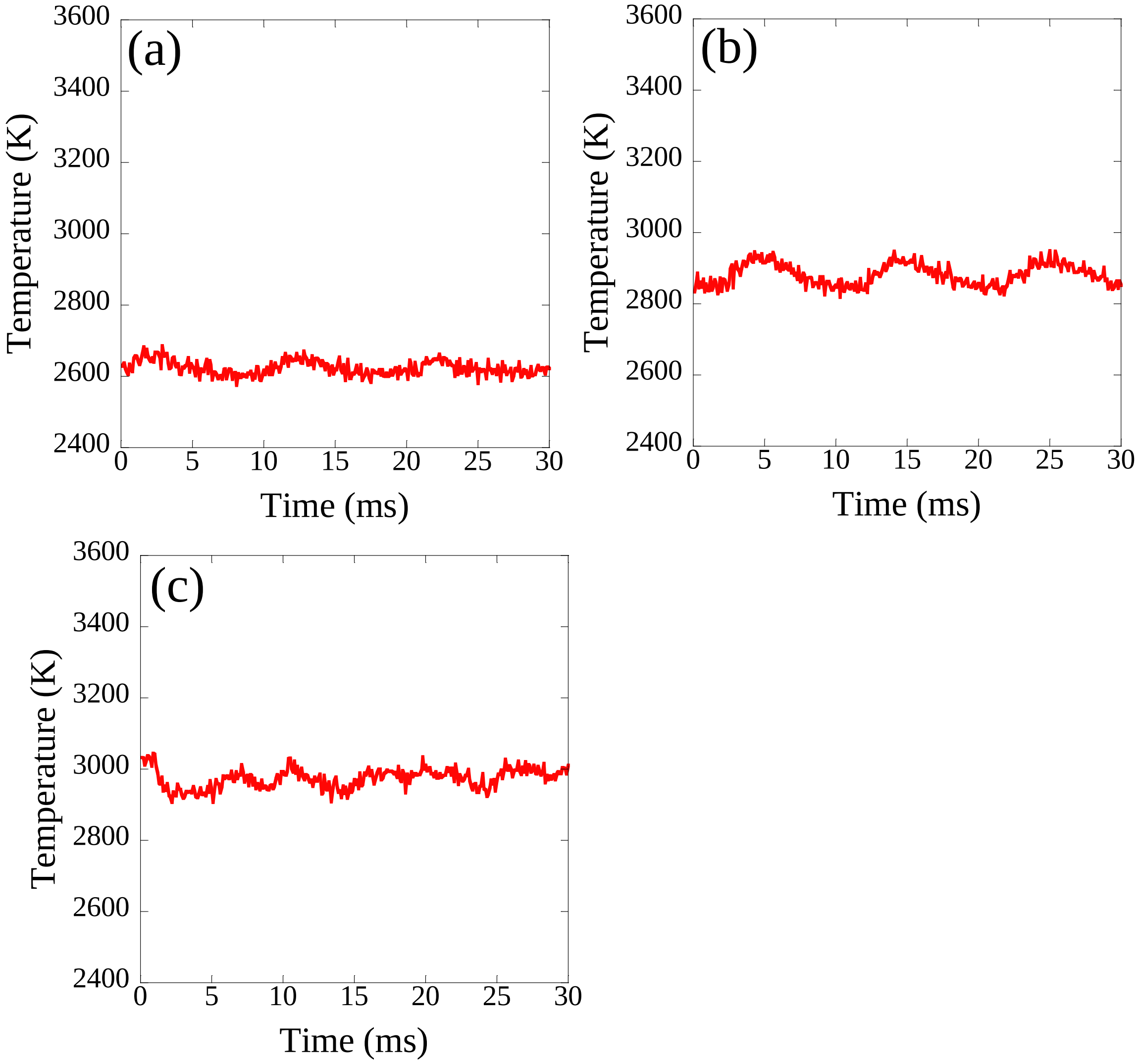

Fig. 3.19 Temperature variation of anode surface with the time in argon arc at different arc currents when the electrode gap distance is fixed at 3 mm. (a), (b), and (c) corresponding to the arc current of 100, 150, and 200 A, respectively.

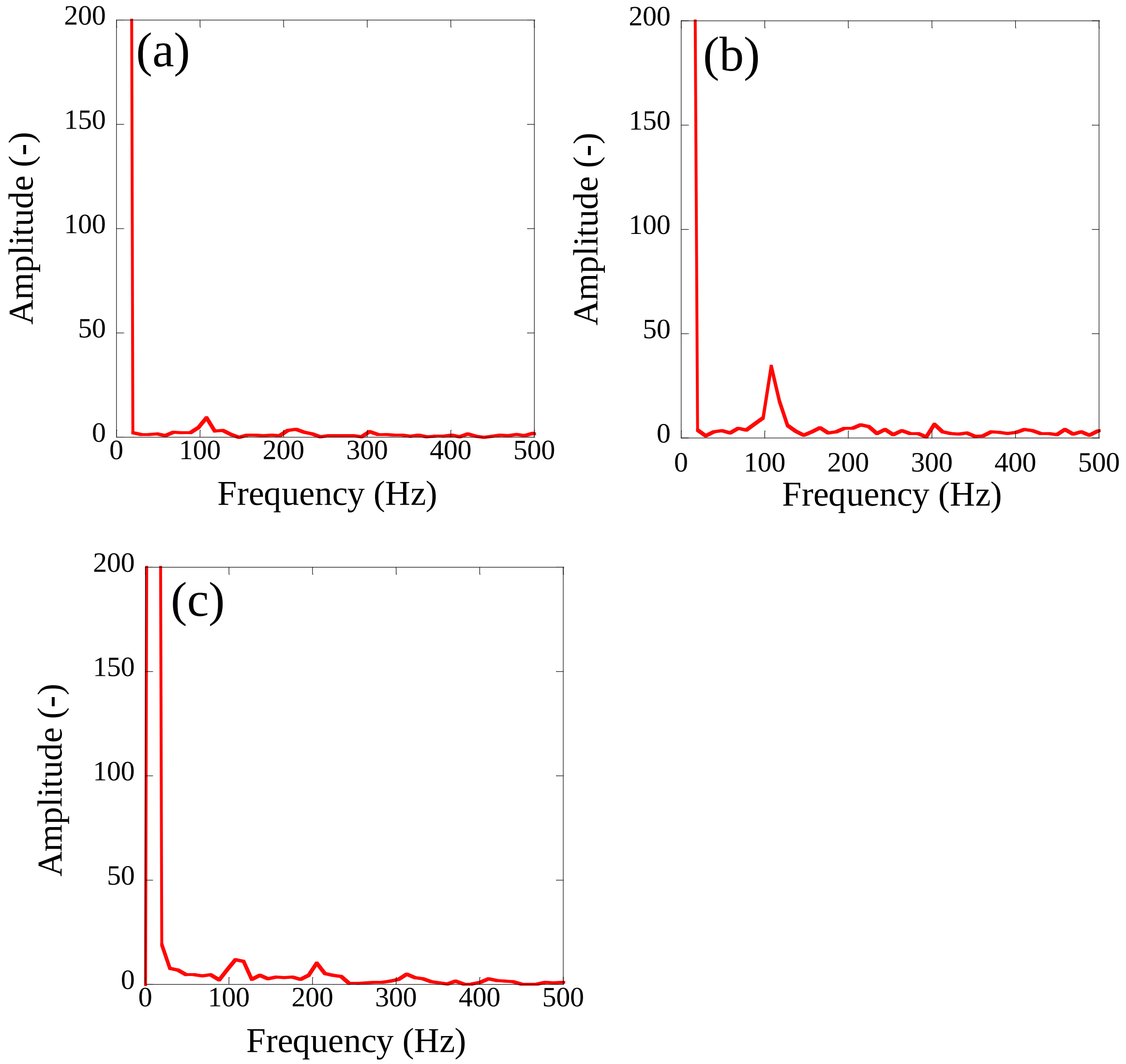

Fig. 3.20 The FFT spectra of anode temperature in argon arc at different arc currents when the electrode gap distance is fixed at 3 mm. (a), (b), and (c) corresponding to the arc current of 100, 150, 200 A, respectively.

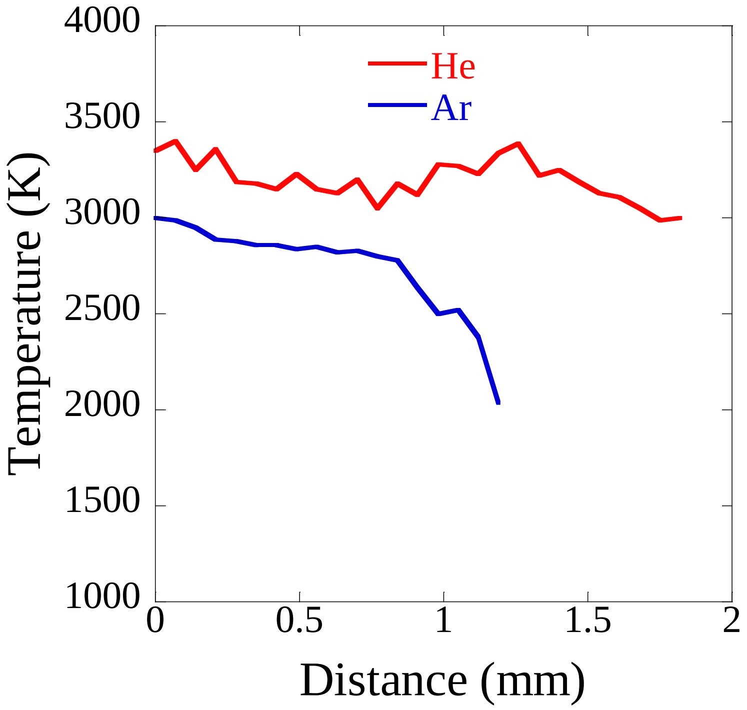

Fig. 3.21 Comparison of the radical temperature distribution between helium and argon arc when the arc current is 150 A, and the electrode gap distance is 3 mm.

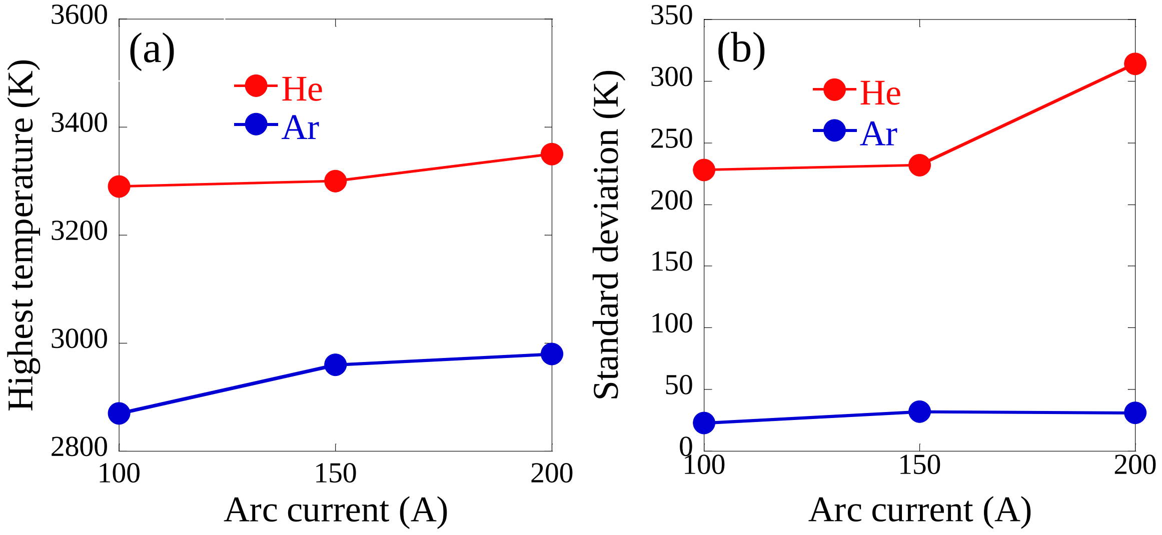

Fig. 3.22 Comparison of the highest temperature (a), standard deviation of temperature variation (b) between helium arc and argon arc when changing arc current.

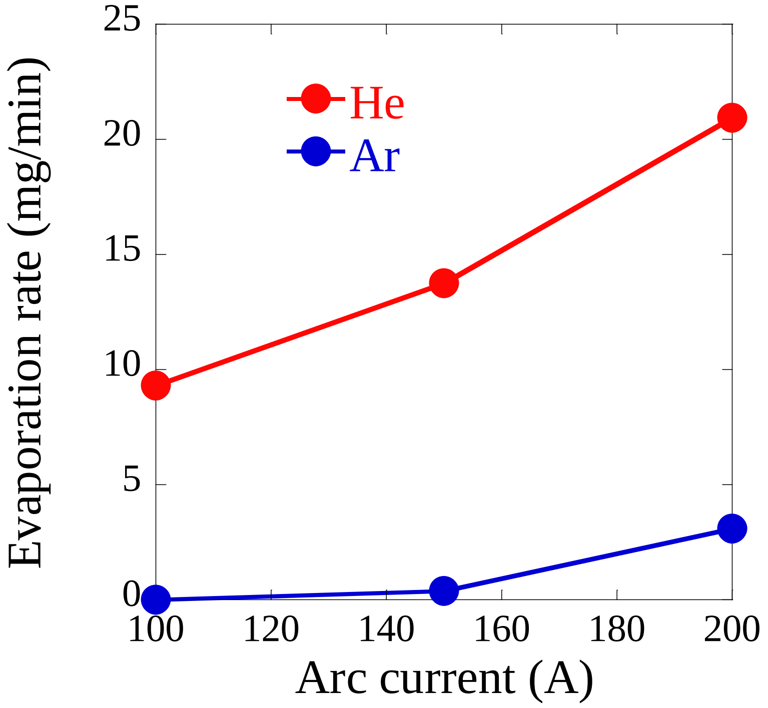

Fig. 3.23 Comparison of the evaporation rate of anode between helium and argon by changing the arc current when the electrode gap distance is fixed at 3 mm.

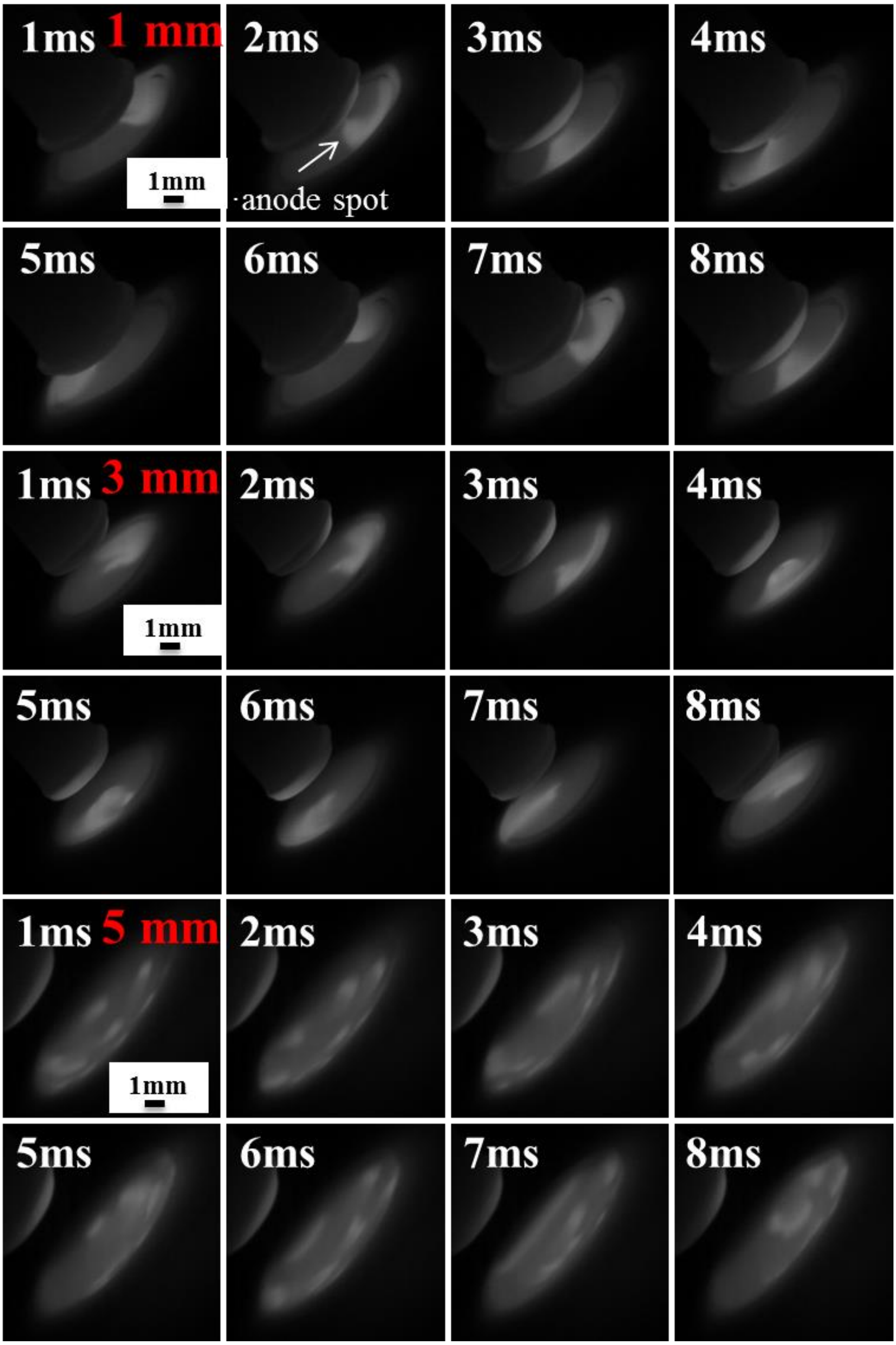

Fig. 3.24 Representative snapshots of high-speed camera for helium arc at different electrode gap distances when the arc current is fixed at 200 A.

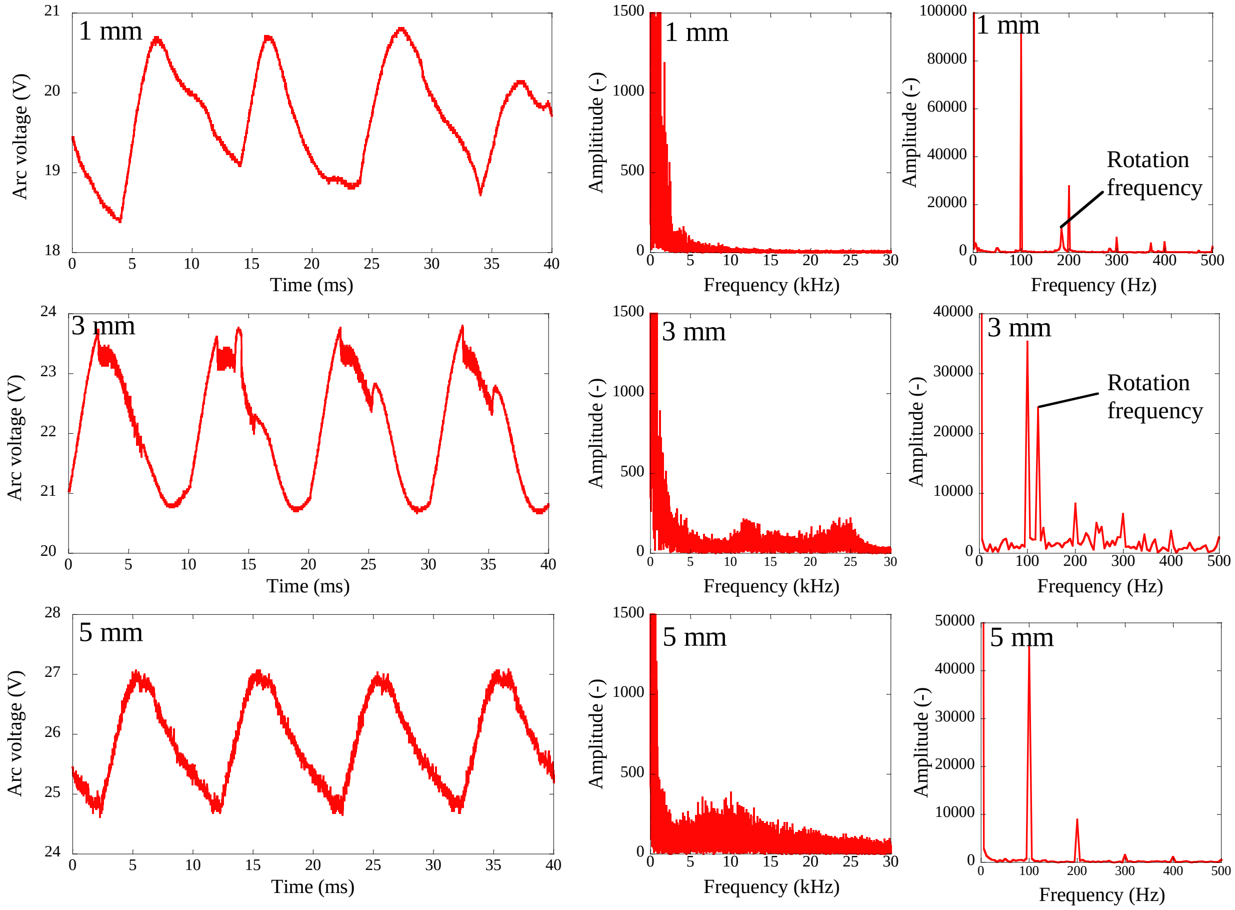

Fig. 3.25 Voltage waveform of helium arc at different electrode gap distances: 1, 3, and 5 mm when the arc current is fixed at 200 A. The corresponding FFT spectra of voltage waveform at different frequency ranges.

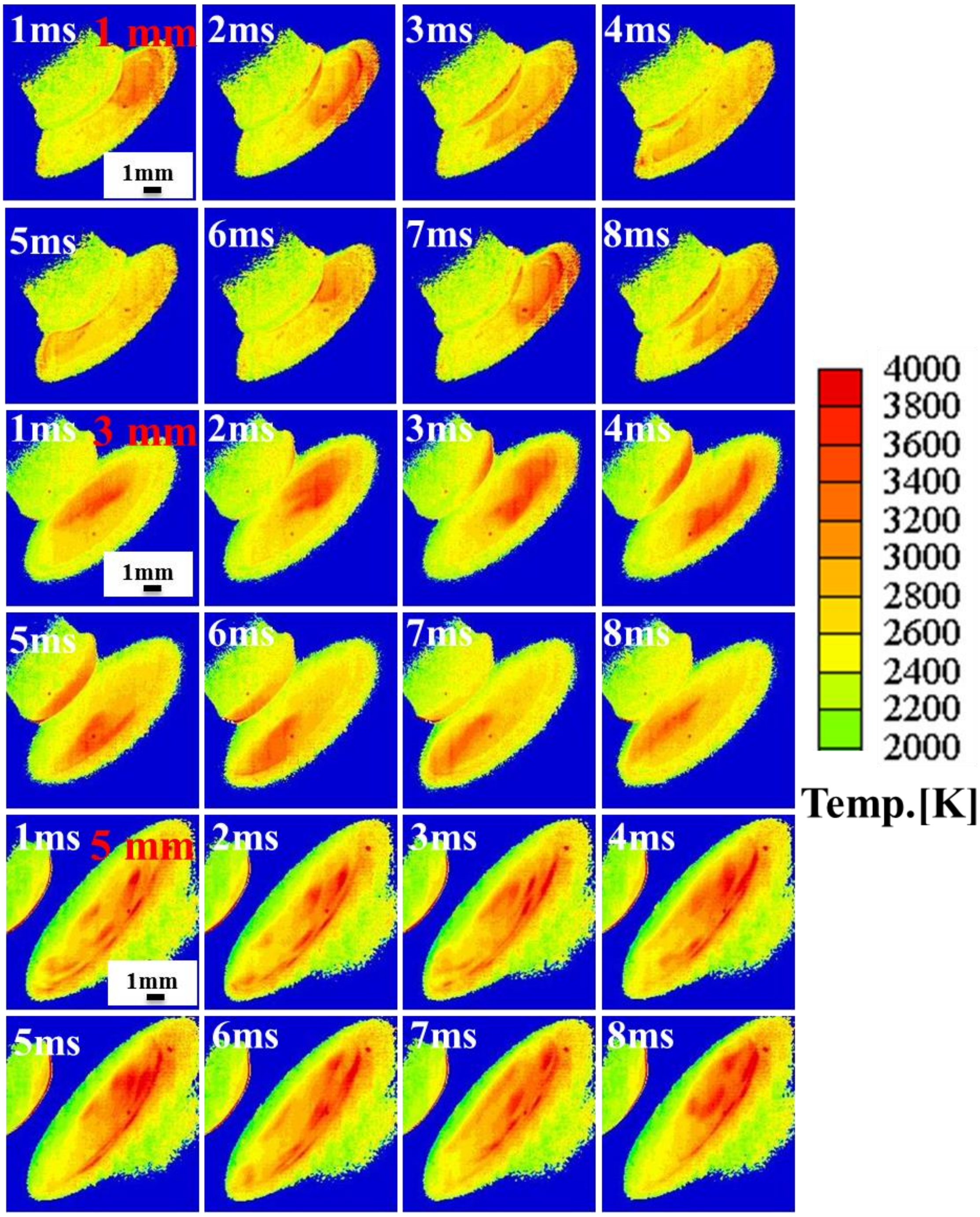

Fig. 3.26 Snapshots of temperature distribution according to time in helium arc at different electrode gap distances when the arc current is fixed at 200 A.

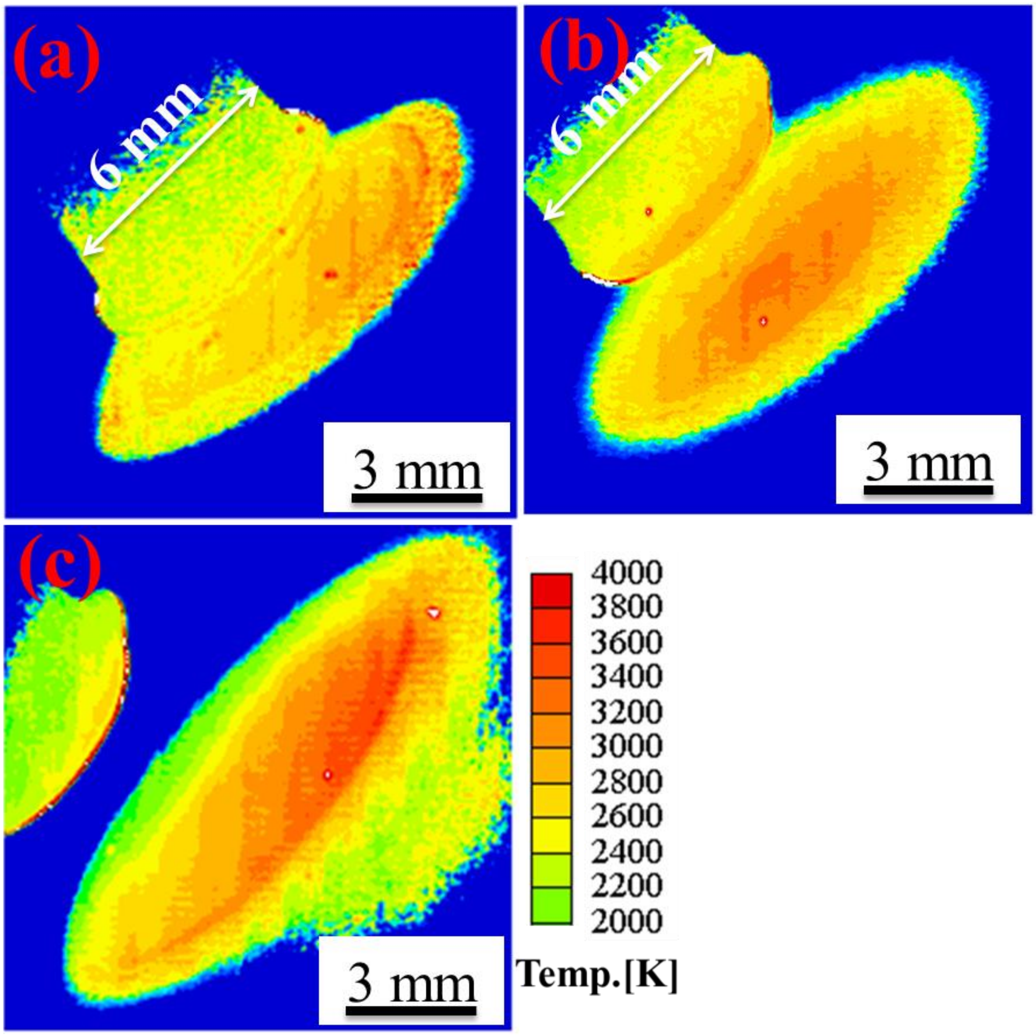

Fig. 3.27 Time average temperature distribution map in helium arc at different electrode gap distances when the arc current is fixed at 200 A. (a), (b), and (c) corresponding to the electrode gap distance of 1, 3, and 5 mm, respectively.

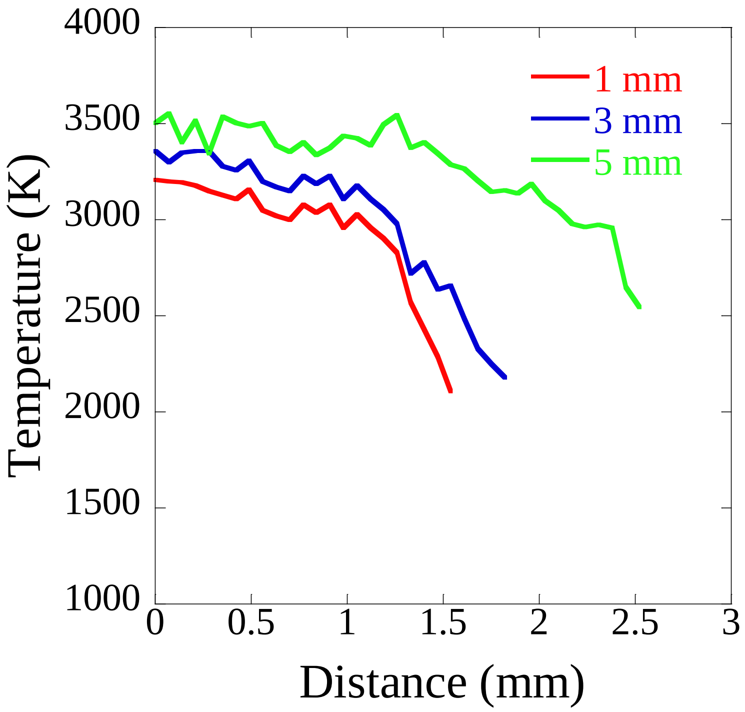

Fig. 3.28 Radical temperature distribution from the central to the edge of anode surface in helium arc when changing the electrode gap distance.

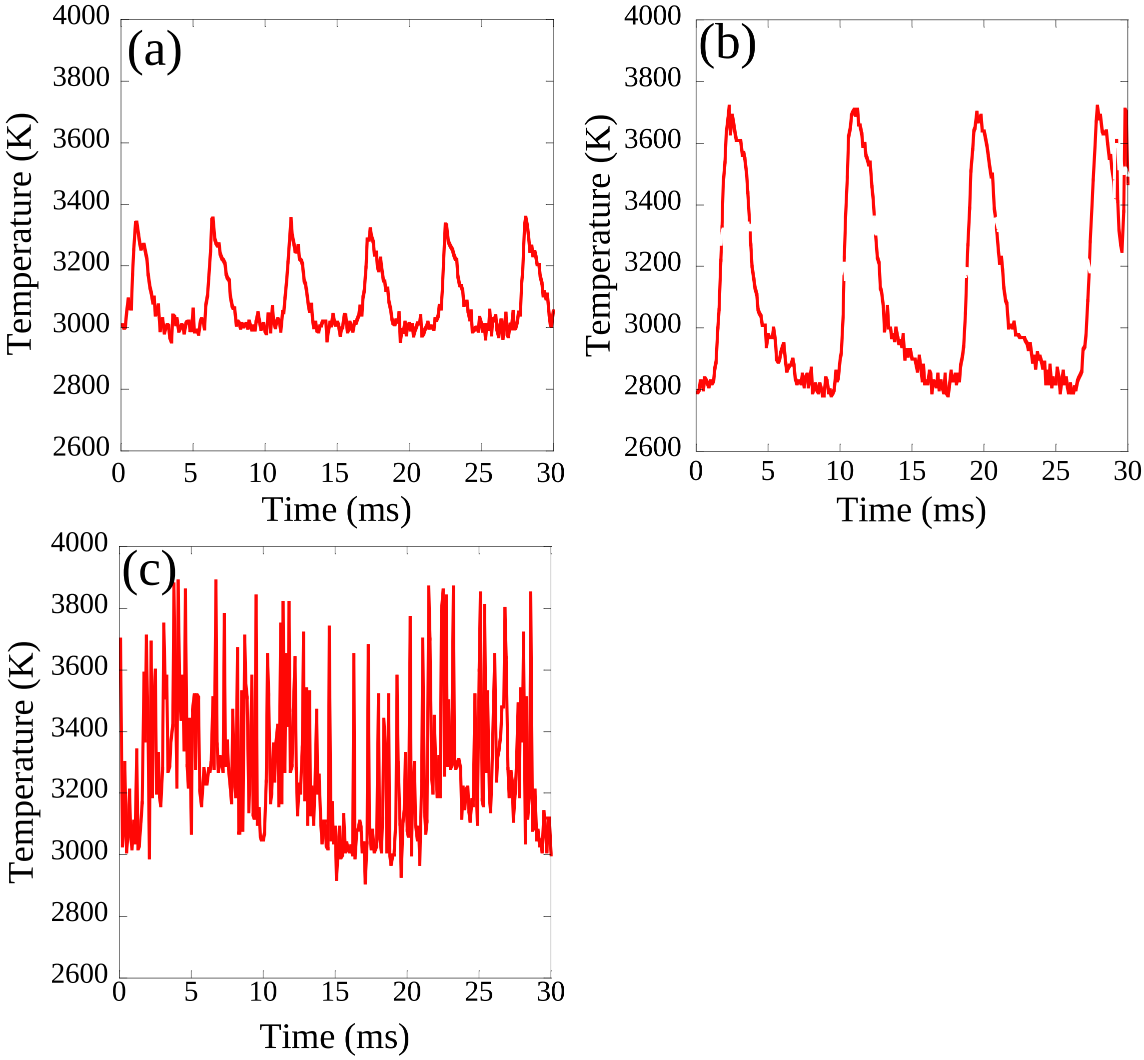

Fig. 3.29 Temperature variation of anode surface with the time in helium arc at different electrode gap distances when the arc current is fixed at 200 A. (a), (b), and (c) corresponding to the electrode gap distance of 1, 3, and 5 mm, respectively.

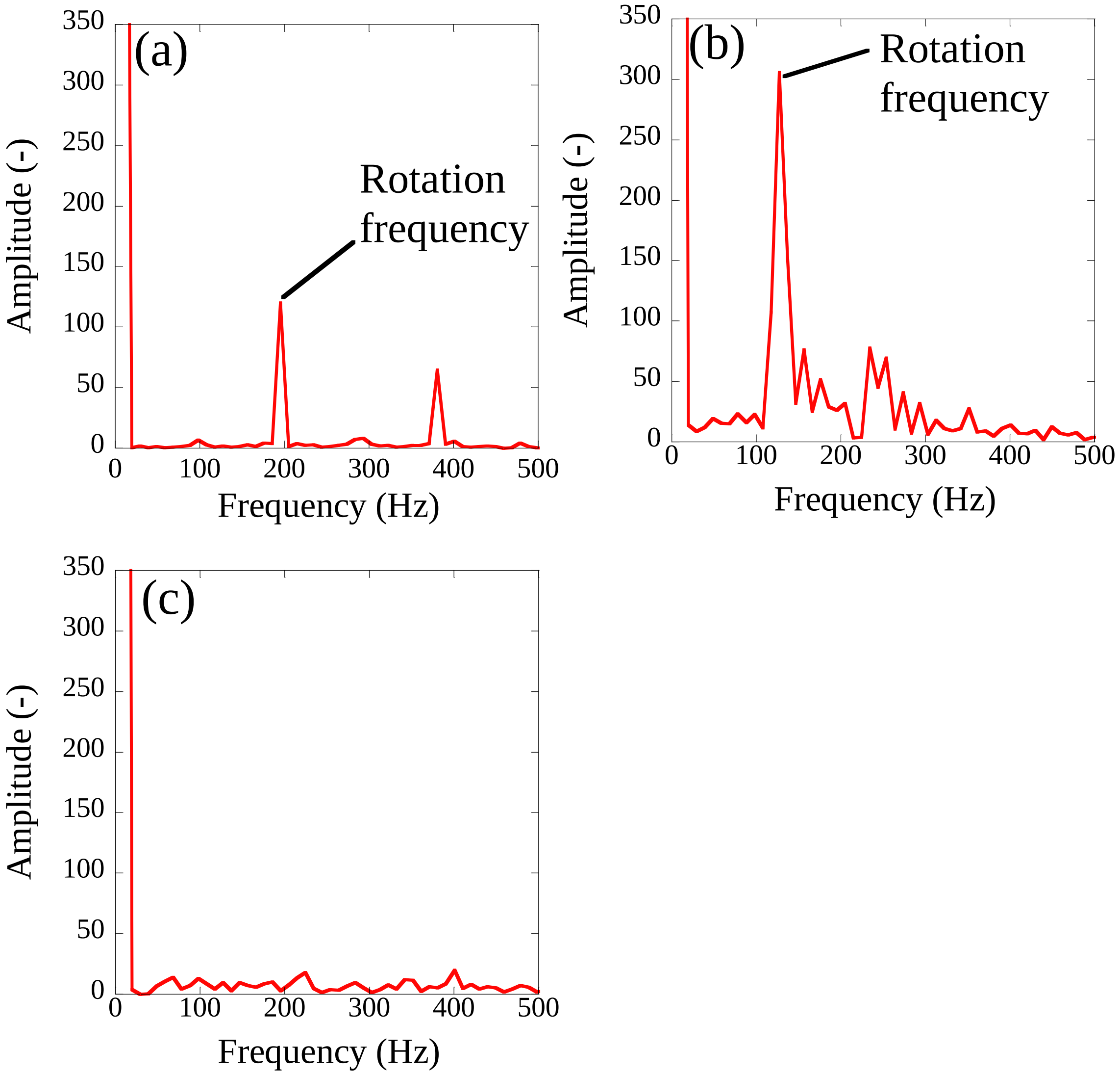

Fig. 3.30 FFT spectra of anode temperature in helium arc at different electrode gap distances when the arc current is fixed at 200 A. (a), (b), and (c) corresponding to the electrode gap distance of 1, 3, and 5 mm, respectively.

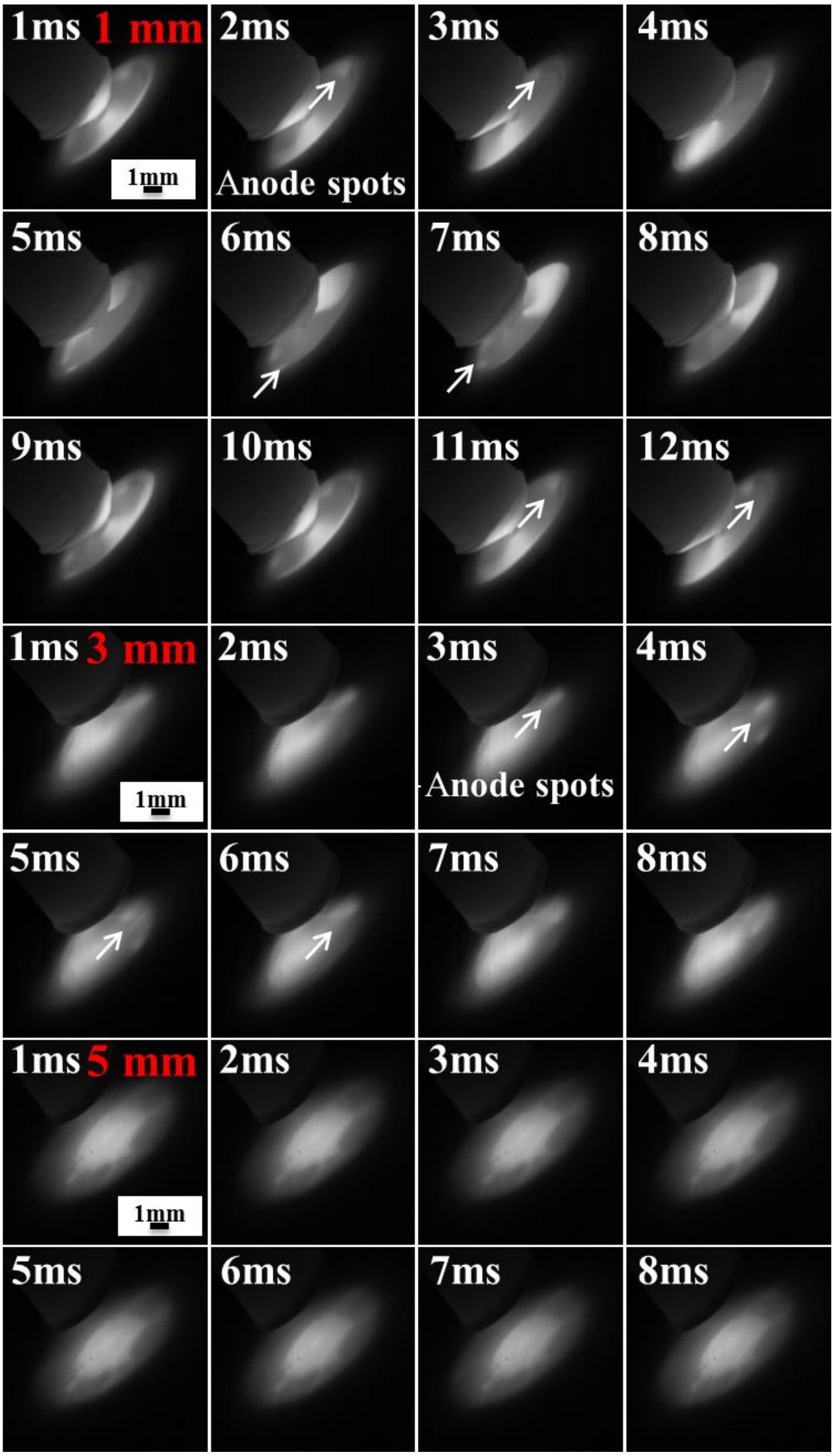

Fig. 3.31 Representative snapshots of high-speed camera for argon arc at different electrode gap distances when the arc current is fixed at 200 A.

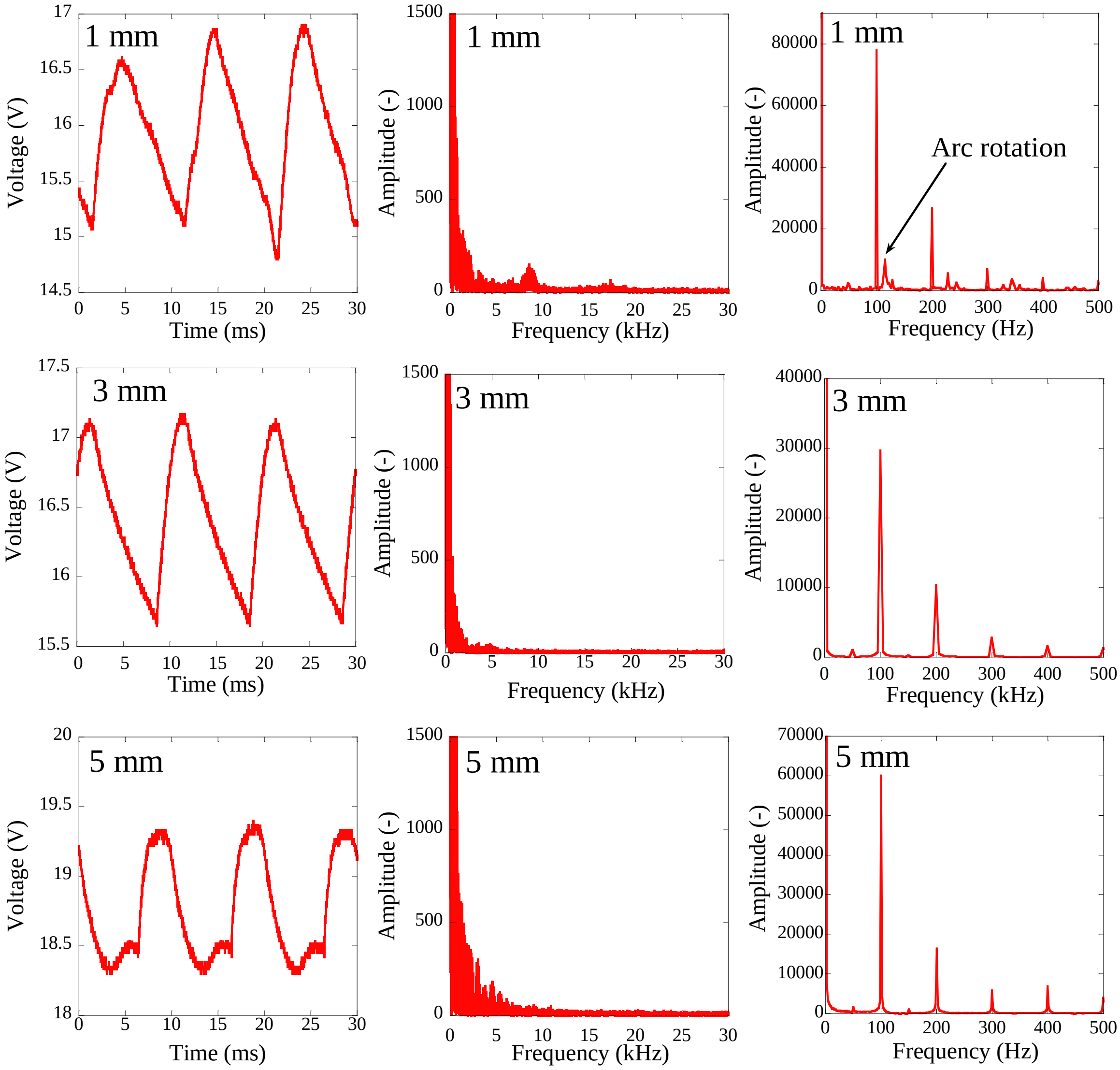

Fig. 3.32 Voltage waveform of argon arc at different electrode gap distances: 1, 3, and 5 mm when the arc current is fixed at 200 A. The corresponding FFT spectra of voltage waveform at different frequency ranges.

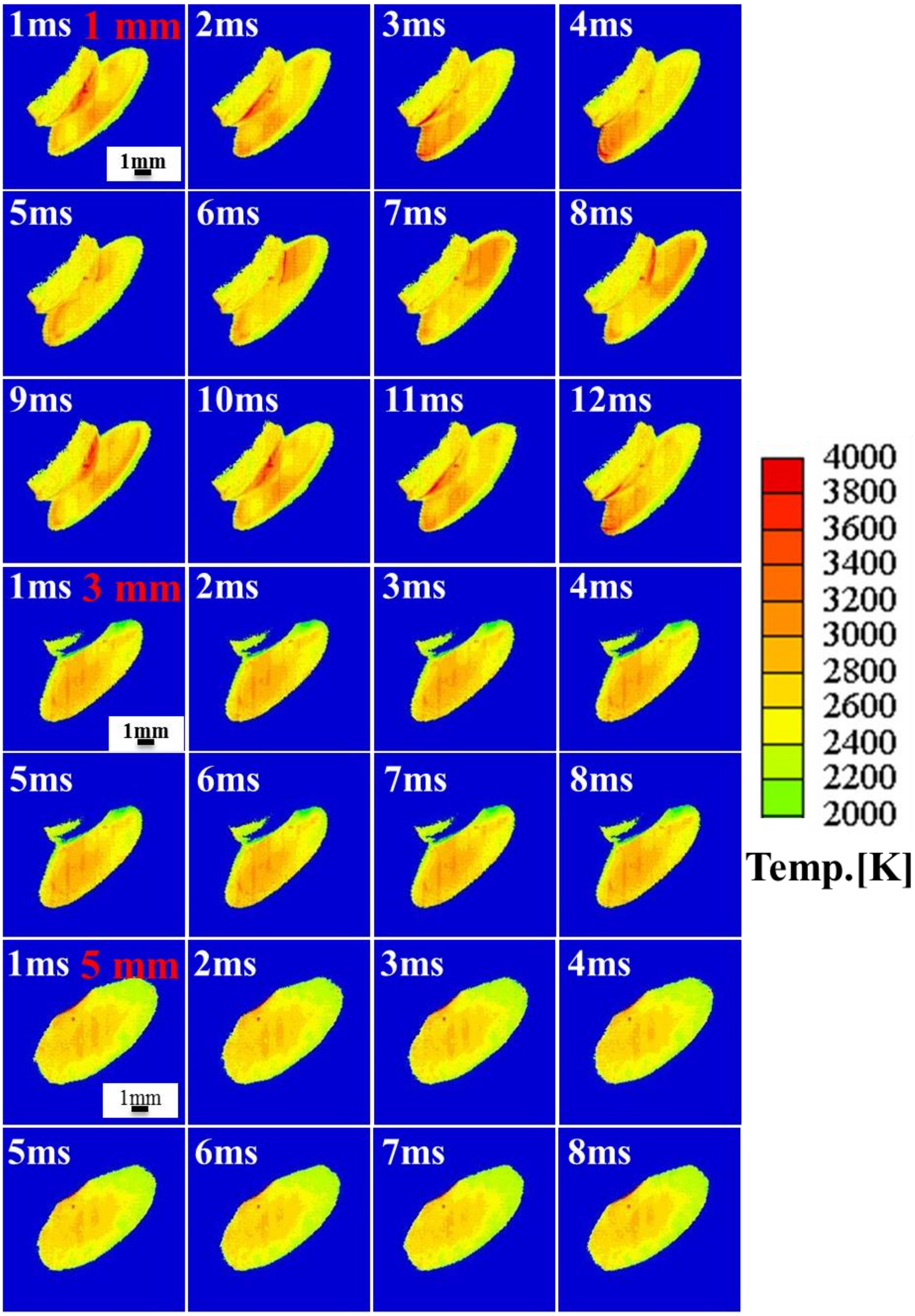

Fig. 3.33 Snapshots of temperature distribution according to time in argon arc at different electrode gap distances when the arc current is fixed at 200 A.

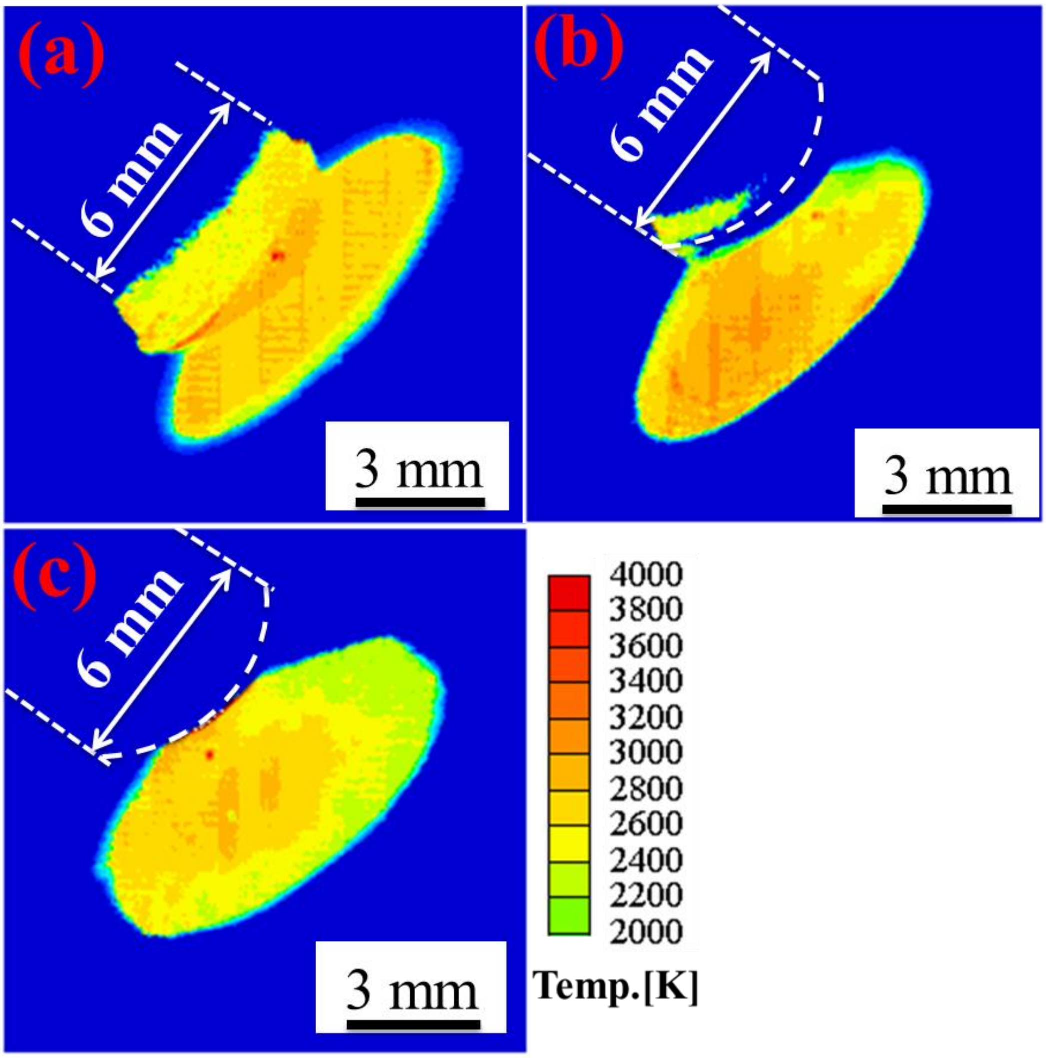

Fig. 3.34 Time average temperature distribution map in argon arc at different electrode gap distances when the arc current is fixed at 200 A. (a), (b), and (c) corresponding to the electrode gap distance of 1, 3, and 5 mm, respectively.

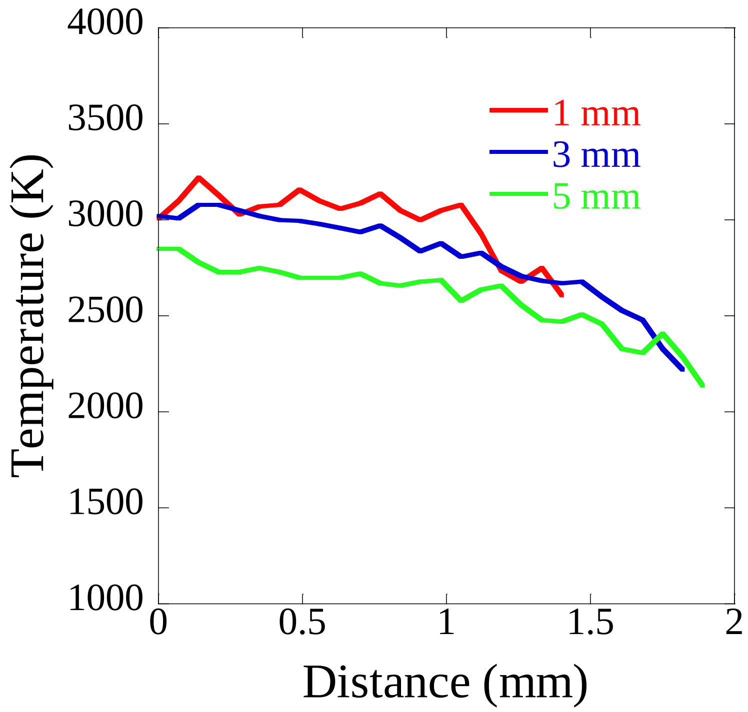

Fig. 3.35 Radical temperature distribution from central to edge of anode surface in argon arc when changing the electrode gap distance.

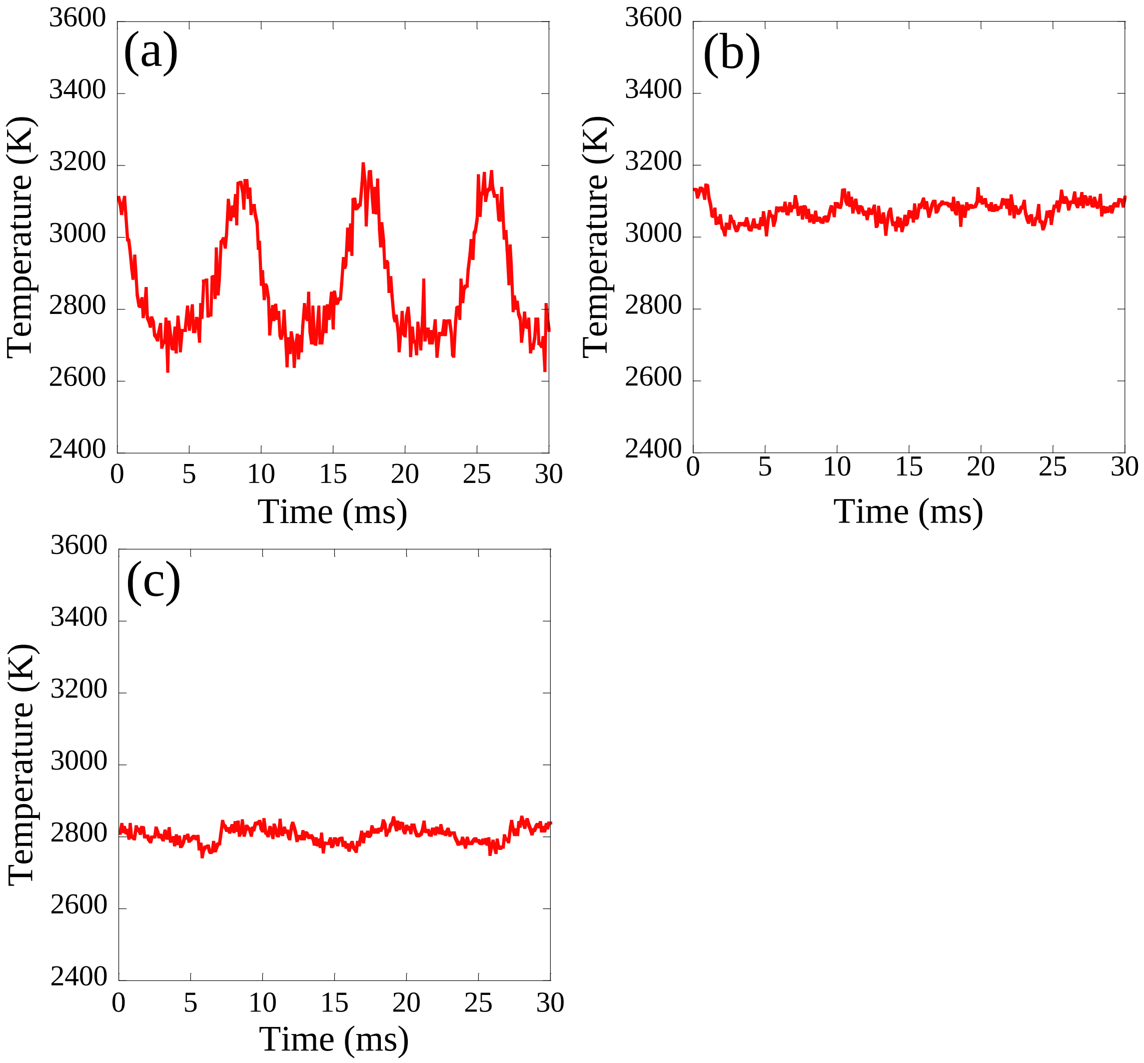

Fig. 3.36 Temperature variation of anode surface with the time in argon arc at different electrode gap distances when the arc current is fixed at 200 A. (a), (b), and (c) corresponding to the at electrode gap distance of 1, 3, and 5 mm, respectively.

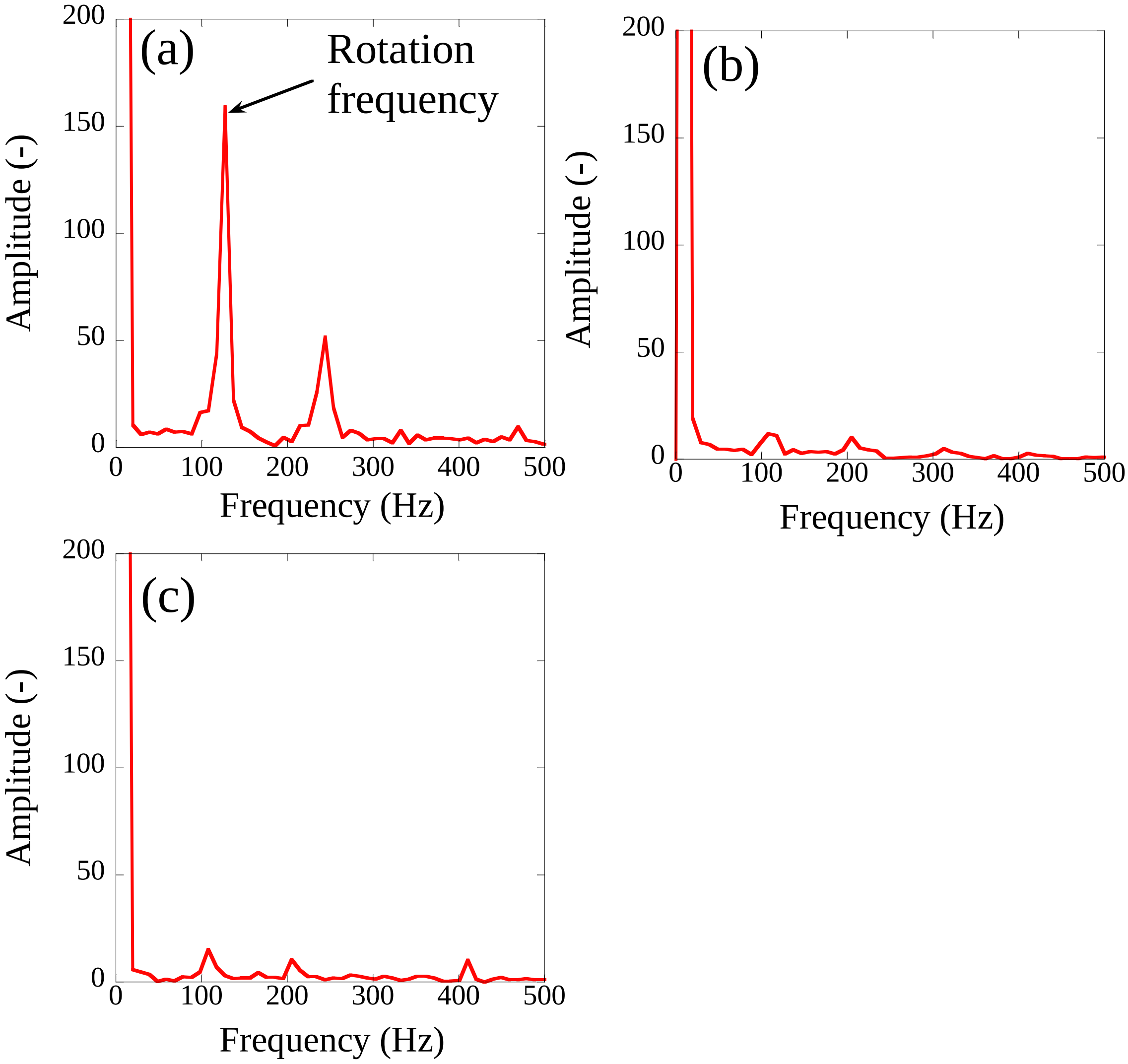

Fig. 3.37 The FFT spectra of anode temperature in argon arc at different electrode gap distances when the arc current is fixed at 200 A. (a), (b), and (c) corresponding to the electrode gap distance of 1, 3, and 5 mm, respectively.

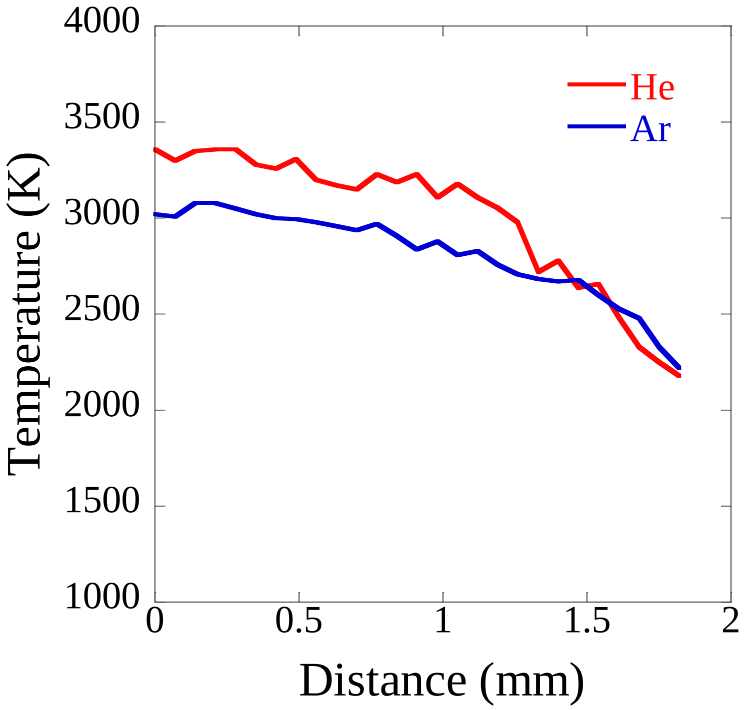

Fig. 3.38 Comparison of the radical temperature distribution under different gases when the arc current is 200 A and the electrode gap distance is 3 mm.

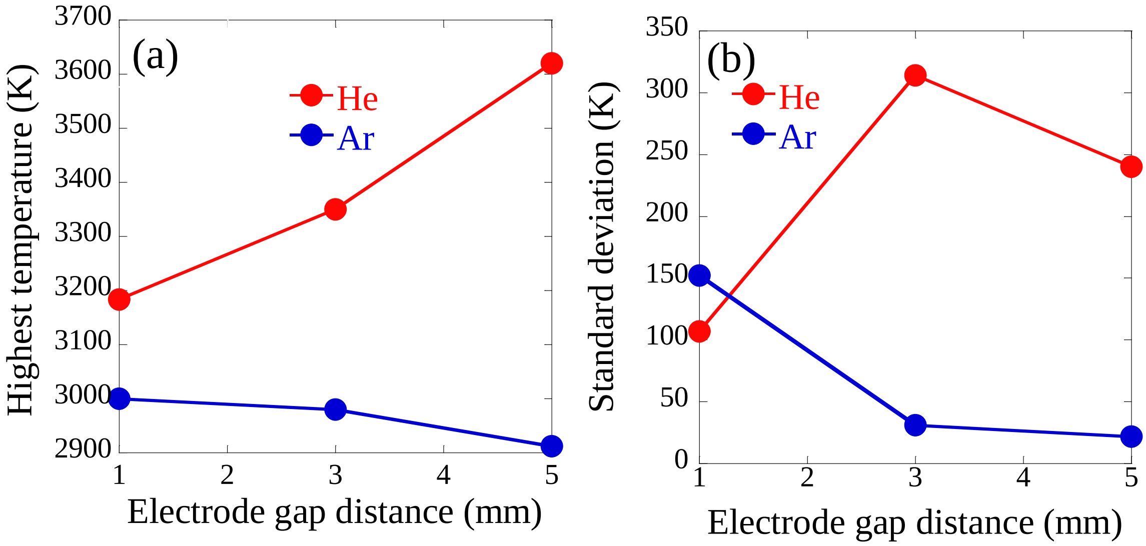

Fig. 3.39 Comparison of the highest temperature (a), standard deviation of temperature variation (b) between helium arc and argon arc when changing the electrode gap distance.

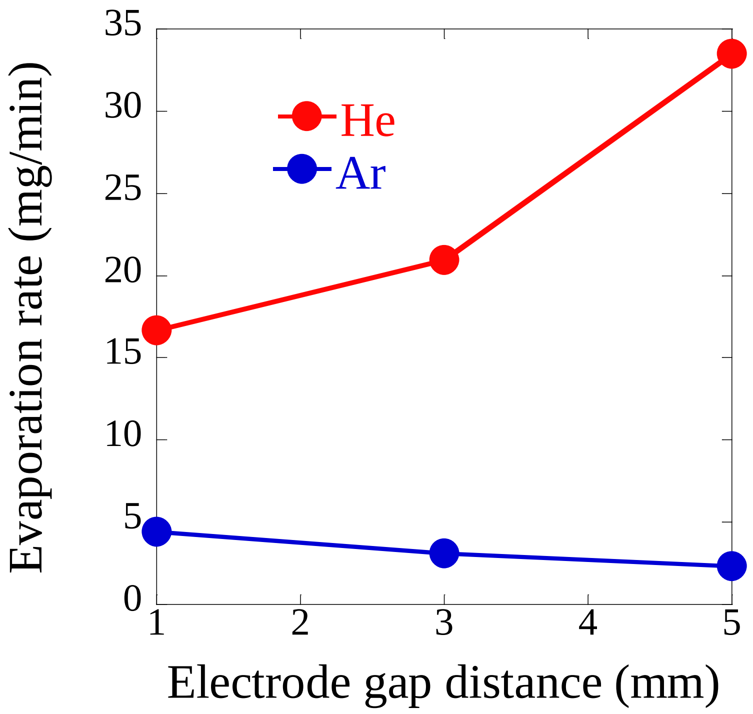

Fig. 3.40 Comparison of the evaporation rate of anode between helium and argon by changing the electrode gap distance when the arc current is fixed at 200 A.

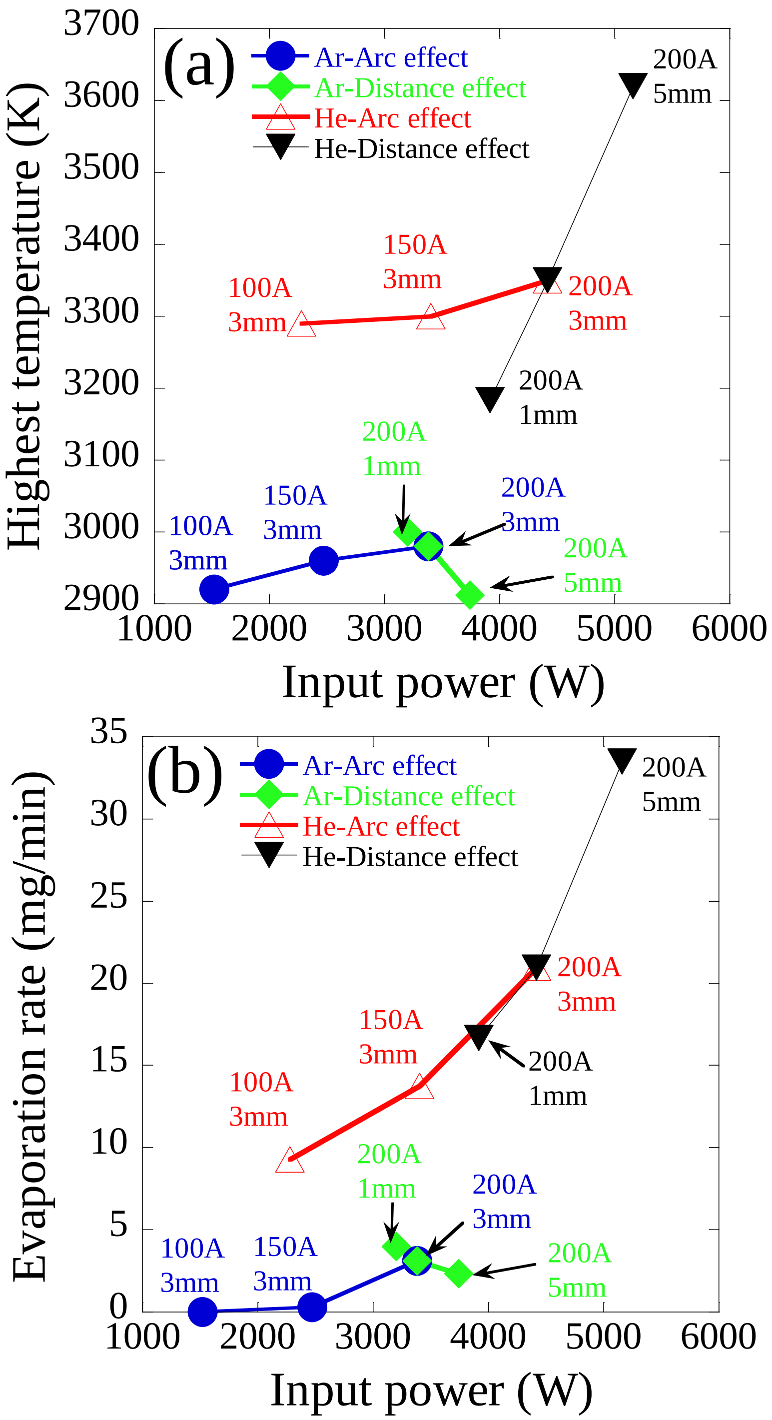

Fig. 3.41 The dependence of the highest temperature (a) and evaporation rate of anode (b) on the input power in helium arc and argon arc

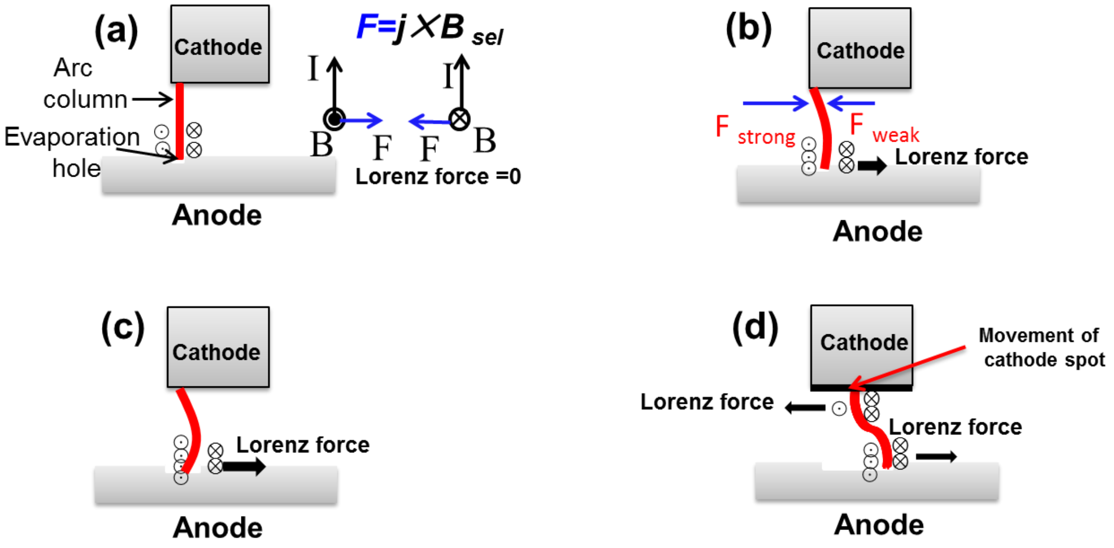

Fig. 3.42 The model of arc spot rotation.

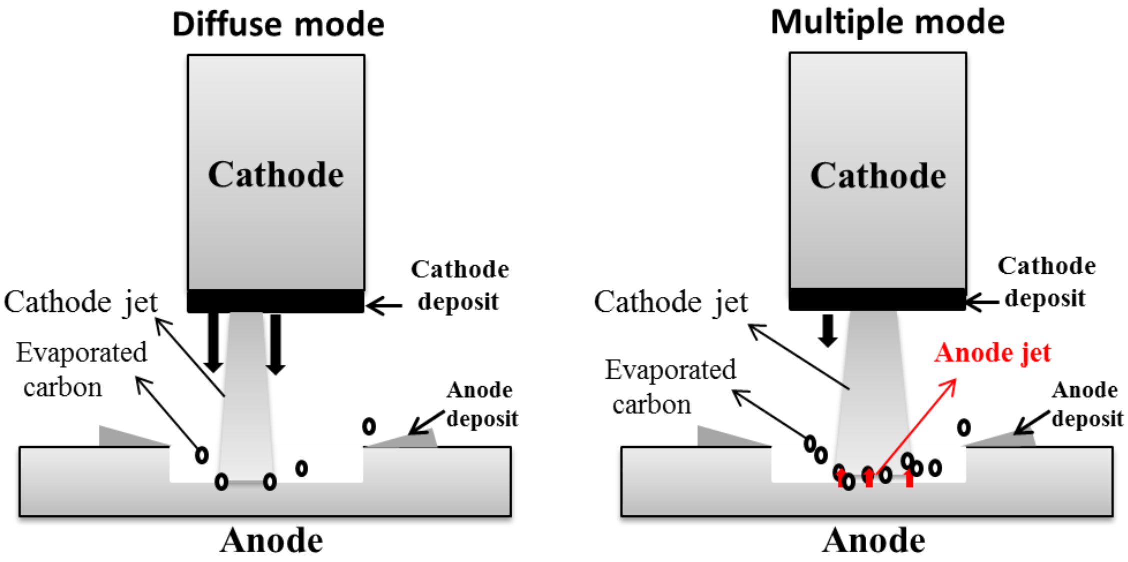

Fig. 3.43 The formation mechanism of different arc-anode attachment modes.

4. Preparation of Carbon Nanomaterial on the Anode Deposit

4.1 Introduction

There has been dramatic interest in carbon nanomaterials since the discovery of fullerenes in 1985 (Shenderova et al. 2002). Since carbon nanomaterials have remarkable physical, chemical, and electronic properties, they show great promise for many potential applications in a variety of technological fields ranging from conductive and high-strength composites to nanoelectronics (Baughman et al. 2002; Geim 2009; Gogotsi 2006; Maauter and Elimelech 2008). Therefore, much effort has been made to prepare carbon nanomaterials. For instance, laser vaporization of carbon was introduced to synthesize fullerenes (Kroto et al. 1985); chemical vapor deposition (CVD) method was used to prepare carbon nanotube and graphene (Yacamán et al.1993; Kim et al. 2009); and mechanical exfoliation method was employed to prepare graphene (Novoselov et al. 2004).

The arc discharge method has also been employed to prepare lots of carbon nanomaterials as an environmentally benign technique. In particular, many investigations have been carried out on the preparation of carbon nanomaterials on anode surface in the arc discharge method. For example, bamboo-like carbon was prepared by using a catalyst under hydrogen atmosphere (Kajiuraa et al. 2002). Carbon nanofiber, microfiber, and pillars were obtained on different positions of the anode surface under hydrogen atmosphere (Luo et al. 2005). Moreover, vertically-aligned carbon nanotube (CNT) was prepared by a catalyst-free hydrogen arc discharge (Cai et al. 2012). According to these works, hydrogen atmosphere is considered as the necessary condition for the growth of tube structured carbon materials on the anode surface. In contrast, Jones et al. prepared MWNT from the anode deposit by arc discharge method without hydrogen. They speculated that positive carbon ion contributes to the formation of MWNT

(Jones et al. 1996). However, the equilibrium composition of carbon at high temperature arc plasma indicates a relatively low concentration of positive carbon ion, in which the growth of MWNT is difficult. Therefore, the growth condition of tube structured carbon materials on the anode surface is still unclear.

The local temperature seems to be responsible for explaining the formation of different products on the anode surface (Luo et al. 2005). However, a narrow electrode gap distance and the strong radiation from the arc plasma in the typical arc discharge obstruct the temperature measurement of electrode surface (Iijima 1991). Therefore, report about the temperature of anode surface is limited. Although the temperature of carbon anode was measured by an optical pyrometer (Yusoff et al. 2006), the relationship between temperature and product was not explained.

In the present work, the anode deposit composed of nano-graphite particles, MWNT, and pyrolytic graphite was obtained on the anode surface by an atmospheric pressure helium arc without catalyst. In addition, necklace-like carbon, and spherical carbon particle were prepared on the anode surface, which is 3 and 5 mm away from the side of evaporation hole, respectively. The temperature distribution of anode surface was measured by two-color pyrometry. Based on measured temperature distribution, the formation mechanisms of those carbon nanomaterials were explained.

4.2 Experimental

4.2.1 Experimental Setup

Fig. 4.1 indicates the schematic illustration of an experimental apparatus for the preparation of carbon nanomaterials and the two-color pyrometry combined with a high-speed camera for temperature measurement. It was introduced in chapter 3 in detail.

4.2.2 Experimental Conditions

The anode was evaporated by the heat flux from the arc, leaving a hole at the arc attaching region on the anode surface. Some of evaporated carbon species were deposited on the peripheral area of the hole to form the anode deposit. Since the evaporated carbon species adsorbed and diffused at the hot anode surface easily, the anode deposit attached to the anode surface tightly. Meanwhile, some of evaporated carbon species formed the cathode deposit on the cathode tip.

As demonstrated in Table 4.1, a graphite anode rod of 30 mm in diameter (99.99%, Toyo Tanso Co., Ltd.) with an inclined top plane was put on a water-cooling copper plate. A graphite cathode rod of 6 mm in diameter (99.99%, Toyo Tanso Co., Ltd.) was placed at an oblique angle from the anode. The arc was generated for 5 min in helium environment at atmospheric pressure. The arc current was controlled at 100, 150, and 200 A at the fixed electrode gap distance of 1 mm. In addition, different electrode gap distances of 1, 3, and 5 mm were used at the fix arc current of 200 A. As shown in Fig. 4.1, the anode surface was observed through a viewport of the chamber by the high-speed camera.

4.2.3 Temperature Measurement

As mentioned in chapter 3, two band-pass filters of 763±3 and 880±5 nm were employed to measure the temperature of anode deposit in helium arc.

4.2.4 Sample Characterization

The morphological and structural characteristics of as prepared anode deposit were examined by scanning electron microscopy (SEM: JSM-6610LA, JEOL). In addition, the microstructures of sample were investigated by transmission electron microscopy (TEM: JEM-2010F, JEOL) at the acceleration voltage of 200 kV. Raman spectroscopy (NRS-2100, JASCO) with 514.5 nm Ar^+ laser excitation was employed for analyses.

4.3 Results and Discussion

4.3.1 Effect of Arc Current

Table 4.2 indicates the growth rate of anode deposit and total carbon evaporation rate at different arc currents. As shown in Table 4.2, the anode deposit growth rate increases with increasing the arc current. This tendency is similar to the total carbon evaporation rate. Large carbon evaporation rate leads to form a large amount of anode deposit. Therefore, the largest anode deposit growth rate of 3.9 $mg \cdot min^{-1}$ is observed with the largest total carbon evaporation rate of 15.7 $mg \cdot min^{-1}$ at the arc current of 200 A. Because less evaporated carbon scatters from the plasma region in the case of low carbon evaporation rate, most of evaporated carbon species are attached to the tip of cathode, leaving a small amount of carbon species to form the anode deposit. The anode deposit growth rates of 0.69 and 1.8 $mg \cdot min^{-1}$ are obtained, corresponding to the arc current of 100 and 150 A, respectively. Therefore, the size of anode deposit is very small in the relatively low arc current of 100 and 150 A.

Fig. 4.3 shows the SEM images of the typical product from the anode deposit according to the arc current at the fixed electrode gap distance of 1 mm. Due to the relatively low arc current, the anode deposit with a small amount can be obtained at the arc currents of 100 and 150 A. As shown in Fig. 4.3 (a), irregular shaped graphitic particles less than 1 μm were obtained when the arc current is 100 A. Although the main products are still graphite particles, few tubes can be seen in Fig. 4.3 (b) when the arc current is increased to 150 A. In contrast, the anode deposit with the inner diameter of 8 mm and the outer diameter of 11 mm is obtained in the highest arc current of 200 A. Fig. 4.3 (c) demonstrates that a large amount of MWNTs are observed in the center position of the anode deposit at the arc current of 200 A.

Morphologies of the anode deposit are observed at different positions as shown in Fig. 4.4. A low magnification SEM image of the anode deposit is presented in Fig. 4.4 (a) when the arc current is 200 A at the electrode gap distance of 1 mm. A closed red circle indicates the side of arc column. High magnification images at different positions which are indicated as (1)-(3) in Fig. 4.4 (a) are shown in Figs. 4.4 (b)-(d), respectively. Lots of graphite particles are observed at position (1) where the nearest position to the arc column is. In contrast, positions (2) and (3) are far away from the arc column, and the corresponding temperatures are lower than that of position (1). As shown in Fig. 4.4 (c), MWNT is obtained at position (2). Dome shaped materials are observed in position (3) as shown in Fig. 4.4 (a). The fractured region of the dome shaped product is demonstrated in Fig. 4.4 (d), the dome shaped product is composed of extended graphite layers with preferred orientation, which reveals close similarity to pyrolytic graphite. This structure is similar to the outer shell of cathode deposit (Ajayan et al. 1997). According to the SEM image, the purity of pyrolytic graphite at the anode deposit can reach over than 98% by counting the number of it. The high purity of pyrolytic graphite can be used as electrochemical detector for liquid chromatography (Wightman et al. 1978), semiconductor, and power conversion. Therefore, the growth temperature of graphite particles, MWNT, and pyrolytic graphite decreases step by step, due to their different growth positions.

TEM images of the anode deposit obtained at 200 A for the arc current and 1 mm for the electrode gap distance are demonstrated in Fig. 4.5. As shown in Fig. 4.5 (a), nano-graphite particles with an irregular shape are observed. Moreover, fewer-layered graphene sheets with a large size are obtained. Fig. 4.5 (b) indicates that the MWNT has the internal core of 3 nm in diameter, and two sets of alternating parallel white and black fringes are clearly visible, which is same as the typical MWNT from the cathode deposit by the conventional arc discharge method (Iijima 1991; Ebbesen and Ajayan 1992). Therefore, there is no difference between the MWNT from the anode deposit and the typical arc-derived MWNT from the cathode deposit.

4.3.2 Effect of Electrode Gap Distance

Figs. 4.6 (a)-(c) indicate the morphologies of MWNT on the anode deposit when the electrode gap distance is varied from 1 to 5 mm at the fixed arc current of 200 A. The growth region of MWNT is indicated by a red rectangle in Figs. 4.6 (a1)-(c1). As shown in Figs. 4.6 (a)-(c), the morphology of MWNT does not show significant difference when the electrode gap distance is varied. However, the distance from the MWNT growth region to the edge of arc column is 0.3, 0.6, and 0.8 mm, corresponding to the electrode gap distance of 1, 3, and 5 mm, respectively. These different growth regions will be explained by the temperature distribution of the anode surface when the electrode gap distance is changed. In addition, other two typical compositions of anode deposit, nano-graphite particle and pyrolytic graphite are obtained in the left-side and the right-side of MWNT growth region, respectively.

4.3.3 Effect of Different Collection Positions

Figs. 4.7 (a)-(b) correspond to the FE-SEM images of the products collected from 3 and 5 mm away from the anode evaporation hole, respectively. The product collected from 3 mm away from the side of anode evaporation hole indicates the necklace-like carbon nanostructures (Okuno et al. 2004). The diameter of the beads is about 60 nm. As shown in Fig. 4.7 (b), it is spherical carbon particle with the average particle size of 70-80 nm for the carbon nanomaterial which is grown in 5 mm away from the evaporation hole.

Figs. 4.8 (a)-(b) indicate the low and high magnification TEM images of necklace-like carbon. As shown in Fig. 4.8 (a), the beads grow into a long neck randomly, necklace-like carbon usually curve smoothly and entangle together. However, the necklace-like carbon does not have graphitic structure. This structure seems to be a transition between spherical particle and tube structured carbon.

Figs. 4.9 (a)-(c) correspond to the Raman spectra of the anode deposit, the products collected from 3 and 5 mm away from the side of anode evaporation hole, respectively. There are two distinct peaks located at 1350 and 1584 cm^{-1}, corresponding to the D band and the G band, respectively. The appearance of the D band is attributed to the induction of significant defects or disorder in nanostructures (Ferrari 2007). The G band is common to all sp^2 carbon forms, corresponding to high frequency E_{2g} first-order mode (Pimenta et al. 2007). The intensity ratio of I_D/I_G provides an index to evaluate the quality of the carbon material. The values of I_D/I_G are 0.21, 0.85, and 0.91 for the anode deposit, the products collected from 3 and 5 mm away from the evaporation hole, respectively. Therefore, compared with products collected from other regions of the anode surface, anode deposit has fewer defects. In contrast to the carbon nanomaterial prepared by other methods, the carbon nanomaterials on the anode deposit indicate fewer defects (Abdulkareem et al. 2007). Moreover, as shown in Fig. 4.9 (a), a narrow full-width half-maximum (FWHM=24 cm^{-1}) in the G band indicates better crystallinity of the anode deposit than the products from other regions of the anode surface.

4. 3.4 Formation Mechanism of Carbon Nanomaterial on the Anode Deposit

The difference between nucleation temperature and deposition temperature of carbon vapor plays an important role in the formation different carbon nanomaterials. Therefore, the anode surface temperature is employed to explain the formation of carbon nanomaterial on the anode surface.

Fig. 4.10 shows the temperature distribution map of anode surface at 200 A and 1 mm for the arc current and the electrode gap distance, respectively. Due to the small size of the anode deposit, the temperature distribution of the anode deposit is difficult to be measured when the arc currents are 100 and 150 A. The black rectangle indicated in the figure means the typical growth position of anode deposit at the arc current of 200 A. The temperature range of anode deposit growth region is from 2400 to 3000 K. This result shows great consistency with the modeling results of the anode temperature (Keidar and Beilis 2009; Keidar et al. 2006). According to the SEM images in Fig. 4.4 (a), the corresponding growth temperatures of pyrolytic graphite, MWNT and nano-graphite particles are in the range of 2400 to 2600, 2600 to 2700, and 2700 to 3000 K, respectively. The MWNT growth temperature is similar to simulation result of some researches (Nardelli et al 1998). As a result of the different thermodynamic stabilities among these carbon nanomaterials on the anode deposit, nano-graphite particle with the least thermodynamic stability can be formed in the region with relatively high temperature (Tománek et al. 1993; Berber and Tománek 2004). Because MWNT is a thermodynamically stable material compared with nano-graphite particle, it grows in the relatively low temperature. Pyrolytic graphite is the most thermodynamic stable material among three typical products in this work; it forms in the lowest temperature region. The anode surface acts as a substrate for the deposition of carbon vapor, which is similar to the formation of pyrolytic graphite by CVD method (Moore 1987).

However, the growth temperature of necklace-like carbon and spherical carbon particle could not be shown in Fig. 4.10, because of the week thermal radiation of carbon electrode in these regions. According to the heat transfer on the anode surface, the growth temperature of necklace-like carbon and spherical carbon particle is about 1200 K and 600 K, respectively (Ostrogorsky et al. 2006). Spherical carbon particle is easy to be formed at the position with low local temperature (Shenderova et al. 2002).

Fig. 4.11 shows temperature distribution maps of anode surface by changing the electrode gap distance at the fixed arc current of 200 A. According to the temperature distribution map, the growth temperature of anode deposit increases with increasing the electrode gap distance. Since the arc length increases with the electrode gap distance, the longer arc length leads to the higher input power in the case of the same arc current. Therefore, the enhanced input power is employed to explain the temperature variation. According to the SEM images in Fig. 4.6, the corresponding growth temperature of MWNT can be obtained. The black rectangles in Figs. 4.11 (a)-(c) indicate the growth positions of MWNT at different electrode gap distances. The same temperature range of 2600 to 2700 K is found for the growth of MWNT on the anode surface when the electrode gap distance is changed, which confirms the grown region of MWNT in Fig. 4.6.

Fig. 4.12 summaries the growth temperature of carbon nanomaterials on the anode deposit under different experimental conditions. As shown in Fig. 4.12, the same growth temperature is found for each carbon nanomaterial on the anode surface while the electrode gap distance is changed. Pyrolytic graphite, MWNT, and nano-graphite particles are grown in the range of 2400 to 2600, 2600 to 2700, and over than 2700 K, respectively. Moreover, the suitable temperature range of 2600 to 2700 K is required for the growth of MWNT on the anode surface rather than the catalyst or the hydrogen atmosphere by the arc discharge method.

According to above temperature results, the growth mechanism of carbon nanomaterials on the anode surface is shown in Fig. 4.13. In the case of high arc current, the strong cathode jet results in scattering of evaporated carbon species from the arc column to form the anode deposit. According to the temperature distribution of the anode surface, the corresponding growth temperatures of pyrolytic graphite, MWNT, and nano-graphite particles are in the range of 2400 to 2600, 2600 to 2700, and over than 2700 K, respectively. The self-assembly formation of carbon nanomaterial occurred when carbon vapor is quenched suddenly at the deposit position where the temperature is lower than the nucleation temperature of carbon vapor (Ebbesen and Ajayan 1992; Gamaly and Ebbesen 1995; Takikawa et al. 2000; Nishio et al. 2004).

The quenching effect plays an important role in the formation of carbon nanomaterial on the anode surface. As shown in Fig. 4.12, the deposition temperature of MWNT is in the range of 2600-2700 K. According to the homogeneous nucleation equation provided by (Girshick et al. 1990), the nucleation temperature of carbon vapor is calculated around 4000 K. Therefore, the difference between nucleation temperature and deposition temperature is in the range of 1300-1400 K for the formation of MWNT. The quenching rate is calculated as the temperature difference divided by the time interval. It is assumed that all of the precursors for forming different carbon nanomaterials on the anode despite have the same velocity of 0.15 m/s, since the size of anode deposit is small (Kundrapu and Keidar 2012). Therefore, the quenching rate for the formation of MWNT is in the range of 1.6×10^5-5×10^5 K/s. Moreover, the following explanations can be used to demonstrate the formation of MWNT in detail.

Since the MWNT from the cathode deposit and the anode deposit have the same structure, the vapor phase growth model can be employed to explain the formation of MWNT (Liang et al. 2012; Harris 2007). Because the growth area is out of the plasma region, the main precursors are carbon atoms. Evaporated carbon atoms collide and coagulate with each other to grow into a cap structure with multi-layers as a tip seed. This cap structure will grow into MWNT by the incorporation of carbon atoms to the active edge site of dangling bonds when suitable quenching condition occurs.

In contrast, nano-graphite particle is grown in the relatively high temperature, since its lower thermodynamic stability than MWNT. The difference between nucleation temperature and deposition temperature of is less than 1300 K. The quenching rate for the growth of nano-graphite particle is in the range of 5×10^5-6×10^5 K/s. On the other hand, the deposition temperature of pyrolytic graphite is in the region of 2400 to 2600 K. This temperature is consistency with the deposition temperature (above 2300 K) of pyrolytic graphite by CVD method (Moore 1981; Guellali et al 2008). The quenching rate for the formation of pyrolytic graphite is in the range of 1.1×10^5-1.6×10^5 K/s. This can be explained by the fact that pyrolytic graphite is thermodynamically stable than MWNT, lower quenching rate is required.

In addition, the evaporated carbon species attach to a lower temperature region which is 3 mm away from the anode evaporation hole, forming the necklace-like carbon. Spherical carbon particles are formed on the anode surface which is 5 mm away from the evaporation hole. According to the heat transfer on the anode surface, the differences between nucleation temperature and deposition temperature are about 2800 and 3400 K for the formation of necklace-like carbon and spherical carbon particle, respectively. Based on the velocity distribution for carbon nanomaterial synthesis by arc discharge method (Kundrapu and Keidar, 2012), the velocities of precursors are estimated at 1.5 and 3 m/s for the necklace-like carbon and spherical carbon particle, respectively. Therefore, the quenching rates are 1×10^6 and 2×10^6 K/s corresponding to necklace-like carbon and spherical carbon particle, respectively. Higher quenching rate contributes to the formation of necklace-like carbon and spherical carbon particle (Sano et al. 2002; Okuno et al. 2004).

4. 3.5 Effect of Attachment Mode on the Purity of Carbon Nanomaterial

Fig. 4.14 indicates temperature variation of anode deposit region with time at different arc-anode attachment modes in helium arc. The anode deposit temperatures at arc currents of 100 and 200 A and the fixed electrode gap distance of 3 mm are selected for comparison. As discussed in chapter 3, these two conditions correspond to multiple attachments and diffuse attachment, respectively. Although the average temperatures of anode deposit in different attachment modes are similar as 2,690 K for the multiple mode and 2,680 K for the diffuse mode, the standard deviations of measured temperature are quite different as 181 K for the multiple mode and 260 K for the diffuse attachment mode, respectively. According to Fig. 4.12, these two positions correspond to the growth of MWNT. However, the temperature behavior in different modes has a significant effect on the purity of carbon nanomaterial on the anode deposit.

The corresponding SEM images of diffuse and multiple attachment modes are shown in Fig. 4.15. Figs. 4.15 (a) and (b) correspond to multiple attachments and diffuse attachment, respectively. According to temperature distribution of the anode deposit, the MWNT with higher purity is obtained in multiple attachment mode than that of diffuse attachment mode. The temperature with large fluctuation results in the low purity of MWNT on the anode deposit in the diffuse attachment mode.

Fig. 4.16 indicates the SEM images of anode deposit in argon arc at different magnifications. According to the SEM images, there is no typical carbon nanomaterial can be observed on the anode deposit. As a result of the low evaporation rate of anode material in argon arc, the productivity of syntheses carbon nanomaterial is very low. Moreover, because of the evaporation of cathode in argon arc, it is difficult to investigate the formation mechanism of carbon material on the anode deposit in argon arc. The present work will not focus on the carbon nanomaterial in argon arc deeply.

4. 4 Conclusion

The anode deposit composed of nano-graphite particles, MWNT, and pyrolytic graphite were prepared from helium arc discharge under atmospheric pressure. In order to investigate the growth temperature of these carbon nanomaterials, the temperature of anode surface was measured by two-color pyrometry successfully. Different products on the anode deposit can be explained by different local temperatures of the anode surface. Deposition temperatures of pyrolytic graphite, MWNT, and nano-graphite particles are in the range of 2400 to 2600, 2600 to 2700, and over than 2700 K, respectively. In addition, the deposition temperatures of necklace-like carbon and spherical carbon particle are about 1200 K and 600 K, respectively. Efficient quenching effect contributes to form thermodynamically stable material, such as spherical carbon particle. Moreover, the MWNT was growth in the temperature range of 2600 to 2700 K, indicating that suitable quenching effect is the necessary condition for the formation of MWNT rather than the catalyst or the hydrogen. Therefore, the quenching effect plays an important role in forming different carbon nanomaterials selectively.

The effect of arc-anode attachment mode on the purity of carbon material from the anode deposit was investigated; carbon nanomaterial with low purity on the special position of the anode deposit was obtained due to the large temperature fluctuation caused by the rotation of arc spot in diffuse attachment mode.

References

Abdulkareem A. S., A. S. Afolabi, S. E. Iyuke and C. H. Piennar. “Synthesis of carbon nanotubes by swirled floating catalyst chemical vapor deposition method.” *Journal of Nanoscience and Nanotechnology* **7**(10), 1-6 (2007).

Ajayan P. M., P. Redlich and M. Rühle. “Balance of graphite deposition and multishell carbon nanotube growth in the carbon arc discharge.” *Journal of Materials Research* **12**, 244-252 (1997).

Baughman R. H., A. A. Zakhidov and W. A. de Heer. “Carbon nanotubes--the route toward applications.” *Science* **297**, 787-792 (2002).

Berber S. and D. Tománek. “Stability differences and conversion mechanism between nanotubes and scrolls.” *Physical Review B* **69**, 233404 (2004).

Cai X., H. Cong and C. Liu. “Synthesis of vertically-aligned carbon nanotubes without a catalyst by hydrogen arc discharge.” *Carbon* **50**, 2726-2730 (2012).

Ebbesen T. W. and P. M. Ajayan. “Large-scale synthesis of carbon nanotubes.” *Nature* **358**, 220-222 (1992).

Ferrari A.C. “Raman Spectroscopy of Graphene and Graphite: Disorder, Electron-phonon Coupling, Doping and Nonadiabatic Effects.” *Solid State Communications* **143**, 47-57 (2007).

Gamaly E.G and T.W. Ebbesen. “Mechanism of Carbon Nanotube Formation in the Arc Discharge.” *Physical Review B* **52**, 2083-2089 (1995).

Geim A. K. “Graphene: status and prospects.” *Science* **324**, 1530-1534 (2009).

Girshick S. L., C.P. Chiu and P. H. McMurry. “Time-Dependent Aerosol Models and Homogeneous Nucleation Rates,” *Aerosol Science and Technology* **13**, 465-477 (1990).

Gogotsi Y. Carbon nanomaterials. 1st ed. Boca Raton: CRC; 2006.

Guellali M., R. Oberacker, M. J. Hoffmann. “Influence of heat treatment on microstructure and properties of highly textured pyrocarbons deposited during CVD at about 1100ºC and above 2000ºC.” *Composites Science and Technology* **68**, 1122-11230 (2008).

Harris P. J. F. “Solid state growth mechanisms for carbon nanotubes.” *Carbon* **45**, 229-239 (2007).

Iijima S. “Helical microtubules of graphitic carbon.” *Nature* **354**, 56-58 (1991).

Jones J. M., R. P. Malcolm, K. M. Thomas and S. H. Bottrell. “The anode deposit formed during the carbon arc evaporation of graphite for the synthesis of fullerenes and carbon nanotubes.” *Carbon* **34**, 231-237 (1996).

Kajiuraa H., H. Huang, S. Tsutsuia, Y. Murakami and M. Miyakoshi. “High-purity fibrous carbon deposit on the anode surface in hydrogen DC arc-discharge.” *Carbon* **40**, 2423-2428 (2002).

Keidar M., A. M. Waas, Y. Raitses and E. I. Waldorff. “Modeling of the anodic arc discharge and conditions for single-wall carbon nanotube growth.” *Journal of Nanoscience and Nanotechnology* **6**, 1309-11314 (2006).

Keidar M. and I. I. Beilis. “Modeling of atmospheric-pressure anodic carbon arc producing carbon nanotubes.” *Journal of Applied Physics* **106**, 103304 (2009).

Kim K. S., Y. Zhao, H. Jang, S. Y. Lee, J. M. Kim, K. S. Kim, J. H. Ahn, P. Kim., J. Y. Choi and B. H. Hong. “Large-scale pattern growth of graphene films for stretchable transparent electrodes.” *Nature* **457**, 706-710 (2009).

Kroto H. W., J. R. Heath, S. C. O'Brien, R. F. Curl and R. E. Smalley. “C_{60}: Buckminster-fullerene.” *Nature* **318**, 162-163 (1985).

Kundrapu M. and M. Keidar. “Numerical simulation of carbon arc discharge for nanoparticle synthesis” *Physics of plasmas* **19**, 073510 (2012).

Liang, F., T. Shimizu, M. Tanaka, S. Choi and T. Watanabe. “Selective preparation of polyhedral graphite particles and multi-wall carbon nanotubes by a transferred arc under atmospheric pressure.” *Diamond and Related Materials* **30**, 70-76 (2012).

Luo S., D. Huang, Y. Huang, X. Dou and X. Zhao. “Orderly evolution in the morphology of the anode deposit in hydrogen arc discharge.” *Carbon* **43**, 109-115 (2005).

Maauter M. S. and M. Elimelech. “Environmental applications of carbon-based nanomaterials.” *Environmental Science &Technology* **42**, 5843-5859 (2008).

Moore A. W. “Highly oriented pyrolytic graphite and its intercalation compounds.” *Chemistry and Physics of Carbon* **17**, 233-286 (1981).

Nardelli M. B., C. Roland and J. Bernholc. “Theoretical bounds for multiwalled carbon nanotube growth.” *Chemical Physics Letters* **296**, 471-476 (1998).

Nishio M., S Akita and Y Nakayama. “Cooling Effect on the Growth of Carbon Nanotube and Optical Emission Spectroscopy in Short-period Arc-discharge.” *Thin Solid Films.*, **464-465,** 304-307 (2004).

Novoselov K. S., A. K. Geim, S. V. Morozov, D. Jiang, Y. Zhang, S. V. Dubonos, I. V. Grigorieva and A. A. Firsov. “Electric field effect in atomically thin carbon films.” *Science* **306**, 666-669 (2004).

Okuno H., E. Grivei, F. Fabry, T. M. Gruenberger, J. G. Aguilar, A. Palnichenko, L. Fulcheri, N. Probst and J. C. Charlier. “Synthesis of Carbon Nanotubes and Nano-necklaces by Thermal Plasma Process.” *Carbon*, **42**, 2543-2549 (2004).

Ostrogorsky A. G and A. C. Marin. “Heat Transfer during Production of Carbon Nanotubes by the Electric-arc Process.” *Heat Mass Transfer* **42**, 470-477 (2006)

Pimenta M. A., G. Dresselhaus, M. S. Dresselhaus, L. G. Cancado, A. Jorioa and R. Saito; “Studying Disorder in Graphite-based Systems by Raman Spectroscopy.” *Physical Chemistry Chemical Physics* **9**, 1276-1291 (2007).

Sano N., H. Wang, I. Alexandrou, M. Chhowalla, K. B. K. Teo, G. A. J. Amaratunga and K. Iimura. “Properties of carbon onions produced by an arc discharge in water”. *Journal of Applied Physics* **92**(5) 2783-2788 (2002).

Shenderova O. A., V. V. Zhirnov and D. W. Brenner. “Carbon nanostructures.” *Critical Reviews in Solid State and Materials Sciences* **27**, 227-356 (2002).

Takikawa H., M. Yatsuki, T. Sakakibara and S. Itoh. “Carbon Nanotubes in Cathodic Vacuum Arc Discharge.” *Journal of Physics D: Applied Physics* **33,** 826-830 (2000).

Tománek D., W. Zhong and E. Krastev. “Stability of multishell fullerenes.” *Physical Review B* **48**, 15461-15464 (1993).

Wightman R.M., E. C. Paik, S. Borman and M. A. Dayton. “Evaluation of the Basal Plane of Pyrolytic Graphite as an Electrochemical Detector for Liquid Chromatography.”

Analytical Chemistry **50** (11), 1141 (1978).

Yacamán M. J., M. M. Yoshida, L. Rendón and J. G. Santiesteban. “Catalytic growth of carbon microtubules with fullerene structure.” *Applied Physics Letters* **62**, 657-659 (1993).

Yusoff H. M., R. Shastry, T. Querrioux and J. Abrahamson. “Nanotube deposition in a continuous arc reactor for varying arc gap and substrate temperature.” *Current Applied Physics* **6**, 422-426 (2006).

Table 4.1 Experimental conditions

Arc current [A]	100, 150, 200
Electrode gap distance [mm]	1, 3, 5
Arc voltage [V]	15-25
Pressure [kPa]	101.3 (Atmospheric pressure)
Plasma gas	Helium
Anode diameter [mm]	30
Cathode diameter [mm]	6
Discharge time [min]	5-10
Cathode	Graphite
Anode	Graphite

Table 4.2. The growth rate of anode deposit and the total carbon evaporation rate by varying the arc current.

Arc current [A]	100	150	200
Anode deposit growth rate [mg·min^{-1}]	0.69	1.8	3.9
Total carbon evaporation rate [mg·min^{-1}]	4.79	10.4	15.7

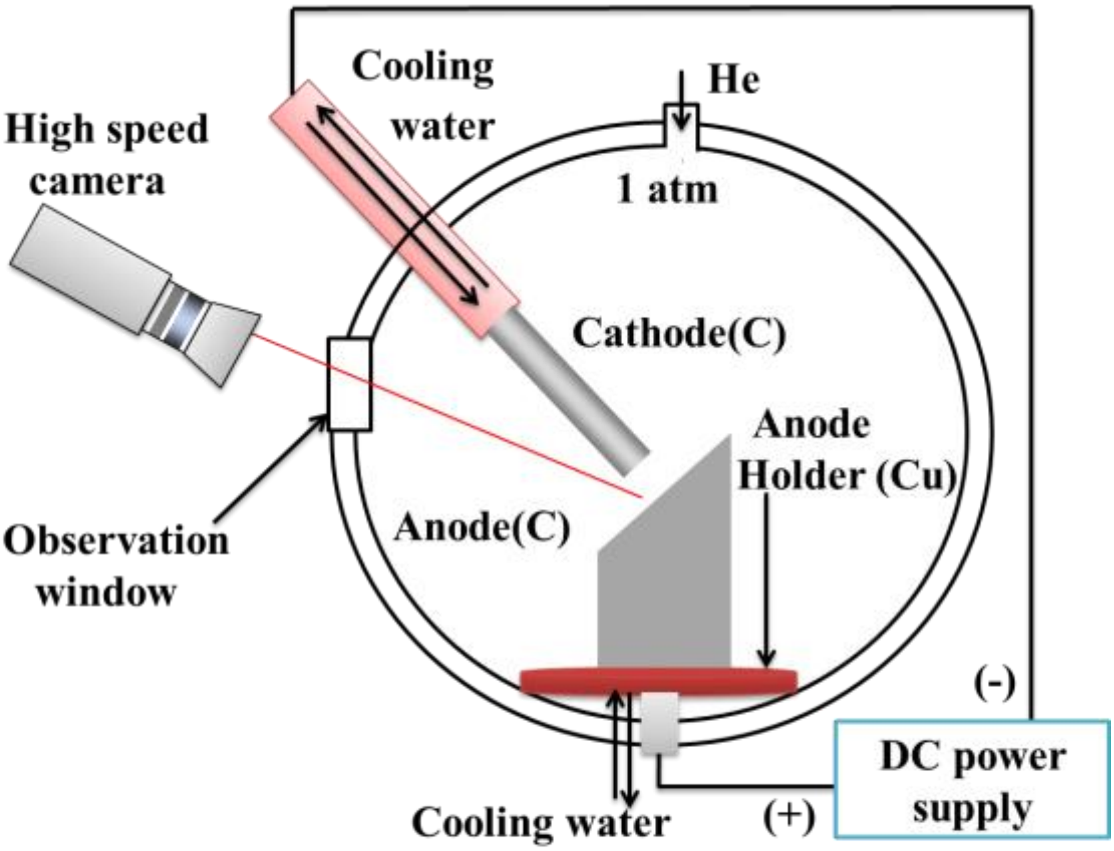

Fig. 4.1 Schematic diagram of an arc discharge system for the preparation of carbon nanomaterials by arc discharge method.

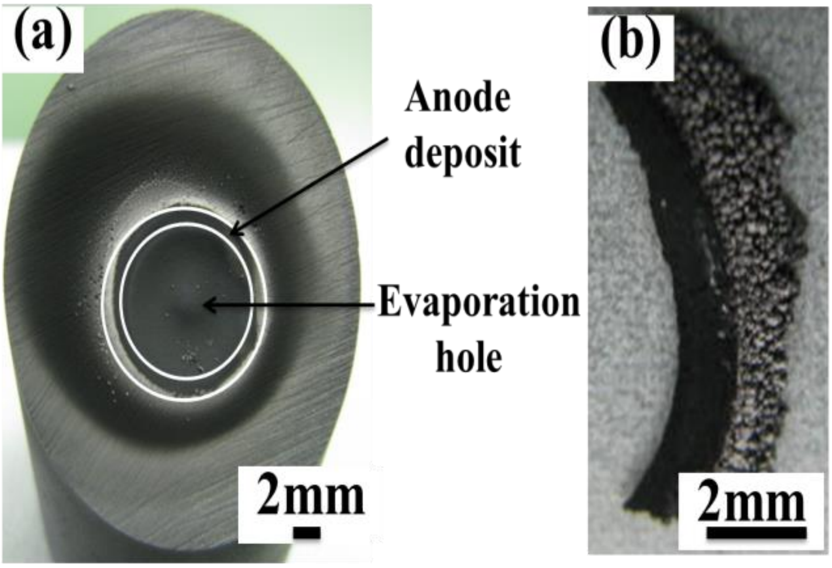

Fig. 4.2 The photos of anode after discharging (a), and a part of anode deposit (b).

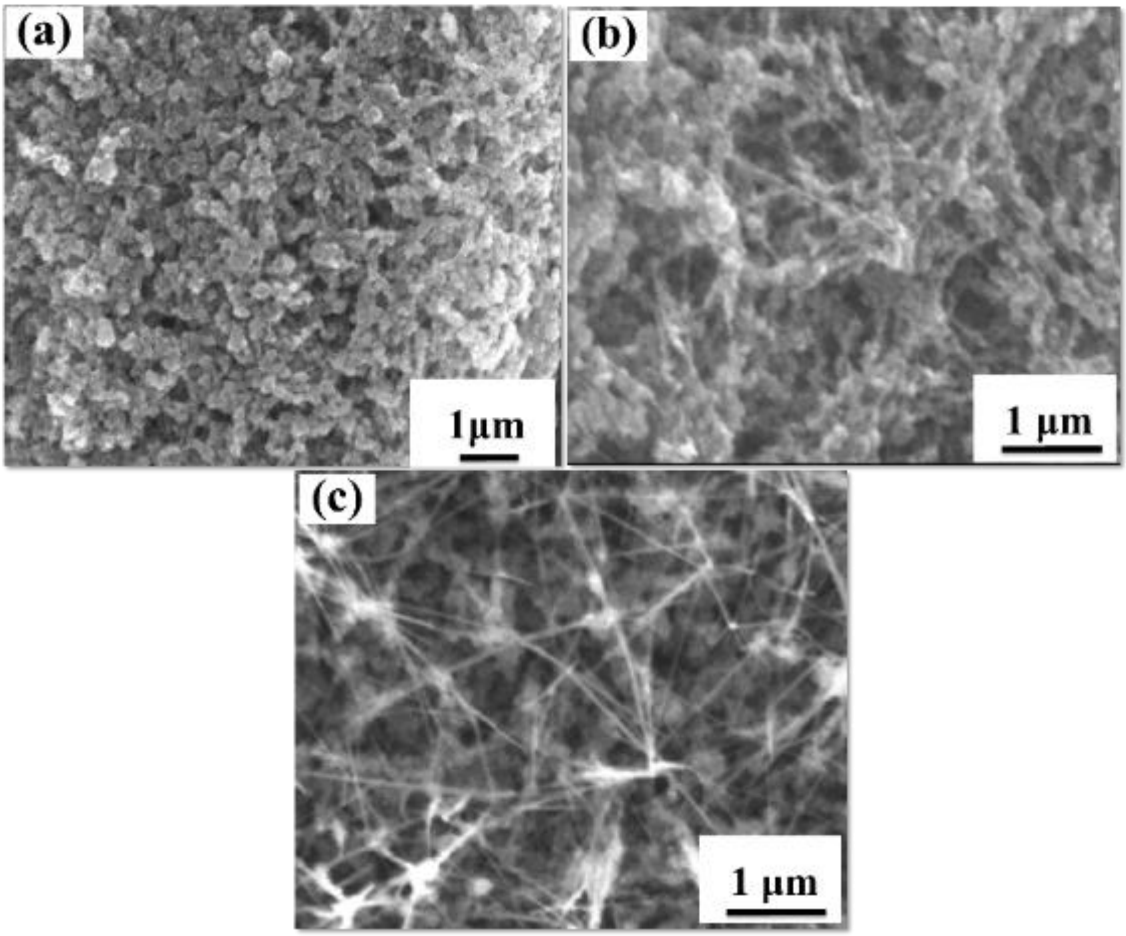

Fig. 4.3 SEM images of the anode deposit according to the arc currents of (a) 100, (b) 150, and (c) 200 A.

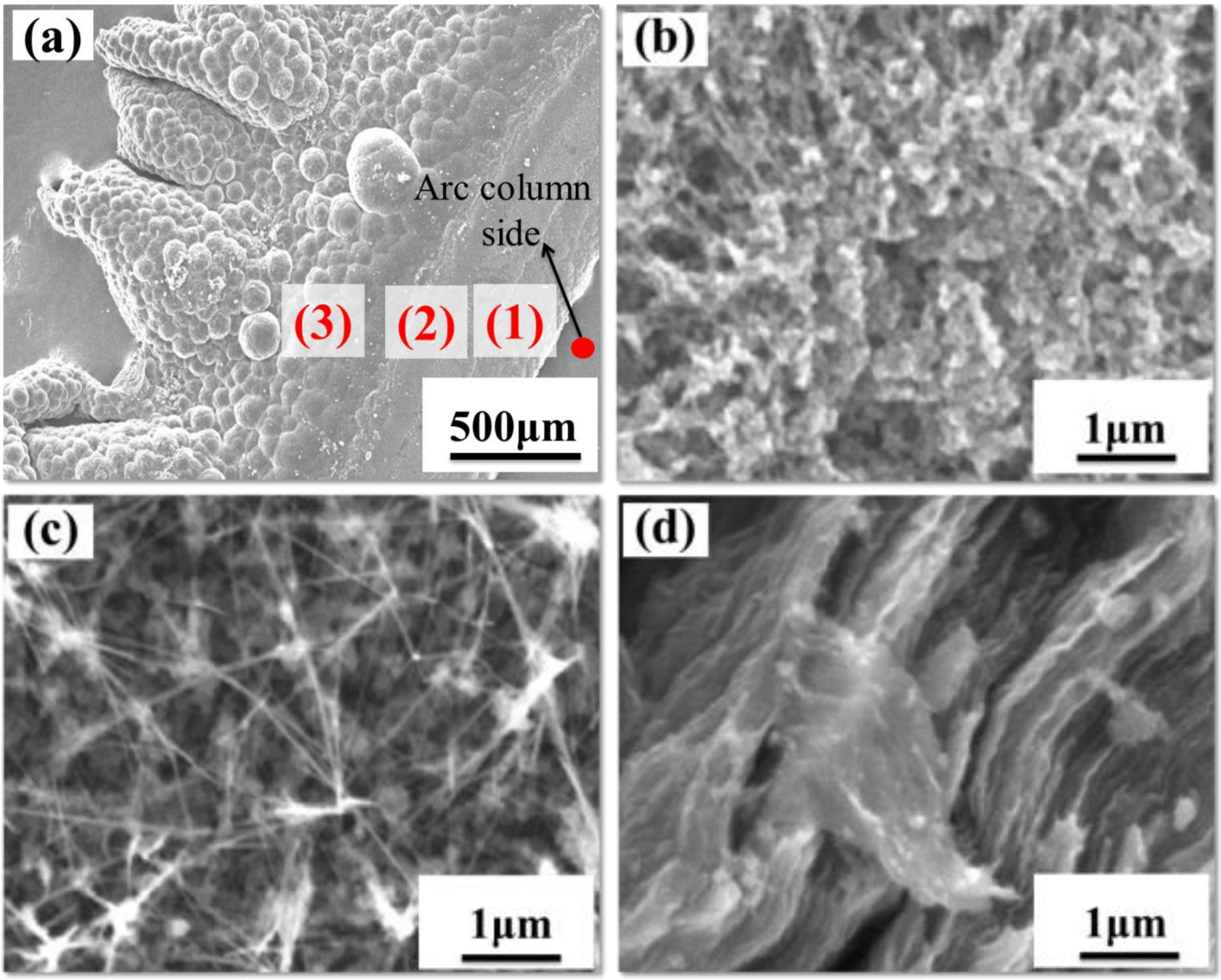

Fig. 4.4 SEM images of the anode deposit at the arc current of 200 A and the electrode gap distance of 1 mm: (a) low magnification image; (b), (c) and (d) correspond to the positions designated by (1), (2) and (3) in image (a), respectively.

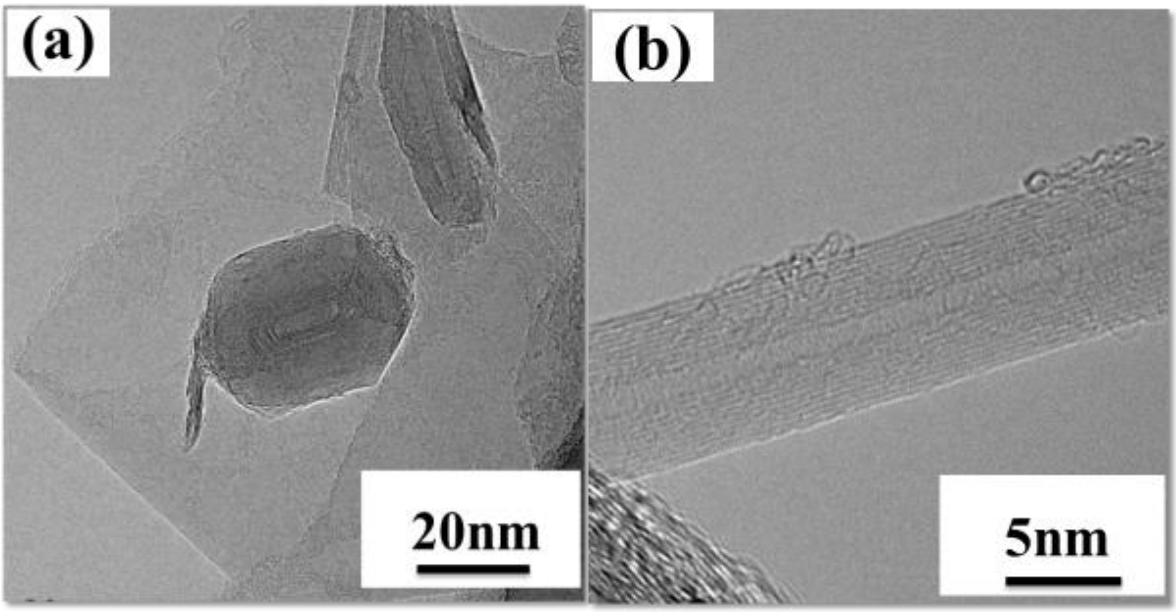

Fig. 4.5 TEM images of the anode deposit with different magnifications at the arc current of 200 A and the electrode gap distance of 1 mm.

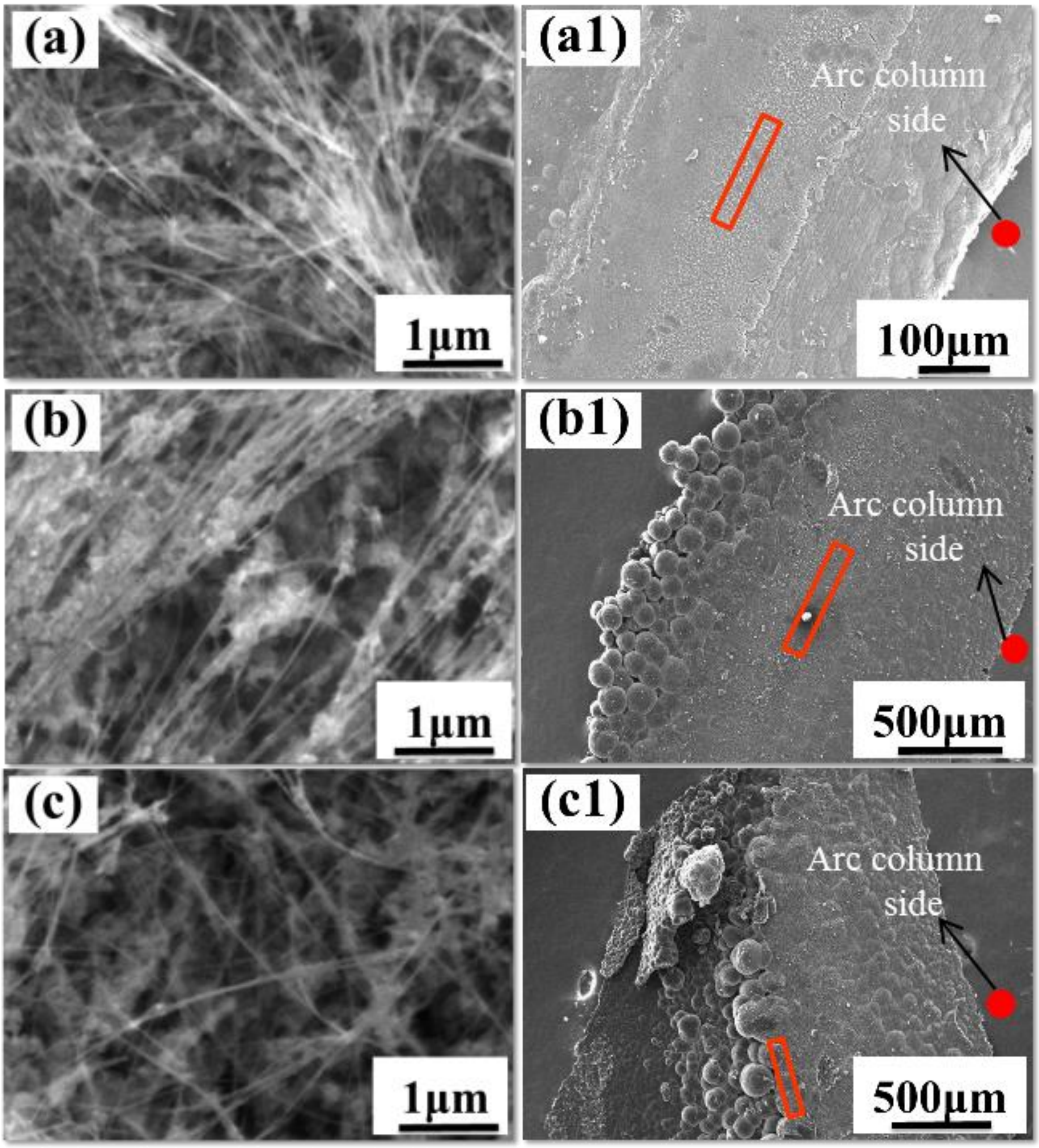

Fig. 4.6 SEM images of the MWNT obtained from the anode deposit at the fixed arc current of 200 A according to the electrode gap distance of (a) 1, (b) 3, and (c) 5 mm, respectively. The red rectangle in the low magnification images of (a1), (b1), and (c1) shows the growth region of MWNT.

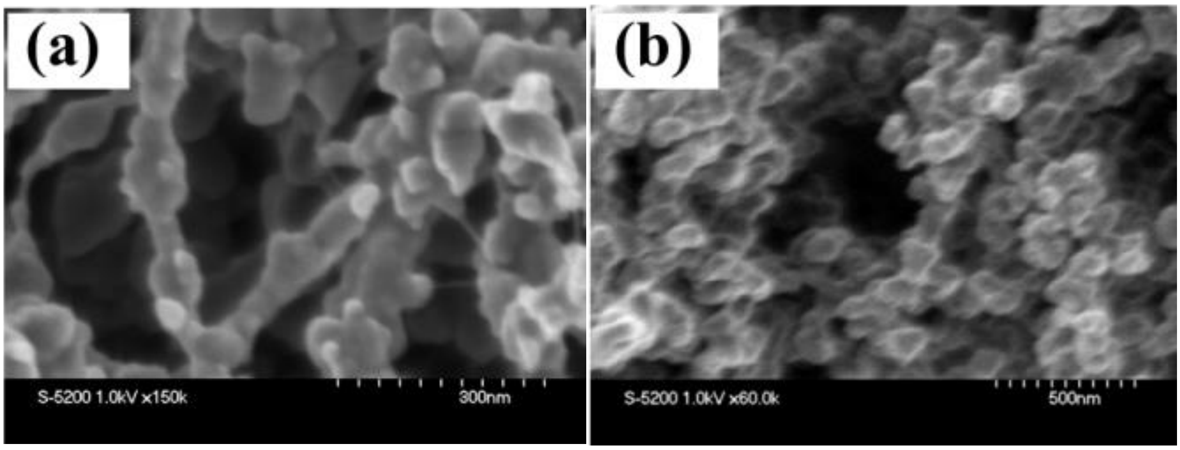

Fig. 4. 7 FE-SEM images of the products on the anode surface: (a) 3 mm and (b) 5 mm away from the side of evaporation hole.

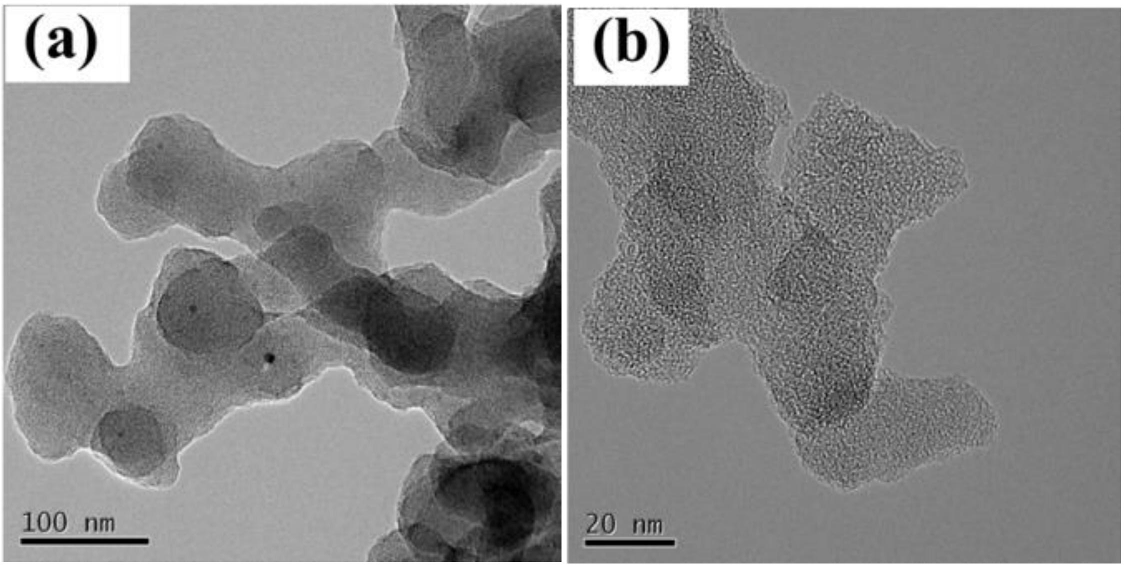

Fig. 4.8 (a) Low magnification and (b) high magnification of TEM image of the necklace-like carbon obtained on the 3 mm way from the evaporation hole.

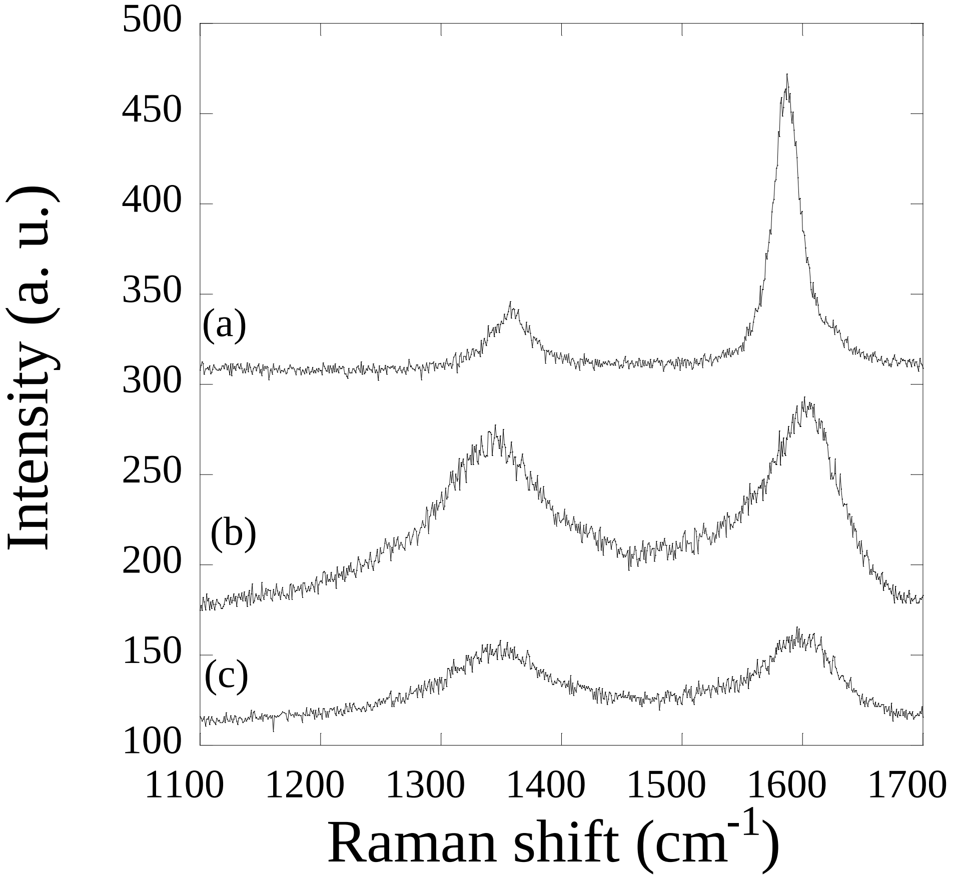

Fig. 4.9 Raman spectra of the products from different positions of the anode surface: (a) anode deposit, (b) 3 mm away from the side of anode evaporation hole, (c) 5 mm away from the side of anode evaporation hole.

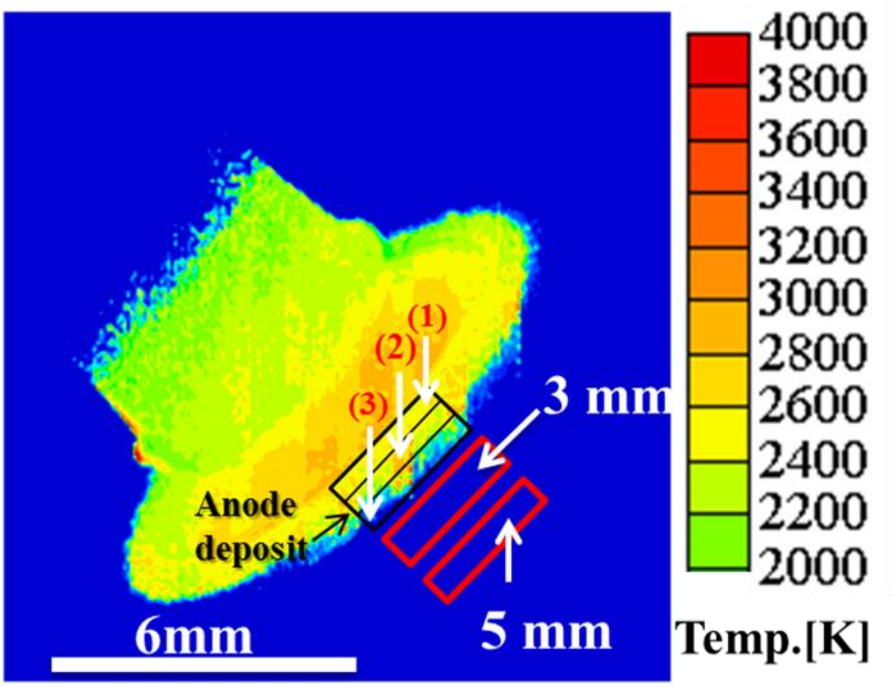

Fig. 4.10 The temperature distribution map of the anode surface when the arc current is 200 A at the fixed electrode gap distance of 1 mm. (1), (2), and (3) correspond to growth region of nano-graphite particle, MWNT, and phyrolitic graphite, respectively.

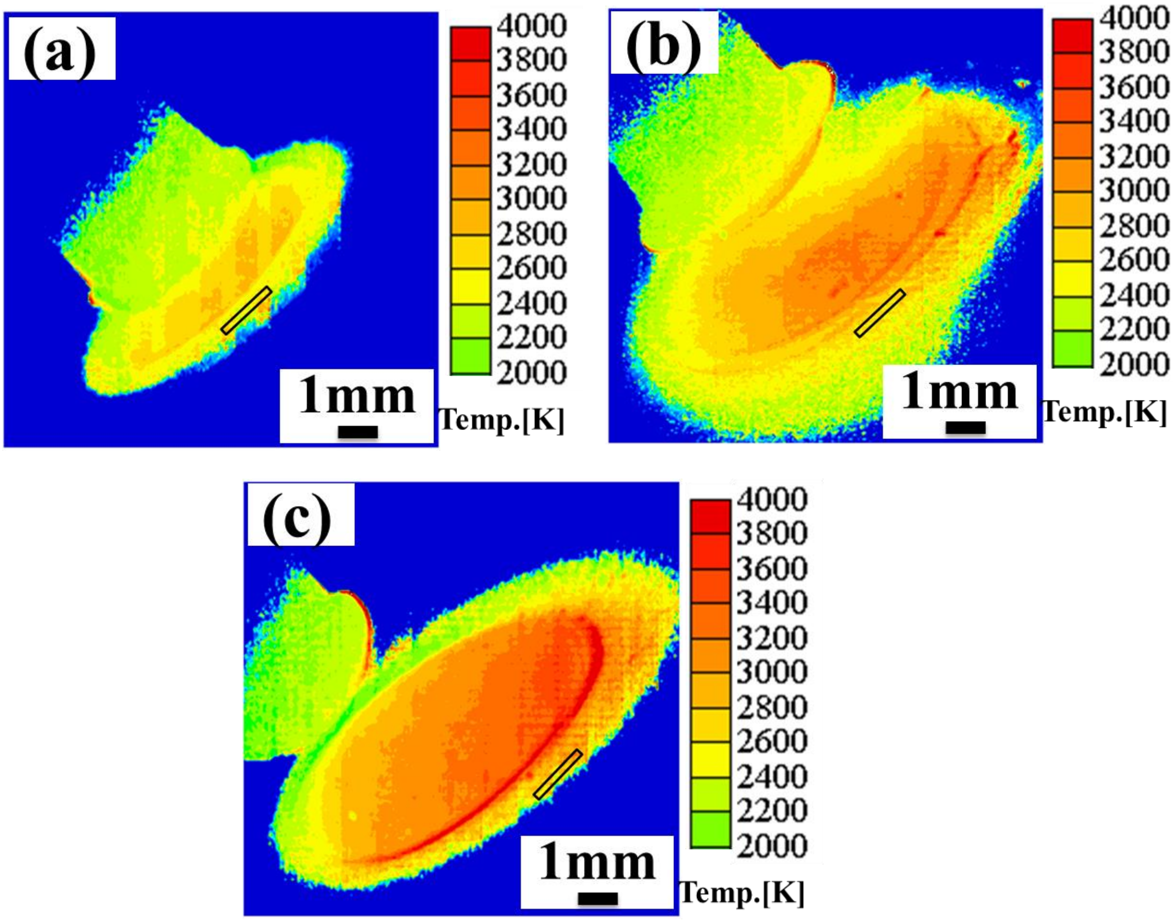

Fig. 4.11 Temperature distribution maps of the anode deposit when the electrode gap distance varied at the fixed arc current of 200 A: (a) 1, (b) 3, and (c) 5 mm, respectively.

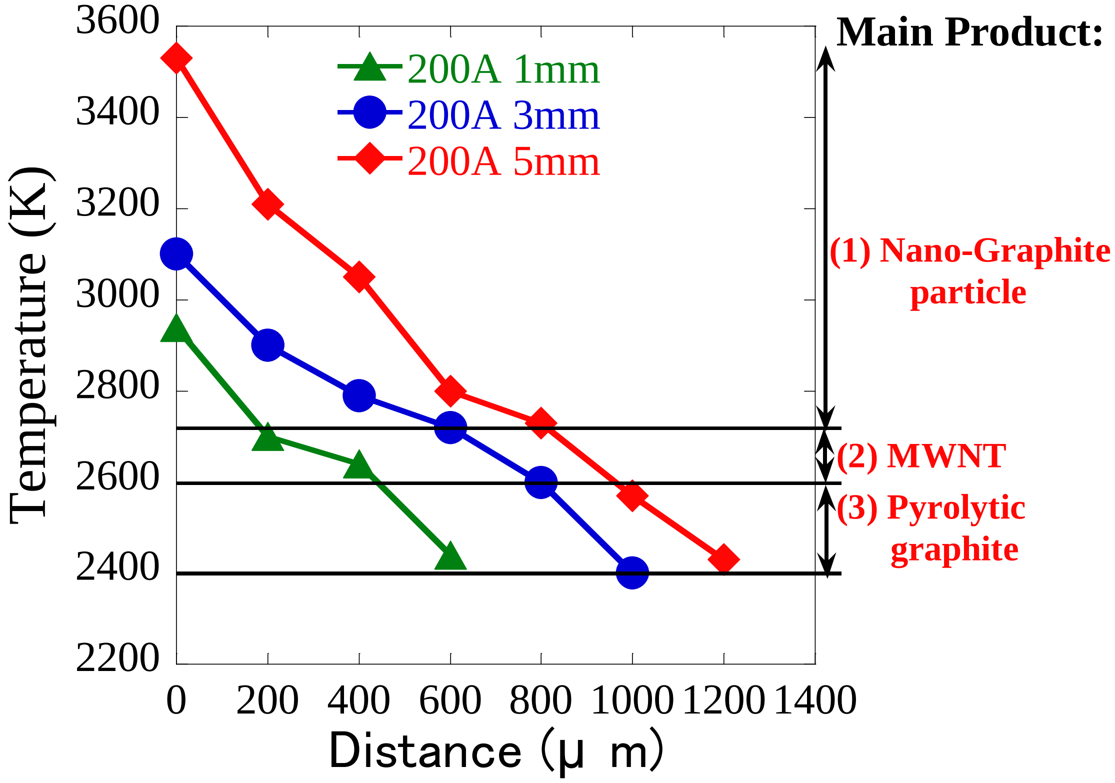

Fig. 4.12 The growth temperature of carbon nanomaterials on the anode deposit under different experimental conditions.

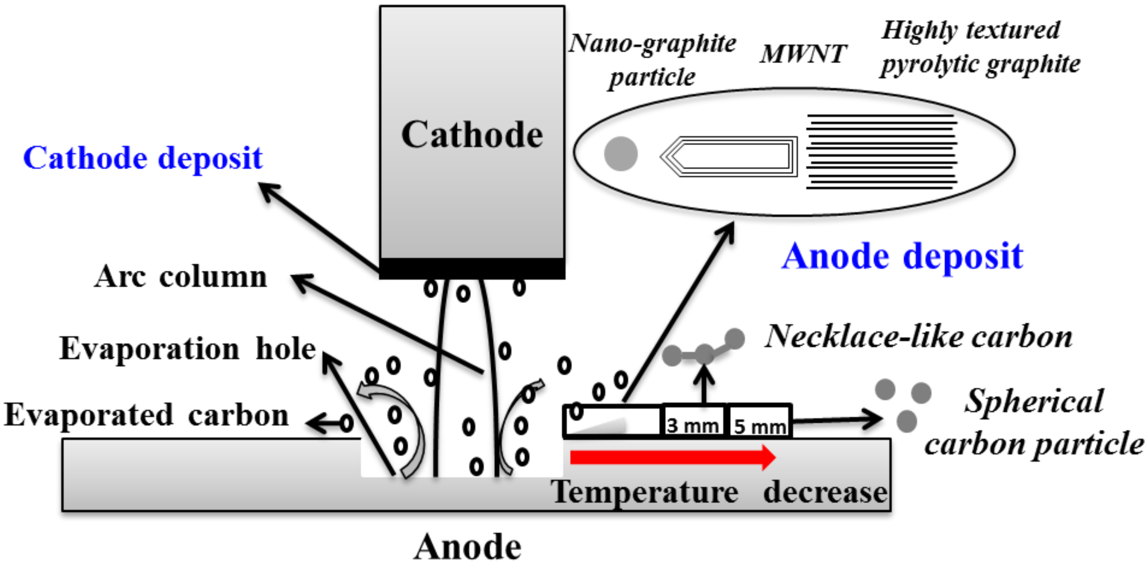

Fig. 4.13 The growth mechanisms of carbon nanomaterials on the anode surface by arc discharge method.

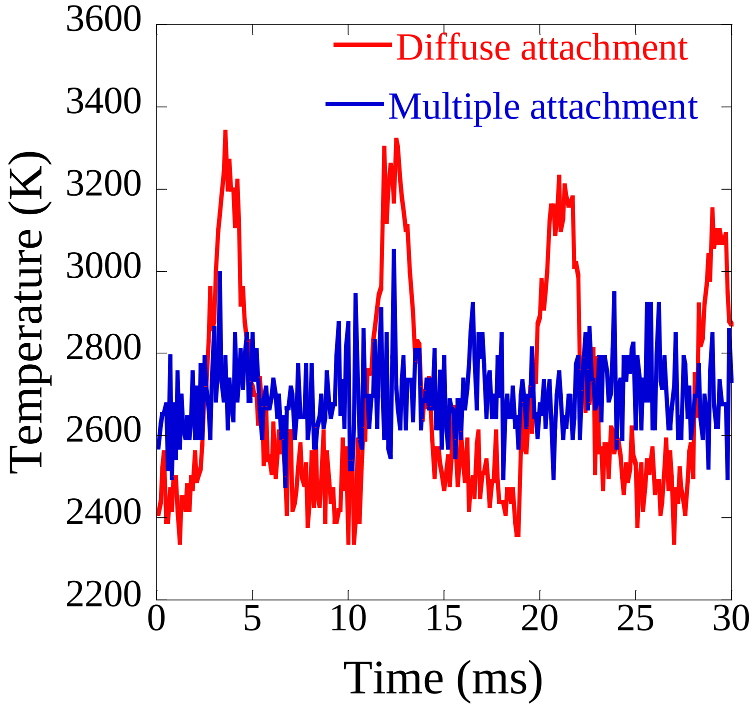

Fig. 4. 14 Temperature variation of anode deposit region with the time at different arc-anode attachment modes under helium plasma.

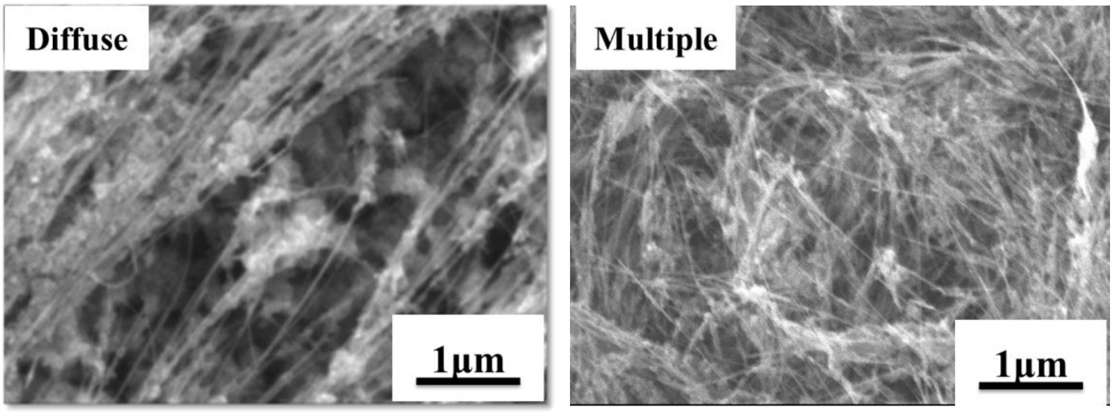

Fig. 4.15 The effect of different arc-anode attachment modes on the purity of carbon nanomaterial from the anode deposit in helium arc.

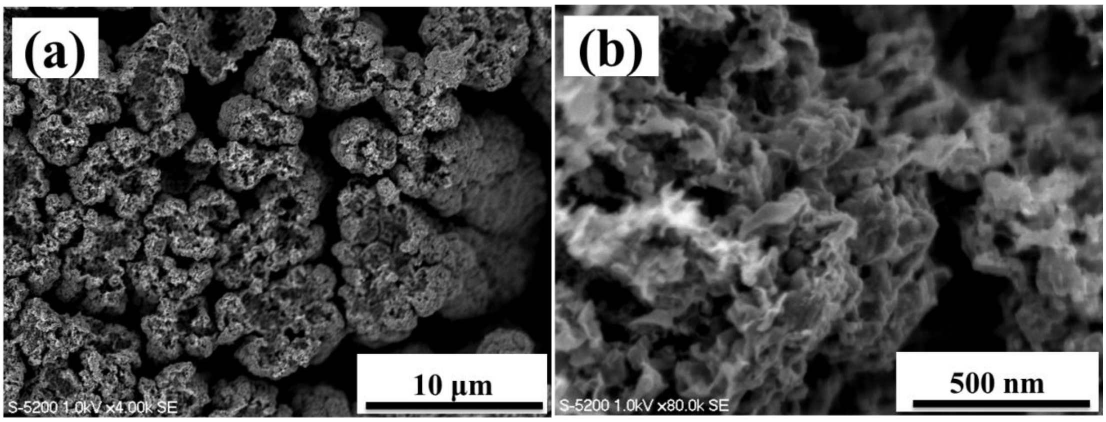

Fig. 4.16 Typical SEM images of anode deposit in argon arc at different magnifications when the arc current is 100 A and the electrode gap distance is 3 mm.

5. Preparation of Carbon Nanomaterial in the Cathode Deposit

5.1 Introduction

Cathode deposit as the main region of obtaining carbon nanomaterials attracts much attention since the discovery of MWNT by arc discharge method (Iijima 1991). Lots of carbon nanomaterials including MWNT, polyhedral graphite particles (PGPs), graphene flakes, and turbostratic graphite were grown in the cathode deposit (Liang et al. 2012; Liang et al. 2013). However, the formation mechanism of theses carbon nanomaterials in the cathode deposit is still unclear, although lots of efforts have been done. Moreover, the reports about the formation mechanism of PGPs are limited up to now, although PGP is one of main product in cathode deposit. The reason is that most of researchers paid more attention to the formation of MWNT, because MWNT has lot of applications, such as field emitter, anode material for lithium-ion battery, and hydrogen storage material and so on (Welna et al. 2011; Michael et al. 2013).

PGPs are polyhedral shape nanoparticles consisting of concentric graphitic shells. They exhibit peculiar elasticity and stability under high pressure, which could be applied as solid lubricant (Nakayama et al. 2004). Moreover, PGPs have the potential to be applied as an electron field emitter (Wang et al. 2010) and super capacitor (Pech et al. 2010; Huang et al. 2010) because of their unique curvature. Therefore, the potential applications of PGPs attract much attention.

In the past several years, the researchers provided lots of explanations about the formation mechanism of MWNTs, neglecting that of PGPs. Iijima et al proposed the open-ended growth at atomic level based on transition electron microscopy (TEM) observation, demonstrating an anisotropic growth of nanotubes (Iijima et al. 1992). The lip-lip interaction model for the stabilization of open growing edge of multi-wall nanotubes was suggested (Guo et al. 1995). In addition, the growth of carbon nanotube was explained from the kinetic point in detail (Louchev et al. 2003).

Although few mechanisms about PGPs formation have been proposed, the relationship between PGPs and MWNTs is still unclear. One researcher put forward that the bending of graphite basal planes is favorable to the formation of PGPs by eliminating the dangling band (Ugarte 1992). Although the growing condition of MWNTs was also described in Ugarte’s work, the relationship between PGPs and MWNTs was not explained. Moreover, the mechanism that carbon ions and C_n cluster are the precursors for the growth of PGPs and MWNTs from a similar initial seed was suggested (Saito et al. 1993). However, the conditions about the growth of PGPs and MWNTs were not explained in Saito’s work. Although they introduced electric field to explain the growth of the nanotubes, many experiments and simulations confirmed that the electric field is in fact neither a necessary nor a sufficient condition for the growth of carbon nanotubes (Ebbesen 1994; Colbert et al. 1994). Moreover, the mechanism was suggested as follows, the carbon atoms contribute to the formation of spherical carbon particles, while carbon ions contribute to the formation of MWNTs (Gamaly and Ebbesen 1995). The discovery of MWNTs on the anode deposit confirmed that carbon ions are not the necessary condition for the growth of MWNTs by the arc discharge method (Jones et al. 1996; Kajiura et al. 2002). Therefore, the mechanisms of PGPs and MWNTs involved remain rather poorly understood. The lack of detailed understanding of these mechanisms has been a serious impediment to apply the arc discharge method for the preparation of PGPs and MWNTs.

In the present work, the cathode deposit mainly composed of PGPs, MWNTs, graphene flakes, and turbostratic graphite was selectively synthesized by arc discharge method when changing the arc current, the anode diameter, and the electrode gap distance. The relative ratio of carbon ions to carbon radicals near the cathode tip was examined as an important parameter to control the growth of these carbon nanomaterials. Based on the different energies of the precursors, the mechanisms of carbon nanomaterial formation in the cathode deposit by the arc discharge method are suggested.

5.2. Experimental

5.2.1 Experimental Setup

The schematic illustration of an experimental apparatus for the preparation of carbon nanomaterial in the cathode deposit is shown in Fig. 5.1. The more detail information about this experimental setup was mentioned in chapter 2 and chapter 3.

5.2.2 Experimental Conditions

As shown in Table. 5.1, a graphite cathode rod (99.99%, Toyo Tanso Co. Ltd) has the fixed diameter of 6 mm. The arc discharge was operated for 8 min in helium environment at atmospheric pressure for each experimental condition. The arc current was changed by 80, 100, and 150 A at the fixed anode diameter of 30 mm and the fixed electrode gap distance of 1 mm. For the anode size effect, different diameters of 10, 15, and 30 mm were used at the fixed arc current of 100 A and the fixed electrode gap distance of 1 mm. In addition, the electrode gap distance was changed by 1, 3, and 5 mm at the fixed anode diameter of 30 mm and the fixed arc current of 100 A.

The anode was evaporated after igniting the plasma due to the high heat flux from the arc discharge. Then, evaporated carbon was deposited on the cathode surface forming the cathode deposit. As demonstrated in Fig. 5.2, the cathode deposit composed of a grey outer shell and a dark inner core was formed by the evaporated carbon from the anode. The inner core as the main region for the growth of carbon nanomaterials was investigated. In addition, the materials obtained from different regions of the experimental apparatus were analyzed to examine the effect of carbon species and temperature on the products. Additional sampling positions of carbon product were inner surface of the chamber, top surface of the anode holder, side surface of the cathode, and top surface the anode.

5.2.3 Spectroscopic Measurements

As shown in Fig. 5.3, an optical spectrometer (iHR-550, HORIBA Jobin Yvon) with a CCD detector (Synapse, HORIBA Jobin Yvon) was used to collect the information of excited species in the plasma. An optical fiber was placed at the window of the arc chamber to measure the plasma emission near the cathode tip. Based on the database of the National Institute of Standards and Technology (NIST), the emission species were identified.

5.2.4 Sample Characterization

The morphological and structural characterization of as prepared products were examined by field emission scanning electron microscopy (FE-SEM: S-5200, Hitachi), scanning electron microscopy (SEM: JSM-6610LA, JEOL), transmission electron microscopy (TEM: JEM-2010F, JEOL), and Raman spectroscopy (NRS-2100, JASCO) with 514.5 nm Ar^+ laser excitation. In the analysis of Raman spectrum, three positions for each sample were measured, and the average relative intensity was calculated for comparison.

5.3. Results and Discussion

5.3.1 Effect of Arc Current

Fig. 5.4 indicates FE-SEM images of the inner core of cathode deposit with different arc currents from 80 to 150 A at the fixed anode diameter of 30 mm. As shown in Fig. 5.4 (a), the cathode deposit is composed of dominant MWNTs with a few PGPs when the arc current is 80 A. It is clearly seen in Figs. 5.4 (b) and (c) that the main products are PGPs in relatively high arc current conditions of 100 and 150 A. Typically, researchers study micrographs and rely on counting the number of particles to determine approximate purity of particle content (Coleman et al. 2000). As shown in the SEM image, the purity of PGP can reach to 92%. In addition, the PGPs stack each other and the shape of PGPs turn into irregular in the highest arc current of 150 A.

The internal structure of PGPs at the arc current of 100 A was investigated by TEM. As shown in Fig. 5.5 (a), particles are obviously composed of overlapping PGPs with small amount of carbon nanotubes. Most of particles are pentahedrons and hexahedrons with the average particle size of 20-30 nm. In addition, Fig. 5.5 (b) reveals that PGP is made up of a faceted concentric graphitic sheet, enclosing a void in the center. The size of internal empty space is about 2 nm, which is larger than that of carbon onion (Ugarte 1995). On the other hand, the interlayer spacing of 0.330 nm between the sheets of PGP is close to the ideal graphitic interlayer space of 0.335 nm, which indicates that PGPs have graphitic structure.

The typical Raman spectra of the inner parts of cathode deposits are shown in Fig. 5.6 according to the arc current. The Raman spectra of MWNTs are shown in Fig. 5.6 (a). There are three distinct peaks located at 1350, 1584, and 2710 cm^{-1}, corresponding to the D band, the G band, and the 2D band, respectively. The appearance of the D band is attributed to the induction of significant defects or disorder in nanostructures (Ferrari 2007). The G band is common to all sp^2 carbon forms, corresponding to high frequency E_{2g} first-order mode (Pimenta et al. 2007). Furthermore, the 2D band can be assigned to an overtone of the first order mode around 1350 cm^{-1} which is related to a phonon near K point in graphene (Nemanich and Solin 1979). It is activated by the double resonance (DR) progress (Dresselhaus et al. 2010). As shown in Fig. 5.6 (b), similar results with MWNTs are also observed in the Raman spectra of PGPs. It is expected that the physical origin of these bands for PGPs may be similar to that of MWNTs. In PGPs case, however, the intensity of 2D overtone is found to be 4.5 times stronger than that of first-order G band. This phenomenon is explained by the DR Raman scattering (Obraztsova et al. 1998; Dresselhaus et al. 2005). PGP with highly curvature structure induces the coupled coherent electronic states between the neighboring carbon layers, resulting in the enhancement of the DR Raman. Although graphene also has a stronger 2D band than G band, PGPs have a much broader and up-shifted 2D band with respect to graphene (Ferrari et al. 2006). Therefore, according to this unique Raman characteristic in PGPs, the ratio of the integrated intensity of the 2D band relative to the G band (I_{2D}/I_G) could be employed to estimate the relative ratio of PGPs in the cathode deposit. In addition, as shown in Fig. 5.6 (c), the products exhibit similar Raman spectra to Fig. 5.6 (b) when the arc current is 150 A, the intensity of 2D overtone is found to be stronger than that of first-order G band.

As shown in Fig 5.7, the ratios of the integrated intensities of the D band relative to the G band (I_D/I_G) and the 2D band relative to the G band (I_{2D}/I_G) in Raman spectra are calculated to explain structural variation of the products by changing the arc current. The intensity ratio of I_D/I_G provides an index to evaluate the quality of the carbon material. A small I_D/I_G value means the higher structural perfection in the products. The I_D/I_G value changes from 0.095 to 0.10 when the arc current changes from 80 to 100 A, indicating that MWNTs and PGPs have similar structure perfection. The I_D/I_G ratio is 0.15 when the arc current reaches to 150 A. According to FE-SEM results, high current results in the irregular form in the products, which leads to the reduction of their structural perfection. Compared with the carbon allotropes prepared by other methods (Sveningsson et al. 2001; Inoue et al. 2012), all of the samples have the low I_D/I_G value.

It indicates that the arc discharge is an effective method to prepare carbon allotropes with low defects. Moreover, the intensity ratio of I_{2D}/I_G could be used to identify the relative ratio of PGPs in the cathode deposit. The I_{2D}/I_G value reaches to the maximum of 2.89 when the arc current is 100 A. The highest I_{2D}/I_G value indicates the highest ratio of PGPs in the products, and such result from the Raman spectra is consistent with the FE-SEM result in Fig. 5.4. The reason for the highest ratio of PGPs in the products will be explained in the discussion section.

5.3.2 Effect of Electrode Gap Distance

Fig. 5.8 shows FE-SEM images of the inner core of cathode deposit with different electrode gap distances from 1 to 5 mm. Fig. 5.8 (a) indicates that the cathode deposit is mainly composed of PGPs with fewer nanotubes at the short electrode gap distance of 1 mm. As shown in Fig. 5.8 (b), the products are the mixture of PGPs and graphene flakes when the electrode gap distance is increased to 3 mm. Although the main products are still PGPs in the case of 3 mm, these PGPs have irregular shapes and sizes compared with those in the case of 1 mm. In addition, Fig. 5.8 (c) shows the main products are graphene flakes and few PGPs when the electrode gap distance is further increased to 5 mm.

TEM images in Fig. 5.9 provide the evidence for the internal structure of different cathode deposits by changing the electrode gap distance. Figs. 5.9 (a), (b), and (c) are the TEM results for the electrode gap distances of 1, 3, and 5 mm, respectively. Figs. 5.9 (a1), (b1), and (c1) correspond to the high magnification images of Figs. 5.9 (a), (b), and (c), respectively. As discussed in the section of 5.31, Fig. 5.9 (a) shows the products are PGPs. The average particle size is about 20-30 nm, and most of them are pentahedrons and hexahedrons. Figure 5.9 (b) and Fig. 5.9 (b1) indicate that the products are composed of PGPs and graphene flakes, and the PGPs have the sizes about 40-50 nm which is larger than that produced in the short electrode gap distance of 1 mm. However, graphene flakes that are composed of few layer graphenes are observed in Fig. 5.9 (c) of the longest electrode gap distance. In addition, a turbostratic graphite with different inter planar distances is found in Fig. 5.9 (c1).

Fig. 5.10 shows Raman spectra of the cathode deposits at different electrode gap distances. As discussed in previous section, a strong G band at 1584 cm^{-1}, a peak D band appearing around 1350 cm^{-1}, and 2D band at 2710 cm^{-1} are obtained. The narrowness of full-width at half-maximum (FWHM, 20 cm^{-1}) in the G band of PGPs coincides with that of highly oriented pyrolytic graphite (HOPG), which points to the high degree of structural perfection of graphitic network in shells (Obraztsova et al. 1998). The Raman spectrum for the electrode gap distance of 3 mm is similar with that of 1 mm. However, obviously low intensity ratio of I_{2D}/I_G is found when the distance reaches 5 mm. Therefore, the product in 5 mm case has a significant structural variation from the product in 1 and 3 mm cases.

The ratios of the integrated intensity of the D band relative to the G band (I_D/I_G) in Fig. 5.11 (a) and the 2D band relative to the G band (I_{2D}/I_G) in Fig. 5.11 (b) are calculated to explain structural variation of the products when the electrode gap distances are changed. The intensity ratio of I_D/I_G provides an index to evaluate the quality of the carbon material. The lower of this value means the higher structural perfection of the material. In Fig. 5.11 (a), the defects increase with increasing the electrode gap distance, indicating that PGPs have better structural perfection than graphene flakes and turbostratic graphite. The intensity ratio of I_{2D}/I_G in Fig. 5.11 (b) is used to identify the relative ratio of PGPs in the products. Therefore, the content of PGPs in the product is decreased with increasing the electrode gap distance.

5.3.3 Effect of Anode Diameter

The anode diameter has a significant effect on the products in the present work. Fig. 5.12

presents FE-SEM images of the inner core of cathode deposit with different anode diameters from 10 to 30 mm at the fixed arc current of 100 A. It is composed of PGPs dominantly with a few nanotubes. As illustrated in Figs. 5.12 (b) and (c), the cathode deposits consist of nanotubes with considerable high purity, wherein the purity of MWNTs increases with reducing the anode diameter, reaching to 85% by counting the number of tubes.

Fig. 5.13 shows typical Raman spectra of the cathode deposits synthesized at different anode diameters. Figs. 5.13 (a), (b), and (c) correspond to the anode diameter of 30, 15, and 10 mm, respectively. The relative intensity of the 2D band is not stronger than the G band in MWNTs, because the double resonance (DR) progress is not significant in MWNTs. Therefore, the I_{2D}/I_G reduces with decreasing the anode diameter, because the content of MWNTs increases in the case of small anode diameter. The intensity of the D band in MWNTs reduces with decreasing the anode diameter in the comparison between Fig. 5.13 (b) and Fig. 5.13 (c).

Moreover, the structural perfection of MWNTs could be identified by the intensity ratio of I_D/I_G as shown in Fig. 5.14. The I_D/I_G ratio decreases from 0.23 to 0.049 when the anode diameter reduces from 15 to 10 mm. The Raman spectra indicate that the MWNTs have the high purity and good structural perfection at the smallest anode diameter of 10 mm. These Raman spectroscopy results are in good agreement with FE-SEM results.

5.3.4 Formation Mechanism of Carbon Nanomaterial in the Cathode Deposit

In order to investigate the effect of carbon precursor on the formation of different carbon nanomaterial in the cathode deposit, the optical emission spectrum measurements were conducted.

Fig. 5.15 shows the calibrated optical emission spectra of the plasma under different arc currents to compare the relative ratio of carbon ions to carbon radicals near the cathode tip. The emission line of atomic carbon (CI) is at 247.8 nm, while peaks located at 283.6, 318.9, 392.1 and 426.7 nm are identified as singly ionized carbon (CII). Atomic helium peaks are located at 385.2, 402.6 and 447.1 nm. At last, the peak around 385.2 nm comes from C_2. In the present work, the major peaks of carbon ions at 283.6 nm and that of carbon radicals at 247.8 nm were compared to evaluate the relative concentration of carbon ions to carbon radicals ($I_{C(II)}/I_{C(I)}$).

Fig. 5.16 presents that the relative intensity ratio of carbon ions to carbon radicals ($I_{C(II)}/I_{C(I)}$) increases from 0.34 to 0.60 when the arc current changes from 80 to 150 A. The input power increases from 1.2 to 2.25 kW when the arc current changes from 80 to 150 A, resulting in the increase of plasma temperature. The temperature plays an important role in controlling the relative concentration of carbon ions to carbon radicals ($I_{C(II)}/I_{C(I)}$). The higher plasma temperature leads to the higher relative concentration of carbon ions to carbon radicals ($I_{C(II)}/I_{C(I)}$).

Assuming that plasma is in local thermodynamic equilibrium state, Saha equation is used to obtain the ionization fractions of individual species (Boulos et al 1994).

$$\frac{n_e n_{r+1}}{n_r} = \frac{g_e G_{r+1}}{G_r}(\frac{2\pi m_e kT}{h^2})^{3/2}\exp(-E_{r+1}/kT)$$

where, n_{r+1} is density of atoms in ionization state $r+1$ (m^{-3}); n_r is density of atoms in ionization state r (m^{-3}); n_e is density of electrons (m^{-3}); g_e is the statistical weight of electrons (is equal to 2); G_r is the partition functions of r-states; G_{r+1} is the partition functions of $r+1$-states; m_e is mass of the electron (kg); E_{r+1} represents the energy required for transforming an r-times ionized atom into an $r+1$-times ionized atom (J); T is temperature (K); h is Planck's constant (JS); k is Boltzmann constant (J/K).

$$G_r = G_r^{trans} G_r^{rot} G_r^{vib} G_r^{int}$$

$$G_{r+1} = G_{r+1}^{trans} G_{r+1}^{rot} G_{r+1}^{vib} G_{r+1}^{int}$$

where, G_r^{trans} is the transition partition function of r-states, G_r^{rot} is the rotation partition function of r-states, G_r^{vib} is the vibration partition function of r-states, G_r^{int} is the internal partition function of r-states, G_{r+1}^{trans} is the transition partition function of $r+1$-states, G_{r+1}^{rot} is the rotation partition function of $r+1$-states, G_{r+1}^{vib} is the vibration partition function of $r+1$-states, G_{r+1}^{int} is the internal partition function of $r+1$-states. The G_r^{trans} is equal to G_{r+1}^{trans}, G_r^{rot} is equal to G_{r+1}^{rot} , and G_r^{vib} is equal to G_{r+1}^{vib}.

$$\frac{n_e n_{r+1}}{n_r} = \frac{2G_{r+1}^{int}}{G_r^{int}}(\frac{2\pi m_e kT}{h^2})^{3/2}\exp(-E_{r+1}/kT)$$

Rewriting the Saha equation for the first ionization($r = 0$, $n_e = n_1$), one finds that

$$\frac{n_e^2}{n_0} = \frac{2G_1^{int}}{G_0^{int}}(\frac{2\pi m_e kT}{h^2})^{3/2}\exp(-E_I/kT)$$

$$n = n_o + n_e \text{ (}n_0\text{ denotes of all neutral particles)}$$

$$P = (n + n_e)kT$$

where, P is pressure (Pa); T is temperature (K). Temperature was calculated by OES results. The ionization degree α can be calculated based on the following definition.

$$\alpha = n_e/n_o + n_e$$

$$\frac{\alpha^2}{1-\alpha^2} = \frac{2G_1^{int}}{G_0^{int}}\frac{(2\pi m_e)^{3/2}(kT)^{5/2}}{h^3 p} \exp(-E_\mathrm{I}/kT)$$

G_1^{int}/G_{r0}^{int} is equal to 0.6 for carbon (Allen C.W. 1973). Therefore, the ionization degree can be calculated. Fig. 5.17 indicates the ionization degree at different arc currents. The ionization degree increases from 0.55 to 0.83 when the arc current is changed from 80 to 150 A. It is attributed to the plasma temperature, higher temperature contributes to higher ionization degree.

Fig. 5.18 shows the calibrated optical emission spectra of the plasma under different electrode gap distances to compare the relative ratio of carbon ions to carbon radicals. Because it is difficult to obtain the emission spectrum in the shortest electrode gap distance of 1 mm, the emission spectrum of 2 mm was chosen for comparison. In Fig. 5.19, the relative intensity ratio of carbon ions to carbon radicals ($I_{\mathrm{C(II)}}/I_{\mathrm{C(I)}}$) increases from 0.47 to 0.88 when the electrode gap distance is changed from 2 to 5 mm. According to above comparison, the lowest relative intensity ratio of carbon ions to carbon radicals ($I_{C(II)}/I_{C(I)}$) is expected at the shortest electrode gap distance of 1 mm.

The increase of relative intensity ratio of carbon ions to carbon radicals could be explained as follows. The experimental results in Table 5.2 indicate that the cathode deposit growth rate is similar even in the change of carbon evaporation rate according to the electrode gap distance. Because carbon radicals scatter from the plasma region during attaching to the cathode in the case of long electrode gap distance, while positively charged carbon species have the large opportunity to attach to the cathode surface due to the effect of electric field. Therefore, the relative concentration of carbon ions to carbon radicals increases with increasing the electrode gap distance. In addition, the input power increases from 1.5 to 2.5 kW when the electrode gap distance changes from 1 to 5 mm, resulting in the increase of plasma temperature. The temperature has a significant effect on the relative concentration of carbon species. According to the thermodynamic calculation, the main species are carbon ions and carbon radicals in the thermal plasma temperature region (10000-15000 K), and the higher temperature leads to the higher relative concentration of carbon ions. Fig. 5.20 shows the ionization degree results calculated by the Saha equation at different electrode gap distances, the same tendency with the ratio of carbon ion to carbon radical measured by OES is obtained, since plasma temperature increases with increasing electrode gap distance.

The calibrated optical emission spectra of the plasma under different anode diameters and the relative intensity ratio of carbon ions to carbon radicals ($I_{C(II)}/I_{C(I)}$) are shown in Fig. 5.21 and Fig. 5.22, respectively. As shown in Fig. 5.22, the relative intensity ratio of carbon ions to carbon radicals ($I_{C(II)}/I_{C(I)}$) reduces from 0.37 to 0.18 when the anode diameter decreases from 30 to 10 mm. This result could be explained by different heat transfer according to the anode diameter. The anode is a heat conductive long rod that is cooled by contacting with ambient helium from the side area by the convection. Moreover, the anode is also cooled by the cooling water from its bottom side by the conduction. Both of convection and conduction increase with increasing the contact area including lateral and bottom surfaces. The contact area increases with increasing the anode diameter, thus the larger anode diameter means the larger anode cooling effect. According to the energy balance equation for carbon evaporation (Fetterman et al. 2008), the carbon evaporation rate decreases with increasing the anode diameter. Measured evaporation rates were 4.8, 10.6, and 27.3 $\mathrm{mg \cdot min^{-1}}$ for different anode diameters of 30, 15, and 10 mm, respectively. Since the same input power was supplied, the higher evaporation rate in the smaller anode diameter contributes to the lower temperature of each particle. Moreover, the higher evaporation rate results in the significant variation of the plasma, which reduces the temperature of the evaporation particles. Therefore, the relative intensity ratio of carbon ions to carbon radicals reduces with increasing the anode diameter. Fig. 5.23 indicates the ionization degree calculated by the Saha equation when changing anode diameter. The ionization degree increases with increasing anode diameter; it can be explained by the plasma temperature variation at different anode diameters. Larger anode diameter leads to higher plasma temperature and larger ionization degree due to low evaporation rate.

Compared with carbon radicals, the carbon ions have higher total energy. The total energy of carbon radicals is the contribution of the dissociation energy and the kinetic energy. However, the total energy of carbon ions is the contribution of the dissociation energy, the kinetic energy and the ionization energy. Moreover, the acceleration energy contributes to the total energy of carbon ions due to the effect of electric field. Therefore, the energy of carbon species could be evaluated by the relative intensity ratio of carbon ions to carbon radicals. The higher ionization degree of carbon indicates the higher energy of carbon species. According to the different energies of the carbon species, the mechanisms of different carbon nanomaterial in the cathode deposit could be explained.

In order to investigate the effect of carbon species and temperature on the product in arc discharge method, the products obtained from different regions were investigated. Figs. 5.24 (a)-(d) show SEM images of nanostructured carbon materials obtained from inner wall of the reaction chamber, top surface of the anode holder, side surface of the cathode, and top surface of the anode, respectively. Figs. 5.24 (a) and (b) indicate that the samples are composed of amorphous carbon with irregular porous structure. It can be explained by the quenching effect, because both the chamber and the anode holder are water-cooled, the extremely sharp temperature gradient from plasma region to the low temperature region is essential to cause rapid solidification of the vaporized carbon, forming amorphous carbon. On the other hand, the sample obtained from the side surface of the cathode in Fig. 5.24 (c) has relatively better crystal-like morphology. Fig. 5.24 (d) indicates the product on anode surface is spherical particle surrounded by amorphous carbon. This structure could be attributed to the annealing effect because of high temperature on the anode surface. Fig. 5.24 (d) shows the best crystal-like morphology compared with products from the other regions. Therefore, this sample was chosen to take further TEM analysis for the investigation of microstructure in detail.

Fig. 5.25 shows particles on the anode surface as obtained by TEM. As shown in Fig. 5.25 (a), most of the products are composed of spherical nanoparticles with diameters about 20 nm. Furthermore, no obvious internal structure could be observed in the high magnification image of Fig. 5.25 (b). It indicates that high temperature condition on the anode surface is not necessary for the growth of PGPs.

As shown in Fig. 5.26, the following mechanism about the formation of different carbon nanomaterials in the cathode deposit could be explained in the present work. Firstly, carbon atoms evaporated from anode collide and coagulate with each other to grow into a cap structure with multi-layers as a tip seed. The inter layers will be stabilized from van der Waals interaction between shells (Ugarte 1992). When the carbon radicals are the dominant species near the cathode region, this cap structure will grow into MWNTs by the incorporation of lower energy species of carbon radicals to the active edge site of dangling bonds. Because, the low energy species of carbon radicals is enough to grow into thermodynamically stable material like as MWNTs. Since the PGPs are thermodynamically unstable material compared with the MWNTs, the carbon species with higher energy is required. Therefore, relatively higher concentration of carbon ions to carbon radicals contributes to the growth of PGPs. PGPs prefers to be obtained than the MWNTs when the carbon ions is the dominant species, because PGPs could reduce the active dangling bonds edge site in virtue of the irradiation of carbon ions (Silinskas et al. 2008). Therefore, the higher energy of the precursors contributes to the formation thermodynamically unstable material such as PGPs. Moreover, the energy level of the carbon species may be a critical parameter that determines the self-assembly of different carbon allotropes. MWNTs are not able to self-assemble and the main products are PGPs when the energy of the species is above a certain threshold value.

The precursors with higher average energy contribute to the formation of thermodynamically unstable materials when increasing the electrode gap distance. In contrast to PGPs, the graphene flakes are thermodynamic unstable (Shenderova et al. 2002), therefore, the formation of graphene flakes and turbostratic graphite could be explained by the higher average energy of precursors in the longer electrode gap distance. It is suggested that these higher energy species could support the tip structure to grow along the planar direction without bending the basal plane to eliminate the dangling bands, which is similar to the point of view of some researches (Volotskova et al. 2010; Guan et al. 2011). As a result, it grows into the graphene flakes (Scalese et al. 2010). However, considering the carbon species with different energy attach to the tip structure from different directions may destroy the directional growth. In this case, the formation of turbostratic graphite is expected.

5.3.5 Comparison of Cathode Deposit with Anode Deposit

The growth rate and deposition efficiency of anode deposit in comparison with cathode deposit are shown in Figs. 5.27 (a) and (b), respectively. The deposition efficiencies are calculated as the mass of anode or cathode deposit divided by total amount of evaporation carbon. As shown in Fig. 5.27 (a), the anode deposit growth rate increases with increasing arc current. Since the evaporation rate increases with arc current, large evaporation rate leads to large amount of anode deposit. Therefore, the largest deposit growth rate of 3.9 $mg{\cdot}min^{-1}$ is observed at the arc current of 200 A. However, the cathode deposit growth rate reaches to the maximum of 7.13 $mg{\cdot}min^{-1}$ when the arc current reaches to 180 A, then reduces with increasing the arc current. This result is attributed to the scatter effect of carbon species at large arc current. Larger ratio of evaporated carbon species scatter from the plasma region to the outside of the plasma, without forming the cathode deposit. Although large carbon evaporation rate can be obtained at the large arc current, the growth rate of cathode deposit reduces when the arc current reaches to some threshold value. On the other hand, as shown in Fig. 5.27 (b), the scatter effect of the carbon species can be employed to explain the decrease of the cathode deposit efficiency with increasing the arc current. In contrast, the anode deposit efficiency can be explained by the increase of carbon evaporation, leading to more carbon species attach to the anode surface forming the anode deposit. As shown in Table 5.3, the typical products of PGP, MWNT, graphene flakes, and turbostratic graphite can be obtained from the cathode deposit, while graphite particles, MWNTs, and highly textured pyrolytic graphite can be prepared from the anode deposit. Therefore, the relationship among experiment parameters and the growth rate and efficiency of deposits provides an index to obtain higher ratio of the desirable products by selecting proper process parameters.

Fig. 5.28 shows the comparison of Raman spectroscopy between cathode deposit and anode deposit. As discussed in previous section, the ratio of the integrated intensity of the 2D band relative to the G band (I_{2D}/I_G) is an important parameter to determine carbon nanomaterial by arc discharge method. As shown in Fig. 5.28, the value of I_{2D}/I_G decreases with increasing arc current for the cathode deposit, and it is less than 1 at the arc current of 200 A, which mainly depends on the composition of cathode deposit. The main product of cathode deposit is PGP at the arc currents of 100 and 150 A, and the content of PGP reduces with increasing the arc current. Therefore, the value of I_{2D}/I_G decreases with increasing the arc current. However, the anode deposit is composed of nano-graphite particle, MWNT, and pyrolytic graphite, the value of I_{2D}/I_G is less than 1. This value does not vary with arc current for the anode deposit, because there is no change for the main composition of anode deposit when increasing arc current.

5.4 Conclusion

PGPs, MWNTs, graphene flakes, and turbostratic graphite were selectively synthesized in the cathode deposit by arc discharge method. The purities of MWNT and PGP can reach to 85% and 92%, respectively, meeting the requirements for applications. According to OES results, the relative ratio of carbon ions to carbon radicals near the cathode tip was employed to explain the formation of these carbon nanomaterials in the cathode deposit. The obtained results can be summarized as follows.

(i) The products are MWNTs, PGPs, and defect PGPs, corresponding to the arc current of 80, 100, and 150 A, respectively.

(ii) The products are PGPs, MWNTs, and high-purity MWNTs when the anode diameters are 30, 15, and 10 mm, respectively.

(iii) Higher energy of the carbon precursors contributes to the formation of thermodynamically unstable materials. MWNTs could be synthesized by the precursors with relatively low energy. In addition, graphene flakes and turbostratic graphite are formed in the long electrode gap distance, due to the higher energy of the carbon precursors.

Furthermore, it provides an idea that the energy of the carbon precursor could be used to control the formation of different carbon nanomaterials in the cathode deposit selectively by arc discharge method.

References

Allen C.W. *“Astrophysical quantities.”* London and Dover, New Hampshire, The Athlone Press (1973).

Boulos, M. I., P. Fauchais and E. Pfender. “*Thermal Plasmas: Fundamentals and Applications.*” New York, Plenum Press (1994).

Colbert, T., J. Zhang, S. M. McClure, P. Nicolaev, Z. Chen, J. H. Hafner, D. W. Owens, P. G. Kotula, C. B. Carter, J. H. Weaver, A. G. Rinzler and R. E. Smalley. “Growth and sintering of fullerene nanotubes.” *Science* **266**, 1218-1222 (1994).

Coleman J. N., D. F. O’Brien, A. B. Dalton, B. McCarthy, B. Lahr, R. C. Barklie and W. J. Blau. “Electron paramagnetic resonance as a quantitative tool for the study of multiwalled carbon nanotubes” *Journal of Chemical Physics* **113** (21), 9788 (2000).

Dresselhaus, M. S., G. Dresselhaus, R. Saito and A. Jorio. “Raman spectroscopy of carbon nanotubes.” *Physics Reports* **409**, 47-99 (2005).

Dresselhaus, M. S., A. Jorio, M. Hofmann, G. Dresselhaus and R. Saito. “Perspectives on carbon nanotubes and graphene Raman spectroscopy.” *Nano Letters* **10**, 751-758 (2010).

Ebbesen, T. W. “Carbon nanotubes.” Annual Review of Materials Research 24, 235-264 (1994).

Ferrari, A. C., J. C. Meyer, V. Scardaci, C. Casiraghi, M. Lazzeri, F. Mauri, S. Piscanec, D. Jiang, K. S. Novoselov, S. Roth and A. K. Geim. “Raman spectrum of graphene and graphene layers.” *Physical Review Letters* **97**, 187401 (2006).

Ferrari, A. C. “Raman spectroscopy of graphene and graphite: disorder, electron–phonon coupling, doping and nonadiabatic effects.” *Solid State Communications* **143,** 47-57 (2007).

Fetterman, A. J., Y. Raitses and M. Keidar. “Enhanced ablation of small anodes in a carbon nanotube arc plasma.” *Carbon* **46**, 1322-1326 (2008).

Gamaly, E. G. and T. W. Ebbesen. “Mechanism of carbon nanotube formation in the arc discharge.” *Physical Review B* **52**, 2083-2089 (1995).

Griem H. R. “*Plasma Spectroscopy*.” McGraw-Hill: New York (1964).

Guan, L., L. Cui, K. Lin, Y.Y. Wang, X.T. Wang, F.M. Jin, F. He, X. P. Chen and S. Cui. “Preparation of few-layer nitrogen-doped graphene nanosheets by DC arc discharge under nitrogen atmosphere of high temperature” *Applied Physics A* **102**, 289-294 (2011).

Guo, T., P. Nikolaev, A. G. Rinzer, D. Tomanek, D. T. Bolbert and R.E. Smalley. “Self-assembly of tubular fullerenes.” *Journal of Physical Chemistry* **99**, 10694-10697 (1995).

Huang, J. S., B. G. Sumpter, V. Meunier, G. Yushin, C. Portet and Y. Gogotsi. “Curvature effects in carbon nanomaterials: Exohedral versus endohedral supercapacitors.” *Journal of Material Research* **25**, 1525-1531 (2010).

Iijima, S. "Helical microtubules of graphitic carbon." Nature 354(6348), 56-58 (1991).

Iijima, S., P. M. Ajayan and T. Ichihashi. “Growth model for carbon nanotubes.” *Physical Review Letters* **69**, 3100-3103 (1992).

Inoue A., T. Seto and Y. Otani. “Onion-like carbon nanoparticles generated by multiple laser irradiations on laser-ablated particles” *Carbon* **50**, 1116-1122 (2012).

Jones, J. M., R. P. Malcolm, K. M. Thomas and S. H. Bottrell. “The anode deposit formed during the carbon-arc evaporation of graphite for the synthesis of fullerenes and carbon nanotubes.” *Carbon* **34**, 231-237 (1996).

Kajiura, H., H. Huang, S. Tsutsui, Y. Murakami and M. Miyakoshi. “High-purity fibrous carbon deposit on the anode surface in hydrogen DC arc-discharge.” *Carbon* **40**, 2423-2428 (2002).

Kundrapu M. and M. Keidar. “Numerical simulation of carbon arc discharge for nanoparticle synthesis” *Physics of plasmas* **19**, 073510 (2012).

Liang, F., T. Shimizu, M. Tanaka, S. Choi and T. Watanabe. “Selective preparation of polyhedral graphite particles and multi-wall carbon nanotubes by a transferred arc under atmospheric pressure.” *Diamond and Related Materials* **30**, 70-76 (2012).

Liang, F., T. Shimizu, M. Tanaka, S. Choi and T. Watanabe. “Preparation of Polyhedral Graphite Particles by Arc Discharge under Atmospheric Pressure.” J*apanese Journal of Applied Physics* **52**, 01AK01 (2013).

Louchev, O. A and J. R. Hester. “Kinetic pathways of carbon nanotube nucleation from graphitic nanofragments.” *Journal of Applied Physics* **94**, 2002-2010 (2003).

Michael F., D. Volder, S. H. Tawfick, R. H. Baughman and A. J. Hart. “Carbon Nanotubes: Present and Future Commercial Applications.” *Science* **339**, 535-539 (2013).

Nakayama, A., S. Iijima, Y. Koga, K. Shimizu, K. Hirahara and F. Kokai. “Compression of polyhedral graphite up to 43 GPa and x-ray diffraction study on elasticity and stability of the graphite phase.” *Applied Physics Letters* **84**, 5112-5114 (2004).

Nemanich, R. J and S. A. Solin. “First-and second-order Raman scattering from finite-size crystals of graphite.” *Physical Review B* **20**, 392-401 (1979).

Obraztsova, E. D., M. Fujii, S. Hayashi, V. L. Kuznetsov, Y. V. Butenko and A. L. Chuvilin, “Raman identification of onion-like carbon.” *Carbon* **36**, 821-826 (1998).

Pech, D., M. Brunet, H. Durou, P. Huang, V. Mochalin, Y. Gogotsi, P. L. Taberna and P. Simon. “Ultrahigh-power micrometre-sized supercapacitors based on onion-like carbon.” *Nature Nanotechnology* **5**, 651-654 (2010).

Pimenta, M., G. Dresselhaus, M. Dresselhaus, L. Cancado, A. Jorio and R. Saito. “Studying disorder in graphite-based systems by Raman spectroscopy.” *Physical Chemistry Chemical Physics* **9**, 1276-1291 (2007).

Saito. Y., T. Yoshikawa and M. Inagaki. “Growth and structure of graphitic tubules and polyhedral particles in arc-discharge.” *Chemical Physics Letters* **204**, 277-282 (1993).

Scalese, S., V. Scuderi, S. Bagiante, S. Gibilisco, G. Faraci and V. Privitera. “Order and disorder of carbon deposit produced by arc discharge in liquid nitrogen” *Journal of Applied Physics* **108** 064305 (2010).

Shenderova, O. A., V. V. Zhirnov and D. W. Brenner. “Carbon nanostructured” *Critical Reviews in Solid State and Materials Sciences* **27**(3-4), 227-356 (2002).

Silinskas, M., A. Grigonis, V. Kulikauskas and I. Manika. “Hydrogen influence on the structure and properties of amorphous hydrogenated carbon films deposited by direct ion beam.” *Thin Solid Films* **516**, 1683-1692 (2008).

Sveningsson M., R. E. Morjan, O. A. Nerushev, Y. Sato, J. Bäckström, E.E.B. Campbell and F. Rohmund. “Raman spectroscopy and field-emission properties of CVD-grown carbon-nanotube films” *Applied Physics A Materials Science & Processing* **73**, 409-418 (2001).

Ugarte, D. “Morphology and structure of graphitic soot particles generated in arc discharge C60 production.” *Chemical Physics Letters* **198**, 596-602 (1992).

Ugarte, D. “Onion-like graphitic particles.” *Carbon* **33**, 989-993 (1995).

Volotskova, O., I. Levchenko, A. Shashurin, Y. Raitses, K. Ostrikov and M. Keidar. “Single-step synthesis and magnetic separation of graphene and carbon nanotubes in arc discharge plasmas.” *Nanoscale* **2**, 2281-2285 (2010).

Wang, M. S., D. Golberg and Y. Bando. “Carbon onions as point electron sources.” *ACS Nano* **4**, 4396-4402 (2010).

Welna T D., L. Qu, B. E. Taylora, L. Dai and M. F. Durstock. “Vertically aligned carbon nanotube electrodes for lithium-ion batteries.” *Journal of Power Sources* **196**, 1455-1460 (2011).

Table 5.1 Experimental conditions

Arc current [A]	80,100, 150
Electrode gap distance [mm]	1, 3, 5
Arc voltage [V]	15-25
Pressure [kPa]	101.3 (Atmospheric pressure)
Plasma gas	Helium
Anode diameter [mm]	10, 15, 30
Cathode diameter [mm]	6
Discharge time [min]	5-10
Cathode	Graphite
Anode	Graphite

Table 5.2 Experimental parameters and results when changing the electrode gap distance.

Electrode gap distance (mm)	1	3	5
Arc voltage (V)	15.0	18.2	25.0
Evaporation rate ($mg\cdot min^{-1}$)	4.8	7.3	19.7
Cathode deposit growth rate ($mg\cdot min^{-1}$)	3.4	3.4	3.0
Cathode deposit ratio (%)	71.7	46.6	15.3

Table 5.3 Comparison of cathode deposit with anode deposit.

	Cathode deposit	Anode deposit
Condition	Low arc current	High arc current
Product	PGP, MWNT, graphene flakes, and turbostratic graphite	Nano-graphite particle, MWNT, pyrolytic graphite
Precursor	C, C_n, and C^+	C, C_n
Mechanism	Energy of precursor	Quenching effect

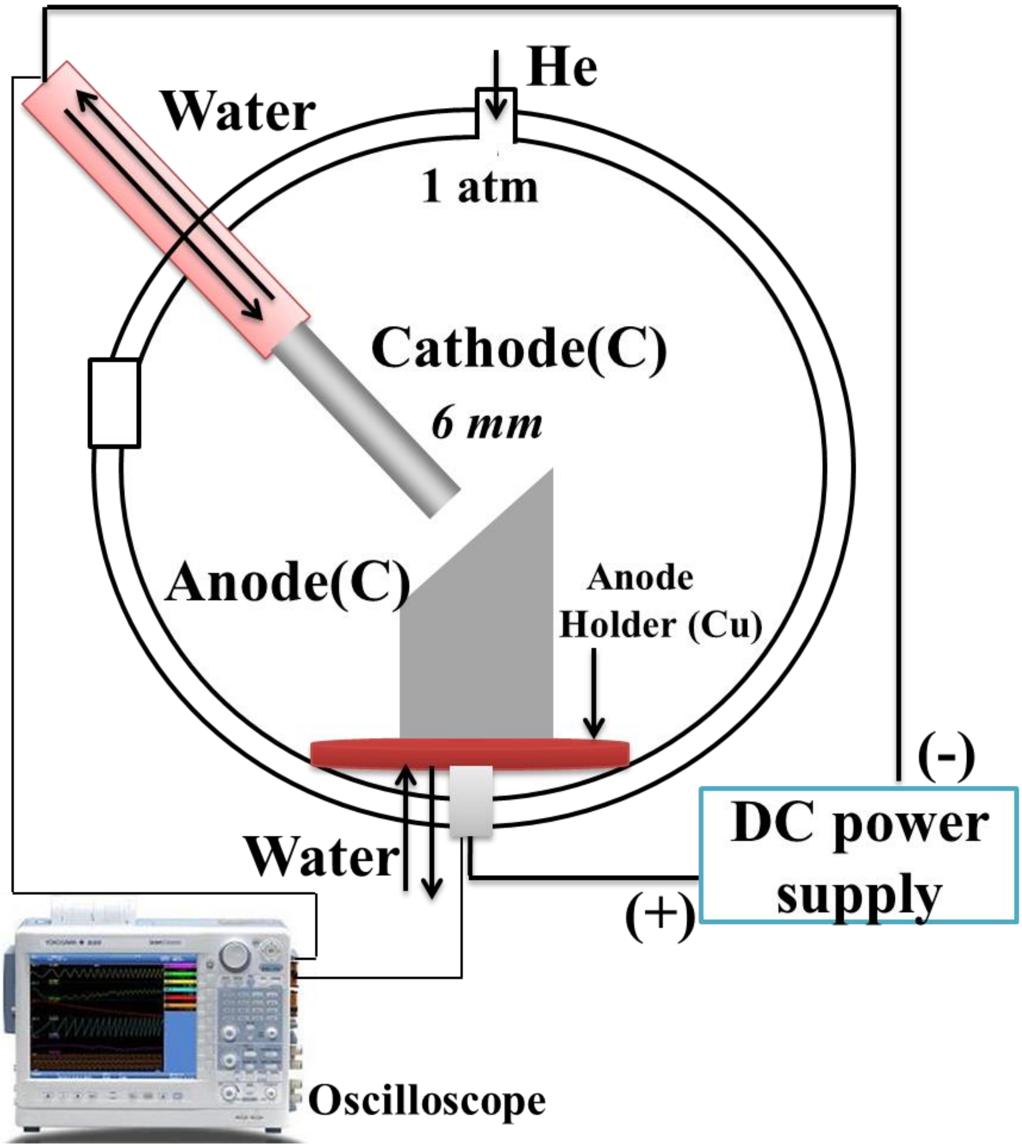

Fig. 5.1 Schematic diagram of experimental apparatus for the preparation of carbon nanomaterials in cathode deposit.

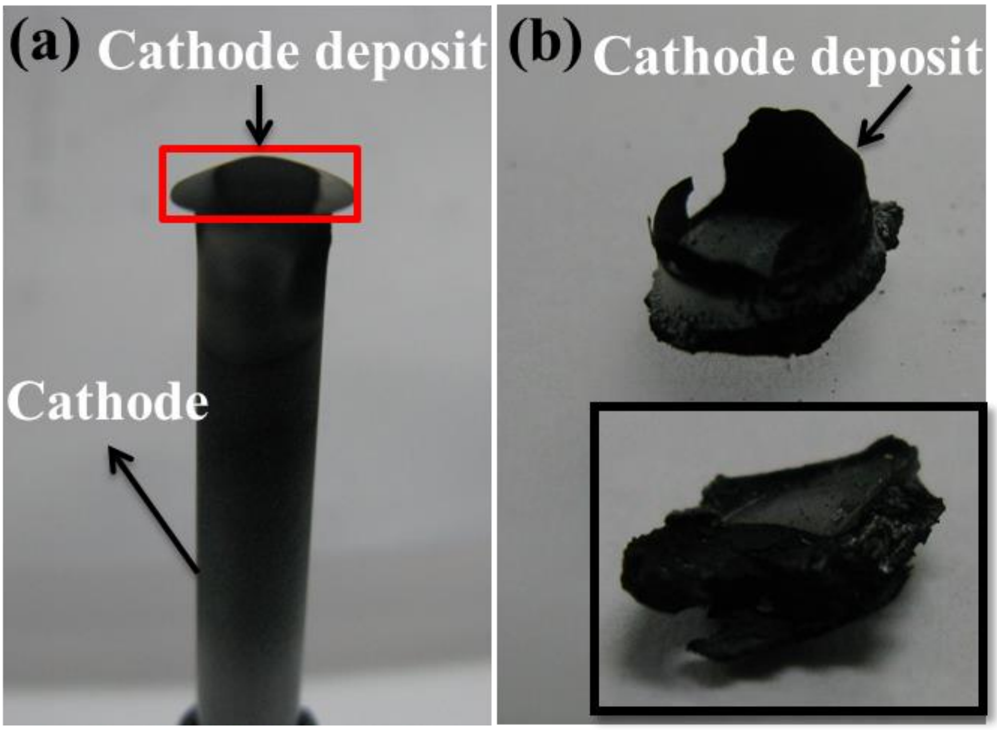

Fig. 5.2 The photos of cathode deposit before separating with cathode (a), and after separating with cathode (b).

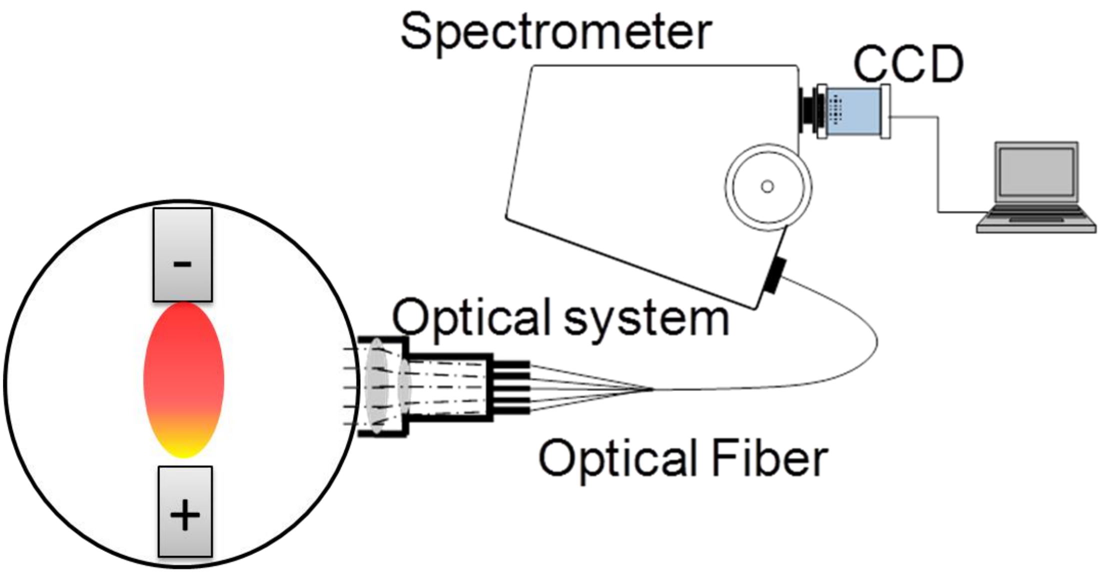

Fig. 5.3 The schematic of the optical system for the spectroscopic measurements.

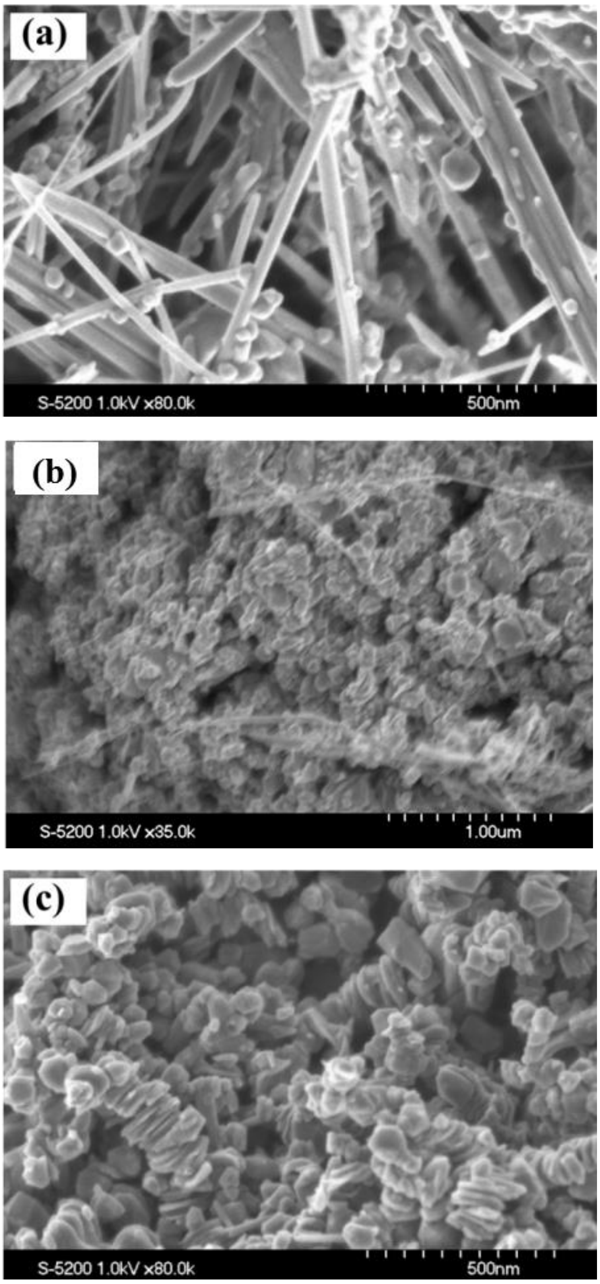

Fig. 5.4 FE-SEM images of the cathode deposit in different arc currents of (a) 80 A, (b) 100 A and (c) 150 A at the fixed anode diameter of 30 mm.

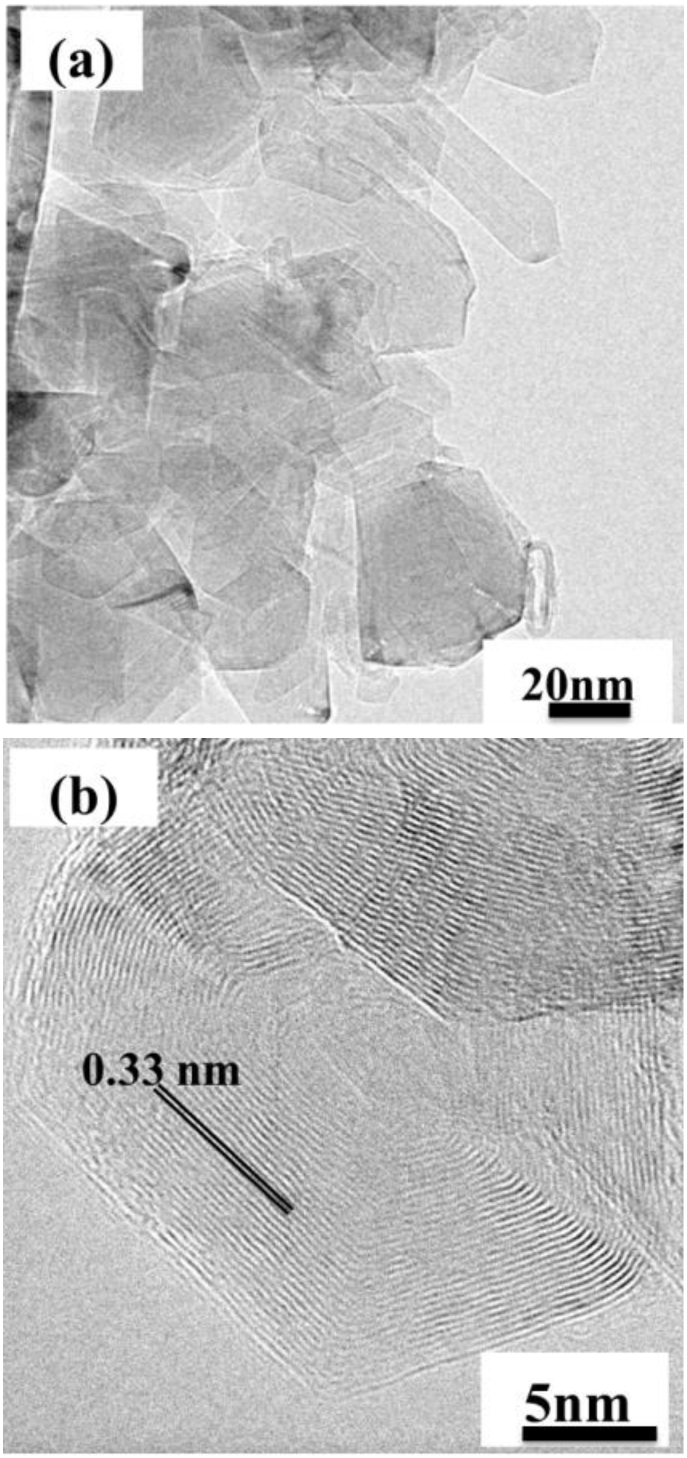

Fig. 5.5 TEM images of the cathode deposit with (a) low magnification and (b) high magnification at the arc current of 100 A and the anode diameter of 30 mm.

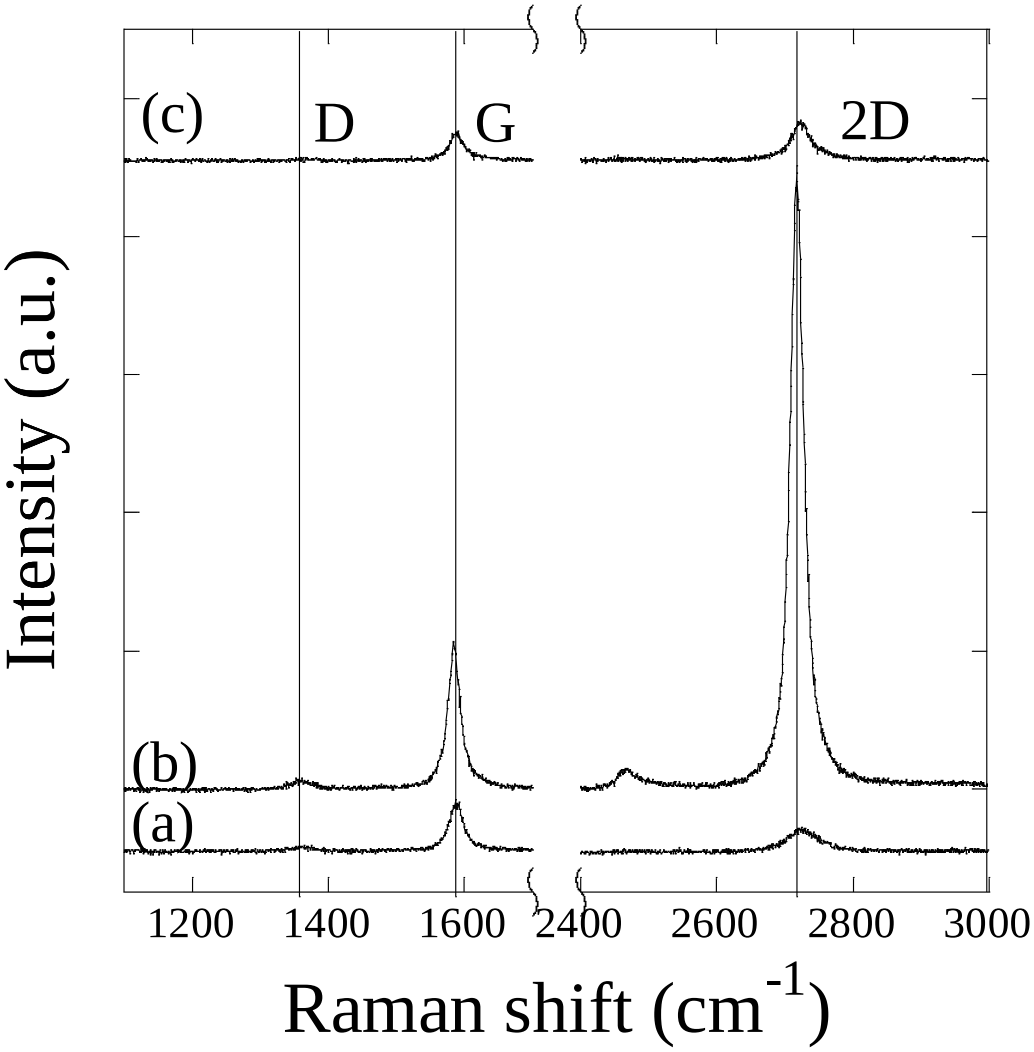

Fig. 5.6 Raman spectra of the cathode deposit according to the arc current at the fixed anode diameter of 30 mm: (a), (b), and (c) correspond to the arc current of 80 A, 100 A, and 150 A, respectively.

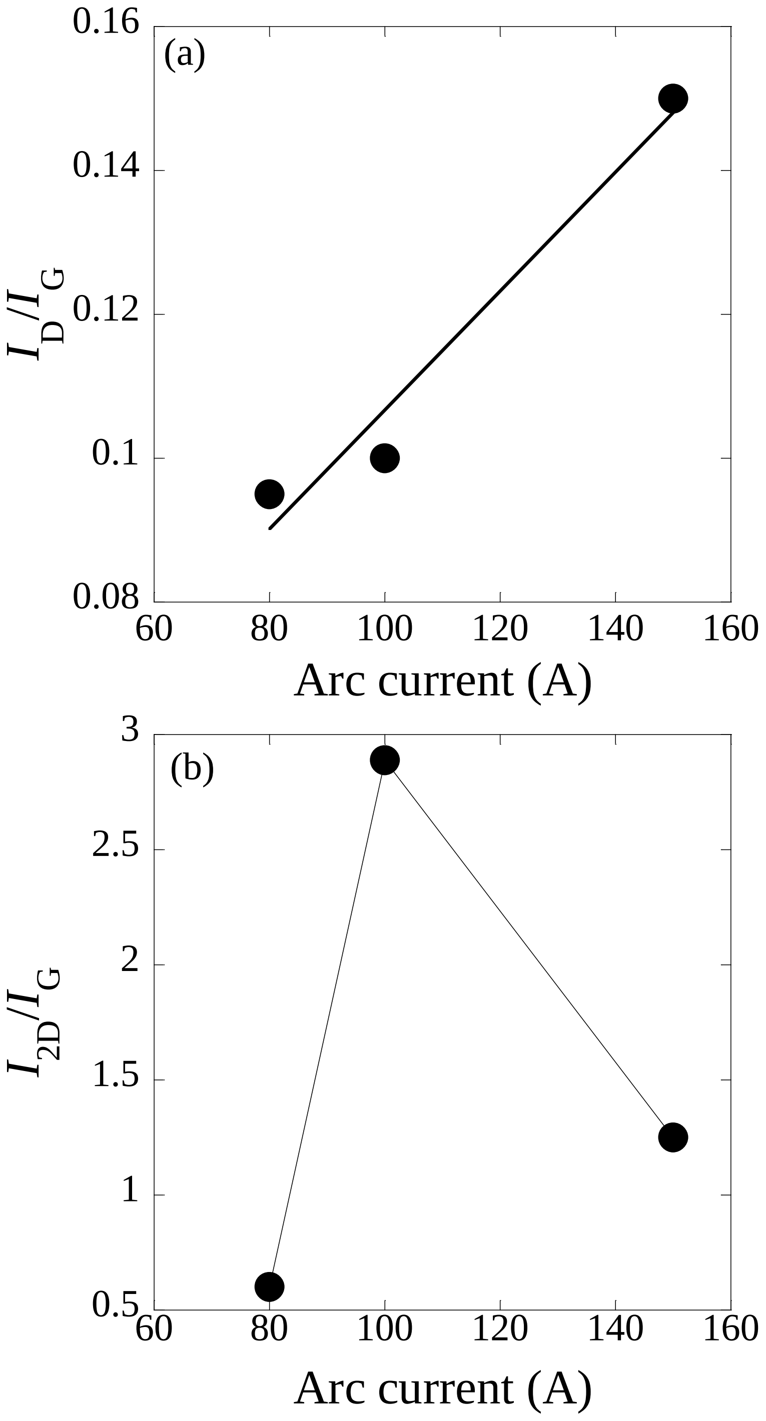

Fig. 5.7 (a) the relative intensity of the D band to the G band (I_D/I_G) and (b) the 2D to the G band (I_{2D}/I_G) by varying the arc current.

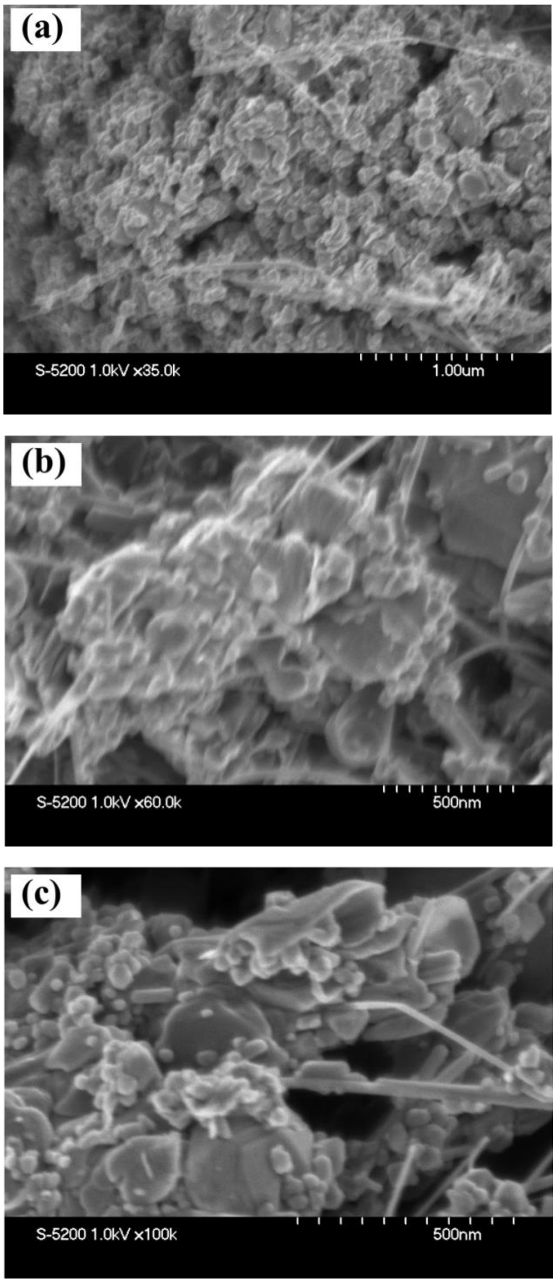

Fig. 5.8 FE-SEM images of the products at different electrodes gap distances: (a) 1, (b) 3, and (c) 5 mm.

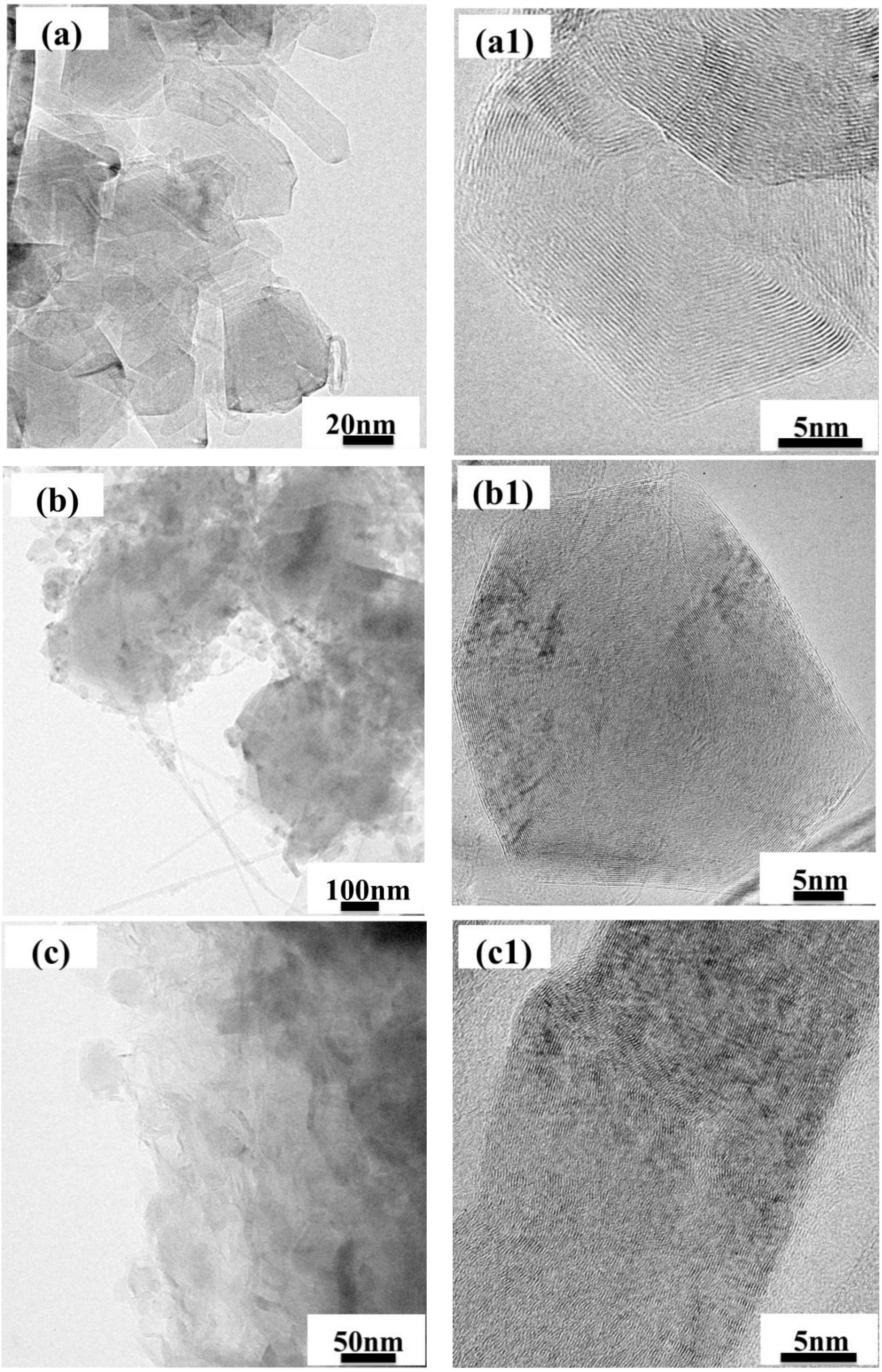

Fig. 5.9 TEM images of the products at different electrodes gap distances: (a) 1, (b) 3, and (c) 5 mm and their high magnification images of (a1) 1, (b1) 3, and (c1) 5 mm.

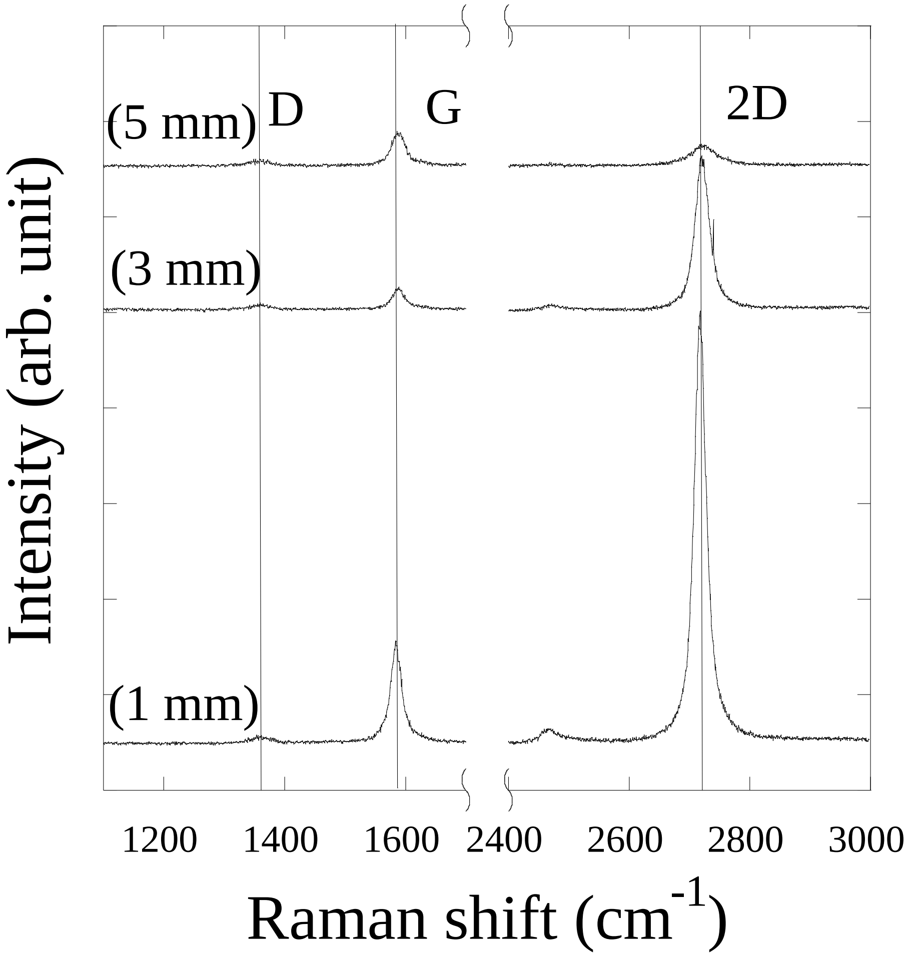

Fig. 5.10 Raman spectroscopy results according to the electrode gap distance.

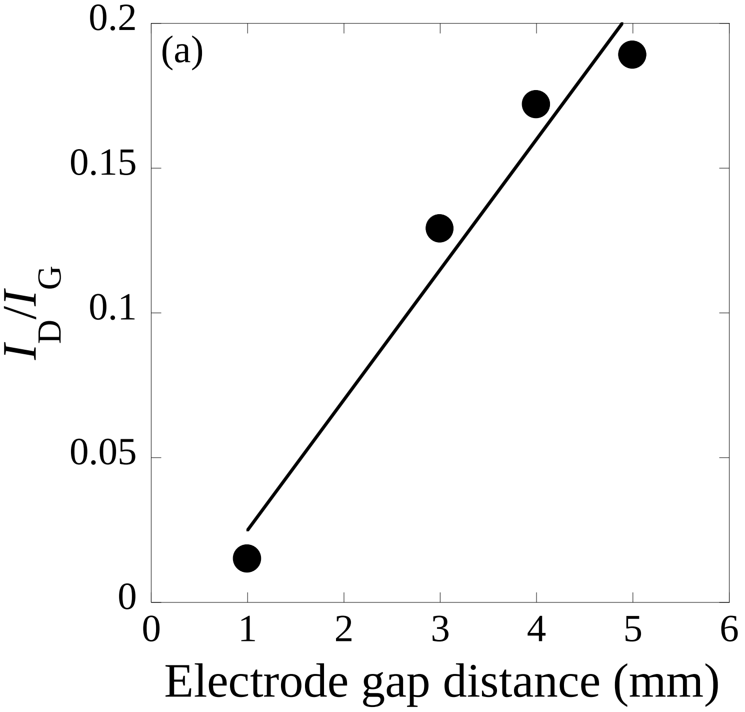

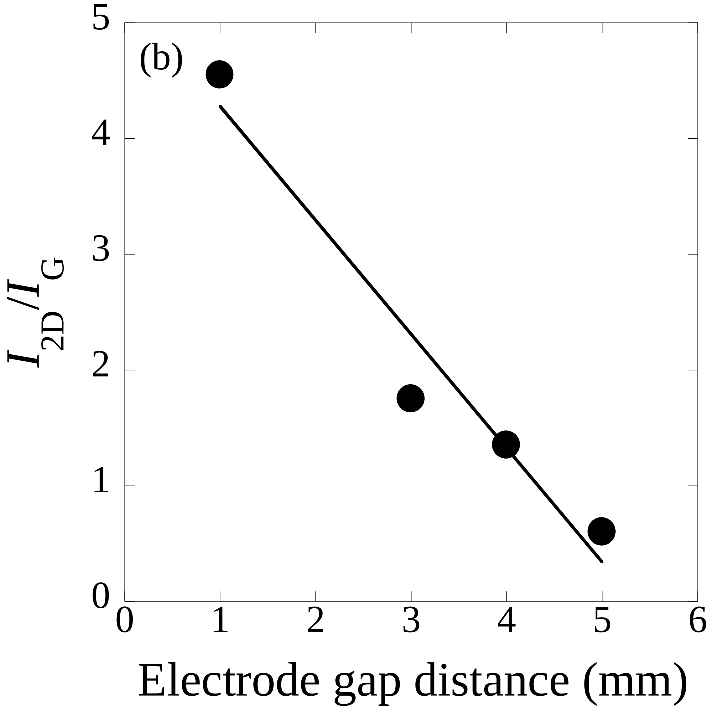

Fig. 5.11 (a) the relative intensity of the D band to the G band (I_D/I_G) and (b) the 2D to the G band (I_{2D}/I_G) by varying the electrode gap distance.

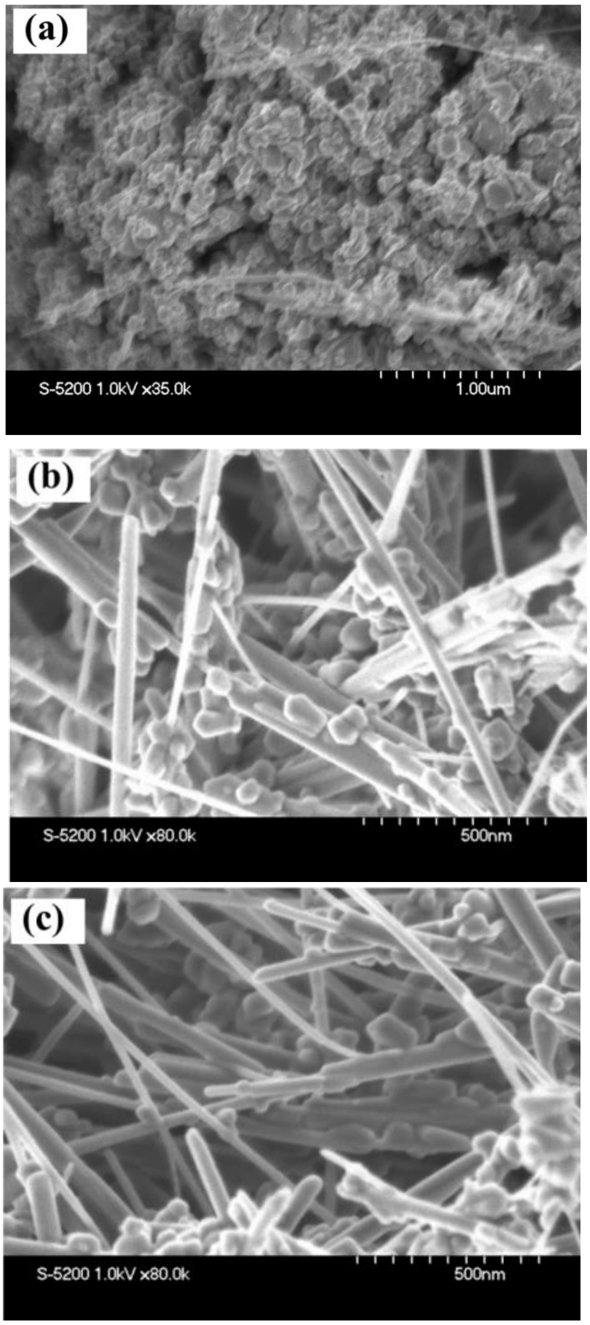

Fig. 5.12 FE-SEM images of the cathode deposit in different anode diameter of (a) 30 mm, (b) 15 mm, and (c)10 mm at the fixed arc current of 100 A.

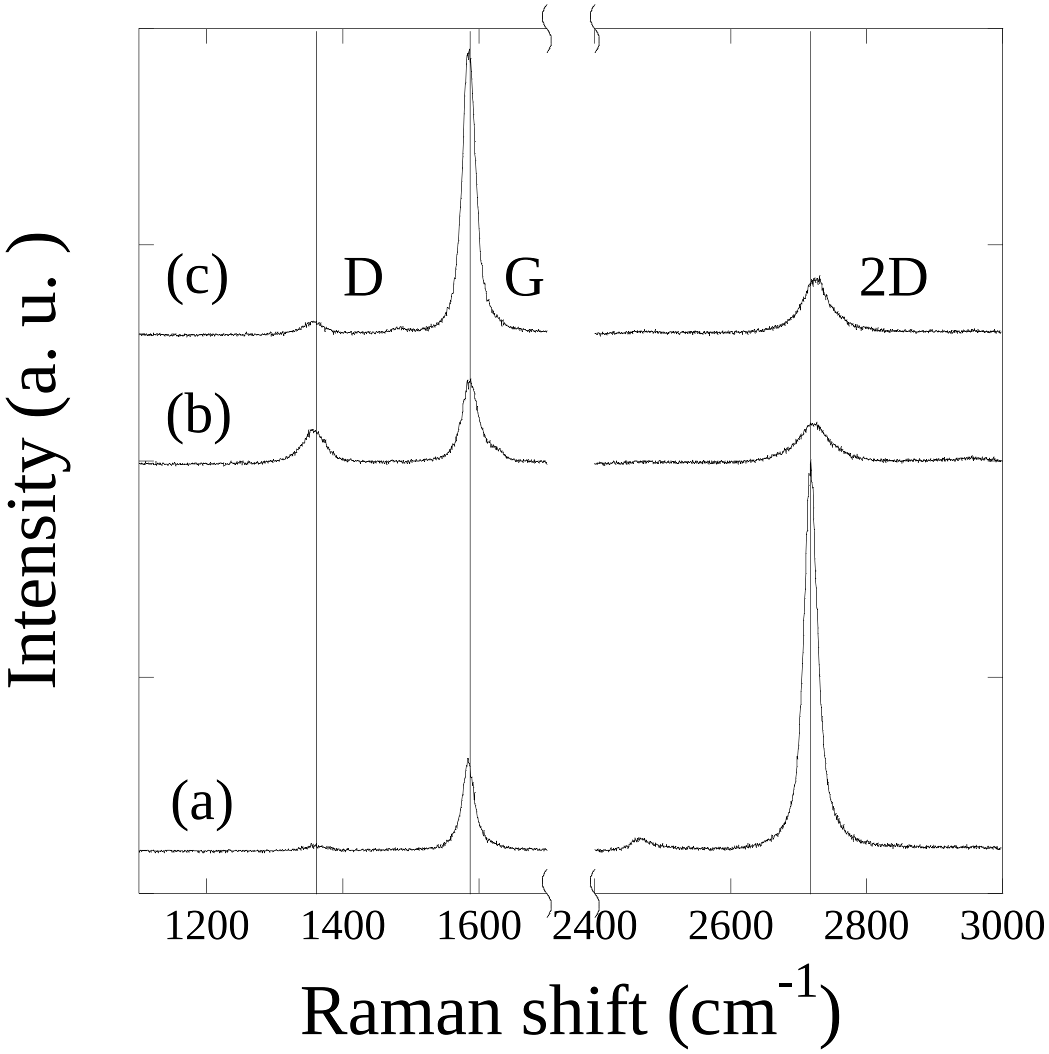

Fig. 5.13 Raman spectra of the cathode deposit according to the anode diameter at the fixed arc current of 100 A: (a), (b), and (c) correspond to the anode diameter of 30 mm, 15 mm, and 10 mm, respectively.

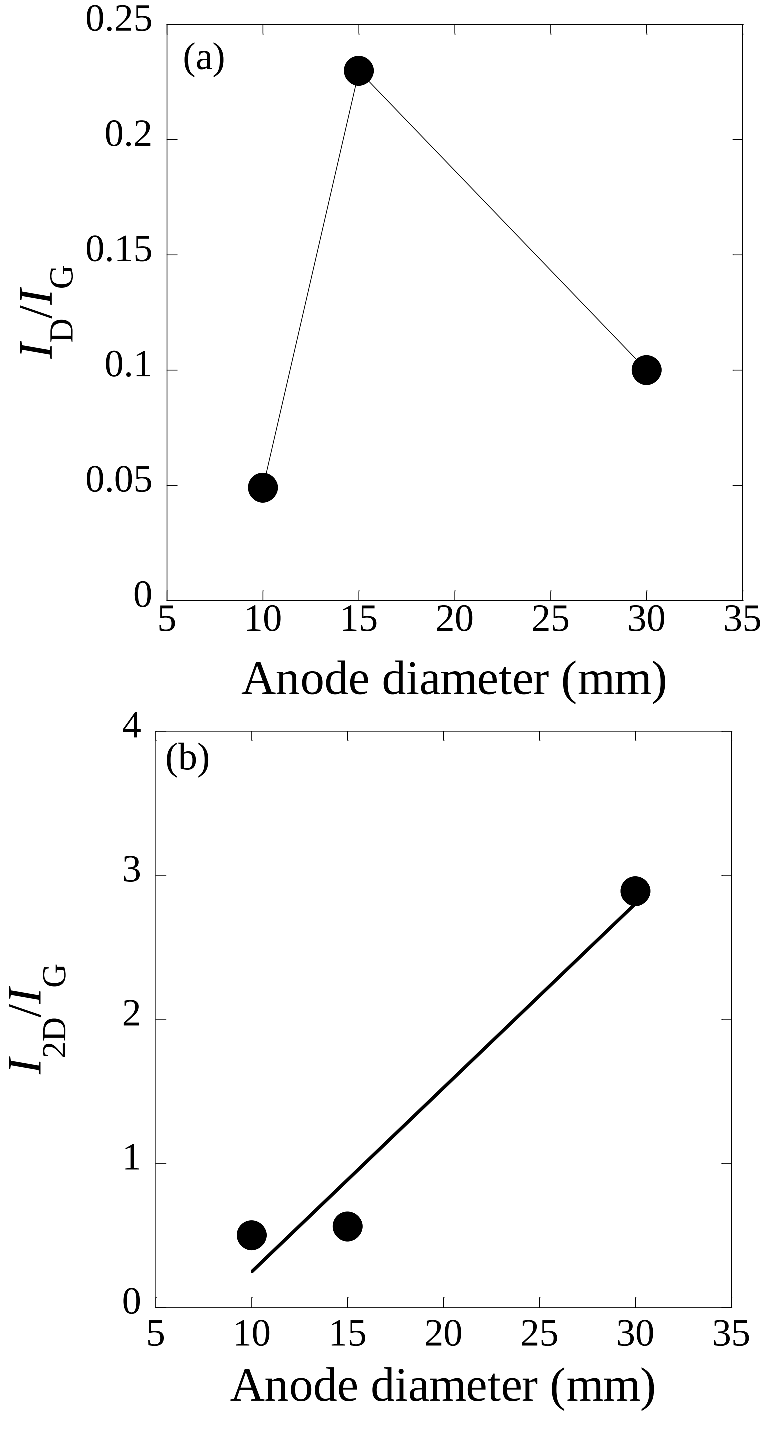

Fig. 5.14 (a) the relative intensity of the D band to the G band (I_D/I_G) and (b) the 2D to the G band (I_{2D}/I_G) by varying the anode diameter.

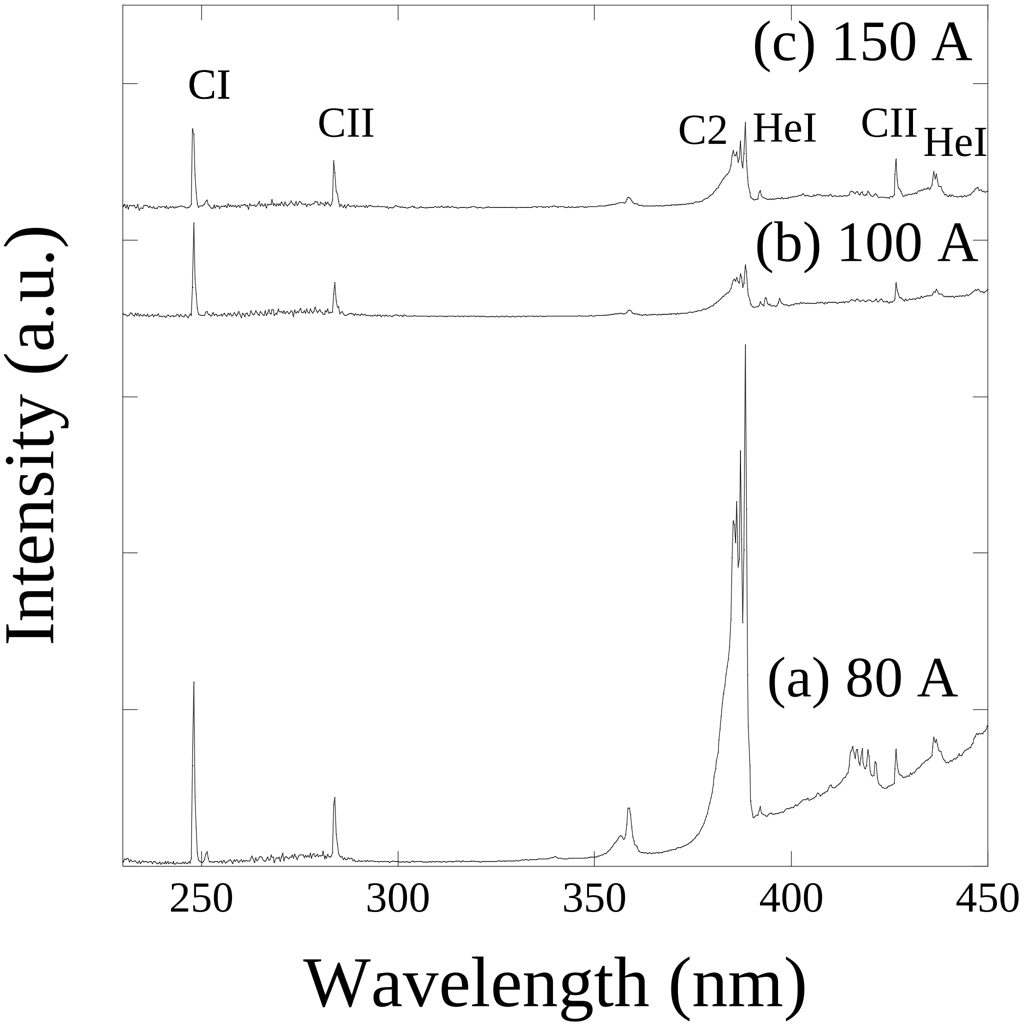

Fig. 5.15 The optical emission spectra of the plasma by varying the arc current: (a) 80 A, (b) 100 A, and (c) 150 A.

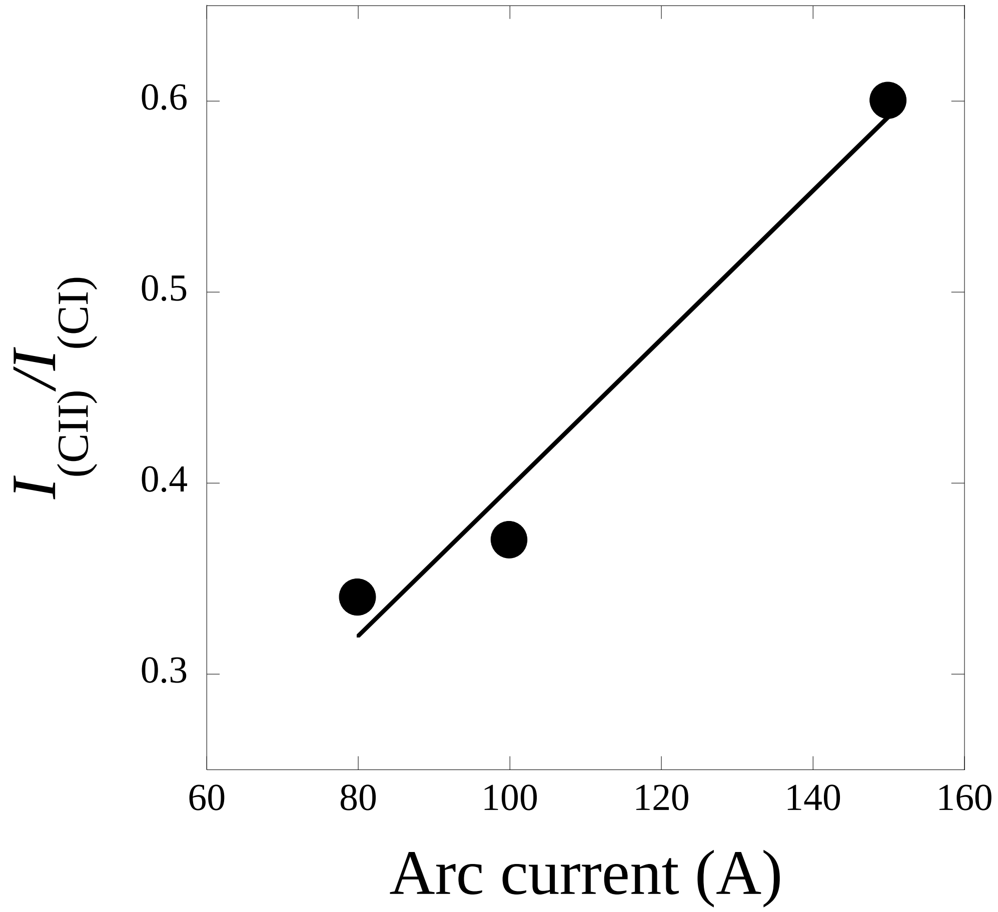

Fig. 5.16 The relationship between the relative intensity of carbon ions to carbon atoms ($I_{C(II)}/I_{C(I)}$) according to the arc current.

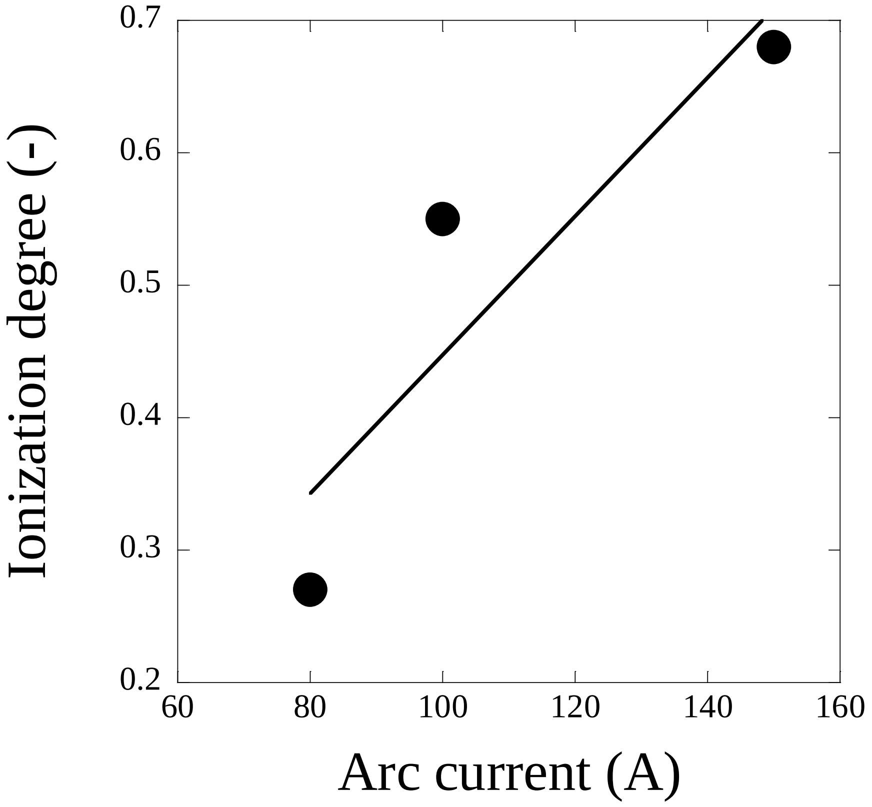

Fig. 5.17 The relationship between ionization degree calculated by Saha equation and arc current.

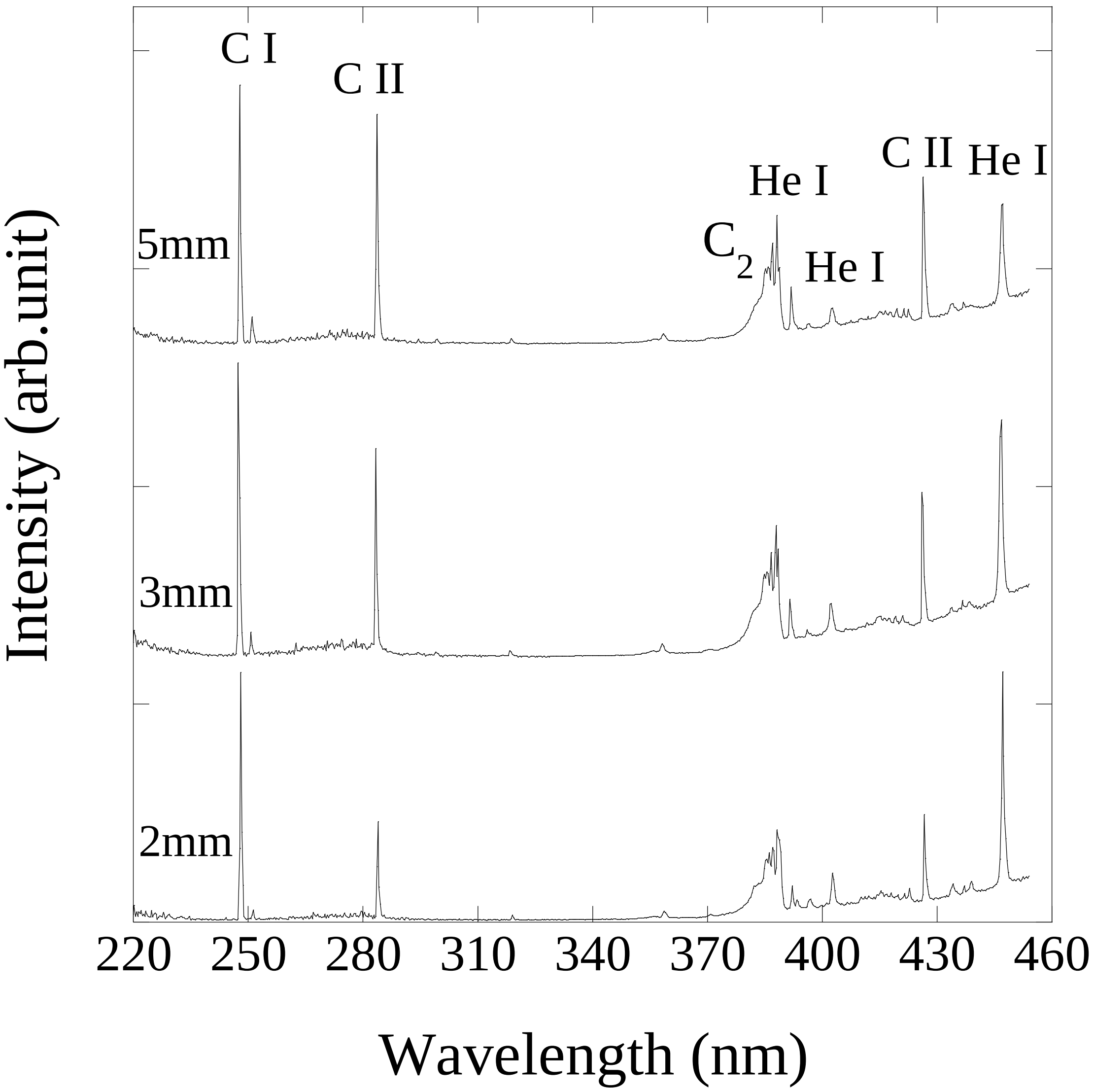

Fig. 5.18 The optical emission spectra of the plasma by varying the electrode gap distance: (a) 2, (b) 3, and (c) 5 mm.

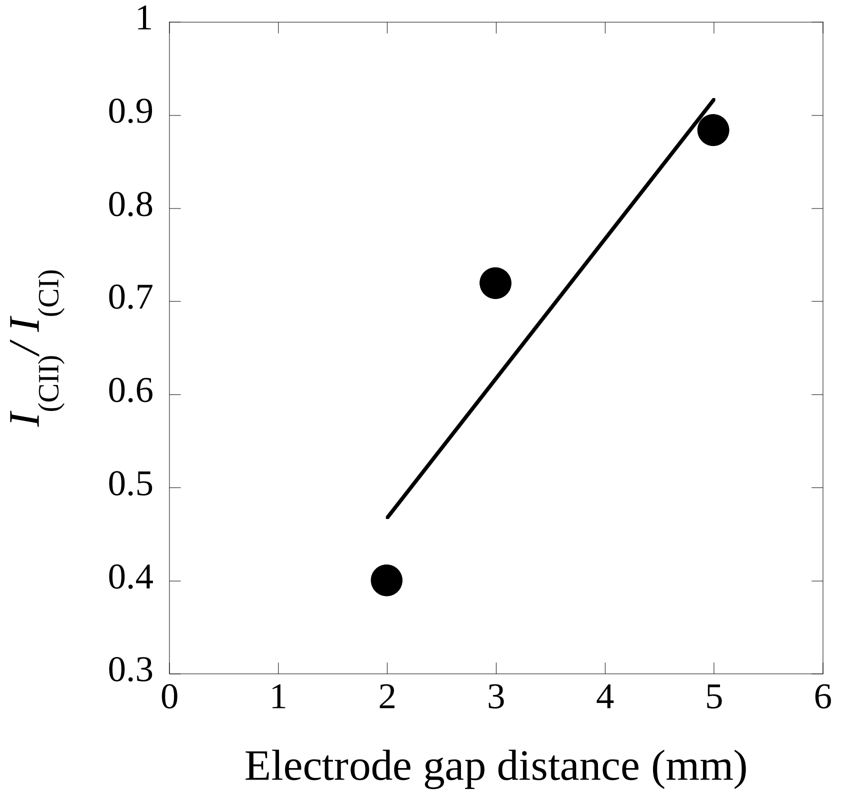

Fig. 5.19 The relative intensity of carbon ions to carbon radicals ($I_{C(II)}/I_{C(I)}$) according to the electrode gap distance.

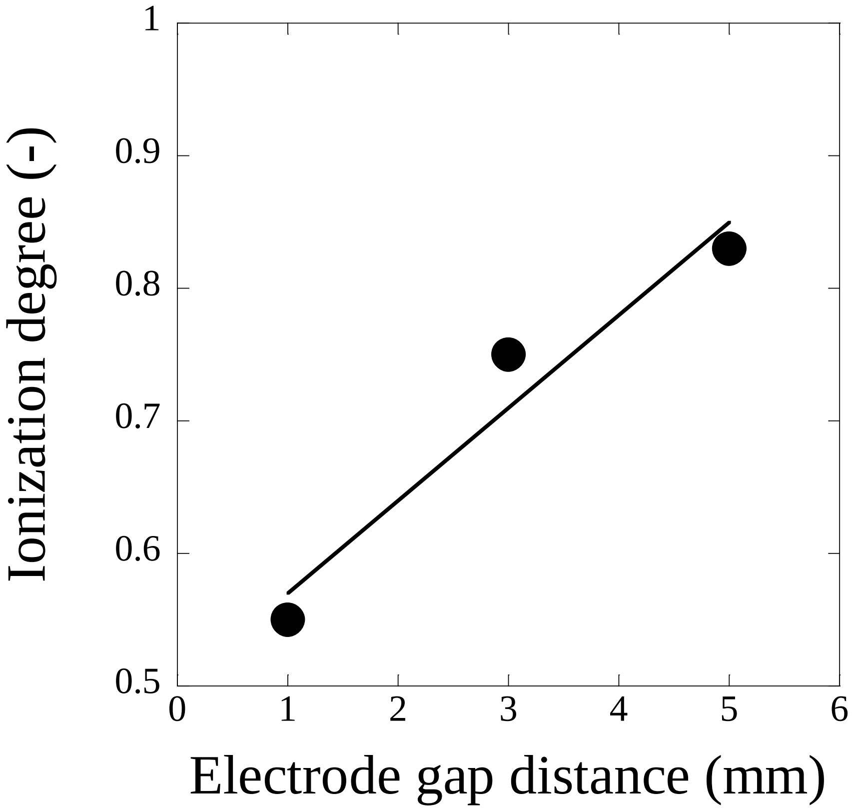

Fig. 5.20 The relationship between ionization degree calculated by Saha equation and electrode gap distance.

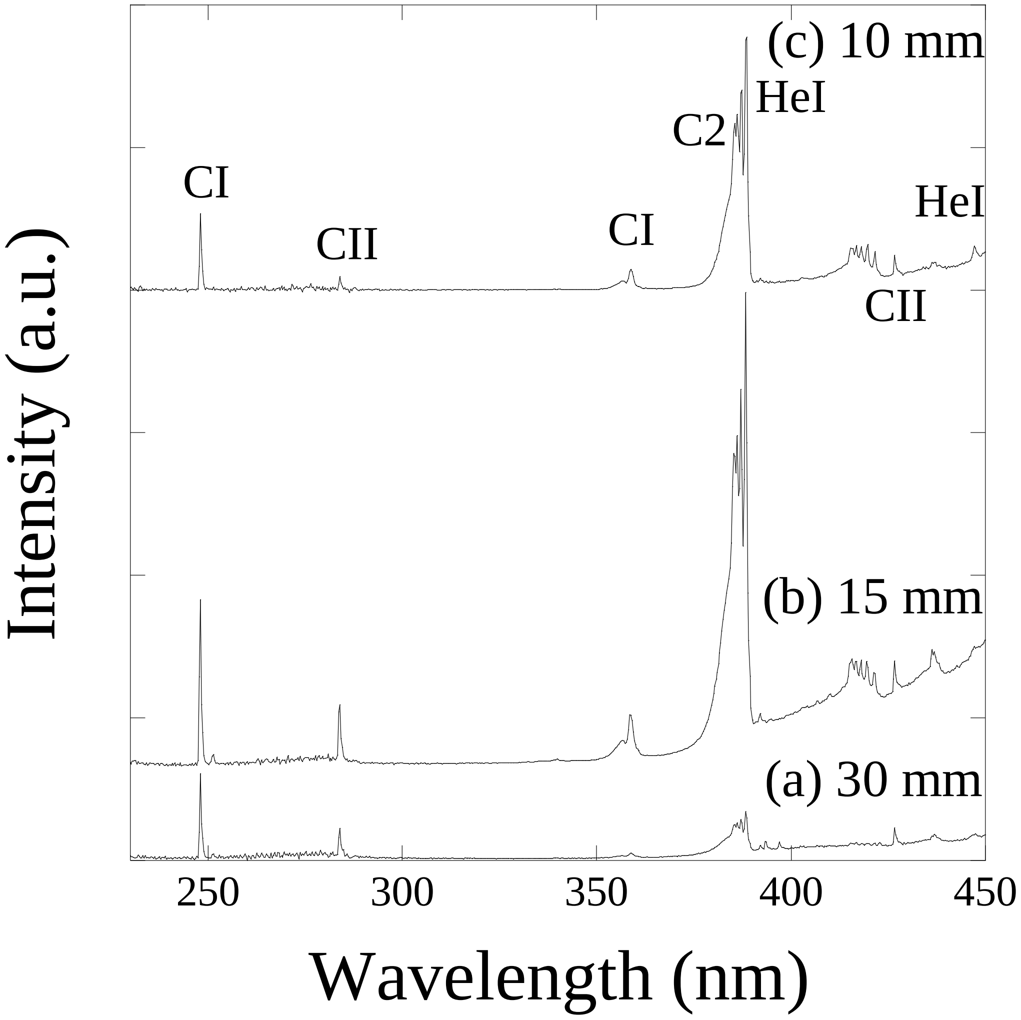

Fig. 5.21 The optical emission spectra of the plasma by varying the anode diameter: (a) 30 mm, (b) 15 mm, and (c) 10 mm.

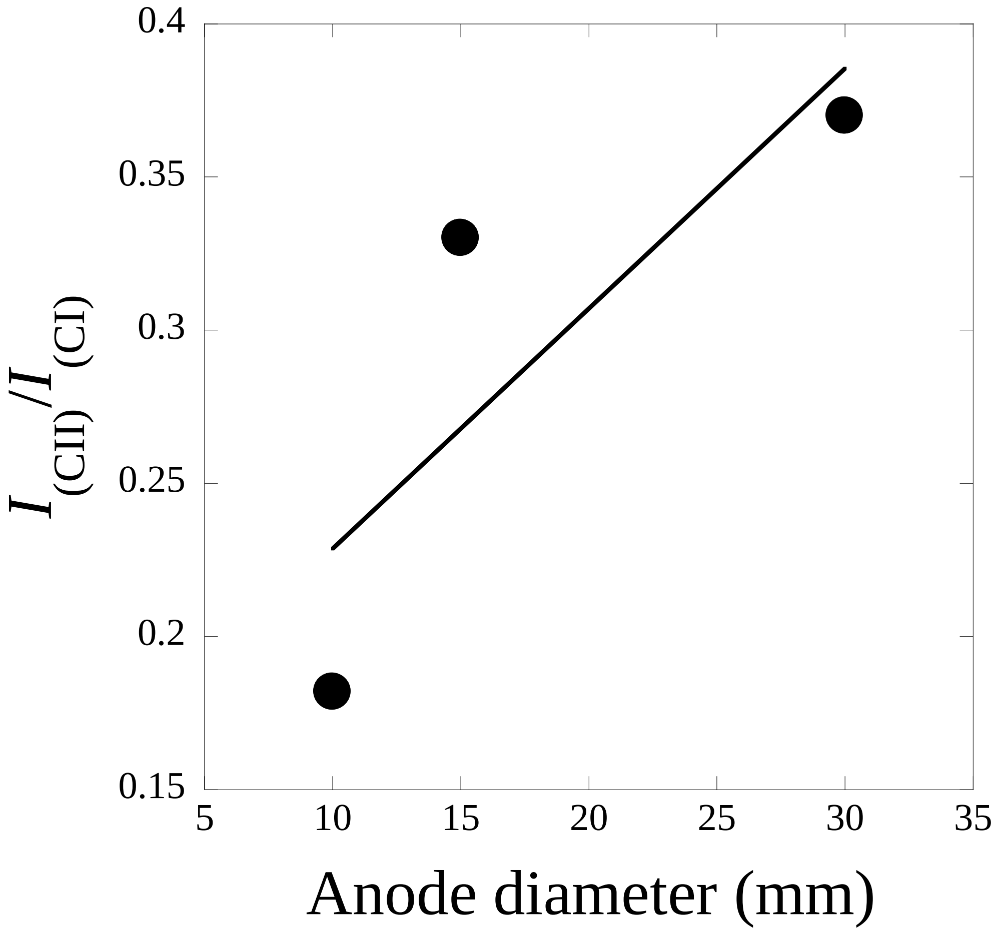

Fig. 5.22 The relationship between the relative intensity of carbon ions to carbon atoms ($I_{C(II)}/I_{C(I)}$) according to the anode diameter.

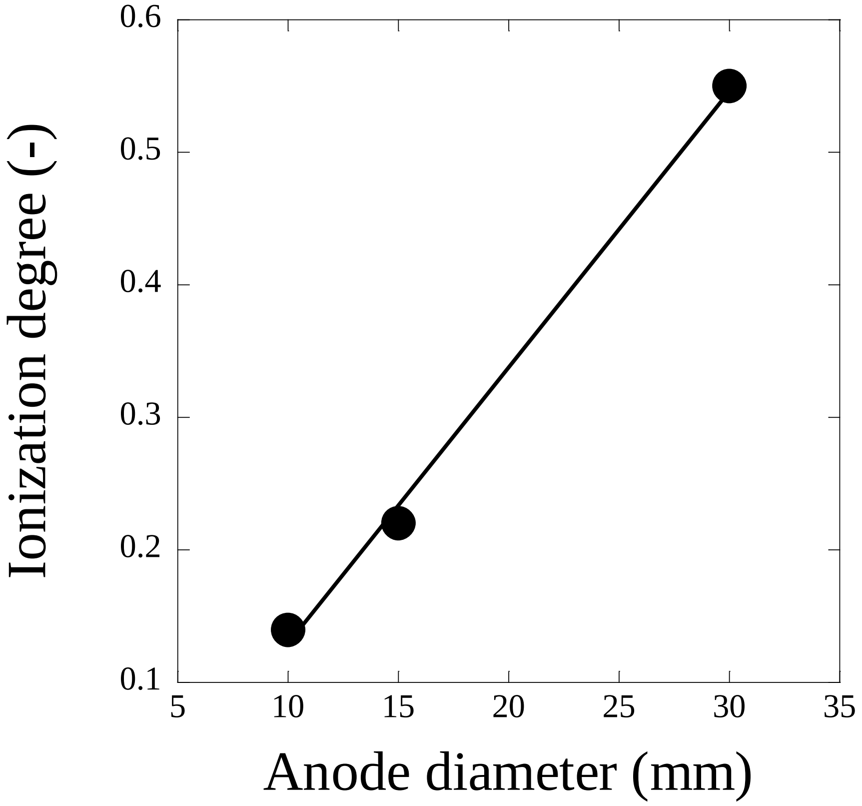

Fig. 5.23 The relationship between ionization degree calculated by Saha equation and anode diameter.

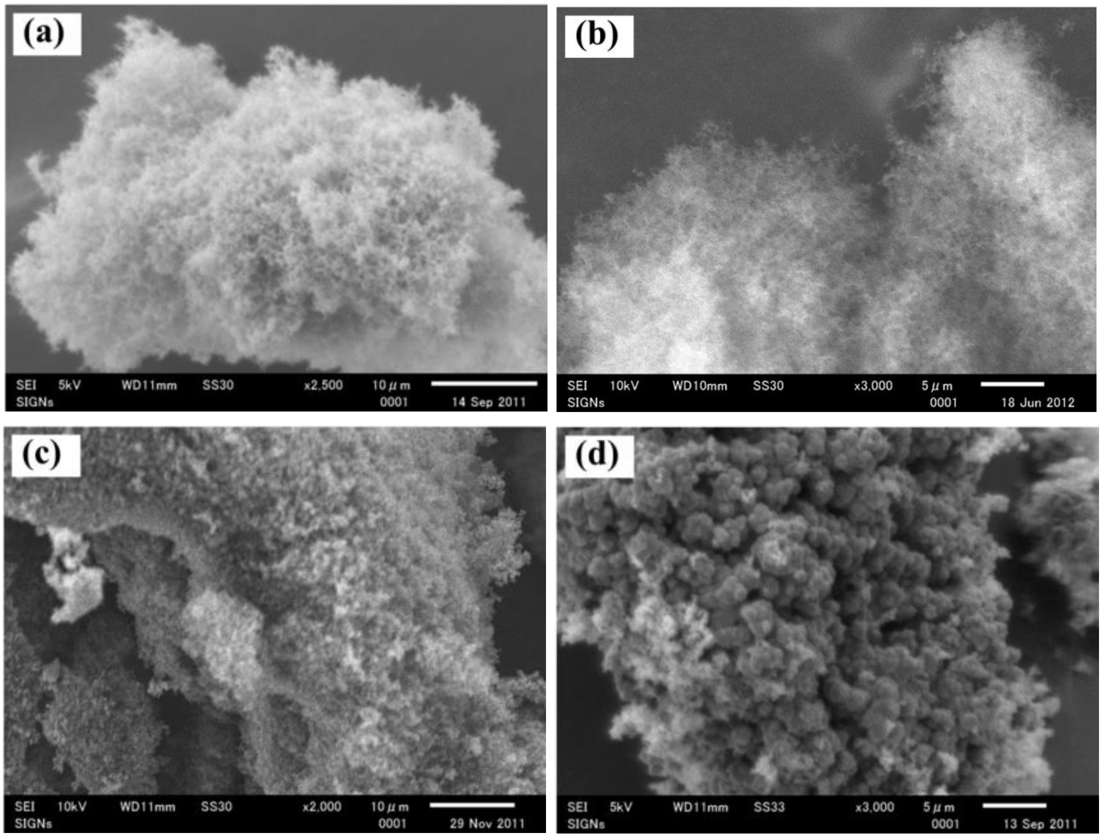

Fig. 5.24 SEM images of the products sampled at different regions: (a) inner wall of the chamber, (b) top surface of the anode holder, (c) side surface of the cathode, and (d) top surface of the anode.

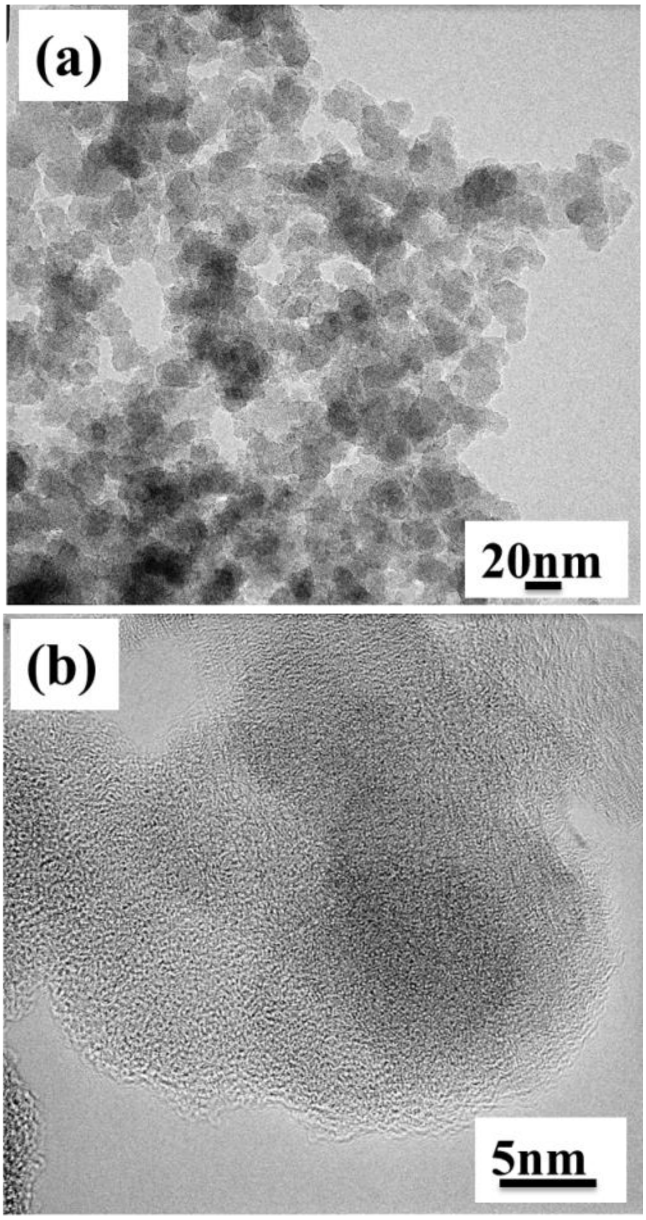

Fig. 5.25 (a) Low magnification and (b) high magnification TEM images of the product on the anode surface with fixed operating conditions of 100 A for the arc current and 30 mm for the anode diameter.

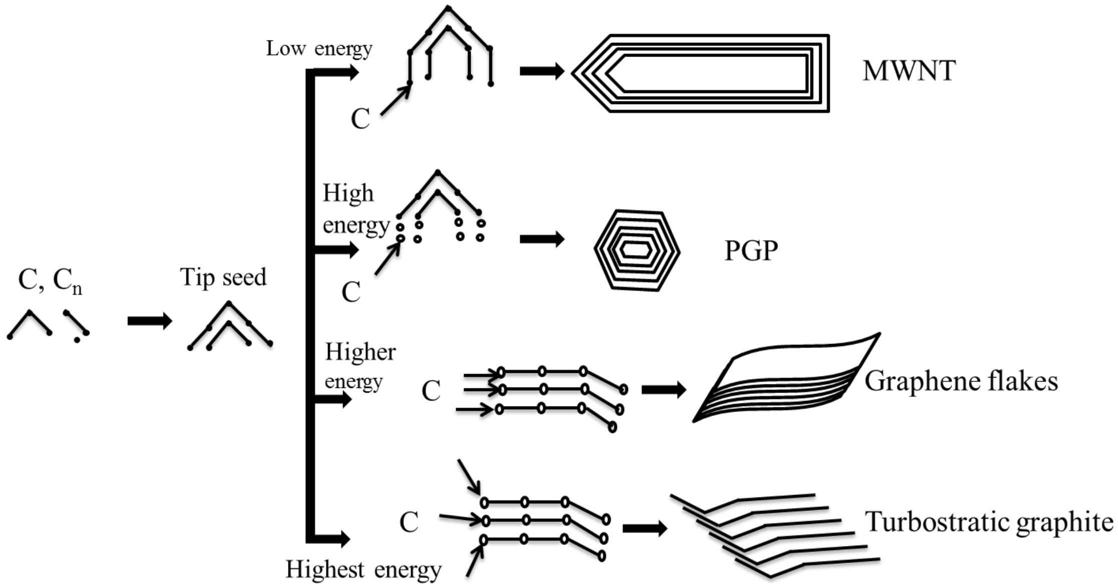

Fig. 5.26 Mechanism for the formation of carbon nanomaterials in the cathode deposit by arc discharge method.

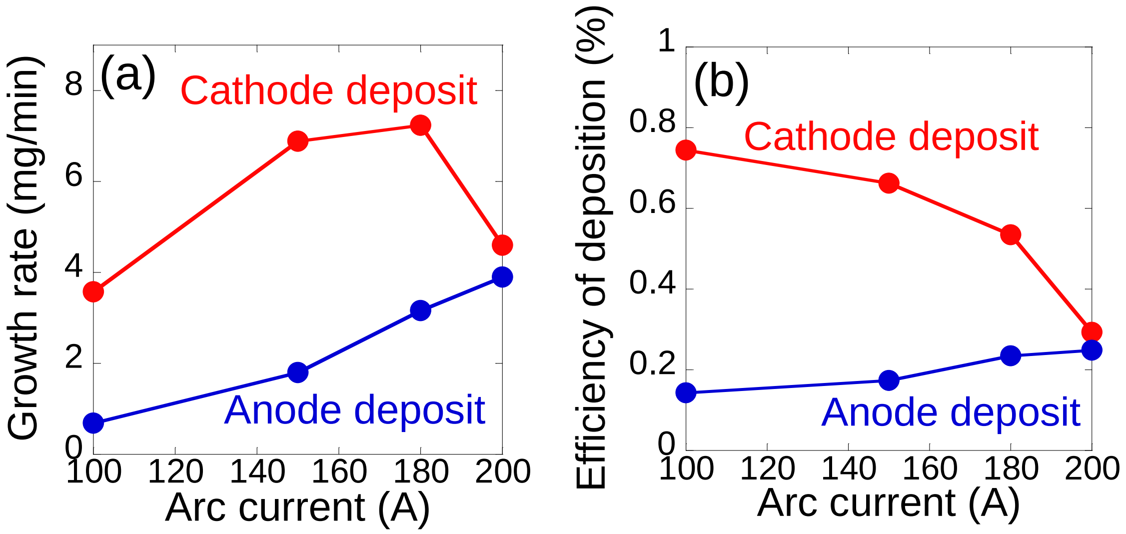

Fig. 5.27 The growth rate of cathode deposit and anode deposit (a) and the efficiency of deposition (b) with changing the arc current.

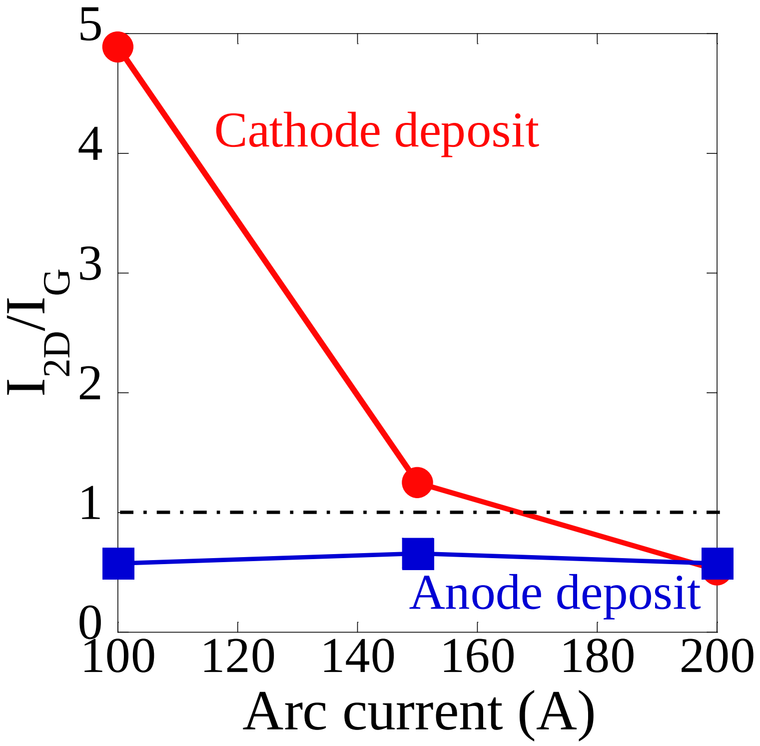

Fig. 5.28 Comparison of the Raman spectroscopy of cathode deposit with anode deposit according to the ratio of the integrated intensity of the 2D band relative to the G band (I_{2D}/I_G).

6. Conclusions

6.1 Summary and Conclusion of Dissertation

The objective of the present study is to investigate two important electrode phenomena, the electrode temperature and the arc-anode attachment by using DC arc discharge method for nanoparticle preparation. Nickel and carbon as raw materials were selected due to their potential applications. Anode surface temperature was measured by two-color pyrometry combined with a high-speed camera which employs suitable band-pass filters during discharge. Therefore, nanoparticle was selectively synthesized by investigating the relationship between arc-anode attachment mode and anode temperature.

In chapter 1, the arc-anode attachment and the electrode temperature as two important electrode phenomena were mentioned in DC arc discharge method. The research direction of the nanoparticles synthesis by thermal plasmas was reviewed after the brief introduction of the principal thermal plasmas process. Especially, the synthesis nanomaterial by thermal plasmas was reviewed. The formation mechanisms of carbon nanomaterial were presented by arc discharge method. At last, the objective of this dissertation was introduced.

In chapter 2, the relationship between arc-anode attachment mode and the temperature of anode surface was investigated when using DC arc discharge method to prepare nickel nanoparticle. Diffuse, multiple, and constricted modes were observed in helium and argon arcs. The attachment mode transitions from diffuse mode to constricted mode when increasing hydrogen concentration. The average particle size increases when the attachment mode transitions from diffuse mode to constricted mode. Nickel nanoparticles with large productivity and small size distribution were obtained in helium arc. The average nanoparticles size of 40 nm with a narrow size distribution can be obtained by controlling shield gas flow rate in helium arc.

In addition, anode surface temperature in helium arc was measured by two-color pyrometry combined with a high-speed camera which employs suitable band-pass filters. Anode surface with high temperature was obtained in constricted mode, due to the constriction of arc spot. The anode jet variation follows the highest temperature variation. The cathode jet variation is opposite to anode jet variation. In multiple attachment mode, the variation of cathode jet follows the arc current variation. In contrast, the cathode jet variation could not follow the arc current variation in constricted mode. The formation mechanism of attachment mode was considered to result from the evaporation of anode material. Understanding the relationship between attachment mode and temperature helps us to prepare nanoparticles with well-controlled of size by controlling arc-anode attachment mode.

In chapter 3, the relationship between arc-anode attachment mode and the temperature of carbon electrode was investigated. Multiple and diffuse arc-anode attachment modes were observed in helium and argon arcs. The arc spot has the frequency around 10 kHz in multiple attachment mode for helium and argon arcs. However, the arc spot moves with a constant frequency in the diffuse attachment mode of helium arc. In contrast, no significant rotation of arc spot rotation was observed in diffuse attachment of argon arc, due to relatively stable of arc.

The temperature of carbon electrode was successfully measured by using two-color pyrometry. The highest temperature in helium arc is higher than that of argon arc, although the input power in argon arc is higher than helium arc. The main reason is the constriction of helium arc, and different arc behaviors between helium and argon. And the temperature behavior is decided by arc-anode attachment mode. The heat flux is low in diffuse attachment when the input power is same. Arc-anode attachment mode and temperature behavior in carbon electrode provide a new way to investigate the formation mechanism of carbon material by DC arc discharge method.

In chapter 4, the formation mechanism of carbon nanomaterial on the anode deposit was investigated. Nano-graphite particles, MWNT, and pyrolytic graphite were prepared at different positions of the anode deposit. In addition, the necklace-like carbon and spherical carbon particle were obtained on the anode surface. According to the temperature distribution of anode surface, deposition temperatures of pyrolytic graphite, MWNT and nano-graphite particles are in the range of 2400 to 2600, 2600 to 2700, and over than 2700 K, respectively. In addition, the deposition temperature of necklace-like carbon and spherical carbon particle is about 1200 K and 600 K, respectively. Efficient quenching effect contributes to the formation of thermodynamically stable material. Moreover, the MWNT was growth in the temperature range of 2600 to 2700 K, indicating that the suitable quenching effect is the necessary condition for the formation of MWNT rather than the catalyst or the hydrogen.

The effect of arc-anode attachment mode on the purity of carbon material on the anode deposit was investigated. Carbon nanomaterial with low purity on the special position of the anode deposit was obtained due to the large temperature fluctuation caused by the rotation of arc spot in diffuse attachment mode.

In chapter 5, the formation mechanism of carbon nanomaterial on the cathode deposit was investigated. PGPs, MWNTs, graphene flakes, and turbostratic graphite were selectively synthesized in the cathode deposit. The products are MWNTs, PGPs and defect PGPs, corresponding to the arc currents of 80, 100, and 150 A, respectively, at the fixed electrode gap distance of 1 mm and anode diameter of 30 mm. The products are PGPs, MWNTs and high-purity MWNTs when the anode diameters are 30, 15, and 10 mm, respectively, at the fixed arc current of 100 A and electrode gap distance of 1 mm. Graphene flakes and turbostratic graphite were obtained at large electrode gap distance. The formation mechanism of these carbon nanomaterials was suggested based on the OES results. Carbon precursors with higher energy contribute to the formation of thermodynamically unstable materials. Furthermore, it provides an idea that the energy of the precursors could be used to control the different carbon allotropes in arc discharge method. The optimum experimental condition for preparing different carbon nanomaterials was summarized by comparing the anode deposit with the cathode deposit.

6.2 Future Research Subjects

DC arc discharge method was employed to prepare nickel nanoparticle and carbon nanomaterial by investigating the anode temperature and arc-anode attachment mode. Topics for future research are as follows:

6.2.1 Further Investigation of Metal Nanoparticle Syntheses

For industrial application, investigation of the optimum condition with large productivity and good arc stability is needed for applying DC arc discharge method to prepare metal nanoparticles. For example, the effects of electrode gap distance, arc current, gas species, and raw material on formation of different arc-anode attachment modes need to be investigated. In addition, some external methods need to be developed to control the arc, such as improvement of the setup or application of external magnetic field. Better controlling the arc contributes to apply DC arc discharge method to prepare nanomaterial with high-volume production and good uniformity.

6.2.2 Further Investigation of Carbon Nanomaterial Syntheses

Investigate the reason of arc spot rotation deeply. Using external magnetic field will help us to understand this phenomenon very well. Similar to metal nanoparticle syntheses, controlling the arc should be conducted for applying this method to prepare carbon nanomaterial with high-volume production. Therefore, the carbon nanomaterial can be synthesized selectively very well by controlling the arc behavior.

Quenching rate plays an important role in the formation of carbon nanomaterial by arc discharge method, one solution to calculate the quenching rate more precisely is needed for better understanding the growth mechanism of carbon nanomaterial. In addition, the effect of gas species on the formation different carbon nanomaterials contributes to understand the formation mechanism of these carbon nanomaterials. Especially, the effect of hydrogen on the formation carbon nanomaterial is still unclear. For example, some reports about using hydrogen to synthesize graphene flakes, however, the real function of hydrogen on the formation of graphene flakes is still unclear. It will be a big improvement if graphene flakes can be synthesized by DC arc discharge method with high-volume production and good controllability.

At last, the potential applications of nickel nanoparticle and carbon nanomaterial will be investigated. Especially, the application of PGP is an attractive field, since the report about application of PGP is limited.

Acknowledgements

I would like to express my sincere appreciation to my supervisor, Dr. Takayuki Watanabe, Professor of the Department of Environmental Chemistry and Engineering, Tokyo Institute of Technology, for his assistance, stimulating suggestions, constant encouragements, and kind support throughout my Ph.D. study. His research philosophy and methodology give me deep impression. Importantly, I have learnt a lot from him, I am sure, which will be especially useful at my different life stages. I am really grateful for his suggestive and the fruitful discussion.

I would like to express my appreciation to Dr. Toshihide Baba and Dr. Takeo Yamaguchi, Professors of the Department of Environmental Chemistry and Engineering, Tokyo Institute of Technology, for their assistance, constructive suggestions, and useful comments in finalizing this thesis. I would also like to express my appreciation to Dr. Akitoshi Okino, Associate Professor of the Department of Energy Sciences, Tokyo Institute of Technology, for his constructive suggestions. I would like to express my appreciation to Dr. Haruro Ishitani, lecture of the Department of Environmental Chemistry and Engineering, Tokyo Institute of Technology, for his valuable suggestions.

I am also grateful to Dr. Manabu Tanaka, a special assistant professor of the Department of Environmental Chemistry and Engineering, Tokyo Institute of Technology. I cannot forget the comments, cooperation, help and the deep discussion at midnight. I have learnt much detail about research from Dr. Manabu Tanaka.

Also, I must express my appreciation to Dr. Sooseok Choi, a special assistant professor of the Department of Environmental Chemistry and Engineering, Tokyo Institute of Technology, who helped me in various ways. Suggestion and encouragement given to me are memorable.

It is necessary to mention that my cordial thanks should be given to all the staffs and

members of Watanabe lab for their cooperation and help. Especially, I am grateful to Ms. Cheng and Ms. Liu for enjoying academic researching and daily life together. I am very pleased to express my gratitude to Mr. Tasuku Shimizu, for cooperative research in Chapter 2 of this doctor thesis.

The financial support from the Ministry of Education, Science and Culture of Japan (Monbusho Scholarship), is highly acknowledged.

Finally, I would like to express my sincere gratitude to my family and friends for their love, tolerance, understandings, and heartfelt support.

January, 2014

Feng Liang